

# Sheffield Hallam University

*Bondcoat developments for thermal barrier coatings*

JONES, Robert Edward

Available from the Sheffield Hallam University Research Archive (SHURA) at:

<http://shura.shu.ac.uk/3137/>

## A Sheffield Hallam University thesis

This thesis is protected by copyright which belongs to the author.

The content must not be changed in any way or sold commercially in any format or medium without the formal permission of the author.

When referring to this work, full bibliographic details including the author, title, awarding institution and date of the thesis must be given.

Please visit <http://shura.shu.ac.uk/3137/> and <http://shura.shu.ac.uk/information.html> for further details about copyright and re-use permissions.

CITY OF S.S. POIN STREET,  
SHEFFIELD, S<sup>Y</sup> WB.

101 610 869 9



**REFERENCE**

ProQuest Number: 10697191

All rights reserved

INFORMATION TO ALL USERS

The quality of this reproduction is dependent upon the quality of the copy submitted.

In the unlikely event that the author did not send a complete manuscript and there are missing pages, these will be noted. Also, if material had to be removed, a note will indicate the deletion.



ProQuest 10697191

Published by ProQuest LLC (2017). Copyright of the Dissertation is held by the Author.

All rights reserved.

This work is protected against unauthorized copying under Title 17, United States Code  
Microform Edition © ProQuest LLC.

ProQuest LLC.  
789 East Eisenhower Parkway  
P.O. Box 1346  
Ann Arbor, MI 48106 – 1346

# **BONDCOAT DEVELOPMENTS FOR THERMAL BARRIER COATINGS**

**ROBERT EDWARD JONES**

A thesis submitted in partial fulfilment of the  
requirements of Sheffield Hallam University for the  
degree of Doctor of Philosophy

March 1999

Collaborating Organisations: Rolls-Royce plc  
Chromalloy UK Ltd

## Abstract

The prime design considerations for modern nickel based superalloys for use in aero gas-turbine engines, are those of mechanical performance, namely good resistance to creep and fatigue with good toughness and microstructural phase stability. Design of the current generation of superalloys has attained these properties at the expense of environmental resistance. This design philosophy has led to the widespread use of surface coatings technology to protect hot-section componentry from the harsh operating environment. The ongoing drive towards higher operating temperatures has led to an interest, over the last few years, in thermal barrier coatings (TBCs). TBCs are duplex coating systems consisting of a thin, insulating, ceramic layer over a metallic bondcoat. The bondcoat provides both environmental protection and the necessary adhesive interface to maintain the adherence of the ceramic during the rigours of operation. Central to the performance of a TBC system is the integrity and adherence of the alumina scale promoted by the bondcoat.

This study aimed to design and optimise a novel bondcoat system that was capable of out-performing the current generation of bondcoats and progress the resultant coating into a production ready status.

This was achieved by comparing the performance of a range of bondcoats of both novel and standard compositions, using the modified scratch test in conjunction with hot isothermal and cyclic furnace tests. The down selected system was then analysed using a range of techniques including optical and electron microscopy, XRD, WDS and SIMS in order to understand the failure mechanisms. The results of the testing programme lead to bondcoat chemistry changes and processing improvements that enabled better performance to be achieved. The bondcoat was optimised and taken to a production standard by using the Taguchi Method of fractional factorial experimental design.

The resultant coating system offered a higher TBC/bondcoat interface temperature capability and extended the life of the system at more moderate temperatures, beyond that offered by systems currently available. The coating system has subsequently been run as a bondcoat for EB-PVD TBCs and has successfully completed the duty cycles on a number of development and test engines.

## Acknowledgements

I would like to express my thanks to everybody who helped me throughout the course of this study, especially my director of studies Dr. Jess Cawley (Sheffield Hallam University), and my industrial supervisor Dr. David Rickerby (Surface Treatment and Coatings Group, Rolls-Royce plc) for their invaluable guidance and encouragement.

I must also thank those members of the project who were roped in to help me, namely Mr. Alan Johnstone, Mr. Jon Higgins and Mrs. Debbie Crofts (Surface Treatment and Coatings Group, Rolls-Royce plc), Mr. John Green, Mr. Rod Wing and Mr. Andy McMillan (Chromalloy UK), Mr. Frank Cullen and Mr. John Fairchild (AEA Technology Harwell). Particular thanks must go to Dr. Gary Fisher (Westaim, Canada) for his help and friendship whilst seconded to Rolls-Royce plc during his own doctoral studies.

Finally, the love, support and encouragement of Linda, my family and friends cannot be under-estimated or over-praised and I am sure I couldn't have done it without them.



LEVEL 1

# Contents

	<u>Page</u>
<b>Chapter 1 – Introduction</b>	1
<b>Chapter 2 – Thermal Barrier Coatings and Component Design</b>	4
2.1 – Designed-in TBCs	5
2.2 – Component Development	6
<b>Chapter 3 – Literature Review</b>	8
3.1 – Superalloy development and the metallurgy of superalloys	8
3.1.1 – The matrix, $\gamma$ - phase	9
3.1.2 – Precipitation hardeners, $\gamma'$ – phase $\text{Ni}_3(\text{Al,Ti})$	10
3.1.3 – Carbide formers	11
3.1.4 – Secondary phases	13
3.1.5 – Processing techniques	14
3.2 – High temperature protective coatings	17
3.2.1 – Diffusion coatings – aluminides	17
3.2.1.1 – High aluminium activity aluminising	19
3.2.1.2 – Low aluminium activity aluminising	19
3.2.1.3 – Limitations of aluminide coatings	20
3.2.2 – Platinum modified aluminides	20
3.2.3 – Overlay coatings	22
3.2.4 – Thermal barrier coatings	23
3.3 – The nature of bonding	27
3.3.1 – Why $\alpha$ -alumina?	27
3.3.1.1 – What is $\alpha$ -alumina?	27

3.3.1.2 – Formation of $\alpha$ -alumina	28
3.3.1.3 – Failure of alumina scales	30
3.3.2 – Active element additions	32
3.3.3 – The effect of sulphur	34
3.4 – Thermal spray coating deposition	36
3.4.1 – Flame spraying	37
3.4.2 – Plasma spraying	38
3.4.2.1 – Plasma generation	39
3.4.2.2 – The plasma–particle interaction	40
3.5 – Sputter processing	42
3.6 – Electron beam - physical vapour deposition	43
3.7 – Method improvements	44
3.7.1 – Optimisation of the LPPS processing technique	44
3.7.2 – The Taguchi Method	45
3.7.2.1 – Assessment of results	46
3.7.2.2 – Interactions	47
<b>Chapter 4 – Bondcoat Developments</b>	<b>49</b>
4.1 – Assessment of bondcoat systems – phase 1	50
4.2 – Testing techniques	51
4.2.1 – Isothermal furnace testing	51
4.2.2 – Sample preparation	52
4.2.3 – Adhesion testing	53
4.2.3.1 – The pull-off test	54
4.2.3.2 – The conventional scratch test	54

4.2.3.3 – The modified scratch test	56
4.2.3.4 – Conventional scratch test theory and the modified scratch test	57
4.2.3.5 – Investigation into the onset of interfacial cracking	58
4.2.4 – Using the modified scratch test	59
4.2.5 – Cyclic furnace testing	60
4.2.5.1 – The cyclic furnace	61
4.3 – Sensitivity of TBCs to substrate materials	64
4.3.1 – testing procedure	65
4.3.2 – Identification of failure mechanisms	67
4.3.3 – Oxidation rates	67
4.3.4 – EPMA of bulk elemental diffusion	68
4.3.5 – Identification of critical elements	70
4.3.6 – Role of titanium in TBC degradation	71
4.3.7 – Reducing the effect of titanium	74
<b>Chapter 5 – Characterisation of the MCrAlY+Pt bondcoat</b>	77
5.1 – Optical metallography of the MCrAlY+Pt bondcoat	77
5.2 – WDS analysis of the MCrAlY+Pt bondcoat	79
5.3 – XRD analysis of the MCrAlY+Pt bondcoat	80
5.4 – Summary of P-phase	81
5.5 – Reactive element distribution in MCrAlY coatings	82
5.5.1 – Yttrium/yttria identification in MCrAlY coatings	83
<b>Chapter 6 – Improvements to the MCrAlY+Pt processing</b>	85
6.1 – Effect of peening on MCrAlY microstructure	85

6.1.1 – Polishing of MCrAlYs	86
6.1.2 – Re-assessment of the peening process	89
6.1.3 – Experimental procedures	88
6.1.4 – Conclusion and discussion regarding MCrAlY finishing	90
6.2 – Optimisation of the spraying parameters using the Taguchi Method	92
6.2.1 – Experimental method	93
6.2.2 – Identification of variables	94
6.2.3 – Identification of potential interactions	95
6.2.4 – Selection of the orthogonal array	95
6.2.4.1 – Phase 1	95
6.2.4.2 – Phase 2	96
6.2.4.3 – Phase 3	98
6.2.5 – Identification of responses	100
6.2.5.1 – Phase 1	100
6.2.5.2 – Phases 2 and 3	101
6.2.6 – Completion of the experiments	102
6.2.6.1 – Phase 1	102
6.2.7 – Assessment of the results of the experimental design	103
6.2.7.1 – Phase 1	103
6.2.7.2 – Phase 2	107
6.2.7.3 – Phase 3	108
6.3 – Effect of MCrAlY thickness on TBC performance	111
6.3.1 – Testpiece manufacture and testing	112
6.3.2 – Limits of the MCrAlY+Pt bondcoat system	113

6.4 – Effect of heat treatment on TBC performance	114
6.4.1 – Scratch testing of the heat treatment trials	115
6.5 – Peening for quality assurance	116
6.5.1 – Assessment of the peened samples	117
6.6 – Grit blasting for improved TBC adhesion	118
6.6.1 – New grit blasting parameters	119
<b>Chapter 7 – Improvements to the MCrAlY+Pt system</b>	122
7.1 – Alternatives to Pt	123
7.1.1 – Production and analysis of testpieces	124
7.1.2 – Discussion Precious Metal Additions to MCrAlYs	128
<b>Chapter 8 – The effects of the MCrAlY composition on bonding</b>	129
8.1 – MCrAlY compositions	129
8.1.1 – Sample preparation and testing	130
8.1.2 – Analysis of the results	131
<b>Chapter 9 – Discussion</b>	134
9.1 – Introduction	134
9.2 – Bondcoat developments	134
9.3 – The effect of substrate chemistry	145
9.4 – Definition of P-phase	148
9.5 – Improvements to the MCrAlY system	149
9.6 – Variations to the CoNiCrAlY+Pt bondcoat	155
<b>Chapter 10 – Conclusions</b>	157
10.1 – Bondcoat developments	157
10.2 – Adhesion testing	157

10.3 – Sensitivity of TBCs to substrate materials	158
10.4 – Characterisation of the MCrAlY+Pt bondcoat	158
10.5 – Improvements to MCrAlY+Pt processing	159
10.6 – Improvements to the MCrAlY+Pt system	160
10.7 – The effects of MCrAlY composition on bonding	160
10.8 – Overall conclusions	160
<b>Chapter 11 – Future Work</b>	<b>162</b>
11.1 – Bondcoat improvements	162
11.2 – Hot corrosion testing	163
11.3 – Component lifing	164
<b>Figures</b>	<b>165</b>
<b>References</b>	

## Figures

	<u>Page</u>
<b>1.1:</b> Diagram of engine development and associated rise in turbine temperature	165
<b>1.2:</b> A state of the art TBC system	166
<b>1.3:</b> Schematic of the research programme	167
<b>1.4:</b> Aged components before and after bondcoat development programme TBC spalled	168
<b>2.1:</b> Design considerations required for a fail-safe component	168
<b>3.1:</b> Tertiary schematic indicating the relative solubilities of elements in the $\gamma'$ -phase	169
<b>3.2:</b> Etched micro specimen indicating the cubic $\gamma/\gamma'$ structure of a Ni-based superalloy	169
<b>3.3:</b> Tertiary schematic representing the effect of composition on oxide formation	170
<b>3.4:</b> Schematic graph comparing the relative performance of coating compositions	170
<b>3.5:</b> Partial phase diagram of the $ZrO_2$ - $Y_2O_3$ system	171
<b>3.6:</b> Schematic of the cross-sectional structure of the bonding $Al_2O_3$ scale in a typical TBC system	172
<b>3.7:</b> (a) Diagram of the build up a thermally sprayed deposit (b): Micrograph of the structure of a thermally sprayed deposit	173
<b>3.8:</b> Diagram of the temperature profile within a plasma plume	174
<b>3.9:</b> Diagram comparing the energy content of a gas to its temperature	174
<b>3.10:</b> (a) Graph of gas velocity against distance in a plasma plume (b) Graph of gas temperature against distance in a plasma plume (c) Graph of gas enthalpy against distance in a plasma plume	175
<b>3.11:</b> Graph of temperature against distance for different operating pressures in a plasma plume	176
<b>3.12:</b> Schematic of an EB-PVD coating rig	176
<b>4.1:</b> Sample identification for phase 1 of the programme	177
<b>4.2:</b> The polishing procedure used for examination of metallic bondcoats	178

<b>4.3:</b> The polishing procedure used for examination of ceramic top coats	178
<b>4.4:</b> Micrograph of scratch track through the bondcoat/TBC interface	179
<b>4.5:</b> Graph of crack extension vs. normal load showing the typical spread of results for one sample. Critical load to cause failure = $20N \pm 5N$	179
<b>4.6:</b> Results from the initial phase of the bondcoat selection procedure	180
<b>4.7:</b> Compositions of superalloys	181
<b>4.8:</b> Scratch test results for an MCrAlY bondcoat on two different substrates after exposure for 25 hours	181
<b>4.9:</b> Oxide thickening rates for the same bondcoat on two different substrates	182
<b>4.10:</b> Schematic of the WDS ladder scan process showing the path of the rastered beam on a 10A peened MCrAlY bondcoat system	182
<b>4.11:</b> WDS traces for Ti and Ta from the MCrAlY/CMSX-4 system in the as processed and aged states	183
<b>4.12:</b> WDS traces for Ti and Ta from the aged MCrAlY/MarM002 system	184
<b>4.13:</b> Schematic representation of the relative time to spall for an MCrAlY bondcoat on different substrate materials	184
<b>4.14:</b> WDS traces for Ti and Ta for the aged MCrAlY/C1023 system	185
<b>4.15:</b> Detail of the TGO in a TBC system showing evidence of debonding	186
<b>4.16:</b> SEM micrographs showing detail from (a) the underside of the spalled $ZrO_2$ (TGO still adherent) (b) the surface of the bondcoat after TBC loss	186
<b>4.17:</b> EDX analysis of a sheared off oxide peg	187
<b>4.18:</b> SEM image of an etched bondcoat showing grain boundary transport of substrate elements	188
<b>4.19:</b> Schematic of oxide-peg and void growth	189
<b>4.20:</b> Comparison of the relative adhesion levels of MCrAlY based bondcoat systems	190
<b>4.21:</b> WDS ladder scan traces of the NiCr/CrC + MCrAlY system as processed and after 25 hours at $1150^\circ C$	191

<b>5.1:</b> MCrAlY+Pt as processed	192
<b>5.2:</b> MCrAlY+Pt as processed (etched)	192
<b>5.3:</b> (a-e) MCrAlY+Pt after 25hour isothermal soaks at 1100, 1150, 1170, 1190 and 1210°C respectively	193
<b>5.4:</b> Schematic of the Al exchange during the ageing of the MCrAlY+Pt system	194
<b>5.5:</b> WDS ladder scans of MCrAlY+Pt	195
<b>5.6:</b> BSE image of the MCrAlY+Pt system	196
<b>5.7:</b> Composition of P-phase by WDS analysis	196
<b>5.8:</b> WDS analysis showing how the compositions of the phases identified in Figure 5.7 vary on exposure to temperature	197
<b>5.9:</b> XRD analysis of MCrAlY+Pt in the as processed condition	198
<b>5.10:</b> Table of $2\theta$ , Å, intensity from XRD data for P-phase	199
<b>5.11:</b> SIMS images of the CoNiCrAlY+Pt coating system	199
(a) $Y_{(metal)}$ distribution – $O^+$ primary beam	
(b) $Y_2O_3$ distribution – $Ar^+$ primary beam	
<b>5.12:</b> Colour enhanced WDS maps of yttrium and oxygen in three standards of MCrAlY	200
<b>6.1:</b> Typical as-sprayed MCrAlY surface finish	201
<b>6.2:</b> Fully processed MCrAlY showing detail of surface “rag” entrapped due to peening	201
<b>6.3:</b> Indication of the effect of oxidation around surface rag on the remnant aluminium content of the coating	202
<b>6.4:</b> Comparison of 10A peened (a) and polished (b) MCrAlY microstructures	202
<b>6.5:</b> SEM image of a sample deeply etched in Br/CH <sub>2</sub> OH showing surface connected oxide (high relief)	203
<b>6.6:</b> Peening media, intensities and coverage used during the initial peening trials	204
<b>6.7:</b> Comparison of the microstructures of the MCrAlY used for the peening trials	204
<b>6.8:</b> Idealised micro-hardness analysis through the thickness of the MCrAlY	205

coating	
<b>6.9:</b> Micro hardness profiles demonstrating the effect of processing on an MCrAlY coating	205
<b>6.10:</b> Schematic of an LPPS system and associated variable parameters	206
<b>6.11:</b> $L_{12}$ ( $2^{11}$ ) orthogonal array (1 = low setting, 2 = high setting)	207
<b>6.12:</b> $L_8$ ( $2^7$ ) orthogonal array and linear graphs	207
<b>6.13:</b> $L_8$ ( $2^7$ ) orthogonal array showing factor levels and location of interacting factors	208
<b>6.14:</b> $L_{16}$ (b) 4/2 mixed level array and linear graphs	209
<b>6.15:</b> Schematic of coated testpiece and coating density calculation	210
<b>6.16:</b> $L_{12}$ array showing the order of experiments and factor levels	211
<b>6.17:</b> $L_4$ ( $2^3$ ) array	212
<b>6.18:</b> Measured responses and calculated average effects for the $L_{12}$ array	213
<b>6.19:</b> (a-c) Average response graphs for phase 1 of the Taguchi design for density, surface roughness and $\beta$ -depletion	214
<b>6.20:</b> Suggested optimal spraying parameters from phase 1	215
<b>6.21:</b> Measured responses and calculated average effects for the $L_8$ array	215
<b>6.22:</b> (a-b) Average response graphs for $\beta$ -depletion and sprayability for phase 2 of the Taguchi design	216
<b>6.23:</b> Measured responses and calculated average effects for the $L_{16}$ array	217
<b>6.24:</b> (a-b) Average response graphs for the $L_{16}$ array for $\beta$ -depletion and sprayability	219
<b>6.25:</b> Comparison of the optimised and the original LPPS parameters	220
<b>6.26:</b> Optimised spraying parameters by the Taguchi Method	220
<b>6.27:</b> Number of cycles to cause spallation of the TBC from different thicknesses of MCrAlY – average result on right	221
<b>6.28:</b> (a-c) Micrographs of the MCrAlY thickness optimisation trials	221

<b>6.29:</b> Thin MCrAlY +Pt	222
<b>6.30:</b> Scratch testing results from MCrAlY thickness optimisation trials	222
<b>6.31:</b> Matrix of the peening media, intensities and coverage used in phase 2 of the peening optimisation	223
<b>6.32:</b> (a-b) Comparison of the surface finishes produced by peening with ceramic bead and steel shot respectively	223
<b>6.33:</b> $\beta$ -depletion distribution chart for phase 2 peening trials	224
<b>6.34:</b> Surface EDX analysis showing detail before (blue) and after (red) citric acid washing	224
<b>6.35:</b> EDX analysis before and after grit blasting demonstrating the removal of surface contamination	225
<b>6.36:</b> Table of parameters used during grit blasting optimisation trials	225
<b>6.37:</b> Graphs of weight loss against time showing the effects of pressure and distance respectively	226
<b>7.1:</b> Graph of the empirical relationship between a number of metal/ceramic diffusion bonds	227
<b>7.2:</b> Table of precious metal coating systems assessed	227
<b>7.3:</b> (a-d) Micrographs of the systems based on alternatives to Pt	228
<b>7.4:</b> Comparison of the compositions of the P-type phases shown in Figure 7.3	229
<b>7.5:</b> Detail of the oxide formed on the MCrAlY+Ir system after 25 hours at 1100°C	230
<b>7.6:</b> Phase stability of P-phase showing the effect of the addition of Rh	230
<b>7.7:</b> BSE micrograph of the Rh enhanced P-phase	231
<b>8.1:</b> Compositions of the MCrAlY type coatings examined	231
<b>8.2:</b> (a) Coating A as processed	232
(b) Coating B as processed	
(c) Coating A after 25h @ 1150°C	
(d) Coating B after 25h @ 1150°C	
<b>8.3:</b> Scratch test results for coatings A and B	232
<b>8.4:</b> Compositions of phases in coatings A and B as processed and aged	233

<b>8.5:</b> XRD traces of coating A and B in the as processed condition	234
<b>9.1:</b> BSE image of Optimised MCrAlY+Pt and EDX analysis of the dark-contrast yttrium rich particulate	235
<b>9.2:</b> Comparison of the $\beta$ -depletion zones of (a) EB-PVD and (b) Taguchi optimised LPPS MCrAlYs after 25 hours at 1100°C in air	236
<b>9.3:</b> Detail of a deep etched MCrAlY showing Y <sub>2</sub> O <sub>3</sub> pegs	236
<b>9.4:</b> SIMS images of Y and Y <sub>2</sub> O <sub>3</sub> in the Taguchi optimised MCrAlY+Pt system	237

## Chapter 1 - Introduction

Within the civil aerospace industry there is a drive towards operating twin engined, high capacity passenger aircraft on long haul flights, predominantly transatlantic and pacific rim. This, coupled with the future market for even larger aircraft, ensures that there must be rapid development and growth of high power, fuel efficient and reliable aero-gas turbine engines.

Figure 1.1 demonstrates how the thrust requirement, from the Rolls-Royce gas turbine engines, has changed over time and how much more powerful it is predicted that the new series of engines must be in order to compete in the market. The increase in thrust rating of these engines is mirrored by the increase in turbine entry temperature (TET), the temperature of the gas stream on entering the high-pressure turbine stage. Improvements in the compression ratio, coupled with improved component design have enabled the fuel burn temperatures to be increased. The resultant boost to the temperatures, within the high-pressure turbine stage, had allowed greater power to be extracted from the hot gas flow and therefore more powerful engines with reduced specific fuel consumption (SFC) to be developed.

The downside to the rapid growth in TET and power output is the difficulty of superalloy design in keeping pace with extreme conditions experienced within the high-pressure (HP) turbine. In conventional turbine design a significant percentage of the relatively cool air, from the compressor stage, is diverted to the "hot-section" in order to cool the nozzle guide vanes and turbine blades. The compressor air is fed through

internal cooling passages and bled out across the surface of the component, via cooling holes, to create an insulating boundary layer over the gas washed surfaces. Continual raising of the TET requires the removal of more and more cooling air from the compressor, resulting in a reduction in the compression ratio and hence limiting the ultimate possible performance. Significant reductions in the cooling air requirement can be made through the use of insulating ceramic layers or thermal barrier coatings (TBCs) [1, 2]. The low thermal conductivity of ceramic TBCs means that a significant drop in temperature is possible across them, resulting in a component/TBC interface temperature at a much more tolerable level without the requirement for excessive compressor fed cooling air. Consequently, the compression ratio can be maintained at a higher level, resulting in a marked increase in potential performance.

Any loss of the TBC would result in rapid degradation of the component, because of the increase in the temperature of the metallic component. It is essential, therefore, to maintain a high degree of bonding between the ceramic TBC and the metallic component under all operating conditions. TBC bonding is maintained through selective oxidation of the metallic layer immediately beneath the ceramic to form an interfacial alumina ( $\text{Al}_2\text{O}_3$ ) layer [3, 4]. Superalloy chemistry does not encourage  $\text{Al}_2\text{O}_3$  formation and so coatings have been developed in order to produce the correct surface chemistry. These coatings have traditionally been "borrowed" from environmental protection systems and have been termed "bondcoats".

Figure 1.2 shows a "state of the art" TBC system.

In order to meet the ever more demanding conditions continual development of TBC systems is essential. Potential improvements lie within three distinct areas.

- i) Reduction in the thermal conductivity of the TBC through modifications to the chemistry and structure of the ceramic.
- ii) Development of the oxide chemistry requirements in order that adhesion be maintained at ever increasing temperatures.
- iii) Meeting the requirements made of the oxide through the chemistry and the manufacturing process of the bondcoat.

The work detailed within this thesis relates to the latter point above, and sits within an on-going research programme addressing all aspects of TBC system developments.

This thesis reports on the development of a novel bondcoat chemistry in order that TBC bonding be improved over the systems considered state of the art at the outset of the research programme, and create a rigid manufacturing method capable of providing the coating as a feasible and viable product.

Figure 1.3 outlines the route taken to develop the new bond coat system and take the industry from the unacceptable position, illustrated in Figure 1.4a, forward to the much more acceptable picture seen in Figure 1.4b.

## Chapter 2 – Thermal Barrier Coatings and Component design

At current technology levels, there are two principle methods of producing ceramic TBC coatings at sufficient deposition rates that make them viable production processes.

These are:

- i) Thermal spray processing
- ii) Electron-beam physical vapour deposition (EB-PVD)

These systems, covered in greater detail in Chapter 3, produce coating of very different character and performance. The relative performance of the coatings is predominantly structure controlled. EB-PVD processing produces a coating consisting of columnar grains growing normal to the bonding interface, whilst thermal spraying builds up a coating consisting of interlocking "splats" lying parallel to the sub-surface.

Comparison of the performance of the EB-PVD coatings over that of the thermally sprayed equivalent leads to the following conclusions:

EB-PVD TBCs have:

- i) improved surface finish
- ii) improved strain tolerance
- iii) improved erosion performance
- iv) finer control over coating thickness/distribution
- v) higher production costs

- vi) higher specific thermal conductivity

Provided that the production costs can be reduced or at least accommodated, and the previously mentioned programme of TBC material/coating developments are successful then there is a strong case for selecting the EB-PVD processing route.

## **2.1 – Designed-in TBCs**

Significant experience has been gained within the aero-engine industry with EB-PVD TBCs through the inclusion of "band-aid" technology to hot-section componentry.

Band-aid is a generic term used to describe "patch" coatings applied locally to trouble spots on in-service components where overheating has been proved to be a problem.

This process of enforced introduction of TBCs into engines has not been necessary for Rolls-Royce, which has therefore been allowed the luxury of a comprehensive study of TBC systems which has led to the development of designed-in thermal barriers.

It is only possible through designed-in TBC systems to gain the maximum advantage from the technology at acceptable levels of risk. In order to get the maximum benefit from designed-in TBCs there are several factors that must be addressed.

- i) higher bondcoat temperature capability - the maximum operating temperatures for the TBC/bondcoat interface must approach that of the design limit for the selected substrate material.

- ii) improvements to durability and reliability - the lifetime of TBC systems must be in excess of the scheduled service intervals so that unexpected failures do not threaten engine performance.
- iii) lifing models must be developed in order to predict the limiting operational capabilities of TBC systems allowing for their safe introduction.
- iv) cost reduction - in order that the technology becomes viable it must be economically favourable over competing technology.

## **2.2 – Component Development**

It would be considered too great-a-risk to introduce a TBC reliant turbine blade “blind” into an engine, it is therefore essential to develop a “half-way house” or fail-safe blade design where benefits can be gained from the TBC without total dependency upon it. The turbine blade must be capable of surviving to the service interval without failure, even if the TBC spalled. It is a careful balancing act between turbine blade design and bond coat capability. Figure 2.1 shows the design considerations made to reach a fail-safe design.

The current blade design (1) shows a position of a low surface temperature capability when compared to the ultimate system of a ceramic turbine blade (5), in addition

considerable cooling air is required to maintain the service life of the conventional blade. Increasing the surface temperature capability through the introduction of a TBC, thus lowering the actual temperature seen by the metallic component, moves the blade design to position (2). This does not fully utilise the TBC, however, as there is no set reduction in the cooling air requirement. This type of blade/TBC design should demonstrate very long life times. Reduction in the cooling air moves the blade position to the left, towards position (3). This represents a blade totally reliant on the TBC, loss of which would lead to a significant reduction in the life time and performance of the component. It is this position that must be avoided at this stage of a controlled introduction of TBC technology. A fail safe blade design must sit just to the right of the cut-off line of TBC reliance. Position (4) represents the trade-off position of utilising the TBC whilst still maintaining a "cushion" of cooling air sufficient enough to enable the blade to survive to the next service interval, even if the TBC does fail.

Increases in the bondcoat temperature capability moves the fail-safe design upward to the ideal system, the same is true of developments made to reduce the thermal conductivity of the TBC. Only after experience and confidence is gained through fail safe blade designs can moves be made towards designing TBC reliant turbine blades. It was this goal to which all aspects of this research programme were conducted.

### 3.1 - Superalloy Development - the Metallurgy of Superalloys

The development of the aero gas turbine engine in the 1930s created a need for specific high temperature alloys. The resultant materials were developed from alloys already in existence. The discovery of austenitic stainless steels, in the period between 1910 and 1915, led the way with the face centred cubic (fcc)  $\gamma$ -phase structure. Almost concurrently, work was being carried out in the arena of aerospace design with the development of turbo-superchargers for high altitude internal combustion engines. These were based on materials utilising conventional strengthening mechanisms in ferritic steels [5, 6]. When seen in conjunction with materials from the electrical industry, namely Ni-20% Cr [7], the scene was set for the development of superalloys.

In 1929 a major step forward was made when virtually simultaneously Bedford and Pilling, and Merica [8] added small amounts of Al and Ti to the Ni-20% Cr alloy. Significant improvements to the creep strength of the material were observed. It was not until 1940, however, that the creep strength improvements were explained, through the work of Bradley and Taylor [8], as being due to the presence of the coherent,  $\gamma$ -phase. Most modern superalloys are based on the  $\gamma/\gamma'$  structure first suggested in 1940.

Modern developments and understanding can split superalloy microstructures into four broad areas:

- (i) the matrix,
- (ii) the precipitation strengtheners,
- (iii) carbide formation, and
- (iv) “secondary” phase formation.

### **3.1.1 - The Matrix - $\gamma$ Phase**

Most superalloys are variations on the basic fcc  $\gamma$ -phase, Ni-Cr matrix. The selection of Ni as a base material for superalloy designers comes from the fact that Ni demonstrates increased temperature capability over Fe-based systems. As the current drive is towards hotter environments within the engine, the temperature capability outweighs the lack of inherent creep resistive properties in the Ni-based systems. The high temperature capability of Ni alloys can be partly attributed to the high tolerance of Ni for alloying without phase instability, due to the almost filled 3d-electron orbital. The oxidation resistance of the Ni-Cr alloys is due to the inherent ability to form stable Cr<sub>2</sub>O<sub>3</sub>-rich protective scales. The addition of elements, such as Co, Fe, Cr, Mo, W, V, Al and Ti, create solid solution hardening effects in the  $\gamma$ -phase. These elements differ in atomic size from Ni by between 1 and 13%. This atomic size differential creates a strain in the  $\gamma$ -lattice, inhibiting dislocation movement.

It is significant that some of the elements listed above as solid solution strengtheners can also act as precipitation hardeners, this is most evident in the cases of Al and Ti, the addition of which resulted in the discovery of the  $\gamma'$  precipitation hardening phase.

### **3.1.2 - Precipitation Hardeners, $\gamma'$ -Phase, $\text{Ni}_3(\text{Al, Ti})$**

$\gamma'$  is an ordered fcc phase of the form  $\text{A}_3\text{B}$ , where A represents the major alloying element or elements such as Ni, Co or Fe, and B represents the additions, either singly or in combination of Al, Ti, Ta and Nb. Although Co and Fe can partition to both the  $\gamma$  and the  $\gamma'$  phases, greater stability is achieved through association with the  $\gamma'$ . Most alloys rely on a combination of Al and Ti to form the  $\gamma'$ -phase but it can occur through the addition of Ti alone, ( $\text{Ni}_3\text{Ti}-\gamma'$ ) [6]. Alternatively with the sole addition of Nb, a body-centred tetragonal (bct) or  $\gamma''$ -phase forms [9]. This behaves in a similar way to the conventional  $\gamma$ -phase. Figure 3.1 shows the relative solubilities of elements in the  $\gamma'$  phase. Precipitation hardening mechanisms strengthen the alloy through impeding dislocation movement by creating physical barriers to the glide planes of dislocations. Dislocation energy is then "absorbed" by forcing them to either loop or climb passed the precipitate or to cut through it. This mechanism differs from the solid solution strengthening approach where a greater dislocation driving force is required to overcome the "back-pressure" created by the strain field induced through the lattice mismatch. In order to achieve the maximum benefit from the  $\gamma'$  precipitates, they would be evenly distributed, as a fine dispersion with close inter-particle spacing. The similarity of the  $\gamma$  and  $\gamma'$  phases enables the fine phase separation; the mismatch

between  $\gamma$  and  $\gamma'$  in the  $\text{Ni}_3\text{Al}$  system for example, is as low as 0.05%. The degree of mismatch also accounts for the microstructure of the superalloy. The familiar cubic precipitate structure seen in modern superalloys, as shown in Figure 3.2, is created when the  $\gamma/\gamma'$  mismatch falls between 0.4 and 1%, less than 0.4% mismatch creates a spherical precipitate, whilst mismatch of greater than 1% causes the precipitates to take on a plate-like structure. Whilst spherical and cubic forms of  $\gamma'$  are seen as beneficial, the plate-like structures are considered detrimental to the mechanical properties of the alloy [10, 11].

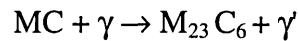
### **3.1.3 - Carbide Formers**

Carbides play a significant role in the performance of many superalloys. Many of the additions made to develop the  $\gamma/\gamma'$  structure are also strong carbide formers, namely Ti, Hf, Nb, Cr and Ta. These form the most commonly seen classes of carbides: MC,  $\text{M}_{23}\text{C}_6$  and  $\text{M}_6\text{C}$ .

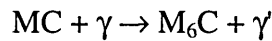
The MC type, being the most stable form, was designed in to act as a "sump" used for slow release of C throughout the life of the component. MC type carbides form with coarse, random cubic or "script", dendritic morphologies, the form of the carbides being controlled by the rate of solidification of the cast alloy. The MC carbides breakdown to form the  $\text{M}_{23}\text{C}_6$  and  $\text{M}_6\text{C}$  structures, this process releases C into the superalloy matrix [12]. In order to prevent excess of these grain boundary carbides forming, Hf additions have been made to superalloy compositions. The Hf "mops-up"

the unwanted C to form stable, intragranular HfC; these form in preference to TaC, NbC and TiC. The degree to which grain boundary carbides form needs to be controlled, as excessive amounts can lead to reduced ductility and creep rupture life.

The controlled breakdown of MC carbides, in early alloys, was critical as it created intergranular layers of dispersion strengthened  $\gamma'$ . This process can be shown through the following equations:



e.g.  $(Ti, Mo)C + (Ni, Cr, Al, Ti) \rightarrow Cr_{21}Mo_2C_6 + Ni_3(Al, Ti)$



e.g.  $(Ti, Mo)C + (Ni, Co, Al, Ti) \rightarrow Mo_3(Ni, Co)_3C + Ni_3(Al, Ti)$

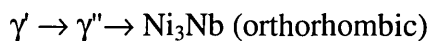
The layers of dispersion strengthened  $\gamma'$  helped to bond grains together, improving the mechanical properties. Trace elements of Zr and B were also added as grain boundary strengtheners, improving the creep-rupture strength in a similar way to the carbides. The effect of greater levels of Hf additions (contorting the grain boundaries to increase the mechanical interlocking of the grains) combined with the move towards directionally solidified and single crystal materials reduced the need for grain boundary carbide strengthening.

The trend during the 1950s towards continuing additions to the complex chemistry of superalloys led to the generation of unwanted secondary phases.

### 3.1.4 - Secondary Phases

The development of alloys with  $\gamma'$  contents in excess of 60%, lead to alloys with structures which changed with time at temperature, resulting in the generation of detrimental phases [13]. Highly alloyed  $\gamma'$  can become metastable and can transform to  $\eta$  (hcp) [11, 14] Although in some cases this phase can add to the hardness of an alloy, in most systems the opposite happens, resulting in soft regions at grain boundaries leading to embrittlement.  $\eta$  can also occur as an intragranular Widmansträten structure, reducing the strength of the alloy [15].

Further alloying additions can be made to reduce the likelihood of the  $\gamma' \rightarrow \eta$  transformation, significantly additions of B can reduce the grain boundary nucleation of  $\eta$ . Some high Nb content alloys have successfully used this transition to harden the alloy through the reaction:

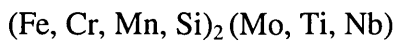


The secondary phase seen to have significant effects on alloys through loss of stress-rupture strength and room temperature ductility is  $\sigma$ -phase. The plate-like structure associated

with  $\sigma$ -phase can be generated in a wide variety of complex alloys, given the correct conditions of stress and temperature. Equally, the structure of the  $\sigma$ -phase can be changed to a less detrimental form or alternatively a reduction to the likelihood of it being formed at all can be made through careful control of heat treatments to the alloy [11, 14].

The last compositionally driven phase discussed here are called Laves phases. Although these phases are generally only seen in Fe containing alloys they are presented here for completeness.

Laves phases are of the form:



and can be seen as blocky, plate-like structures. Excessive concentrations of Laves phases can lead to degradation of room temperature ductility.

As moves were made to optimise superalloy chemistry the above mentioned phases became more commonly seen. Taking a retrograde step in compositional chemistry was impossible due to the increased demands on superalloy materials. The saving grace of superalloy design came through improvements made to processing techniques.

### **3.1.5 - Processing Techniques**

The major revolution in alloy manufacture came about in the early 1950s with the advent of vacuum melting. Vacuum melting allowed greater control of compositions and therefore improved the removal of detrimental alloy impurities. As compositions developed further, it became evident that the main cause of alloy failure was through a lack of ductility brought about by the need for greater percentages of  $\gamma'$ . This lack of ductility led to failure through a creep-rupture of the alloys. Versnyder, Guàrd and Pearcey [8] illustrated that significant improvements could be made through removal of the grain boundaries lying normal to the direction of the applied load. Through careful control of the temperature gradient in the mould, columnar grains could be encouraged to grow, virtually removing the transverse grain boundaries. This process was shown to improve the ductility of an alloy and therefore improved the tertiary creep life. The reduction in the number of grain boundaries impinging the surface of components increases the difficulty and, therefore, the likelihood, of crack initiation. Improvements were therefore seen in the thermomechanical fatigue resistance of "directionally solidified" or DS, over conventionally cast components. The logical progression of this development was the removal of all grain boundaries ultimately leading to single crystal materials.

This process was achieved through two alternative techniques:

- (i) use of seed crystals, and
- (ii) through physical constrictions to DS growth.

Seed crystals initiate solidification of a molten mass by reducing the initiation energy required and hence beginning crystal growth ahead of the bulk of the material.

Physical constraint ahead of the solidification front in DS casting allows only one grain to continue to grow. This single grain then enters the component mould solidifying the casting as a single crystal.

With the advent of single crystal alloys, the need for grain boundary strengthening mechanisms was removed, allowing for higher heat treatment windows. Higher heat treatment temperatures resulted in a more uniform  $\gamma/\gamma'$  distribution, thus improving, still further, the properties of the alloy [13, 14, 16]

The advances made in alloy composition and processing control now allow alloys to operate at temperatures up to 0.9  $T_m$ , within 300°C of their incipient melting points [17]. In order to achieve the ideal mechanical properties, the ability for alloys to resist oxidation and hot corrosion has been sacrificed. The adoption of surface engineering techniques has been critical in order to operate within the extreme conditions experienced in the gas turbine. Coatings which provide resistance to oxidation and corrosion or that reduce the operating temperature of the surface of the components have been designed. These coatings can be separated into three distinct areas, which will be discussed in detail in chapter 3.5:

- (i) diffusion coatings,

- (ii) overlay coatings, and
- (iii) thermal barrier coatings

### **3.2 - High Temperature Protective Coatings**

Despite the developments made in superalloy design, the chemical compositions still remain a compromise between mechanical properties and chemical stability/corrosion resistance. The ideal solution is at present unobtainable from a single material. It has long been appreciated that surface treatments can extend the useful life of components. The original and still most cost effective surface treatment used for superalloys is aluminising; a process by which the surface layers of the superalloy are enriched in aluminium by diffusion of the aluminium species from either a vapour or a chemical pack. Aluminides being the most basic of the high temperature protective systems offer only limited performance at temperatures in excess of 1100°C or in severe corrosive environments. These types of diffusion coatings can be improved by the addition of platinum. Platinum modified aluminides (Pt-Al) have been shown to offer superior oxidation and corrosion resistance, [18], over the more basic systems. Continued development of coatings has led to the complex chemistries seen within overlay coatings.

### **3.2.1- Diffusion Coatings (Aluminide)**

By enriching the surface of a component with Al the system is more likely to form a good, adherent  $\text{Al}_2\text{O}_3$  scale on exposure to high temperatures. Several techniques have been developed in order to achieve this type of surface enrichment, the most basic of which is by pack cementation.

During pack aluminising, the most common method, a component is submerged in a pack consisting of Al powder, an halide activator (typically  $\text{NH}_4\text{Cl}$ ,  $\text{NaCl}$  or  $\text{CF}_2$ ) and an inert powder filler. The airtight container is heated to within the range  $750\text{-}1000^\circ\text{C}$  (depending on the process) for between two and twenty four hours. During this period, the halide activator decomposes and forms a gaseous aluminium halide. When the vapour comes into contact with the surface of the component it dissociates, releasing the halide gaseous ions back into the pack to react with more of the aluminium reserve, leaving behind the aluminium which diffuses into the surface of the component [19, 20, 21].

Economic and environmental considerations as well as performance requirements are driving the industry away from the pack process towards gas-phase and chemical vapour deposition (CVD) techniques. In these systems, the components are supported remote from any powder in a carrier gas with the aluminising species being carried to the component by a vapour transport process. CVD processing takes the concept further by removing the need for a pack by providing all the reactants in gaseous form. There are engineering benefits to be gained from gaseous processes in that intricate

shapes can be coated, such as internal cooling passages without danger of contamination from the pack particles.

There are two mechanisms by which the Al species grows at the surface of the components, these are dependent on both temperature and the aluminium activity of the pack or vapour being used.

#### 3.2.1.1 - High Aluminium Activity Aluminising

In this process lower temperatures are used in conjunction with a high aluminium activity pack. The growth is mainly by inward diffusion of the aluminium, which then reacts with the Ni content of the substrate. The predominant phase produced is  $\text{Ni}_2\text{Al}_3$  with some Al rich  $\beta$  NiAl.

$\text{Ni}_2\text{Al}_3$  is a brittle phase that decomposes at low temperature, this is unsuitable for turbine blade protection but can be modified by heat treatment. The treatment allows further Ni to diffuse from the substrate to the Al rich layer to form  $\beta$ , NiAl. This is a far more ductile and oxidation resistant phase [22]. The resultant microstructure consists of three layers of  $\beta$ -phase with increasing levels of contaminant elements from the substrate [19, 22, 23].

### 3.2.1.2 - Low Aluminium Activity Aluminising

Higher coating temperatures allow Ni to diffuse out from the substrate to react with the Al producing a predominantly outwardly grown coating. This process results in a double layered coating. The outer layer consists mainly of  $\beta$ , NiAl with some other elemental additions from the outward diffusion process [22]. The inner layer consists of mixed phases generated as a result of the localised reduction in the level of Ni present in the superalloy.

### 3.2.1.3 - Limitations of Aluminide Coatings

Alloying elements diffusing out from the substrate during exposure to high temperature environments can poison the protective  $\text{Al}_2\text{O}_3$  scale, increasing its growth rate and decreasing the oxidation performance of the coating. The inward growth nature of high activity processes leads to a greater concentration of detrimental elements in the coatings. The higher contaminant levels lead to a lower level of performance when compared to the low activity processes in oxidation [18]. This effect combined with contamination from lower grade fuel and corrosion from harsh environments lead to the modification of aluminide coatings with Pt group rare earth metal additions.

### 3.2.2 - Platinum Modified Aluminides

Platinum modified aluminide coatings have been shown repeatedly to out perform plain aluminides in simple oxidation and also offer a greater resistance to hot corrosion [19, 20, 24].

Production of a platinum aluminide (Pt-Al) consists of depositing a thin layer of Pt onto the surface of the component prior to the aluminising process. With high activity aluminising processes an outer layer containing a mixture of phases is formed, if the platinum activity is high enough then a continuous outer zone will be formed of PtAl<sub>2</sub> if not, then a  $\beta$ , (Ni,Pt)Al precipitate will be present [20, 25]. As PtAl<sub>2</sub> is hard and brittle then high activity Pt-Al coatings are susceptible to cracking.

As with plain aluminides the low activity Pt-Al coatings out perform the high activity forms. Low activity processing forms an outer layer of PtAl<sub>2</sub> precipitated in a  $\beta$ , (Ni,Pt)Al matrix on top of a Ni rich  $\beta$  phase [20, 26]. Low activity Pt-Al coatings demonstrate higher resistance to thermal fatigue cracking and are less susceptible to rumpling (a surface-creep lead process causing corrugations in the coating) [18].

Pt-Al coatings have been shown to out perform plain aluminides by up to five times in cyclic oxidation tests. There is some debate as to why this is so. Early on in the development it was believed that the Pt would reduce the rate at which Al was lost to the substrate by acting as a diffusion barrier. Although this has been shown to not be the case it is likely that the Pt inhibits the outward movement of elements from the

substrate material. It has been shown that Pt-Al phases promote the slow growth of an extremely adherent alumina scale [27], as Pt does not form an oxide at the operational temperatures of consideration.

Pt does however seem to be peculiar in that no other elements improves the performance of aluminide coatings in the same way. Pd and Rh have been tried in this role, but have not performed as well. This has been put down to hydrogen embrittlement during the coating process.

### **3.2.3 - Overlay Coatings**

Overlay coating systems offer advantages over conventional diffusion coatings as their composition can be tailored to suit the proposed operational conditions. Better thermal fatigue resistance as well as other mechanical properties can be achieved through optimisation of the composition, as can the oxidation or corrosion resistance of the coatings [28]. The presence of reactive elements such as the rare earths and lanthanoids Y, Hf, Ce and La has been demonstrated to significantly increase the cyclic oxidation performance of overlays [24], although the precise role of the elements is disputed. Overlays are typified by the M-CrAl-X type coatings where M represents Ni, Co or Fe (or a combination thereof) and X represents the reactive element additions.

The initial development work was carried out by Pratt and Whitney and Airco Temescal on Co based systems, where the addition of Cr successfully resulted in the lowering of

the Al requirement of the coating whilst retaining the capability to form an  $\text{Al}_2\text{O}_3$  scale. Previous attempts at increasing the Cr content of diffusion coatings had proved difficult due to the low solubility of Cr in  $\beta$ -NiAl (approximately 3%). Al has been shown to increase the ductile to brittle transition temperature (DBTT) of coatings, resulting in poor mechanical properties at temperature [19]. The effect on oxidation of the addition of Cr to a Ni-Al system is shown in Figure 3.3. As can be seen  $\text{Al}_2\text{O}_3$  is still formed when the Al content is as low as 10 at. % when in the presence of as little as 5 at. % Cr. This is beyond the capability of an aluminide coating, where  $\beta$ -NiAl readily decomposes to  $\gamma'$ - $\text{Ni}_3\text{Al}$  and becomes unable to generate an  $\text{Al}_2\text{O}_3$  scale.

MCrAlX coatings are typified by a dual-phase microstructure of a fine dispersion of  $\beta$ -(Ni/Co)Al in a Cr rich  $\gamma$  matrix [29, 35]. The balance between Co and Ni results in differences in performance with regard to oxidation and corrosion as well as the previously mentioned effect on DBTT. Higher levels of Co result in a reduction in DBTT and show an increase in corrosion resistance [30]. The opposite is true for higher Ni contents. This trade off is shown schematically in Figure 3.4.

The most recent developments to overlay systems are targeted at either increasing the oxidation/corrosion resistance through the addition of low levels of reactive elements such as Si, Re and Ta [30, 31, 32, 33] or improving the creep strength by stiffening the coating with carbides and oxides.

The initial overlays were produced by electron beam – physical vapour deposition (EB-PVD) because of the necessity for an oxygen free coating environment; this technique has generally been superseded by vacuum and low pressure plasma spraying (VPS and LPPS) processes. These techniques overcome many of the problems of compositional conformity associated with the EB-PVD process seen when trying to evaporate complex alloys of elements with different vapour pressures.

### **3.2.4 - Thermal Barrier Coatings**

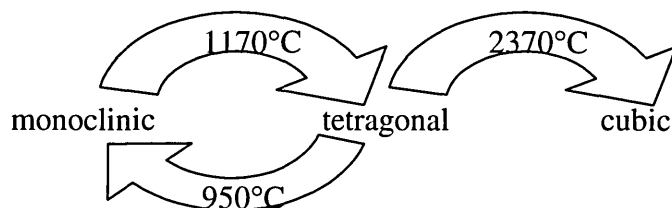
Within this study a thermal barrier coating (TBC) is a thin layer of ceramic insulation applied to the external surface of a hollow, internally cooled turbine aerofoil. A TBC provides performance, efficiency and durability benefits by reducing turbine cooling air requirements and lowering metal temperatures [34, 35]. Currently, components exposed to the hot gas stream, produced by the combustion of the fuel, are cooled from within and across the surface (via cooling holes) with air by-passed from the cool compressor region. The subsequent film of cool air across the surface of the component provides a degree of insulation but at the cost of aerodynamic performance. The use of a TBC can:

- (i) Provide increased turbine gas inlet temperatures whilst maintaining a constant alloy (component) temperature, thus increasing engine efficiency and performance.

(ii) Decrease the use of cooling air in components at constant gas and component temperatures, thus increasing efficiency.

(iii) Decrease alloy/component temperature at constant gas operating temperatures, thus increasing component life and engine reliability [34, 35].

With the overall temperature in the hot zone of the aero-engine increased, the substrate/component materials are at risk of rapid attack should the ceramic TBC spall away. As previously mentioned the most commonly utilised ceramic systems are based on zirconia, which exhibits thermal expansion characteristics similar to superalloy materials. Keeping  $\Delta\alpha$ , the difference in coefficients of thermal expansion of two materials, as small as possible helps to reduce the stresses induced from the thermal cycling experienced during engine operations. Pure zirconia, however, undergoes phase transformations around the operating temperatures seen within aero engines.



[34]

The monoclinic to tetragonal phase change is accompanied by a 3-10% volume change, the stress from which may cause cracking, leading to ceramic loss. Zirconia can be "stabilised" by the addition of compounds such as CaO, MgO or Y<sub>2</sub>O<sub>3</sub>. These additions

stabilise the cubic form of zirconia throughout the operating temperatures seen within the gas turbine engine. Zirconia stabilised with CaO and MgO are, however, shown to destabilise on thermal cycling [36], whilst partially stabilised forms of the Y<sub>2</sub>O<sub>3</sub> additions to zirconia exhibit further benefits over the fully stabilised form. Figure 3.5 shows the ZrO<sub>2</sub>/Y<sub>2</sub>O<sub>3</sub> phase diagram. Although  $\Delta\alpha$  is kept to a minimum by careful material selection, mismatch still occurs. This can lead to two modes of failure in a thermally sprayed TBC. Slow cooling of coated samples, typical of laboratory testing, allows more rapid contraction of the metallic substrate resulting in compressive stresses in the ceramic topcoat. These stresses are relieved by micro cracking of the ceramic parallel to the ceramic/substrate interface. Coalescence of these microcracks can result in bulk material loss. Rapid cooling, as seen in engine service, from the ceramic side of the component causes the ceramic to contract more rapidly than the substrate resulting in tensile forces in the topcoat, these are then relieved by cracking normal to the coating/substrate interface. These cracks allow attack of the substrate but do not lead to ceramic loss [37].

In order to reduce the effect of compressive and tensile stress on the ceramic, an alternative processing route is used. A compositionally similar topcoat is deposited by electron beam - physical vapour deposition (EB-PVD). The microstructure of an EB-PVD ceramic is fundamentally different to that of an air-plasma sprayed ceramic. By tailoring the conditions within the EB-PVD coater the ceramic grows in columnar form. Individual columns are poorly bonded to adjacent columns but are tightly bonded to the underlying substrate. This extremely fine columnar structure is highly tolerant of thermal strains induced by  $\alpha$ -mismatch and significantly reduces the amount of

material lost due to strains within the ceramic. Subsequent laboratory testing has shown EB-PVD TBCs to fail at the thermally grown oxide separating the ceramic topcoat from the substrate/bondcoat; it is suggested [38] that this failure is caused due to:

(i) Creep of the bond coat or substrate

or

(ii) The increase in interfacial strain caused by the oxide growth.

### 3.3 – The Nature of Bonding and Al<sub>2</sub>O<sub>3</sub> Protection

#### 3.3.1 - Why $\alpha$ - Al<sub>2</sub>O<sub>3</sub>?

The mismatch in physical properties between a metallic substrate or coating and a ceramic TBC makes the strength of the bonding interfaces critical in order that adhesion may be maintained.

The conditions experienced within the HP stage of a gas turbine ensure that components form surface oxides. The interface between the TBC and the bondcoat is such a situation, and it is obvious, therefore, that the critical bonding required must come from the oxide formed at this interface.

In order for the oxide to maintain its properties over the proposed life time of the component it should be highly stable, free from cracks and pores and be both coherent and adherent and preferably be slow growing. It has been shown that  $\alpha$ -phase alumina comes close to fulfilling these requirements [39].

##### 3.3.1.1 - What is $\alpha$ -Alumina?

$\alpha$ -Al<sub>2</sub>O<sub>3</sub> is a CPH phase with the trivalent cations (Al<sup>3+</sup>) occupying  $\frac{2}{3}$  of the octahedral interstices. The highly stoichiometric structure in combination with the large

conduction band gap, which makes electron transport difficult, results in the observed slow growth rate, stability and density of the oxide [40].

The nature of the Al/Al<sub>2</sub>O<sub>3</sub> bond is not fully understood, it is, however, proposed that the bonding may be, essentially, a covalent bond between the outer electrons of the aluminium (3s, 3p) and the oxygen (2p) [41]. It has also been proposed that the bonding may be due to the transfer of valence charges. On thermal excitation, the outer electrons of the anion (oxygen) move from the valence band into the conduction band of the cation (metal). It is then possible for the bonding electrons in the cation to transfer to the valence band of the anion. The greater the degree of electron transfer the greater the strength of the bond, increased thermal excitation would therefore improve the bonding between the ceramic and metal [41].

At elevated temperatures, >1000°C, α-Al<sub>2</sub>O<sub>3</sub> becomes the dominant species. It has been shown, however, that at lower temperatures and during the initial stages of Al<sub>2</sub>O<sub>3</sub> formation, other phases can be present.

#### 3.3.1.2 - Formation of α-Al<sub>2</sub>O<sub>3</sub>

In order to encourage alumina formation the process must be chemically and energetically favourable. Chemically, for alumina to grow, the following equations must hold true:





Where M represents the bulk metallic species in the system i.e. Ni, Co, Cr etc.

Energetically, the formation of alumina will only occur if the free energy of formation of  $Al_2O_3$  is sufficiently more negative than that of the competing MO.

It has been shown, however, that during the initial stages of oxidation, the above process is competitive until an equilibrium, steady state is achieved. In the Ni based systems, commonly associated with the aero gas-turbine industry, the initial product of high temperature ( $>900^\circ C$ ) oxidation is based on the dominant species and forms mixed oxide spinels of the form  $Ni(Cr,Al)_2O_4$  and NiO. The initial rapid growth of the NiO soon gives way to the formation of  $Cr_2O_3$  beneath it. It is beneath this phase that the initial alumina phases form. The initial phases formed are considered meta-stable as they rapidly transform to more stable states. It has been proposed that the first transitional phase to form is of the  $\gamma$ -phase morphology. The  $\gamma-Al_2O_3$  forms via  $\delta$  and  $\theta$  phases [42, 43].

The stable form of  $Al_2O_3$  spreads through a lateral growth mechanism across the exposed surface, creating a continuous "sea" of  $\alpha-Al_2O_3$  with floating "islands" of  $Cr_2O_3$  topped with Ni based spinels.

It is suggested that the presence of Cr in the alloy helps to initiate the transformation from  $\gamma$  to  $\alpha$ -Al<sub>2</sub>O<sub>3</sub> and subsequently maintain the stability of the phase below the temperatures normally associated with the transition from meta-stable phases. Cr also reduces the activity of Al required to develop a continuous scale [44]. Once formed the  $\alpha$ -Al<sub>2</sub>O<sub>3</sub> can grow in one of two ways, either through anion (oxygen) transport inwards through the scale to the thermally grown oxide (TGO)/alloy interface, or through cation (aluminium) movement out through the scale towards the free surface of the TGO (or the TGO/TBC interface). The movement of cations is predominantly through the lattice of the alumina [39, 45], whilst that of the anions, although temperature dependent can be either through the lattice or along grain boundaries. At temperatures below ~1600°C, however, the dominant mode for the anionic species is that of grain boundary diffusion [39].

Movement along grain boundaries, being the more rapid process, becomes the growth-rate-controlling step. If this process can be slowed then the oxide thickening process can also be slowed. Additions of active elements have been tried in order to attempt this, as discussed later. The morphology of the alumina scale supports the theory of predominant inward grain boundary controlled oxide growth, as equi-axed grains at the free surface become elongated as one moves inwards through the scale, ultimately becoming columnar in structure near to the TGO/alloy interface. The resultant oxide structure is shown schematically in Figure 3.6, after [46].

### 3.3.1.3 - Failure of Al<sub>2</sub>O<sub>3</sub> Scales

As has been mentioned it is critical that there is sufficient aluminium present within the system to maintain  $\alpha$ -Al<sub>2</sub>O<sub>3</sub> growth. If the Al level does fall below that critical level (typically 5 mass% in a Ni,Al,Cr system, for example) then competing metallic species are likely to form oxides. These mixed oxide spinels do not have the mechanical properties associated with  $\alpha$ -Al<sub>2</sub>O<sub>3</sub> and can become initiation sites for interfacial cracking.

The mismatch between the coefficients of thermal expansion of the substrate and oxide can lead to very high shear stresses at the interface during thermal cycling. These stresses can lead to crack initiation and buckling of the scale [37, 47].

Preferential cation and anion movement through the scale can also lead to buckling. Although the rate-controlling step during scale growth has been identified as the anion movement down grain boundaries, there is some competing cation movement outward along these diffusion paths. It is proposed that cation and anion movement along grain boundaries can lead to oxide formation within the scale leading to the development of compressive stresses and hence buckling. These buckling mechanisms result in interfacial voids, and hence reduce the degree of scale bonding [40, 48]. Other mechanisms have been proposed for void formation, such as the presence of sulphur at levels of 100ppm, however, it has also been suggested that the sulphur becomes associated with the voids after their formation. The presence of screw dislocations at the interface, have been proposed as a mechanism to form voids, by movement of

material into the bulk of the substrates [40]. Within this study it is suggested that the presence of Ti at the TGO/substrate interface destabilised the  $\alpha$ -Al<sub>2</sub>O<sub>3</sub> enough to form voids.

The presence of water vapour on anhydrous  $\alpha$ -Al<sub>2</sub>O<sub>3</sub> can have a dramatic effect on the bonding at the interface. Whether this is due to the stresses induced through the volume change on re-hydration of the oxide to Al<sub>2</sub>O<sub>3</sub>-H<sub>2</sub>O or Al<sub>2</sub>O<sub>3</sub> 3H<sub>2</sub>O or whether the effect is more related to a stress corrosion mechanism at the already initiated, crack tip, is being debated. The additions of so called active elements or rare-earths (REs) have been made to  $\alpha$ -Al<sub>2</sub>O<sub>3</sub> forming systems in order to delay the onset of the failure mechanisms.

### **3.3.2 - Active Element Additions**

It has been widely acknowledged that the addition of so-called "active" elements, such as yttrium, hafnium and the lanthanoids, significantly improves the oxide scale adhesion on alumina forming alloys [49, 50, 51].

The actual role the active elements play is uncertain, however, with many benefits being attributed to the additions. These can be distilled down to the six most commonly reported.

- (1) The effect of yttrium or vacancies is disputed. Some suggest that yttrium in the oxide scale encourages vacancy formation and hence allows growth stress relief through a creep mechanism. Others suggest that yttrium acts as a ‘vacancy sink’, preventing pore formation at the TGO/substrate interface and hence improving bonding.
- (2) There is also some contention as to the benefits gained by the effect of yttrium on the size of oxide grains. It is suggested that YAG ( $Y_3Al_5O_{12}$ ) crystals sit on grain boundaries and hence restrict the size of the grains by “pinning” the grain boundaries. The benefits of small grains, it is proposed, come through the grain boundary sliding accommodating the growth stresses induced.
- (3) The YAG crystals on the grain boundaries prevent rapid outward diffusion of cations and hence encourage inward oxide growth.
- (4)  $Y_2O_3$  particles sites at grain boundaries in the substrate encourage inward oxygen transport, resulting in extensions to the broad oxidation front, in the form of oxide “pegs”. It is suggested that the presence of the pegs results in a convoluted TGO/substrate interface along which a crack must run during spallation. The increased crack length required to negotiate the tortuous route would require more energy to cause spallation leading to a greater tolerance to spallation stresses.
- (5) It is also proposed that the presence of yttrium-containing particles at the interface during the early stages of oxidation promotes  $\alpha$ - $Al_2O_3$  formation in preference to

the formation of transient oxides, and hence resulting in a more stable oxide structure earlier on in the process.

(6) The most convincing arguments for the role of active element additions, is that of “sulphur-getters”. Y, Ce and La sulphides, for example have larger negative energies of formation than does aluminium sulphide. It has been shown quite conclusively, that the removal of sulphur from the oxidation process results in a far more adherent alumina scale. It is however less clear of the actual role sulphur plays in the degradation of TGO/substrate bonding.

[52, 53]

Acting as a sulphur getter is unlikely to be the role played by hafnium as it forms more stable compounds with oxygen, nitrogen and carbon (as can be seen from standard free energies of formation), these elements are often in greater abundance than sulphur in many superalloy/coating combinations.

### **3.3.3 - The Effect of Sulphur.**

One of the earliest studies highlighting the effect of sulphur on scale adhesion was published in 1983 [54], although the work was carried out on Cr<sub>2</sub>O<sub>3</sub> scale adhesion on stainless steel, the observations can be paralleled to superalloy type compositions. It was demonstrated that sulphur segregated to the metal/scale interfaces that became exposed during scale spallation. This work created significant interest and initiated a

large number of subsequent work programmes designed to understand the role sulphur was playing in oxide scale adhesion.

It has since been shown that very low levels of sulphur contamination are sufficient to cause deleterious effects on  $\text{Al}_2\text{O}_3$  adhesion, with levels typically below 10ppm and lower [55], some as low as 4ppm [56]. Work by Smialek [57] has suggested that concentrations as low as that only sufficient to generate a half monatomic layer to form can disrupt bonding.

The actual mechanism of adhesion degradation is hotly debated. It has been suggested that segregation of sulphur to oxide grain boundaries alters the scale growth kinetics, promoting outward diffusion of damaging elements which act to embrittle the oxide, hence reducing the ability of the scale to withstand the thermal and growth stresses experienced [58]. In contrast, Grabke et al [59], suggested that the negatively charged sulphur ion,  $\text{S}^{2-}$ , is too large to be accommodated at the metal/oxide interface and so segregates to voids and only once at the void does it exaggerate the effects of stress. Conversely, it has been suggested that once at voids, sulphur plays no further role in oxide detachment [60, 61]. Furthermore, work by Hou and Stringer [55], under ultra high vacuum conditions has shown sulphur to be present at the interface remote from voids.

What is generally agreed, however, is that sulphur is detrimental to oxide adhesion.

A significant amount of research has been directed at examining ways to reduce the effects of sulphur contamination; these include additions of active elements, as previously discussed, where the presence of rare earths or lanthanoids can reduce the predicted levels of sulphur to as little as 0.15ppb [56]. The effectiveness of particular reactive element additions are sensitive to operating temperature, for example, the addition of zirconia is beneficial to  $\text{Al}_2\text{O}_3$  bonding at 1100°C in FeCrAlX alloys where as at 1300°C in the same systems no benefits have been observed [56].

Alternative methods of sulphur removal have been achieved through heat treatments in reactive atmospheres [62]. The presence of  $\text{H}_2$  reacts with the sulphur to form  $\text{H}_2\text{S}$ , subsequent component polishing or grit-blasting treatments remove the sulphur containing compounds. In testing, the modified systems demonstrated improved oxidation resistance; the performance of the systems was comparable to that of active element containing samples.

It is clear, therefore, that sulphur contents of alloys and coating systems must be carefully controlled in order to achieve the best environmental protection possible.

### **3.4 - Thermal Spray Coating Deposition**

Many coatings, including those of metallic and ceramic composition, can be deposited using variations of the thermal spraying technique. These techniques offer advantages

over conventional plating and diffusion processes such that complex chemistries, as those seen in overlay type coatings, can be deposited.

Thermal spraying techniques produce coatings by propelling molten, superheated particles from a “gun” towards the substrate. On contact with the relatively cold component surface the microscopic droplets plastically deform and rapidly solidify into flattened discs commonly known as “splats”. The subsequent build up produces a continuous coating as the splats become mechanically interlocked or keyed together. This process is shown schematically in Figure 3.7(a) and the resultant microstructure is shown in Figure 3.7(b) [63]. The resultant coating is highly stressed due to the stresses induced by the rapid solidification process. These structures are usually heat treated, which relieves the stresses, and the splats diffuse together to form an homogenous structure.

Thermal spraying techniques have developed considerably since their conception during the 1920's with a stepwise increase in performance being made possible with the development of the plasma gun during the 1950's [64]. Equally important developments to the technique include the exclusion of atmospheric reactants ( $O_{2(g)}$ ) through Ar shrouded spraying environments, to vacuum plasma spraying (VPS).

### **3.4.1 - Flame Spraying**

Flame spraying techniques provide the heat input to the particles via the exothermic burning of liquid or gaseous fuels. The resultant gaseous expansion helps to propel the heated particles, injected into the flame immediately downstream of the gun; this role is primarily fulfilled, however, by the high volume flow rates of the carrier and primary gas combination. The primary is usually an inert gas such as Ar or He, the singular role of which is to act as a propellant. The carrier gas also acts as a propellant but its main purpose is to provide the gun with the pre-alloyed powder used to form the coating. Flame spraying has mostly been superseded by more advanced systems. Most of the developments have been aimed at increasing the energy into the particles; these have also tended to improve the cleanliness of the process by removing contaminants introduced through the fuel. Most modern systems now provide the heat input by use of plasmas.

### **3.4.2 - Plasma Spraying**

In order to produce coatings of high integrity it is beneficial to increase the energy input into the coating media, as ideally all particles should be molten on impact in order to maximise inter-particle contact and hence reduce porosity [69, 70]. The heat input is mostly provided, in modern systems, by an electrically ionised gas plume or plasma. With the high temperatures experienced within plasma systems exclusion of oxygen is essential in order to produce metallic coatings. There are three main methods of

removing the partial pressure of  $O_2$  in the coating environment, the most basic is a technique similar to MIG welding, where an envelope of inert gas floods the plasma plume and component. The next phase improvement is to enclose the system in a chamber flooded with Ar, known as Argon Shrouded Plasma (ASP). The most advanced and most expensive technique is Low Pressure or Vacuum Plasma Spraying (LPPS or VPS). In this system the gun and component are contained in an evacuated chamber, back filled with a low pressure of Ar. This effectively excludes all of the  $O_2$  and hence improves the resultant coating quality. The removal of the atmosphere considerably alters the physics of the spraying process; this will be discussed later in section 3.6.2.2.

#### 3.4.2.1 – Plasma Generation

The propellant, normally an inert gas or a combination of two gasses, an inert and a diatomic, passes through the nozzle of the gun. The nozzle takes the form of a hollow circular anode with a cathode supported centrally; a high potential difference is set up across the gap, which results in a pulse of current creating an arc (an electrically conducting channel in a gas). A steady d.c. current of typically hundreds of amps at a potential of ~50V then sustains the arc. The arc strips the outer shell electrons from the atoms of the gas leaving the positively charged ions to cascade towards the cathode. The rapidly moving electrons and ions collide with other neutral atoms or molecules in the gas, dissociating any molecules and ionising the subsequent atoms; this collection of energetic particles is known as a plasma. The ions and electrons are propelled, by

the gas pressure/thermal expansion effect towards the component. The recombination of electrons and ions releases the energy in the form of heat, up to 15000°C, see Figure 3.8 [65]. The introduction of the coating media, usually via a carrier gas, results in the particles becoming molten and superheated to very high temperatures (~1000's °C). The introduction of relatively small amounts of secondary, diatomic, gas boosts the temperatures further, as diatomic molecules release additional quanta of energy upon recombination. The dissociation of diatomic gases occurs at lower temperatures than does the ionisation of most process gases, hence making the process more efficient; this is shown in Figure 3.9 [66]. Typical combinations of primary, secondary and carrier gas species are shown below:

- |      |           |   |                |
|------|-----------|---|----------------|
| (i)  | primary   | = | Ar             |
|      | secondary | = | H <sub>2</sub> |
|      | carrier   | = | Ar             |
| (ii) | primary   | = | Ar             |
|      | secondary | = | He             |
|      | carrier   | = | Ar             |

Example (ii), although it does not contain a diatomic species, does contain He. The small size of He atoms necessitates high energy to strip electrons and hence the energy released on re-combination is significantly higher too.

The generation of successful coatings is critically dependent on the interaction between the plasma and the powder particles. This interaction is effected by a number of variables that are discussed below.

#### 3.4.2.2 - Plasma-Particle Interaction

As previously stated, ideally all particles should be molten on impact with the substrate, this is influenced by a number of conditions within the plasma plume. The way in which the heat energy is transferred to the particles is dependent on the velocity and temperature profile of the plasma flame, the physical properties of the powder particles and the injection conditions they are subjected to. The thermally sprayed coating systems within this study were produced by LPPS techniques, the plasma plume generated under those conditions will, therefore, be of most interest.

The low operating pressure within the coating chamber reduces the atmospheric braking effect on the plasma plume. This has a considerable effect on the physics of the process. Work by Takeda et al [67, 68] predicted that:

- (i) The gas velocities within an LPPS system would be considerably higher than in an APS system, Figure 3.10(a),
- (ii) The plasma plume would retain higher temperatures further from the gun nozzle, figure 3.10(b),
- (iii) The enthalpy of the gas would remain higher overall, figure 3.10(c)

This work has also been verified experimentally by Wolf and Longo, [69] where temperature measurements of the plasma were made at given distances from the nozzle, see Figure 3.11. The work demonstrated that although the particles are introduced into a hotter environment, in the plasma plume, the resultant reduced time of flight means that they don't necessarily arrive at the substrate any hotter. In order to resolve this issue most LPPS compatible powders have a smaller average diameter over those used in atmospheric spraying techniques and are introduced directly into the hottest part of the plasma. The introduction of the powder into the plasma also requires a balance of forces. The carrier gas pressure must not be so great that the particles are simply blown through the plasma, nor be too little and allow the powder to be deflected out of the plume; this parameter is closely interrelated to the particle size.

The effects of the above variables not being carefully controlled and balanced can be seen in Figures 3.7(a) and (b), where inefficiently heated particles become included in the coated as "un-melts" resulting in porosity and poor inter-splat cohesion [63].

It is evident, therefore, that in order to obtain the optimum coating performance from a thermally sprayed metallic coating, careful design and control over all the spraying parameters in combination must be achieved.

### 3.5 - Sputter Processing

Sputtering techniques produce coatings through the atomistic build up of a coating material onto the substrate via a process of plasma induced material transfer. In sputtering processes the target material (that which will form the coating) is negatively biased in relation to the substrate and process chamber walls. The partial pressure of an inert gas, typically Ar, becomes ionised due to the induced electric field. The positively charged Ar ions accelerate towards and impact upon the target, the resultant collision sputters off target material as a result of the momentum exchange. This momentum exchange provides enough energy for the sputtered material to be projected, as a cloud of particles, some of which will be ionised, towards the substrate, where it condenses to form the coating.

The major drawback to sputter processing has traditionally been the slow deposition rate. This can be enhanced by confining the plasma by use of magnetron induced magnetic fields, this increases the ion density and so increases the yield. Other techniques are also used such as steered arc where the material is evaporated away from the surface of the target. A secondary concern over the use of sputtering as a production coating technique, is the necessity to use RF plasmas for the deposition of insulating materials. Conventional d.c. biasing of insulating materials causes a build up of charge on the target, leading to a cessation of the sputtering process. The yields of all these techniques however are significantly lower than those gained by EB-PVD.

### **3.6 - Electron Beam – PVD (EB-PVD)**

EB-PVD is a low pressure coating process by which a sacrificial ingot of material is evaporated using high-powered electron-beam guns. The evaporant subsequently condenses onto the relatively cool substrate material. The process allows the deposition of metallic or ceramic materials in either an inert or reactive environment. The process remains a predominantly a line of sight process, despite a degree of gas scattering of the vapour, induced by the operating gas. The structure of the resultant coatings can be tailored by the control of substrate temperature, operating pressures and gun power, as well as other parameters, although to a lesser extent.

With deposition rates of up to 25 $\mu$ m per minute, EB-PVD has proved to be a viable production process within the aerospace industry, for the deposition of metallic environmental protection coatings and ceramic thermal barrier coatings. The degree of structure control available with this technique has allowed the development of columnar, strain tolerant ceramic coatings, which are beginning to find widespread use within the new generation of gas turbine engines.

Figure 3.12 shows a schematic of a typical EB-PVD coating rig.

### **3.7 - Method Improvements**

#### **3.7.1 - Optimisation of systems with multiple variables**

The conventional method of optimising the parameters in a system with multiple variables would be to utilise full factorial process control experiments. Full factorial matrix of experiments was impractical within this study because of a large number of variables associated with the LPPS process. A full factorial matrix would require a series of experiments to be completed where one variable would be altered at a time until all possible configurations were completed. A system with seven variables set at two levels (high and low) would require  $2^7$ , (128) experiments.

Even after completing 128 runs the relationships between the two levels of the variables would have to be assumed as linear as no intermediate information would be available, this would require more experimental runs. Full factorial design would ordinarily be made more manageable by the use of fraction factorial design. Carefully selected runs from the full matrix would yield almost as much information as would the complete matrix. Several design strategies utilise fractional factorial design, notably the Taguchi Method.

### **3.7.2 - The Taguchi Method**

The Taguchi method of fractional factorial design is based around a specially constructed set of "orthogonal" arrays. An array consists of columns and rows, where the columns are represented by variable factors, (temperature, pressure etc.) and the rows by trial or experiment numbers. When a two-tier design, the most basic array, is considered, the variable factors are set at two levels (high and low designated by 1 and 2). When two adjacent columns are examined it is evident that the two levels in any trial can combine in one of four ways (1.1), (1.2), (2.1) and (2.2).

When two adjacent columns include all these combinations at least once then the two columns are said to be balanced or orthogonal. When this premise is extended to include any two columns, not necessarily adjacent, then the whole array is considered orthogonal [72].

Essentially, all that is required of an operator is to select a suitable array that will accommodate all the variables and complete the series of described experiments.

The Taguchi Method was developed to ensure conformity of experimental design. Conventional fractional factorial design has the potential to produce different results if different experiment designers faced the same problem, as the selected fraction of the experiments may result in a different bias. The use of a pre-ordained series of experimental arrays reduces this risk. The main criticism levelled at the Taguchi method is the concern over "interacting" variables. It is possible that two or more

variable may interact in such a way that slight modification to one may seriously effect the way another operates. The Taguchi method does not automatically consider this possibility, but is reliant on the operator to spot potential interactions and select arrays that can accommodate them [73].

Fractional factorial experiment design, must, in order to be successful, require feedback in order that parameter optimisation can be calculated.

#### 3.7.2.1 - Assessment of Results

The Taguchi Method requires that each trial should produce quantifiable results or responses. The response may be a simple measurement ie. density or length, or a more subjective quantity provided it can be given a value ie. taste or quality on a scale from 1 to 10 [74]. The most straightforward way of assessing the results is through the use of average response graphs. These give a comparison of how the overall response is effected by a particular factor when set at each of its levels. Selection of the best level, with regard to the average response for each factor, will result in a set of optimised parameters. The method with which to calculate the average performance for each level of a factor is simple. For example, if the average response for factor A at level 1 is required, then simply add the responses for all the trials containing A1 and then divide by the number of such trials. If this is then repeated for all the factors at all levels, the relative performance for each factor/level combination can be assessed. For example if the response being considered is density and the Taguchi method has been employed in order to increase the density of the product, then the level of each factor which

produced the highest average performance should be selected, ie. if  $A1 > A2$ , then A1 is chosen. A limitation of the basic two level design becomes evident at this point. No information is gained about levels in between those selected, and hence a straight-line relationship must be assumed. For greater degrees of accuracy, arrays must be selected with a greater number of levels included in them.

The average response graphs obtained from three of four level designs give an indication of the way in which the response is effected by varying the factor. i.e. A cubic or exponential relationship would be highlighted.

### 3.7.2.2 - Interactions

The importance of identifying possible "interacting terms" and accommodating them into an array had already been indicated.

The average performance ratio for each factor is affected to a greater or lesser degree by all the other factors. These "ghost" effects usually represent the combined effect of two or more factors i.e. Potential interactions. These secondary effects are known as "aliased-pairs". Usually the effect of aliased-pairs is negligible, if, however, there is a significant interaction between two variables the secondary effect of the aliased-pair becomes exaggerated. If the experiment designer is unaware of the interaction the results from the array become distorted, culminating in non-optimised parameters. If the potential interaction is suspected, however, careful array selection and experimental design can accommodate the effect of the aliased-pair. Selection of an array with an

excessive number of factors allows the significant factors to be placed where the aliased-pairs of potential interactions will fall into unused columns [75]. Careful array design also allows potential interactions to be identified in order that they can be accommodated into later designs. If, for example, it is suspected that an interaction between two factors is possible, the factors can be arranged within the selected array so that the aliased-pair of the potential interaction falls with a non-significant variable. The average performance graph of the non-significant factor should be almost flat i.e.  $A1 \cong A2$ ; if there is a significant interaction occurring then the associated aliased-pair would exaggerate this slope. The operator could then produce a new array suitable to accommodate the interaction and hence design the new parameters to include it.

As can be seen it is often necessary to run several series of experiments in order to produce optimised parameters.

## Chapter 4.0 - Bond Coat Developments

The current state of the art environmental protection systems fall into two main categories, as discussed earlier in Chapter 3.2. These two groups are:-

- 1) Diffusion Coatings
- 2) Overlay Coatings

Diffusion coatings of interest can be sub-divided into two further groups:-

- 1(a) Aluminides
- 1(b) Platinum-Aluminides

It was these three groups 1(a), 1(b) and 2 that provided the starting point for the development of the novel bond coat systems that were assessed, alongside the more conventional systems, in the initial phase of work completed for this thesis.

The initial phase of this work was to quickly assess the list of potential systems and reduce the number to a shortlist that would go forward to the next phase for further analysis.

The novel bondcoat systems, generated for this study, were principally based on attempts to combine beneficial aspects of all three types of coating group. In addition

to this, the effect of aluminium activity and platinum content in the coatings was to be examined.

Figure 4.1 shows a list of bondcoats that were assessed in the initial phase of work, separated into four categories, the three mentioned above and a fourth entitled Modified Coatings which contains the development coating systems.

#### **4.1 - Assessment of Bondcoat Systems - Phase 1**

The large number of samples described in Chapter 4.0, above illustrated that a technique was required in order to assess the systems and significantly reduce their number.

The modified form of the scratch test had shown in earlier work [38] that the technique had the capability of differentiating between the performance of different bond coat systems, with regard to TBC adhesion. It was decided to use the scratch test to “rank” the performances of the phase one composites.

The initial screening procedure, however, was simply to isothermally soak test pieces cut from the test bars. Failure to pass this initial test excluded the bond coat system from further analysis.

## **4.2 - Testing Techniques**

### **4.2.1 - Isothermal Furnace Testing**

Sections approximately 10mm long were cut from the 8mm diameter test bars using Struers grinding wheel cut-off machines. Care was taken during this procedure to ensure no mechanical damage incurred which could subsequently influence the testing procedure.

Two samples from each bond coat were contained in low-sided high-purity alumina crucibles and exposed in still laboratory air. The alumina “boats” prevented potential contamination from the furnace effecting the test results. The crucibles were placed in the hot zone, of the furnace, which were regularly assessed for conformance to ISO9000, calibrated to  $\pm 10^{\circ}\text{C}$ .

The samples were left to “soak” for the allotted time at temperature and then removed and allowed to air cool to ambient temperature before being examined. If after this examination it was shown that the TBC had become partially or completely detached, the bond coat system was considered to have failed the test and the TBC to have “spalled”. Those samples, which did not spall, were then mounted in cross-section and prepared as described later.

In phase one, the samples were all exposed for 100 hours at temperatures of 1050, 1100 and 1150°C. The initial testing temperature of 1100°C represented the “gate” through which samples had to pass to warrant further assessment.

#### **4.2.2 - Sample Preparation**

In order to examine the interfacial region of the bondcoat/TBC system, either metallographically or mechanically (see Chapter 4.2.3 - Adhesion Testing), the samples had to be mounted and prepared in cross section. It was known that metallographic preparation of columnar EB-PVD TBCs resulted in a broken, disrupted microstructure.

In order to produce a representative microstructure the TBC columns required support through a binding media. The columnar-structure allowed infiltration by a liquid epoxy resin. The epoxy thermoset was melted onto the samples, pre-heated to 180°C. The samples were then heated for a further hour at this temperature to allow the epoxy to harden. The samples, once cool, could then be mounted as per conventional test pieces.

In order to reduce the effects that temperature and pressure, associated with the use of Bakelite mounting media, would have on the state of stress at the bond coat interface, the samples were mounted in a cold-setting resin, “Triofix”, supplied by Struers.

Two polishing procedures were used during sample preparation depending on which feature was of interest. The procedure outlined in Table 4.2 was that used to produce the ideal finish required when examining the metallic components of the coating

system; whilst that outlined in Table 4.3 was the ideal preparation for the ceramic components. The latter polishing procedure was required when measuring the relative adhesive strengths of the bondcoat systems, with the modified scratch test, as careful examination of the thermally grown oxide/bondcoat interface is critical to the technique.

#### **4.2.3 - Adhesion Testing**

The large number of samples within the initial phase of this study made it necessary to utilise a test that was capable of ranking the relative performance of those test pieces quickly and accurately. Several test methods have been developed in order to measure or qualify the state of adhesion between a coating and substrate. The most commonly used test methods for checking bonding are destructive mechanical tests rather than non-destructive evaluation techniques.

The mechanical tests generally apply a force to the coating/substrate interface. The force may be normal to the interface, as in the "pull-off" test or parallel to it, as in the shearing stress test.

The force required to just cause failure is recorded as the strength of the bond.

Of these tests the pull-off test has gained popularity with thick-film testing, whilst the scratch test has proved popular with thin film testing.

#### 4.2.3.1 - The Pull-Off Test

A force is applied normal to the interface in the pull-off test, the process is relatively quick and easy to perform and so has become almost a standard test within the industry. In this test coatings are applied to one-inch diameter buttons of the substrate material. The arbours of the pull-off test rig are adhered to the top and bottom flat faces of the coated test button using an adhesive film (FM 1000); this is cured at 200°C prior to testing. The test specimen is then loaded in a tensile test rig at a rate of 8-10 MPa/min. The ultimate value of load is recorded, this is related to the tensile strength of the bond.

There are problems with this test method, however, as often the failure will occur in the adhesive, and not at the interface of interest. The maximum adhesion that can be measured is limited by the strength of the adhesive typically 40-80 MPa. The adhesive can actually penetrate porous coatings and effect the interfacial bond. The test is also limited to flat test pieces and hence could not be used on components.

#### 4.2.3.2 - The Conventional Scratch Test

The scratch test was developed as a method of measuring the adhesion of thin films to the substrate material. In this process a hardness indenter or diamond stylus, typically a Rockwell "C" hemispherical diamond (200µm in diameter) is loaded normal to the coated surface until a predetermined load is reached.

The sample is then traversed unidirectionally relative to the stylus whilst the load is steadily increased at a known ramp-rate. When the load reaches a critical value the coating debonds causing failure. Knowing the load ramp-rate and the transverse speed of the table, the critical load can be calculated from measurements made from the sample. The critical load to cause failure is typically quoted in Newtons.

Failure of the coating can be detected using several techniques such as detection of the acoustic pulse associated with the failure of the coating, or in some cases the change in tangential friction can be measured when the substrate is exposed by coating spallation.

It can be shown from solid mechanics theory that for a spherical contact (the diamond stylus) with a plane (the coating/substrate system) of contact area  $Xa^2$ , the maximum pressure acts at a point  $^{2}/_3a$  beneath the centre of the point of contact. The situation changes, however, if the contact is sliding, as in the case of scratch testing.

In this case, the point of maximum pressure moves towards the surface and forwards of the indenter with the additional component of the frictional force.

It is obvious, therefore, that conventional scratch testing is only suitable for thin coatings, as the point of maximum pressure could never penetrate deep enough to effect the interface region of a thick coating.

#### 4.2.3.3 - The Modified Scratch Test

Lopez, Beltzung and Zambelli first developed a scratch test technique for the assessment of thick films in 1998 [15].

Fixed depth scratch testing, using a sclerometer with a Vickers pyramidal indenter was carried out to determine the adhesion and cohesion of alumina coatings produced by plasma spraying.

This work was predominantly concerned with the abrasive properties of the coating, with little importance being placed on the coating to substrate adhesion. Unlike thin film testing the scratch track crossed the interface between substrate and coating on a metallographically prepared cross-section. The test was further developed under an Engineering Coatings (ENCO) Club programme, where a standard scratch testing machine was used to test air and vacuum plasma sprayed samples. In this case, unlike the earlier work, a Rockwell "C" diamond indenter was used, as for conventional scratch testing, to produce the scratch tracks. During this programme it was observed that:-

- 1) Failure occurred at the coating/substrate interface, with cracks being visible running along the interface. The load required to just cause interfacial cracking was considered the critical load,

- 2) A cone of material was removed from the coating surface as the indenter passed through it. The size of the cone was believed to represent the cohesive strength of the coating.

#### 4.2.3.4 - Conventional Scratch Test Theory and the Modified Scratch Test

During testing of thin films, the coating becomes detached due to the combined action of frictional and ploughing forces. Hamilton and Goodman [80] described the distribution of the stresses under the sliding stylus in the following ways.

The stylus induces a shear stress in the sample that is proportional to the applied load (from Amonton's Laws) which is transmitted through the bulk of the composite sample. As the mechanical properties of the coating and substrate are different, there is a discontinuity in the shear stress at the interface, which when sufficiently high, induces adhesive failure. This discussion can be considered over simplified as the stylus produces a "bow-wave" ahead of it, hence complicating the stress system. Burnett and Rickerby [81] have identified three contributing factors which lead to the stresses responsible for thin film detachments.

- i) An elastic/plastic indentation stress
- ii) An internal stress
- iii) A tangential frictional stress

Bull et al [82] have extended this analysis where each of the above contributions is expressed in terms of their effect on the measured coefficients of friction of the substrate and the coating.

In addition, residual stresses in the coating itself, resulting from the method of deposition and metallographic procedure will strongly influence the loading required to cause failure.

#### 4.2.3.5 - Investigation to Determine the Onset of Interfacial Cracking

Work was completed at the Atomic Energy Authority at Harwell [83] in order to attempt to determine the cause of interfacial cracking during the modified scratch test. Scratch tests were performed using indenter loads of 10Kg on a TBC deposited onto an LPPS bond coat.

During the tests the frictional coefficient,  $\mu$ , between the indenter and the test piece and the acoustic emission were recorded with respect to indenter position.

Comparison of the acoustic emission and the change in  $\mu$  were used in conjunction in order to determine the on-set of interfacial cracking.

As the indenter passed from the bond coat into the ceramic a detectable reduction in  $\mu$  was associated with a peak in the acoustic emission. Optical observation of the scratch

track demonstrated that cracking did not occur until the indenter had passed into the ceramic. This suggested that the major factor influencing the results was the frictional force between the diamond stylus and the ceramic TBC.

The frictional force therefore would put a tensile force on the interface and essentially drag the coating from the substrate, and not as it would first appear as a result of compressive force "pushing" off the coating ahead of the indenter.

#### **4.2.4 - Using the Modified Scratch Test**

The technique outlined above was used in order to "rank" the coating systems, by determining the load required to just cause interfacial debonding after isothermal furnace exposures. The residual strength was expressed in terms of the normal load applied to the diamond indenter, and was denoted as  $L_c$  (critical load to just cause cracking). The process used to determine  $L_c$  is described below.

Samples prepared as described in Chapter 4.2.2 were clamped into the jaws of the table on the CSEM Revetest scratch tester such that the diamond stylus was positioned 1-2mm above the substrate material, 3-4mm in-board of the bond coat. The diamond was then automatically lowered into contact with the sample, until the pre-set load (determined by the operator) was reached. The motorised table then traversed the sample beneath the indenter such that a scratch was generated in the specimen. The indenter moved, relative to the sample, from the substrate, through the bond coat,

oxide, TBC and out into the mounting media. The resultant scratch lay in a direction normal to the plane of the bond coat/TBC interface. Figure 4.4 shows the effect on the TBC bondcoat interface of the scratch track

If the amount of energy imparted to the bond coat/oxide interface were greater than the bonding energy, then the resultant energy would be dissipated through the propagation of a semi-circular crack front.

The diameter of the cracked or debonded area would be proportional to the resultant energy for a particular load, or alternatively proportioned to the strength of the bond. By plotting a graph of normal load against measured crack length (see Figure 4.5) of a number of scratches a straight-line graph could be produced. The point at which the regressed line intersected the x-axis was considered to be the critical load to just cause cracking,  $L_c$ . The value of the  $L_c$  was used as an aid to ranking the different bondcoat systems.

The results of the initial phase of testing are shown in Figure 4.6.

#### **4.2.5 - Cyclic Furnace Testing**

During the operational life of an aero engine, only a small percentage will be spent at maximum operating temperature i.e. during take-off at maximum power. The cumulative time spent at full throttle can be calculated and represented during

development engine testing as a sustained period at maximum temperature. The maximum power setting is the most demanding of the engine with the extended periods between becoming less significant. In order to simulate the high temperature period of engine life with laboratory test pieces, isothermal soak trials can be employed. The isothermal soak trials used during this study were based on a cumulative period of maximum power of sixteen hours, resulting in a twenty-five hour soaks test inclusive of a factor of safety.

The twenty five hour isothermal soak tests do not, however, represent the cyclic nature of the high temperature period of the engine life.

It was believed that a cyclic test might highlight a different mode of bondcoat/TBC system failure. This concern lead to the development of the cyclic furnace. The test was designed to examine cyclic oxidation and not to replicate the real engine environment.

#### 4.2.5.1 - The Cyclic Furnace

In order to attain as high thermal transients as possible during testing, the samples were removed from the hot zone of the furnace and force-cooled. Initially this was to be achieved with a water quench, the water being sprayed onto the hot samples, followed by a drying air blast prior to re-insertion into the furnace. The rapid water-quench proved too severe, however, for the sample holders and a forced air blast was soon adopted as standard. In order to ensure reproducibility, it was required that the samples

were placed into the same region of the furnace during heating and removed to the same position for optimal cooling. Positioning of the samples was achieved by a remotely positioned compressed air driven piston, connected in parallel to a temperature resistant ram.

Sensors detected the position of the piston and enabled fine control of the ram position to be achieved. Although the ram was made from temperature resistant FeCrAlY rod, the temperatures within the furnace would be sufficient for it to creep under any bending moment this would prevent the ram from operating. The bending moment was reduced to zero by positioning the whole apparatus vertically ensuring the load on the ram acted down along its length. The test pieces were then held in a removable support positioned on top of the ram.

This configuration obviously required that the tube furnace would be mounted vertically. Heat loss from the top of the furnace tube was kept to a minimum by insertion of an insulating ceramic bung. Furnace temperature control feedback was provided by a thermocouple positioned in a protective ceramic sleeve passed down through the top-bung into the centre of the test piece environment. This hot zone was calibrated in order to maintain a maximum of  $\pm 5^{\circ}\text{C}$  temperature variation. The samples were moved into the hot zone from below and held in position surrounding the control thermocouple.

Although the presence of the sample holder acted as a bottom-bung to help maintain the correct temperature within the furnace, the insertion of a large mass of relatively cold

material resulted in a rapid cooling of the furnace. This cooling effect was immediately detected by the control thermocouple, resulting in the furnace controller providing additional power input until the furnace reached the correct working temperature, this took approximately 15 minutes. Although the test piece holder acted like a bung, it potentially could act as a heat conduction path to an infinite heat sink, ie. ambient laboratory air, this risk was kept to a minimum through design of the holder/ram assembly. The heat-bung effect of the sample holder was held as remote as possible from the FeCrAlY ram, with a minimum contact area between the two, and an insulating layer of air separating the body of the holder from the ram. The holder was designed to generate as little stress within itself as possible during the thermal cycling.

This was achieved by construction from loosely connected thin plates that could move to relieve the build up of stresses. Early welded holder designs resulted in buckling and warping of the fabrication after only short periods of exposure. The lightweight design kept the thermal mass to a minimum and hence enabled the total cycle time to be kept as low as possible. The time taken from sample insertion through heat-up, 1 hour exposure, removal and air quench to 50°C was just 95 minutes.

The samples were examined once every twenty four hours or approximately every fifteen cycles. During this examination the samples were cooled to ambient temperature from 50°C in a water bath. The examination was essentially to determine whether the TBC had spalled since the previous examination.

TBC spallation usually occurred on contact with water or water vapour, the dry atmosphere within the cyclic furnace, in most cases, did not cause TBC spallation.

### **4.3 - Sensitivity of TBC's to Substrate Materials**

The initial phase of the down selection procedure, outlined above, was carried out on test pieces manufactured from the nickel-based superalloy, MarM002DS. This material is a directionally solidified superalloy of the type described in Chapter 3.1. It was highlighted, subsequent to the initial testing phase, that any future turbine blades were more than likely to be manufactured from single crystal material, such as CMSX-4, in order to cash-in the benefits offered by this generation of superalloy material. Figure 4.7 compares the chemistries of MarM002 and CMSX-4.

It was seen as prudent, at this early stage, to ensure there were no unseen difficulties in manufacturing the potential bondcoat systems onto this new generation of material. As can be seen from Chapter 3.7, no mention of the substrate material was made in the literature, as to it being a contributing factor in the degradation modes of bondcoats and TBC systems. It soon became evident from the subsequent testing that this presumption had been a considerable oversight by previous workers in this field.

The baseline bondcoat systems and those of greatest potential from the initial testing phase were produced onto CMSX-4 bars as per Phase 1. These samples were then tested in a similar manner to the MarM002 test pieces, as described in Chapter 4.1.

The results from the second phase of the testing programme demonstrated that the change from DSMarM002 to CMSX-4 had a considerable effect on the “life” of TBC coated components.

#### **4.3.1 - Testing Procedure**

The large number of test pieces associated with the initial stage of the selection procedure necessitated a reduction in the overall time taken to complete the testing. It has been assessed [76], that the cumulative time that an engine, for a civil airliner, would typically spend at the maximum operating conditions used during take-off and landing, can be represented by an isothermal soak of approximately 20 hours.

The maximum operating conditions equate to the maximum core temperature seen within the engine during normal running. It was decided, therefore, that with an allowance for a 25% factor of safety the testing conditions used during this phase of the programme would be set at 25 hour isothermal soaks at representative and progressive engine temperatures. These considerably shorter furnace times allowed for a more detailed temperature capability assessment of the bond coat systems of interest. The testing temperatures were extended from three to five, allowing the maximum temperature of interest to be extended to 1210°C.

The interval between testing temperatures was reduced to 20° steps at temperatures over 1150°C because of the much-increased rate of diffusion at these elevated temperatures, this relationship is demonstrated by the Arrhenius equation:

$$D = D_0 e^{-\frac{Q}{RT}}$$

The 20° interval was the smallest possible considering the accuracy placed on the furnaces of ±10°C.

The testing conditions were, therefore:

25h @ 1100, 1150, 1170, 1190 and 1210°C

As before, the systems were assessed using the scratch testing technique subsequent to the furnace testing.

In addition, to those samples transferred to the “new” substrate material, CMSX-4, some systems were repeated on MarM002 and tested to the new testing schedule in order to provide a direct comparison of the effect of the substrate on component life.

Figure 4.8 clearly shows the effect of changing from MarM002 to CMSX-4. This trend was repeated across the range of bondcoat systems with one notable exception, the MCrAlY+Pt bondcoat.

This result questioned the accepted modes of failure for TBC systems. It was essential to try and establish the mechanisms causing the radical differences observed.

#### **4.3.2 - Identification of Failure Mechanisms**

The differences observed in the performance of a bond coat on different substrates indicated that there was a strong likelihood of a chemistry lead failure mode over the generally accepted mode of oxide thickening. The possibility of the oxide thickening rates being effected by the substrate chemistry seemed improbable because of the relatively remote position of the point of failure in comparison with the substrate. This is particularly true of the MCrAlY based bondcoats examined where the MCrAlY can be up to 150 $\mu$ m thick.

#### **4.3.3 - Oxidation Rates**

In order to address this concern the oxide-thickening rate was measured for two parallel bondcoat systems on different substrates. As with the modified scratch testing technique, the oxide thickness was measured at 16 equispaced positions around a test piece mounted in cross-section. The test pieces were oxidised by isothermal furnace soaking for a constant exposure time at different temperatures. The TGO thicknesses were then plotted against time for comparison, see Figure 4.9. As can be clearly seen,

the oxidation rates of the bondcoat on different substrates are directly comparable. It is known from the earlier testing, however, that the TBC life for this bondcoat on CMSX-4 is significantly less than on MarM002. It can therefore be concluded that the oxide-thickening rate was not directly responsible for the change in TBC life.

It was assumed at this stage that an element or combination of elements, that were not free to move in MarM002, were diffusing through the bondcoat from the CMSX-4 and disrupting the oxide bonding. The ideal tool for assessing bulk transport of elements was the electron probe micro analyser (EPMA) using wavelength dispersive spectroscopy (WDS).

#### **4.3.4 - EPMA of Bulk Elemental Diffusion**

Two MCrAlY based systems (RT122), one on MarM002 and the other on CMSX-4, were aged for 25 hours at 1150°C. The samples were then mounted in cross-section in conducting Bakelite and prepared according to the procedure described in Figure4.3.

This procedure ensures that the integrity of the multi-phased structure is maintained. Comparison of the as processed and aged samples gave an indication of how elements diffused through the bond coat. The analysis technique used to assess this movement was a modified version of the line-scan, and was termed a “ladder-scan”. The ladder scan enables multi-phased systems to be assessed by measuring an average composition over a 50µm x 1µm area. The analysis area is achieved by “rastering” the analysis spot

over the distance mentioned above; this is done parallel to the plane of the TBC/bondcoat interface. The beam is then stepped at 1 $\mu$ m intervals progressively, from the substrate, through the coating and out into the mounting media or TBC. The average compositions for each step are recorded relative to their position in the sample. A composition profile of mass % or atomic % against distance can then be plotted of each of the elements recorded. Figure 4.10 represents the above process in schematic form. It is worth noting that the values produced by this technique cannot be used to identify the true composition of particular phases, as the results are average figures only. Any detailed analysis should be done using the traditional spot analysis technique.

Figure 4.11 compares the ladder scans from an as-processed system, MCrAlY on CMSX-4, with the equivalent system after isothermal soaking. Comparison of the aged sample with Figure 4.12, highlights the differences seen in the compositions immediately beneath the TGO when CMSX-4 was the substrate material. It was clearly shown that in the case of the CMSX-4 substrate, significantly more Ti and Ta were present in the outer portion of the coating. Comparison of the compositions of CMSX-4 and MarM002, see Figure 4.7, helped to explain the differences identified above. Although at first glance the levels of Ti and Ta appeared to be higher in MarM002 and therefore, more liable to diffuse to the TGO region, in reality the higher level of C in MarM002 played a significant role. MarM002, being a directionally solidified alloy, requires the C when in conjunction with the refractory elements Ti, Ta and W to aid grain boundary pinning as described in Chapter 3.1. The development of CMSX-4, a single crystal alloy, has no requirement for the levels of C seen in MarM002. The

levels of Ti and Ta, however, remain at a relatively high level due to the tendency for these elements to promote  $\gamma'$  formation;  $\gamma'$  being critical for the mechanical performance of single crystal superalloy.

These elements diffused on thermal exposure, towards the oxygen rich TGO producing the concentration gradient seen in the Figure 4.12 and thus reducing the overall energy state of the system. This chemical driver to form relatively stable oxides is not sufficiently strong enough to overcome the activation energy and break down the stable C forms of these elements, as seen in the case of MarM002.

Comparison of the WDS ladder scans for CMSX-4 and MarM002 based systems resulted in the assumption that the reduction in performance seen in the case of CMSX-4 was related to the diffusion of either Ti, Ta or a combination of the two.

#### **4.3.5 - Identification of Critical Elements**

In order to clarify this position a third coating system was produced using C1023 as the substrate material. Figure 4.7 identifies that C1023 has no Ta in its composition. Testing of this system, as above, should highlight any detrimental role played by Ta. If a significant detriment was seen through the change from MarM002 to C1023 it could be assumed that Ti was the element primarily responsible for the reduction in TBC life.

Figure 4.13 compares the performance of an MCrAlY (RT122) based bondcoat on three different alloys, MarM002, CMSX-4 and C1023 at 1100°C. The results show clearly that MarM002 does not impair the performance of the bondcoat when compared to CMSX-4 or C1023. When used in conjunction with the compositional data of the substrates and the evidence from the EPMA ladder scans, see Figure 4.14 for the C1023 systems, it was assumed that the critical element to be considered when assessing TBC/bondcoat adhesion was Ti.

At this stage it was uncertain what role was being played by Ti in order to cause such significant effects on oxide adhesion.

#### **4.3.6 - Role of Titanium in TBC Degradation**

Although Ti had been identified as the likely cause of premature TBC spallation, no mechanism had been proposed at this stage. It was important to understand the role of Ti in order to attempt to reduce its effects. Several methods were used to study the degrading defects of the Ti on the TGO/TBC bonding.

Using optical metallography, it became evident that the generic failure mode had not altered with the change from MarM002 to CMSX-4; the point of failure of the TBC system was still the interface between the TGO and the bondcoat, see Figure 4.15. In all cases the TGO could still be shown to be adherent to the spalled PYSZ. Optical metallography also highlighted a difference between diffusion-based systems and

MCrAlY type bondcoats. During TBC spallation the interfacial crack cut through the “root” of the yttrium pegs level with the broad oxidation front. This left the pegs embedded in the MCrAlY bondcoat. This mechanism argues against one of the suggested roles of yttrium in oxide bonding, namely Y pegging mechanically keying the oxide into the metallic coating, creating a convoluted path for the crack tip to follow, hence reducing the energy of the crack. However, once initiated, the crack tip would appear to have sufficient energy to cut through the oxide pegs rather than follow the TGO bondcoat interface.

As the generic failure mode seemed not to have changed, more detailed analysis was required to determine the role of the Ti.

Samples were aged to failure, as described earlier, in isothermal furnace soaks and any spalled TBC collected for examination. The underside of the spalled TBC was to be examined and compared to the metallic surface it was originally in contact with, using a combination of SEM and energy dispersive x-ray analysis (EDX). The ceramic TBC was mounted onto a metallic stub with the underside of the TGO uppermost and coated with C to provide a conductive path for the incident electron beam.

Analysis of the spalled material showed the underside to have retained approximately 80% of the Al<sub>2</sub>O<sub>3</sub> scale. The remaining 20% of the area was evenly distributed across the underside of the TBC, showing as small “islands” of ZrO<sub>2</sub>, see Figure 4.16

EDX analysis of both regions gave no indication of any features that would help to explain the role of Ti. Examination of the metallic side of the sample interface showed a similar ratio of 80% freshly exposed metallic surface and 20%  $\text{Al}_2\text{O}_3$  islands. The distribution of the islands of  $\text{Al}_2\text{O}_3$  matched the gaps seen in the opposing face. Closer examination of the  $\text{Al}_2\text{O}_3$  islands showed that in some cases remnants of the  $\text{ZrO}_2$  columns were still attached to the  $\text{Al}_2\text{O}_3$ , see Figure 4.16(b). It is suggested that in these instances the  $\text{Al}_2\text{O}_3$  scale has become mechanically keyed into the surface of the bondcoat through small undulations introduced during the grit-blasting process prior to TBC deposition. The subsequent crack followed the path of least resistance across the top of the “pit” into the TBC and back through the  $\text{Al}_2\text{O}_3$  to the TGO/bondcoat interface. The majority of cases, however, showed the remnant oxide was in the form of yttria/alumina pegs. Figure 4.17 shows the top of the sheared  $\text{Al}_2\text{O}_3$  peg. EDX analysis of the metallic surface showed no concentration of elements at the surface, the EDX trace being representative of an aged bondcoat.

No features were in evidence that suggested anything other than recently exposed bondcoat material. Analysis of the alumina pegs, however, showed a different picture. Analysis of the sheared top of a peg reveals that the majority of the peg was alumina, as expected, with a concentration of yttria at the centre.

More surprisingly a “torus” shaped void could be identified in the bondcoat around the top of the peg; there was also a greater concentration of Ti associated with the peg when compared to the surrounding metal.

It has been shown [77] that Ti diffuses rapidly along grain boundaries, this is also clearly demonstrated in Figure 4.18. As Y associates to these higher energy sites, it should not be unexpected to find both Y and Ti occupying similar sites. The higher concentration of Ti in contact with the Al<sub>2</sub>O<sub>3</sub> scale could significantly alter the growth mechanisms of the TGO, according to the theory presented by P Fox and G J Tatlock, [78]. It is shown that Ti<sup>4+</sup> ions will substitute for Al<sup>3+</sup> ions, in the ratio of 3:4 resulting in a vacancy. The introduction of vacancies into the Al<sub>2</sub>O<sub>3</sub> results in localised thickening of the oxide, in turn producing large lateral strains, resulting in buckling of the film, see Chapter 3.2. Oxide buckling could explain the voids observed around the “roots” of the yttria pegs. As the voids continue to grow with thermal exposure it is possible that they could reach a critical size sufficient to initiate cracking and ultimately TBC spallation. The process is shown schematically in Figure 4.19.

It could also be argued, however, that the phenomenon is caused by an alternative process of micro void coalescence. The diffusion of Ti to the TGO interface would occur over the whole of the sample, with a greater concentration along grain boundaries, as previously discussed. The Ti ions would produce vacancies by the same process as described above, the coalescence of these vacancies into micropores and subsequently into pores could lead to a critical defect size, sufficient to initiate cracking.

The energy of the crack tip would be great enough to take the line of least resistance across the top of the oxide pegs, the pegs would remain embedded in the bondcoat due to mechanical keying but would be surrounded by pores. Where the crack had cut

through the pores at the root of the pegs the impression of the torus shaped void could be the result.

#### **4.3.7 - Reducing the Effect of Titanium**

It became evident that the diffusion of Ti from the substrate through the bondcoat to the oxide scale should be prevented or at least delayed in order to improve the performance of the bondcoat. As Ti was a key element in the composition of the substrate materials of interest, CMSX-4, some form of barrier layer was required to achieve the above goal.

As discussed earlier, the Ti content of MarM002, although larger than that of CMSX-4 was largely combined with Ta and C to form stable carbides. The C levels in CMSX-4 are insufficient to “tie-up” the free Ti within the composition. An attempt was made to modify an MCrAlY coating system, to introduce low levels of C at an intermediate position between the substrate and bondcoat. The carbon was to be introduced in the relatively stable state of a CrC.

On thermal exposure, free Ti would react with the CrC in an exchange reaction, releasing Cr into the surrounding material and “binding” the Ti into the more stable TiC form. The released Cr would not be in sufficient quantities to effect the properties of the bond coat or substrate. A commercially available thermal spray powder was identified as having the correct composition, VF83 a NiCr/CrC mixture, suitable for deposition by air plasma spraying.

A thin layer, of the order of 30µm thick, was deposited onto CMSX-4 pins, these pins were then coated with an LPPS MCrAlY bondcoat and EBPVD TBC. The samples were tested as previously with a series of 25 hour isothermal furnace soaks at different temperatures and subsequently the residual strength of the TBC adhesion was measured using the modified scratch test.

In addition, two of the systems, (as processed and 25 hours at 1150°C) were then remounted in conducting Bakelite and EPMA ladder scans were produced.

Analysis of the ladder scans allowed the chemical performance of the system to be assessed.

Figure 4.20 shows the performance of the modified bondcoat when compared to an equivalent standard of the MCrAlY(RT122) system, for comparison the performance of the MCrAlY + Pt system is included. As is evident, no benefit was gained in TBC performance from the addition of CrC, in fact the opposite occurred to the detriment of 20°C to the ultimate temperature achieved.

The detriment in performance was probably due to a combination of poor/porous microstructure coupled with the inclusion of oxygen into the VF83 layer from the APS technique.

The EPMA ladder scans, Figure 4.21, show that the role of the C rich layer did achieve, to a limited degree of success, the required goal. An increase in concentration of Ti is clearly evident in the aged sample at the interface between the MCrAlY and the CMSX-4. Unfortunately the diffusion of the Ti continued through this concentrated region to the TGO, the levels at the scale were comparable to those in MCrAlY systems without the CrC additions.

Although this technique showed promise at this early stage, there was insufficient time available to concentrate on these additions when it was clearly shown in Figure 4.20 that additions of Pt were producing far better results.

## **Chapter 5 - Characterisation of the MCrAlY + Pt Bondcoat**

The identification of a novel bondcoat invariably lead to the requirement of more detailed analysis of the coating system. Three primary techniques were chosen to examine the form and chemistry of the bonding phases. The initial technique, and the most simplistic was optical metallography. This technique helped to establish the rules of the way in which the system degraded as well as clarifying the data generated by the other techniques. Secondly, Wavelength Dispersive Spectroscopy (WDS) was used to identify the compositional chemistry of the phases observed in the CoNiCrAlY+Pt bondcoat. The final technique utilised was X-ray diffractometry (XRD); this enabled the crystallographic structure to be determined.

By combining the information generated from all three techniques a simple model of the structure of the phases in evidence could be established.

### **5.1 - Optical Metallography of the MCrAlY + Pt Bondcoat**

The process of diffusing platinum into the surface of the CoNiCrAlY overlay changed the form and distribution of the  $\beta + \gamma$  phases identified in earlier chapters. Figure 5.1 shows how the darker Al-rich  $\beta$ -phase becomes denuded at the near surface region and becomes replaced by a continuous band of a phase of similar contrast immediately beneath the outer surface. When etched in a standard two stage electrolytic etch of 10N sodium hydroxide solution followed by 10% phosphoric acid, the platinum enriched

near surface phase becomes a bright contrast phase significantly different from the  $\beta$ -phase in the bulk of the coating, see Figure 5.2.

Micrographs taken of the bondcoat after isothermal furnace soaks at increasing temperatures show how the structure changes as it becomes increasingly denuded in aluminium through losses to the substrate and to scale formation, see Figure 5.3. The  $\beta$ -phase breaks down as aluminium diffuses towards the outer phase in order to replenish the aluminium lost to the oxide. The form of the outer phase changes little during this process, however, a second Pt-rich phase forms immediately beneath the oxide scale, between the scale and the Pt-rich  $\beta$ -type phase. The  $\beta$ -type phase seemed to be acting like a reservoir of aluminium, losing aluminium to form the more stable  $\text{Al}_2\text{O}_3$ , in the process forming the intermediate Pt-rich  $\gamma$ -type phase, whilst at the same time drawing aluminium from the body of the coating by destabilising the  $\beta$ -phase. This process is shown schematically in Figure 5.4. The stability of the outer phase was limited to  $1210^\circ\text{C}$  where the continuous band became interrupted and much reduced in % area. It is shown later in Figure 7.5 how the area % of the outer bright contrast phase changed with increasing temperature.

The next step was to identify the composition of the phases present and how these changed with exposure to temperature.

## 5.2 - WDS analysis of MCrAlY + Pt

WDS was chosen as the preferred analysis technique because of the greater ability to separate characterisation peaks when compared to the more commonly used EDS. Ladder scans (see Chapter 4) were produced of the MCrAlY+Pt system in order to examine the bulk elemental movements through the bondcoat. See Figure 5.5. In each of the samples identified above four regions were analysed.

- i) Bright contrast outer phase (A)
- ii) Dark contrast outer phase (B)
- iii) Bright contrast inner phase (C)
- iv) Dark contrast inner phase (D)

A,B,C and D are identified on the back-scattered electron (BSE) SEM image shown in Figure 5.6. The as-received composition of region A is identified in Figure 5.7. The graphs plotted in Figure 5.8 show how the levels of the influencing elements vary in the outer phases with exposure to increasing temperatures. As can be seen, the compositions of the outer phases remain remarkably consistent, with the main changes occurring to the levels of tramp elements (Ti, Ta etc.), increasing with increasing temperature. By combining this data with the data generated by XRD analysis, a structure of the outer bonding phases can be produced.

### 5.3 - XRD Analysis of MCrAlY + Pt

The limited penetration depth of the  $\text{CuK}\alpha$  radiation through PYSZ due to the large absorption coefficient ( $\mu/\rho$ ), necessitated the XRD analysis of the samples to be completed on test pieces produced without the TBC topcoat. The incident area of the X-ray beam (approximately 10mm x 4mm) allowed accurate analysis of the surface of the standard 8mm diameter pins to be achieved. XRD diffractographs were produced of samples in both the as processed condition and after isothermal furnace soaks of 25h at 1150°C. Figure 5.9 shows the traces produced from this analysis with Figure 5.10 tabulating the data. The characteristic pattern, when compared to Joint Council for Powder Diffraction Standards (JCPDS) file, produced no suitable match. The closest fit to the trace, using a least squares fit, yielded a tetragonal cell with interplanar spacing of:

$$a = 8.84\text{\AA} \quad \text{and} \quad c = 7.95\text{\AA}$$

This fit excluded the peak at 1.49Å

The most accurate fit, without excluding peaks, identifies a triclinic phase with parameters of:

$$a = 3.14\text{\AA}, \quad b = 3.53\text{\AA}, \quad c = 2.76\text{\AA}$$

$$\alpha = 89.8^\circ, \quad \beta = 90.4, \quad \gamma = 94.0$$

This fit would suggest a large distorted cubic type cell.

The “new” phase was given the nomenclature “P-phase” to identify it as unique. The XRD analysis confirmed the WDS and optical data suggesting that P-phase was particularly stable.

#### **5.4 - Summary of P-phase**

The analysis of the near surface phases produced when platinum is diffused into an MCrAlY coating and the degradation processes which occur with subsequent heat-treatments are summarised below.

Diffusing platinum into the surface of the MCrAlY produces a continuous band of P-phase immediately beneath the TBC. The P-phase was formed by the destabilisation of the  $\beta$ -phase by the presence of the platinum. The  $\beta$ -phase broke down into  $\gamma$ -phase releasing aluminium which formed the thermodynamically more stable P-phase.

Subsequent oxidation of the bond coat lead to the lowering of the aluminium content of the P-phase directly in contact with the aluminium oxide scale.

The loss of aluminium from the P-phase to form the oxide resulted in the formation of the platinum rich  $\gamma$ -phase. The aluminium lost from the P-phase, via the platinum rich

$\gamma$ -phase, to form the  $\text{Al}_2\text{O}_3$  scale was replenished by further degradation of the  $\beta$ -phase in the MCrAlY.

This dynamic process has been demonstrated to be capable of sustaining P-phase for 25 hours up to a temperature limit of 1210°C. After this exposure the P-phase becomes non-continuous. The breakdown of this layer is synonymous with TBC loss. It is proposed that the P-phase can contain up to 0.5 atomic % titanium in its crystal structure, limiting the levels that can diffuse to the oxide interface. The graphs shown in Figures 5.8 indicate the levels of titanium in the outer regions of the bondcoat, (A) being the bonding  $\gamma$ -phase, (B and C) the P-phase and (D) the  $\gamma$ -phase beneath the P-phase. As can be seen the levels of titanium in the P-phase are approximately twice those seen in the surrounding coating. The breakdown of P-phase releases this store of titanium, which then leads to the disruption of the oxide and, ultimately, to TBC loss, see Chapter 4.

### **5.5 - Reactive element distribution in MCrAlY+Pt Bondcoats**

It is well documented that Y has a significant effect on the performance of protective coatings (see chapter 3). To this end MCrAl coatings were developed into MCrAlYs. The deposition techniques usually associated with this family of coatings often include high temperatures which could potentially result in the Y content becoming oxidised. What is unclear from the literature is whether Y-oxide ( $\text{Y}_2\text{O}_3$ ) offers the same performance enhancement as Y metal when incorporated into the TGO. It is evident,

however, that  $Y_2O_3$  would not diffuse to the oxygen-rich interface as Y metal would; and hence only a very limited proportion of the Y in the coating could aid in the oxide adherence.

The requirement to change the processing technique from EB-PVD to the more economically viable LPPS, increases the probability of oxide contamination within a coating. A programme of work was undertaken to examine the effect of the processing technique on the Y/ $Y_2O_3$  content of the coating.

#### **5.5.1 - Y/ $Y_2O_3$ Identification in MCrAlY Coatings**

Initial attempts were made to determine the state of the Y content of the coatings using WDS mapping. Samples of CoNiCrAlY deposited by argon – shrouded plasma (ASP), LPPS and EB-PVD were produced. It was known at this stage that the EB-PVD samples would out perform the LPPS that would equally out perform the ASP samples when used as bondcoats. This ranking was related to the partial pressure of  $O_2$  in the processing environment. Samples were mounted in cross-section in the as-processed state and after exposure for 100h at 1100°C. WDS maps were taken of all the samples for Y and O. Comparison of the associated maps would help to indicate whether the Y was present as an oxide or metal. Comparison of the as-processed samples and the aged equivalents would indicate the mobility of the Y content and also the likelihood of it reacting in situ and not diffusing as expected. The relatively large probe size in

conjunction with the fine dispersion of the Y particles resulted in only limited success and the results were not conclusive. These are summarised in Figure 5.12.

It was decided that secondary ion mass spectroscopy (SIMS), may offer finer resolution than the WDS technique. SIMS offers the ability to map for oxide directly through selection of the primary beam type. In this study, two primary beams were used,  $O^+$  and  $Ar^+$ . Using an  $O^+$  ion beam enhances the ion yield of metals by up to two orders of magnitude over using an  $Ar^+$  primary. When using the  $Ar^+$  beam, only those areas where the metal had combined with  $O_2$  appear as bright in the image. It was theoretically possible, therefore, to compare the Y and the  $Y_2O_3$  contents of the coatings directly. Figure 5.11 compares the images produced by the  $O^+$  and  $Ar^+$  primary beams of the LPPS MCrAlY+Pt system. The figure shows that Y is present throughout the coating with concentrations at both substrate/coating and the MCrAlY/Pt interfaces. The  $Y^+$  image shows that at these two interfaces the Y is combined as oxide. This is particularly the case in the areas of 'rag' where the surface has become folded and entrapped due to the peening operation, immediately beneath the Pt layer.

The SIMS analysis of the other systems supported the results from the WDS analysis, in that the performance of the MCrAlY coatings was related to the degrees of free Y present in metallic form. The SIMS analysis of the LPPS system indicated that there was potential for improvement through optimisation of the spraying parameters.

## **Chapter 6 - Improvements to CoNiCrAlY+Pt Processing**

As demonstrated in Chapter 4, there was potential for considerable improvement to the performance of the LPPS processed CoNiCrAlY+Pt bond coat system. The complete manufacturing method and coating design was broken down into component stages, each aspect was reviewed and moves made, where necessary, to improve the processing parameters. These experiments are reported and discussed within this chapter.

### **6.1 - Effect of Peening on MCrAlY Microstructure**

The standard processing of MCrAlY coatings generally includes an intense peening operation after the diffusion heat treatment stage. The peening operation was designed to remove the as-processed surface roughness from the coating. See Figure 6.1. The coarse surface finish produced by the thermal spray processing was removed by the mechanical deformation of the outer portion of the coating. The larger "asperities" of the as-sprayed structure were plastically deformed into the troughs between them. This resulted in a relatively smooth surface, which received a light vibro-polish to achieve the desired finish. Figure 6.2 shows the fully processed MCrAlY(CoNiCrAlYHfSi) structure. Examination of Figure 6.2 highlights the entrapped surface oxide in the heavily deformed outer portion of the coating. This surface "rag" provided diffusion paths for oxygen to penetrate into the coating. At elevated temperatures the oxidation of the surrounding metal would create an uneven oxidation front leading to localised aluminium depleted regions, see Figure 6.3. Without the correct chemistry at the

oxide/metal interface  $\alpha\text{-Al}_2\text{O}_3$  cannot form, increasing the likelihood of spinel formation, see Chapter 3.7.

It was considered that the intensity of the peening operation was sufficient to cause bulk deformation of thin-walled components, rendering them unusable. With the move towards single crystal materials there was further concern over initiation of re-crystallisation as a result of cold-working the near surface region of the component. When coupled with the undesirable oxidation performance, the cost of the peening process and the relatively poor surface finish it was considered prudent to re-assess the MCrAlY processing route.

The obvious alteration was to remove the reliance on peening and move towards a polished-only MCrAlY coating.

### **6.1.1 - Polishing of MCrAlYs**

In order to achieve the required surface roughness, without the reliance on the peening operation, a considerable increase to the polishing time was required. Trials were carried out to assess the effectiveness of different media on the rate of material removal and ultimate surface finish achievable.

In conclusion to the polishing trials, in order to achieve the required surface finish from an as-sprayed MCrAlY, 24 hours of vibro-polishing in CE7 media was required.

It became apparent, however, when comparing the original "10A" MCrAlY to the polished equivalent, differences in performance were observed. After isothermal soak trials of the two systems at 1100°C, the polished-only sample demonstrated significant internal oxidation and exaggerated  $\beta$ -phase depletion. Figure 6.4 compares the 10A standard with the polished equivalent. By etching away the metallic component of the MCrAlY coating in the solution of 10% bromine in methanol it was clear to see that the internal oxidation was linked to the free surface through convoluted oxide paths. See Figure 6.5. This highlighted a previously unnoticed benefit of the peening process. It appeared that the plastic deformation of the near-surface region was closing rapid oxygen-diffusion paths by bringing the two faces into intimate contact, allowing inter-diffusion to occur on heat treatment, effectively "sealing" the surface region. The cutting action of the polishing media failed to lead to the closure of these paths, allowing subsequent rapid internal oxidation to occur. In an attempt to prevent this, the peening stage was re-assessed.

### **6.1.2 - Re-assessment of the Peening Process**

Attempts were made at retaining the improved surface finish, achieved through the modified polishing procedure, by altering the processing route to include the peening stage after polishing. It was decided to assess the effectiveness of various media and peening intensities on the densification of the polished MCrAlY coatings.

8mm diameter MarM002DS bars, 110mm in length, were over-coated with an LPPS MCrAlY. The MCrAlY was then polished to achieve a surface finish of  $Ra < 30 \mu$  inch. Metal Improvement Company (MIC) then peened these according to the matrix of media and intensities shown in Figure 6.6. It was decided the best way in which to assess any changes in the properties of the coatings, due to the affect of the peening, was with a combination of metallographic inspection, through-thickness microhardness measurements and isothermal heat treatments in air and vacuum.

### **6.1.3 - Experimental procedures**

The test pieces were coated as one batch, in an attempt to reduce process variability. One pin was removed after the polishing procedure to be used as a baseline comparator. The remaining test pieces were then peened according to the matrix outlined in Figure 6.6, (one pin per processing route). After peening, a section was removed from each pin and mounted in cross-section in conducting Bakelite. The remainder of the pin was then vacuum heat treated, as per the standard processing route, for one hour at 1100°C. A further section was removed and mounted as mentioned above. A final section from both the peened and un-peened test pieces, both in the heat treated condition, was taken at this stage, in order to examine the effect of thermal exposure in air. Once the final 25 hour isothermal exposure to air at 1100°C had been completed, the samples were mounted as before. All the samples were then polished, using the standard bondcoat-

polishing procedure as outlined in Chapter 4.2. The samples could then be compared, to assess the effect of the peening process.

The effects of the heat treatments could be distinguished using optical metallography. In the as-sprayed and polished condition the microstructure appeared fully dense, with few pores or fissures visible. The coating consisted of a two-phase structure, with a very fine distribution of  $\beta$ -phase in a  $\gamma$ -phase matrix, typical of the MCrAlY type composition shown in Figure 6.1. After the vacuum heat treatment, there was an easily distinguishable inter-diffusion zone between the MCrAlY and the substrate and the  $\beta$ -phase had coarsened slightly. At this stage, it was impossible to distinguish any differences caused by the peening process. Even after the 25-hour soak test, there appeared to be no appreciable differences between any of the systems. In all cases the  $\beta$ -phase became more coarse, the inter-diffusion zone became deeper and a  $\beta$ -phase depleted zone developed beneath the T.G.O at the surface. The  $\beta$ -depleted layer was comparable across the range of samples examined. These changes can be clearly seen in Figure 6.7.

It was supposed that any increase in density of the coating, due to the peening process, could be detected through measurement of the hardness of the coating. In order to determine the depth of penetration of any hardness increase, microhardness measurements were taken through the thickness of the coatings in cross-section. The resultant hardness measurements could then be plotted against distance from the surface of the coating.

Although not an exact representation of the method employed, Figure 6.8 gives an idealistic indication of what was attempted. In reality a larger number of randomly positioned measurements were taken from four opposing positions on each sample. The average results were then plotted to give a realistic representation of the hardening effect. It was considered important to repeat this exercise on samples both before and after heat treatment and after ageing, as an apparent increase in hardness could be achieved through the introduction of dislocations produced by cold-working of the coating. The heat cycles would anneal the MCrAlY and, therefore, any measured hardening would be as a result of the closure of pores and hence represent the increase in coating density.

Figure 6.9 represents the measured hardness results from the system exposed to the most intense peening operation from the matrix, i.e. 15A ceramic bead. Comparison of the traces shows an increase in measured hardness of the coating. On subsequent heat treatment and ageing, however, the hardening effect due to the peening operation diminishes. The final trace shows a similar profile to the un-peened sample.

#### **6.1.4 - Discussion of MCrAlY Finishing**

It must be concluded, therefore, that peening of MCrAlY type coatings, after polishing, does not significantly increase the density of the coating or reduce the level of internal porosity. The limited effect of the peening process on the polished surface was

probably due to the media spreading the impacting load over a large contact area as opposed to the situation more akin to single point asperity contact in the unpolished condition.

It can be shown that when a spherical particle impacts on a surface, plastic deformation occurs at the point of maximum pressure,  $P$ , beneath the surface ( $2/3a$ , where  $a$  = radius of contact area). In order to create sufficient plastic deformation to close pores etc. then deformation of the surface must occur. In order to achieve this a contact pressure of  $6K$  must occur where

$K$  = maximum value of shear stress,  $\tau$  (in uniaxial stress situations  $K = \tau_{\max} = \sigma/2$ ).

Therefore the peening intensity required to effect the porosity of the coating must impose a local pressure of:

$$P = 6K = 3\sigma$$

As  $P = N/A$

then  $P = N/A = 3\sigma$

The force required to cause plastic deformation is significantly affected by the contact area. The normal loading (N), due to the peening media, required to just cause plastic deformation is directly related to the normal stress ( $\sigma$ ) and the contact area (A).

It follows, therefore, that smaller contact areas, i.e. asperities, require less force to cause plastic deformation and hence less force is required to close pores.

In order to achieve the goal of closing porosity in the polished MCrAlY coatings, peening intensities in excess of 15A would be required. As 15A is a more intense operation than the original process it is obvious, therefore, that peening after polishing was not a viable processing route. It was decided that a more fundamental change was required, namely the reappraisal of the LPPS processing parameters.

## **6.2 - Optimisation of the spraying parameters using the Taguchi Method**

As discussed in the previous chapter, the reliance on the peening operation to remove some of the variability in the MCrAlY coatings was not viable because of the concerns over potential damage to components.

The attempt to change the processing route to allow for a less intense peening operation was unsuccessful, with the modified process failing to close internal porosity in the coatings. It became obvious, therefore, that a more fundamental change to the processing route was required. The principles of single-source manufacture effectively

excluded the possibility of changing the processing system from the LPPS standard, as the supplier was not able to offer appropriate alternatives. The only option remaining was to improve the LPPS processing. The large number of variables within the LPPS system excluded the possibility of completing a full factorial experimental design, a partial factorial design was, therefore, necessary. It was essential that the results, and if necessary, the experiment, could be used at other manufacturing sites. To this end the use of orthogonal arrays described for use with the Taguchi Method of experimental design was seen as beneficial. The link between the Taguchi Method and orthogonal arrays is described in Chapter 3.7.

### **6.2.1 - Experimental method**

It was decided that the most appropriate way to approach the optimisation of the LPPS processing method was through a phased programme. It was expected that a minimum of two, most probably three, phases would be required in order to achieve the goal. In the ideal case of a two-phase programme, the initial stage would be a scoping trial, which would result in an approximate set of processing parameters. The processing window would be refined in the second phase, resulting in a set of parameters that would produce the optimal coating performance available from the LPPS system. In the second, and most likely case, a three-phase programme would be required. The additional phase would examine the role of any interacting variables, allowing them to be accommodated in the final experimental design. As previously discussed in Chapter 3.7, the Taguchi Method of experimental design does not automatically recognise and

deal with variable interactions. The role of the operator/experiment designer is critical in identifying and responding to interactions. In the case of the LPPS system the large number of variables affecting the resultant coating increased the likelihood of interactions occurring.

Each phase of the experimental design could be broken down into approximately the same identifiable stages.

- (i) Identifications of variables
- (ii) Identification of (potential) interactions
- (iii) Selection of the appropriate orthogonal array
- (iv) Positioning of variables in the array
- (v) Identification of responses
- (vi) Completion of experiments according to the array
- (vii) Repeat of (vi)
- (viii) Selection of optimised parameters through analysis of the results
- (ix) Clarification of the optimised parameters

### **6.2.2 - Identifications of variables**

In order to achieve the most from the optimisation programme it was essential to identify all the variables in the process. If, in the first phase of the programme, assumptions were made as to which variables were deemed the most important and the

secondary variables were ignored, the effectiveness of the Taguchi Method would be impaired. Examination of the spraying process currently adopted, identified eleven variables, See Figure 6.10. These covered all aspects of the process from the obvious, i.e. gun current, to the less obvious, i.e. sample pre-heat. It was considered impractical to change some of the fundamental aspects of the LPPS process, such as the spraying gases, as these would change the whole nature of the technique and would therefore require a much larger and therefore considerably more costly series of experiments.

### **6.2.3 - Identification of Potential Interactions**

Examination of the identified variables gave an indication of those factors that were most likely to react. It was evident at this stage that an understanding of the process being optimised was essential in order to complete the task successfully.

The co-dependent nature of the powdered source material and the powder-carrying gas pressure suggested the possibility of these two factors interacting. Operator experience also suggested a relationship between the powder and the gun-current. It was proposed, therefore, that these two coupled-factors should be considered as the most likely to interact.

### **6.2.4 - Selection of the Orthogonal Array**

#### **6.2.4.1 - Phase 1**

As discussed in Chapter 3.7, there are a limited number of orthogonal arrays from which to select the most appropriate for the task. In the case being discussed, there were eleven variables with the potential of at least two interacting pairs. Selection of an array suitable to accommodate this problem would lead to an experimental matrix of considerable size. The optimisation programme, in this situation, was to interrupt production and the length of time required to complete the experimental matrix was therefore, to be kept to a minimum. It was considered most appropriate to use as small a matrix as possible.

In order to accommodate eleven variables at two levels, the most simple case, an  $L_{12}$  array was selected. See Figure 6.11. Unfortunately, the  $L_{12}$  array does not have a corresponding linear graph, and so unlike the majority of orthogonal arrays the interactions cannot be separated out. The interactions instead of being compounded to only one column are spread more or less evenly across all the columns. This makes studying interactions impossible. It is only possible to study the average response graphs after completing the series of experimental runs, identifying the optimal settings and producing a conformance test piece. If the performance of this testpiece differs from that predicted, then it is likely that something has been missed. This information in conjunction with the average-response graphs from variables believed to be non-significant, can identify the possibility of interacting terms.

By selecting the smallest possible array ( $L_{12}$ ) it was hoped that time would be saved if no interaction occurred. If the conformance test piece failed to perform as predicted, then a second phase experiment would still be required.

#### 6.2.4.2 - Phase 2

As previously identified there were two pairs of variables that were likely to interact. Knowing this allowed the phase two array to be designed in order to examine the interaction, if this was required when the results of the first phase were completed. The two pairs of potentially interacting factors are:

- (i) Powder flow rate and gun current B, C
- (ii) Powder flow- rate and carrier-gas pressure B, K

(See Figure 6.10)

In order to accommodate these pairs and their potential interaction within an orthogonal array would require an array with at least five factors at two levels. The smallest orthogonal array capable of accommodating this number of factors is the  $L_8 (2^7)$  array. This array would allow two additional factors to be examined. When studying an interaction it is good practice to include an unlikely interaction as a baseline. In this case it was considered that the sample pre-heat could not conceivably interact with the other three factors being examined. Sample preheat I, was included, therefore, to verify the array. The additional factor was set to be the interaction between I and another factor B, C or K. Figure 6.12 shows the  $L_8 (2^7)$  array and the corresponding linear

graphs. The linear graphs indicate the positions where aliased-pairs will occur. By studying these linear-graphs it is possible to place the factors into columns of the array, such that columns are left free to accommodate the aliased-pairs that represent the interacting terms. Figure 6.13 shows the placement of the factors and the positions where the interacting terms will occur. The resultant average effects graph will indicate whether an aliased-pair produces a significant response. If this occurs then it is probable that the factors contributing to the aliased-pair are interacting. Similarly if no significant response is registered then there is no interaction. The baseline aliased-pair, I and B, C or K should show no interaction. If a response occurs for the baseline an error has been made and a redesign of the matrix should be considered.

#### 6.2.4.3 - Phase 3

The results from Phase 2 indicated that an interaction was occurring between two factors. Knowing this allowed the final experimental design to be established. Again, in an attempt to keep the experimental matrix as small as possible decisions were made regarding some of the variables from the phase 1 trials. From phase 1 it was shown that some factors did not alter the measured response for  $\beta$ -depletion significantly, this allowed them to be set to convenient levels and potentially removed from the list of variables. Other variables did however, have a significant effect on the responses. Of these variables some only had two settings, for example nozzle type (Factor F), the setting was selected that gave the better result and the variable removed from the array.

Phases 1 and 2 had examined the effects of variables set to two levels, assuming a linear relationship. For the final experimental matrix, it was decided to examine the interaction in greater detail, whilst further optimising the remaining variables. It was concluded that the best way to achieve this was by using a mixed level array. The most appropriate array for this purpose was the  $L_{16}(b)$  array, see Figure 6.14.

By studying the linear graphs for this array it can be seen that by the investigation of the BC interaction at 4 levels makes it possible to study five further variables at two levels. This arrangement allowed the baseline factor I, to be included once again.

Allocating the factor set to four levels, to be one of the interacting pair allowed a detailed examination of the interaction to be carried out.

## **6.2.5 - Identification of Responses**

### **6.2.5.1 - Phase 1**

In order to assess the output from the experimental matrices, the Taguchi Method is reliant on numerical responses. Each individual row of the orthogonal array represents one experimental run. The  $L_{12}$  array selected for the phase 1 design required, therefore, twelve separate runs to be made in order to complete the matrix. (It is usual, however, to complete the test matrix twice, in order to ensure repeatability - a total of 24 runs). For each of these runs a measurable result or response was required so that the optimal

processing parameters could be calculated. As the goal of the optimisation was to remove the pores from the MCrAlY coating, and to produce a coating that was resistant to oxidation, then a measure of these factors was most appropriate. The removal of pores would, in theory, result in a more dense coating, therefore, a measure of the coating density was a suitable response. The test bars would be measured, length and diameter, prior to the coating being deposited. Once the MCrAlY had been sprayed and polished, the diameter of the bars would again be measured, as would the length of the coated section. The bars would also be reweighed. Subtracting the initial mass from the coated mass would give the mass of the coating. By treating the coating as a hollow cylinder the volume of the coating could be established. Combination of the two values would give the density of the coating. See Figure 6.15.

An indication of oxidation resistance, in two-phase MCrAlY type coatings, is the way in which the aluminium rich  $\beta$ -phase degrades. As the aluminium is “used-up” during the formation of the protective or bonding oxide scale ( $\text{Al}_2\text{O}_3$ ), the  $\beta$ -phase transforms to  $\gamma$ -phase resulting in a denuded zone at the oxygen-rich interface. It is clear, therefore, that a coating that maintains the  $\beta$ -phase for the longest period, at temperature, is able to supply aluminium in order to generate the protective scale for longer, thus extending the useful life of the coating. In terms of TBC adhesion, as long as  $\alpha\text{-Al}_2\text{O}_3$  is being formed and not mixed oxide spinels, the coating is capable of supporting the ceramic for longer. It was proposed that the depth of the  $\beta$ -depleted zone could be used as a measure of the quality of the coating. Two samples would be taken from the coated and polished test pieces and exposed for 25 hours at  $1100^\circ\text{C}$  in

still air. The “aged” samples would be mounted in cross-section and metallographically prepared.

A number of measurements would then be made at equidistant points around the circumference of each sample, recording the depth of the  $\beta$ -phase depleted zone. The average of the 32 measurements would be taken as the response of  $\beta$ -depletion for that sample/experiment number.

The third response considered at this stage was based on the assumption that improvements to the spraying parameters would create a finer “splat” structure resulting in a smoother surface finish. It was proposed that surface finish measurements in the as-sprayed condition would be used as another response. Measurements would be taken along the length of the test bar, care being taken to ensure the stylus of the measuring equipment was placed along the top and normal to the surface of the test piece.

The resultant Ra value obtained for each test piece would be used directly as the response.

#### 6.2.5.2 - Phase 2 & 3

Resulting from the difficulties seen with the selected responses in Phase 1, a modified set was chosen for successive experiments.  $\beta$ -depletion was still considered a critical

measure of coating performance and was, therefore, retained as a response. An additional response was included at this stage because of the difficulty experienced by the LPPS operators, during some of the deposition runs of phase one. Some of the combinations of factors proved to be very difficult to spray, leading to instability in the plasma plume and resulting in molten metal dripping from the gun.

An arbitrary response was therefore included to be recorded by the operator after each experimental run. This response was termed “sprayability” with each run being given a score out of ten, one being difficult to spray, ten being easy.

## **6.2.6 - Completion of the Experiments**

### **6.2.6.1 - Phase 1**

In the ideal case, the order in which the experiments or trials would be carried out within each phase would be random, or more usually simply would follow the order of the experiments as laid out in the orthogonal array. This would produce the most statistically “pure” results, as repeatedly changing from one variable setting to another would prevent any progressive change in any particular factor. This is most easily represented by example; if a machining operation was being optimised and two types of cutting tips were being examined as one of the variables, then progressive wear and debris build up could potentially occur if one tool was used repeatedly.

If the tool were changed after each experimental run, then a true result would be obtained. In the case being studied here, as previously mentioned, the speed with which the process could be completed was of prime importance, as the production capability of the LPPS rig was being tied up. Examining the list of identified variables highlights the need to vent and break the vacuum of the spraying chamber in order to switch from one setting to another. The breaking of the vacuum system could, potentially, introduce a leak into the chamber. A leak would cause oxide particles to become incorporated into the subsequent coatings. In order to ensure no leaks are in evidence after such a system break, oxide level assessment test pieces are produced as standard practice. The production and assessment of each of these test pieces requires at least 30 minutes, in the interim period the LPPS rig cannot be used. It is evident that reducing the number of occasions where this was necessary significantly sped up the whole process.

In this situation, it was deemed most appropriate to arrange the order of the experiments so that the need to break the vacuum was kept to a minimum. Figure 6.16 shows the order in which the trials of phase one were completed. The repeat of the array of experiments allowed a degree of variation to be introduced into the process, this was achieved by simply reversing the order shown in Figure 6.16.

## 6.2.7 - Assessment of the Results of the Experimental Design

### 6.2.7.1 – Phase 1

As previously mentioned, the first phase of the Taguchi Method used in this study incorporated eleven variables set to two levels in an  $L_{12}$  array. The responses selected to assess the effects on the resultant coatings performances were:

- i) Coating Density
- ii) Surface Roughness
- iii)  $\beta$ -phase Depletion

The aim of the first phase was to assess the effect of each variable on the resultant coating and to produce an approximate set of parameters from which subsequent phases could result in an optimised spraying process. This can be achieved by plotting the “average effects” of each variable factor, at each level, for a particular response. Visual inspection of the average effects graph for a response, can help to determine the best levels for each factor required to improve the process with regard to that response. Calculation of average effects is relatively straight forward, but is most easily described through example.

Consider a factor, A, set to two levels  $A_1$  and  $A_2$ , in an  $L_4$  array, see figure 6.17. In the  $L_4$  array the factor appears set to level 1 in experiments (trials) 1 and 2. Each of these trials will produce something with a measurable response, termed  $R_1$  and  $R_2$

respectively. It is the arithmetical mean of these response values that gives the average effect for factor A at level 1, see below:

$$\bar{A}_1 = (R_1 + R_2) / 2$$

This holds true for all the factors set to all levels i.e.:

$$\bar{B}_2 = (R_2 + R_3) / 2$$

$$\bar{C}_1 = (R_1 + R_4) / 2 \text{ etc.}$$

In the  $L_{12}$  array being considered there will be a total of sixty-six calculations to make in order to complete the average effects for all eleven factors set to two levels for each of the three responses. It is often easier to examine the results of these calculations by plotting the average effects against response, linking individual factors, e.g.  $A_1$  and  $A_2$  together indicates the significance of that factor through the slope of the connecting line. Namely, the steeper the gradient, either positive or negative, the greater the effect on the response by changing the level of that factor from one to another.

Once the series of trials for phase one had been completed, as laid out in Figure 6.11 and the three responses measured, then the average effects for each response type were calculated. The results are shown in Figure 6.18. Graphical representations of the average effects for each response are shown in Figures 6.19(a), (b) and (c) respectively.

According to the average effects graphs shown in Figures 6.19(a), (b) and (c), the LPPS system could be optimised to produce either a dense coating, a smooth coating or an

oxidation resistant coating, as each graph suggests a different set of parameters would be optimal. At the outset of the experimental design, assumptions were made about the three responses selected. It was assumed that the best coating would demonstrate all three properties. At this stage, further assumptions were made; the accuracy of measuring the density of the MCrAlY coatings was suspect due to the difficulty in measuring the actual volume of material deposited, errors could be incurred due to tapering of the coating and overspray around the end of the test piece. Similar concern was expressed over the measurement of the surface roughness due to the curvature of the surface being measured. It was decided, therefore, to concentrate on using the  $\beta$ -depletion measurement as a reproducible indicator of the performance of the coating. Because of the differences in thickness produced by varying the powder feed rate, the  $\beta$ -depletion term was expressed as a percentage of the overall thickness of the relevant coating.

At this stage of the Taguchi Method it would be normal to produce a test piece with the parameters predicted by the average affects results. It would have been possible to produce a coating from parameters selected as compromise between the three sets of suggested parameters, however, a compromised coating would have subsequently been produced. It was decided, therefore that the  $\beta$ -depletion response should be used to predict the optimised parameters. Figure 6.20 shows the parameters selected in order to produce the testpiece.

Some provisos were made as to the selection of the parameters. Firstly, the nozzle to be used was the “93” nozzle, the experience gained from the operator suggested that the alternative, “141” nozzle would not have the life requirement for a production system; material build-up on the nozzle occurred at too fast a rate. Secondly, the powder fraction “1A” was to be used, this decision was made for commercial reasons. These parameters were used to calculate the performance of the confirmation test piece according to the equation below:-

$$Y_{opt} = T/N + (\overline{A_x} - T/N) + \overline{B_x} - T/N + (\overline{C_x} - T/N) + (\overline{K_x} - T/N)$$

where  $Y_{opt}$  = the  $\beta$ -depletion response for the optimised parameters.

T = Sum of the  $\beta$ -depletion responses for the matrix

N = Number of responses

x = The appropriate level for the average effect selected i.e. 1 or 2.

When the confirmation testpiece was produced and assessed, the measured response did not match the predicted. It became evident that something had been missed during the experimental design, this led to the, previously mentioned, second phase, to examine the potentially interacting variables.

### 6.2.7.2 - Phase 2

As mentioned in Chapter 6.2.5, the responses measured in the phase 2 programme were different from those of the phase 1 experiment. The difficulty of measuring, accurately and repeatedly the density and surface roughness of the coatings meant that these were no longer considered suitable responses. The  $\beta$ -depletion response was supplemented with the “sprayability” term, identified during deposition.

Figure 6.21 shows the average effects for  $\beta$ -depletion and sprayability as calculated using the procedure laid out in phase 1 above. When plotted out to produce the average effects graphs, see Figures 6.22(a), (b), assessment of the results becomes more straight forward. At this stage most emphasis was placed on the  $\beta$ -depletion response rather than the, unproven, sprayability term. In this phase the sprayability term was to be assessed for feasibility rather than to be used as a tool, the aim was to use this response in the final design to ensure the resultant parameters were realistic.

It is evident from Figure 6.22(a) that there are three significant factors, indicated by the greater degree of slope of the lines for B, C and BC. This is a clear indication that an interaction between factors B, powder flow rate, and C gun current occurs during processing.

The other potential interactions that were considered, BK, BI or KC could be disregarded at this stage as the responses elicited from the allocated columns were non-

significant. The baseline term, I, sample preheat, confirmed the validity of the experiment by remaining non-significant as expected. Identification of the interacting terms allowed the final phase of the optimisation programme to be designed making allowance for the interacting terms. The results from “sprayability” encouraged the use of this term as support for the transition of the results of the phase 3 experiment into a production standard. A confirmation testpiece was not required from the phase 2 experiment as the role of this matrix was simply to identify the interacting terms.

#### 6.2.7.3 - Phase 3

The average effects produced for the phase 3 design were calculated as previously discussed for phases 1 and 2, the results are laid out in Figure 6.23.

As the experiment was designed to examine in greater detail the effect of the BC interaction, then the factor B, powder flow rate, was set to four levels. This resulted in two sets of values being produced for the BC interaction corresponding to the two levels apportioned to factor C, gun current. The benefits of having a factor set to more than the basic two levels are clearly demonstrated by the average response graphs shown in Figures 6.24(a) and (b). The curved response produced by factor B for  $\beta$ -depletion shows that selecting either of the limiting parameters B1 or B4 would not produce the desired result, in fact B2 would appear the most appropriate. Interpretation of the average response graphs for matrices examining the effect of an interaction is not as straight forward as for the more simple cases previously examined. For those terms

not involved in the interaction, the determination of the optimum parameters is completed as identified earlier.

The case seen here for the  $\beta$ -depletion response is fairly straightforward. The significance of the factor C is evident from the slope of the line; with C2 giving the most favourable response with regard to minimum  $\beta$ -depletion. The curved response from B shows that the optimal response is clearly B2. It should be re-iterated at this point, however, that C and B do not act individually but interact. It is, therefore, the interaction term BC that should be considered. In a two level design there would be two responses plotted for an interaction between B and C: (B1C1 and B2C2) and (B1C2 and B2C2). Any combination of these parameters that gave the lowest response would be selected. B being set to four levels complicates the situation. It is still clear, however, that the optimum response comes from the B2C2 combination; this corresponds to the individual parameter settings. The situation appears, at first glance, more complicated in the case of sprayability, but it can be approached in the same way. The curved response for B shows B1 to be the condition required to produce the highest degree of sprayability.

In this case, C gives a fairly flat response with C1 showing slightly better performance than C2. Examining the interacting terms, the highest response comes from B1C1, although the difference between B1C1 and B1C2 is only marginal. Figure 6.25 shows the two sets of optimal parameters for  $\beta$ -depletion and sprayability respectively. It was deemed important for a production system to perform well in both responses, in order to

achieve a combination of a good product with manufacturing equipment reliability. To achieve this a balance was struck between the two sets of optimised parameters. Comparison of the sets of parameters shows only a little correspondence, i.e. A1, E2 and I2. The other non-significant factors were set to a level most appropriate to reasoned judgement. The response graph for D for  $\beta$ -depletion is almost flat, therefore, priority to D can be given to the sprayability term i.e. D1. K acts equally and opposite to both responses, it was decided that the priority should be given to the higher gas pressure setting of K2 to reduce the likelihood of powder blockage during production. In order to produce a good  $\beta$ -depletion response, it was critical to select C2. In isolation the B2 response would be predicted to produce the better result, however, the effect of B was minimised by the interaction making any level acceptable. When considering the sprayability response it was clear the B1 should be selected when in combination with either C1 or C2. The ideal compromise positions for B and C would, therefore, be B1 and C2.

Figure 6.26 shows the optimised parameters required to repeatedly produce a coating with good oxidation resistance.

### **6.3 - Effect of CoNiCrAlY Thickness on TBC Performance**

Ideally, a coating system would be included during the component design stage, enabling dimensions to be closely adhered to; dimensions such as the throat area (distance between vane aerofoils) or the thickness of the trailing edges of blades.

Control of these, and other, dimensions enables the ideal efficiency of the engine to be approached. In reality a compromise position is often required, where coatings become specified further along in the design process or as completely retrospective improvements to components. In the latter situations the coating profiles must be modified in order to lessen the impact on critical measurements. In the case of diffusion coatings, this is less of a problem when compared to truly additive coatings, such as overlays, or in the worst case an overlay as a bondcoat for a TBC.

In situations where additive coating TBC systems must be kept as thin as possible, the reduction of coating thickness can be a double-edged sword. By reducing the thickness of the TBC the metal surface temperature increases and hence the performance requirement of the bondcoat increases; this is often coupled with a reduction in the thickness of the bondcoat. It is necessary, therefore, to understand the limiting thickness' for overlay based bond coat systems. In order to study this limiting parameter, a series of bondcoats with four thicknesses of the MCrAlY component, of the CoNiCrAlY+Pt system, were produced. The relative performances of these bondcoat systems were compared.

### **6.3.1 - Test Piece Manufacture and Testing**

The test pieces were manufactured from the bar stock described in earlier chapters, 8mm diameter x 110mm long CMSX-4 bars. Three thicknesses of MCrAlY were sprayed, using the LPPS technique, to thicknesses of approximately 50, 100 and

150 $\mu\text{m}$ . The Pt coated samples was subsequently heat treated at 1150 $^{\circ}\text{C}$  in vacuum, for 1 hour prior to the second grit-blasting operation used to clean the surface before coating with EB-PVD TBC. By following the same processing route, the run to run variability was reduced, ensuring any differences highlighted by the testing was as a result of the different thicknesses of MCrAlY employed. Six samples from each batch were produced and tested in order to produce a representative spread of results. The cyclic furnace test proved to be the most appropriate test for a comparison of this nature, as samples from different batches could be tested concurrently.

As before, the test pieces were cycled between  $\sim 80^{\circ}\text{C}$  and 1135 $^{\circ}\text{C}$  until spontaneous spallation of the TBC occurred. The number of cycles successfully completed prior to TBC loss was recorded as the “life” of the bondcoat system. Figure 6.27 shows the comparison of the number of cycles to failure for each batch of samples. As can be seen, the best performance was achieved from samples with  $>100\mu\text{m}$  of MCrAlY.

The performance of the thinner MCrAlY system was, however, not far short of the thicker samples. What can be seen from the micrographs of the sample specimens from each of the groups (see Figure 6.28), however, is that the process of diffusion of the Pt to form P-phase has completely denuded the MCrAlY of  $\beta$ -phase. It was decided, on the strength of the microstructure and the slightly reduced performance, that 50 $\mu\text{m}$  of MCrAlY would be the limiting specified thickness for CoNiCrAlY+Pt bondcoats.

### 6.3.2 - Limits of the MCrAlY+Pt System

In order to examine the effects of reducing the thickness of the MCrAlY, on the MCrAlY-based bondcoat system, a set of test pieces were manufactured with the overlay sprayed to simulate the typical thickness' seen in areas of overspray during component production. The depth of the coating in these areas would typically be of the order of 15 $\mu$ m. Onto this MCrAlY the Pt was plated to full thickness (7.5 $\mu$ m); the electroplating technique, used to deposit the Pt, does not lend itself to the production of tapered thickness' of coating. Figure 6.29 shows the resultant microstructure of the test pieces. As can be seen, the structure is not as regular as that seen in Figure 6.28; the critical phase, as regards TBC bonding, namely the P-phase, is not continuous and so would not offer the benefits seen in other systems. When these samples under went cyclic testing, the results were far below those achieved from the earlier samples with full thickness MCrAlY, with non of the thin MCrAlY samples successfully completing 50 cycles at 1135°C. These poor test results confirmed the initial limiting structure of minimum CoNiCrAlY thickness, when combined with the Pt plating, to 50 $\mu$ m.

In order to ensure that this limit was achieved in production, it was stated that Pt plating was to be limited to areas where controlled thicknesses of MCrAlY could be achieved. The Pt plating "stop-off" masking was to be applied to just beyond (approximately 5mm) any MCrAlY fade out region.

## **6.4 - Effect of Heat Treatment on TBC Performance**

The initial MCrAlY+Pt test pieces, discussed in Chapter 4 were exposed to an unusual heat treatment cycle during manufacture. As these samples were basically a feasibility trial test batch the effect of the heat treatment cycle was unknown and, therefore, ignored. The excellent results from the initial testing, however, resulted in a need for a detailed understanding of the process, it transpired that the initial trial samples had been included in a batch of components being heat treated as part of a brazing process. This process had resulted in the samples being heat-treated at temperatures as high as 1190°C. This very high temperature was unacceptable as part of an initial production process as it “used up” too much of the available heat treatment window for the substrate material. A modified heat treatment cycle was, therefore, necessary.

Samples were produced of MCrAlY+Pt and then heat treated to diffuse in the Pt plating and form the required microstructure at a range of temperatures prior to TBC deposition. The samples were then to be scratch tested to determine any differences in the TBC adhesion produced by the different heat treatments.

### **6.4.1 - Scratch Testing of Heat Treatment Trials**

The samples were Pt plated to nominally the same thickness of 7.5µm. One batch of the samples was then heat treatment for 1 hour at 1100°C in vacuum. In order to differentiate between the batches of samples they were exposed to isothermal furnace

soaks, as previously described, prior to mounting and scratch testing. Samples were exposed for 100 hours at 1100°C and 1150°C and the residual adhesion levels measured. Figure 6.30 shows the comparison of the relative adhesion levels determined by the scratch test. Analysis of the results clearly showed increased levels of adhesion, especially in the as processed state, in the samples exposed to the higher heat treatment temperatures. It is worth noting at this point, that none of the samples successfully passed the 100 hour at 1150°C exposure; this was not unexpected as the substrate material used in this trial was CMSX-4 and not MarM002, as was used in the initial assessment programme, (see Chapter 4.1). As a direct comparison, samples with just an MCrAlY bondcoat were tested along side the Pt modified versions, the performance of these test pieces was considerably inferior. As before, the samples heat treated at 1190°C showed the best performance, however, the preferred heat treatment window for CMSX-4 was at the lower temperature of 1150°C. The results of this testing showed that there were no significant drop-off in TBC/bondcoat performance if the heat treatment temperature was reduced to this more acceptable level.

In order to maintain substrate material integrity, the maximum heat treatment temperature for the MCrAlY+Pt was reduced to 1150°C in vacuum.

## **6.5 -Peening for Quality Assurance**

Experience from using overlay type coatings has shown that some form of quality assurance is required to ensure the integrity of the coating/substrate interface.

Previously, due to the peening operation traditionally carried out after spraying and diffusion heat treatment, the integrity of the bond had been tested. The changes to the MCrAlY spraying parameters meant that the peening stages had become superfluous and so had been removed from the process. It became evident that a lower intensity peening operation could be used to ensure adherence of the coating, as this had been used, previously on EB-PVD overlays. The experience gained, indicated that peening on the 'A'-scale did not threaten component conformance. The requirement to re-visit the peening process as a measure of quality assurance, after polishing of the MCrAlY, allowed any beneficial effects to be re-assessed.

As before, a range of peening media was assessed, see Figure 6.31, however, unlike the previous testing, the intensity of the peening was not an issue, all the systems were peened with an intensity of 10N. The main drivers for the assessment of a range of media were economic, contamination and surface finish. To complement this testing, the issue of performance enhancement was addressed. This was not considered a high priority as the effects of peening had already been demonstrated.

The samples were prepared as for the previous peening experiment, the peening was again completed at M.I.C. and the testing carried out at Rolls-Royce.

### 6.5.1 - Assessment of Peened Samples

The surface finish and contamination levels of the samples were examined using SEM and EDX techniques. The testing showed that the least surface contamination occurred when the samples were peened with the ceramic bead. This was, however, at the expense of the economics of the process; ceramic bead was the most expensive medium, this was compounded by the need to change the media regularly due to the short life span of the bead caused by it shattering during the process. The angular nature of the shattered bead lead to the surface of the test piece being deeply “cut”, see Figure 6.32. The more “smeared” nature of the surface produced by the steel shot was seen to have a two-fold benefit. Firstly, the smearing effect of the surface layer would seal any residual defects left by the polishing process, preventing oxygen ingress into the coating, and secondly, the smoother surface finish would be less prone to the generation of growth defects during the ceramic deposition. Unfortunately, the steel shot left a noticeable level of iron contamination on the surface of the test pieces. Previous experience at Rolls-Royce with iron contamination on nickel based substrates indicated that this was readily removed by a simple ultrasonic citric acid wash. The full matrix of samples was exposed for 25 hours at 1100°C and compared to a sample that had received no peening process. The comparison of the  $\beta$ -depletion gave an idea of how each media effected the performance of the coating. The  $\beta$ -depletion measurements were taken in the same way as was done previously during the Taguchi optimisation of the spraying parameters, namely thirty two measurements were made around the test pins. The  $\beta$ -depletion measurements were plotted against “frequency-

bins”, i.e. 0-2 $\mu$ m, 2-4 $\mu$ m etc. as a method of examining the relative performance of the samples. Figure 6.33 shows the comparison of the unpeened sample, the stainless steel shot peened sample both before and after citric acid wash. As can be seen there is a marked improvement in the performance, with regard to  $\beta$ -depletion, of the system after peening and again after cleaning. The effectiveness of the citric cleaning process is demonstrated through the comparison of the EDX analysis of the surface before and after cleaning, shown in Figure 6.34.

The 10N stainless steel shot peen was subsequently adopted as the QA check on the MCrAlY coating prior to the Pt plating process.

## **6.6 - Grit Blasting for Improved TBC Adhesion**

Examination of the final phase of the bondcoat-processing route raised a degree of concern regarding material removal. As stated in earlier chapters, the amount of Pt on the MCrAlY+Pt bondcoat is critical; aggressive grit blasting prior to the deposition of the TBC could potentially remove some of the outer portion of the bond coat. It is the outer portion, the Pt-rich P-phase, which provides the correct chemistry to generate the Al<sub>2</sub>O<sub>3</sub> layer required to maintain TBC adhesion. In former state of the art bondcoat systems, the outer portion of the coating had not been as critical. The grit blasting procedure had been set in order to achieve the required goals of cleanliness and surface finish without the need to guard against material removal. The previous grit blasting parameters were set at 30-40 psi and 220-grit brown alumina; there were no controls on

nozzle to workpiece distance or the maximum time for each component. The final control was with the operator who used experience to determine whether a component was adequately prepared and met with a visual standard. With the advent of the surface sensitive bondcoat system, greater control was required.

#### **6.6.1 - New Grit Blasting Parameters**

The use of an automatic test piece feed mechanism allowed careful control of the parameters during the experimental procedure. The mechanism rotated the samples around the longitudinal axis and translated the bars in both positive and negative directions on the same axis. The nozzle could be fixed in any position within the blasting chamber, this enabled the nozzle to workpiece distance to be controlled. Test bars were manufactured of MCrAlY+Pt bondcoats following the full processing route up to the point of pre-TBC deposition grit blasting. Initial trials with the automatic system were to “calibrate” the machine in relation to the manual operator. The sample rotation was set to the maximum rate, whilst the x-axis translation speed was set to ensure the whole of the surface of the test piece was evenly grit blasted in one complete pass, without leaving a spiral blasted pattern. The parameters were set to replicate those used during standard processing, i.e. 30-40 psi, 220-alumina grit and a nozzle to workpiece distance of approximately 100mm. The automatic processing allowed the test piece to be examined after every complete cycle of the machine, comparison in this way, to a visual standard produced by an experienced operator, allowed calibration of the machine to be achieved. EDX analysis of the surface of the test piece before and

after grit blasting showed a significant reduction in the levels of surface contamination as indicated by the reduction in the Ti peak, see Figure 6.35. When examined in cross-section, however, there was evidence of some loss of P-phase. Although in this case there had been no evidence of the complete removal of the P-phase, it was conceivable that under conditions other than laboratory control there was the possibility that excessive material could be removed. During grit blasting the sample had taken on a uniform pale grey colour, all evidence of variations in colour or “patchiness” was removed. It was decided that at this stage no change would be made to the media used, provided that the required results could be achieved by changes to the pressure and spray distance. Figure 6.36 shows the array of times, pressures and distances used during the initial phase of the grit blasting trials.

One test piece was used to measure the effects of a pressure or distance with time by recording the mass change that occurred after each time interval. By plotting mass against time, the rate of material loss could be determined, see Figure 6.37. Cross sectional metallography of identically prepared samples to those used for the weight change experiment gave an indication of the bond coat loss of section related to a particular weight loss. This technique allowed a limiting weight loss to be determined for the type of test piece used, which could then be cross-correlated with the pressure/distance experiments, the outcome of which would give a maximum gritting time per set of parameters. Parameters were selected that produced a material weight loss which fell below the limiting line after a time considered to be adequate to cover the worst case condition of an operator dwelling on one region for several seconds.

Once selected, these parameters of 15 psi at a distance of 175mm, were used in the second phase of the trials. The next phase was to ensure adequate cleaning of the surface was being achieved. For each set of parameters a sample was marked with protective tape leaving approximately 15mm of metal exposed at one end. Again using the automatic blasting cabinet, the samples were gritted, after set periods of time more of the test piece was revealed so that the cumulative time seen by each 15mm section increased progressively, leaving one section unblasted. The 15mm sections produced were compared to the required visual standard and the time required to just meet the standard was recorded. The surface of each section was then analysed using the EDX system to assess the remaining levels of contamination; the time required to chemically clean the surface was recorded. Using the new parameters, however, did not produce a chemically clean surface even though the visual standard had been adhered to. In order for operators to ensure a suitably clean surface, the time blasted under these conditions was doubled. The new parameters for grit blasting were sufficiently forgiving that the longer exposure time still fell within the safe working envelope described by the material loss experiment above.

To ensure that operators, trained to work to a visual standard, produced an acceptable product the work instruction was amended to grit blast to the visual standard and then repeat the operation. As shown in Figures 6.37 the effect of distance is marked, the workpiece to nozzle distance was therefore critical. Operators were prevented from reducing this distance by attaching a “cage” to the nozzle, which physically prevented components being too heavily gritted.

## Chapter 7 - Improvements to the CoNiCrAlY + Pt System

As discussed in earlier chapters, higher operating temperatures enable gas turbines to operate more efficiently or alternatively to produce more power. It has been identified that for civil engine use (i.e. <25 hours at maximum power) a maximum operating temperature for the MCrAlY + Pt bondcoat interface had been set at 1210°C. The potential to increase this temperature offers significant benefits to an engine development programme.

Work on the development of environmental protection coatings [84], has suggested that additions of alternative precious metals, such as rhodium could offer improvements over the standard coating systems. In order to investigate the possibility of transferring these gains across the bondcoat technology, a programme of work was initiated to examine the effects of various precious metals of TBC bonding and phase stability. In addition to the potential performance benefits, cost reduction could also be achieved through the use of alternative metals.

The second route to making potential improvements to the bondcoat system was through the chemistry of the overlay. Work by Hondros, [85] showed that the adhesion of  $\alpha$ -alumina to nickel based alloys could be improved by varying the levels of additions such as Co and Cr, see Figure 7.1. To this end, the effects of changing the overlay composition from CoNiCrAlY to NiCrAlY and CoCrAlY were assessed.

## 7.1 - Alternatives to Platinum

The transition elements in the region of platinum in the periodic table were assessed for suitability for use in the bondcoat system. Certain elements were readily dismissed due to their known properties. Osmium was known to produce poisonous compounds and so was not a favoured option for a production process. Gold and silver were known to produce low melting point eutectics and so were evidently unsuitable for a high temperature application.

This left four potentially useful precious metals, ruthenium, rhodium, palladium and iridium.

Associated literature [86] suggested that rhodium and palladium could be readily electroplated, all be it that the thickness of the plate, in the case of rhodium was limited because of the highly stressed nature of the deposit. Difficulty in plating iridium [87] and the unavailability of suitable ruthenium plating solutions for these trials leads to these materials being deposited by an alternative PVD technique, sputtering. The limited time scale available for this work prevented a detailed optimisation of the 'appropriate coating thickness' and heat treatments from being carried out and so the parameters used for the platinum-based system were adopted.

### **7.1.1 - Production and Analysis of Test Pieces**

Samples of CoNiCrAlY were sprayed onto CMSX-4 test pieces using the optimised parameters. These samples were then prepared as for platinum plating, up to the plating stage, the samples were then coated with the combinations of precious metals described in Figure 7.2. The samples were then heat treated and over coated with TBC. The testing programme consisted of 25 hour isothermal soaks, as before, up to 1210°C, further temperatures were then included dependent upon the coating systems performance.

Figures 7.3(a-d) show the samples prior to testing. In most cases a layer similar in appearance to P-phase can be seen near to the metal/ceramic interface.

In the majority of the samples examined, the performance did not match that of the platinum based system, with one exception, the platinum/rhodium combination. This system matched the performance of a P-phase modified overlay, maintaining TBC adherence up to 1210°C.

Samples coated with palladium (Pd) did not perform as well as the standard system, losing the ceramic topcoat after exposure to 25h at 1100°C, 60°C below the expected temperature for a Pt modified overlay. In the as-processed condition it can be seen that Pd did not form a continuous stable phase at the metal/ceramic interface, and that “fingers” of the enhanced phase extended into the overlay further than would be expected of P-phase. After 25h at 1150°C almost all the enhanced phase had dissolved,

no improvement in performance occurred over a standard MCrAlY coating. When comparing the WDS analysis, as tabulated in Figure 7.4, P-phase and the Pd phase have identical levels of precious metal and aluminium, a ratio of approximately 20:35 atomic %. The only significant differences being in the levels of Cr and Ni, there is very little Cr in the Pd phase, apparently substituting for Ni in the crystal structure, with a ratio of 3:30, Cr:Ni compared to 7:25 in P-phase. After exposure to 25h at 1150°C the levels of Pd in the enhanced phase had dropped considerably more than Pt in P-phase, this supports the evidence from the optical metallography, that the Pd phase is less stable than P-phase, despite the Al levels remaining high. The Pd lost to the MCrAlY was replaced by Ni and Cr.

Comparison of the XRD analysis shows that Pd does not produce the recognised pattern for P-phase. Further analysis of the Pd based system was not pursued due to the associated lack of performance. The difficulty associated with the highly stressed nature of the ruthenium (Ru) electroplate was mirrored in the sputtered coating. The relatively thin Ru layer proved to be very brittle, chipping and spalling from the MCrAlY. Poor sample preparation played a key role in preventing good diffusion into the MCrAlY. In areas where a clean interface had been produced, diffusion of the Ru did occur, resulting in a phase similar, in optical metallographic terms, to P-phase. As this occurred in isolated regions, only limited data was gained from these test pieces, and no reliable WDS analysis could be made, equally XRD data would have been unreliable.

The sputtered layers of iridium (Ir) proved more successful and reasonable coatings were produced.

Furnace testing of those coatings, however, proved them to be poor bondcoats.

Exposure to temperature caused these systems to generate an alumina scale initially, however, once the Al had been used from above the Ir enhanced layer, the coating began to form mixed oxides and temperatures in excess of 1150°C caused internal oxidation to occur.

Figure 7.5 shows the initial oxide layer at the ceramic/metal interface and the subsequent internal oxidation. It is worth noting, however, that the Ir enhanced phase remained stable up to 25h at 1210°C (no further trials were completed as ceramic loss had occurred at 1100°C). The way in which the coating broke down suggested a very stable phase which limited the diffusion of Al to the outer scale. Once the initial levels of Al in the outer portion had been oxidised, the Ni, Cr and Co then began to oxidise. This hypothesis is supported by the WDS analysis, which showed that the phases formed during the test piece production had an unusual composition consisting mostly of Ir and Al, 34 and 43 atomic % respectively. The outer portion of the enhanced layer consisted of a two-phase region, the bright contrast enhanced Ir containing phase embedded in a predominantly Co and Cr phase.

Although this system did not perform successfully as a bondcoat, there appeared to be potential for further study in the area of using Ir as an Al diffusion barrier, this is discussed further in Chapter 10.

The final system examined was the Pt/Rh combination. This system produced an enhanced phase very similar in appearance to P-phase, but with much improved stability at elevated temperatures. Figure 7.6 shows the relative stabilities of P-phase and the Rh modified phase. As can be seen the Rh enhancement ensures that the phase remains stable out to temperatures in excess of 1270°C for 25h exposures. This compares well to the P-phase which had completely dissolved after 25h at 1210°C. Despite the improved stability of the phase, no improvement to the temperature limit for TBC adhesion was evident. BSE images of the Pt/Rh phase show a different as-processed structure to P-phase, see Figure 7.7. This difference may be due to the double layer plating process, as after exposure to temperature this difference disappears. WDS analysis of the system shows that initially there were high levels of the Pt/Rh and Al in the coating; subsequent heat treatments caused the levels to drop to a range more in keeping with P-phase, Ni replacing the Pt and Rh as they diffused into the MCrAlY. After isothermal soaking the only notable difference between P-phase and the Pt/Rh phase was the slightly higher level, 34 atomic % compared to 31 atomic %, this did not have the same detrimental effect as it seemed to have in the Pd based system. XRD analysis in the as-processed condition did not show any evidence of P-phase, again this could have been due to the double stage processing route leaving a higher level of Pt and Rh at the surface; limiting the penetration depth of the x-rays preventing the enhanced phase from being assessed. The increased phase stability of this phase makes the Pt/Rh system an obvious choice for further assessment, this is discussed further in Chapter 10.

### **7.1.2 – Discussion of Precious Metal Additions to MCrAlYs**

It would appear that Pt is almost unique in the ability to improve the bonding/alumina formation of MCrAlY type coatings, with one notable exception Rh. It should be noted, however, that the improvements seen with Rh were in conjunction with high levels of Pt; again highly stressed coatings limited the thickness achievable in Rh plating. Improvements similar to those seen with Rh may also be seen with other precious metals when used in conjunction with Pt. Investigation into these potential systems must, however, fall outside the scope of this study. The improvements to the phase stability seen from the addition of Rh were not mirrored in the bonding capability of the coating system. Given the proposed failure mechanism of P-phase based systems, it is difficult to understand why the Rh modified system did not perform better.

It would seem that there is considerable room for improvement with this group of bondcoat systems by alloying Pt with other precious metals. This would, unfortunately, significantly increase the cost of the coating assuming the continued use of the electroplating process.

The competitive nature of the type of work undertaken in this study ensured that the variations in MCrAlY composition that were available for study were limited. As has been previously stated, the MCrAlY “base coating” has been used for some considerable time as an environmental coating. To this end many patents have been filed [33, 88, 89, 90], regarding the coating chemistry. These patents have significantly reduced the number of useful compositions available for testing. The general move within the industry to CoNiCrAlY’s, see Chapter 3, has meant that only limited availability of other types of MCrAlY’s. It was possible, however, to examine the role of Ni and Co on the composition and performance of the Pt enhanced MCrAlY.

### **8.1 - MCrAlY Compositions**

The MCrAlY used during the initial stages of this study was based around the patented composition tested previously on Rolls-Royce engines. This composition was based on the CoNiCrAlY outlined in Figure 8.1. The purpose of this phase of the work was to vary both the Ni and Co content in successive coatings and hence allowing the role played by these elements to be examined. The compositions available for study are outlined in Figure 8.1.

### 8.1.1 - Sample Preparation and Testing

The test pieces were processed in the same manner as earlier samples. A diffusion heat treatment; polishing, peening and grit blasting prior to deposition of the Pt layer followed deposition of the MCrAlY onto 8mm diameter bars. The 7.5 $\mu$ m of electroplated Pt were diffused into the MCrAlY in order to generate P-phase (1h at 1150°C in a partial pressure atmosphere). One sample for each coating type was retained at this stage in order that XRD analysis could be carried out of the phases produced. The remaining samples were then processed as for EBPVD TBC deposition.

TBC coated samples were isothermal furnace tested for 25h exposures at a range of temperatures from 1100°C upto 1210°C to assess the performance as bondcoats. Figures 8.2(a-d) compare the microstructure of the bondcoats in the as-produced state and after 25h exposure at 1150°C.

As previously, the samples were mounted and polished to the appropriate procedure to allow the residual adhesion levels of the bondcoat and TBC to be measured using the modified scratch test. Figure 8.3 shows the results of the testing. Samples, furnace tested at the same time as for scratch testing, were prepared for WDS analysis. The probe analysis was aimed at comparing the resultant phase compositions produced in the different coatings by the addition of Pt. The table outlined in Figure 8.4 compares the Pt enhanced phases to the composition of P-phase and the Pt enriched  $\gamma$  phase of the standard system.

### 8.1.2 - Analysis of the Results

Examination of the BSE micrographs in Figure 8.2 shows that the Pt enhanced phase (P-phase type) extends deeper into the body of the MCrAlY base coat than would be expected in the standard system. This microstructure is linked to the manufacturing method for coatings A and B. Both systems were deposited by EBPVD as opposed to the LPPS technique used to produce the standard system. EBPVD tends to produce coatings with columnar structures, rather than the splat structure associated with thermal spraying techniques. The column boundaries act as fast diffusion paths for the Pt, resulting in the long extended “fingers” of the Pt rich phase (shown as bright contrast regions in the micrographs). The bulk of the phase does, however, remain in the vicinity of the metal/ceramic interface. After exposure to 25h at 1150°C, the microstructure takes on the form more akin to P-phase.

The furnace soaks and scratch testing results shown in Figure 8.3, show that the CoCrAlY based bondcoats almost match the CoNiCrAlY system in ultimate performance, with coating A retaining the ceramic even after 25h 1210°C. Coating B did not perform quite as well despite the ceramic still being adherent after cooling from 1210°C. On mounting the sample the TBC became detached showing that it had only limited adhesion. The low levels of adhesion measured in Coating A after exposure to 1210°C show that there was not a significant difference in performance between the two coatings. The similar performance was not surprising considering the similarities identified by the WDS probe analysis of the bonding phases.

In the as-processed condition, the only identifiable difference between coatings A and B is the slightly higher Cr content in the P-type phase of Coating B.

The slightly higher Cr levels were to the detriment of the Pt content. The composition of P-phase shows that Pt, Co and Ni are interchangeable, with the sum of the atomic % of these elements being approximately equal in all three systems.

After exposure to 1150°C, the main change in all three coating is the Pt/Ni exchange, as the Pt diffuses into the coating to be replaced by Ni diffusing outward from the substrate material.

As has been identified earlier, the ceramic bonding is actually through the Pt-enhanced  $\gamma$ -phase. It is in this phase that the main differences between Coatings A and B can be identified. The considerably higher levels of Co in the MCrAlY of Coating A are reflected in the (Pt- $\gamma$ ) phase, as are the lower Cr levels. It is likely that the better performance observed from the standard system comes from the higher Al content of the (Pt- $\gamma$ ) phase. By maintaining a high level of Al, the phase will be more able to generate a pure  $Al_2O_3$  scale for longer.

The work by Hondros [85] on the correlation between the work of adhesion and the interfacial energy, see Chapter 3, suggests that the higher Al content is only part of the explanation for the observed behaviour.

It is suggested that the composition of the phase beneath the  $\text{Al}_2\text{O}_3$  scale affects the bond strength directly due to the interfacial free energy; the lower the value, the greater the adhesion. Hondros also showed that a compound of Co and Ni in the ratio of 3:2 had a much lower interfacial free energy with  $\text{Al}_2\text{O}_3$  than did either of the elements alone. This would seem to be born out in results here, with the standard system having a Co:Ni ratio of the order of 1:1 compared to the coatings A and B with ratios of the order of 6:1. The difference from the ideal ratio being influenced by the further alloying additions. The bonding between Pt and  $\text{Al}_2\text{O}_3$  being greater than for either Ni or Co and therefore, probably, not influencing the ideal composition as greatly as either Ni or Co.

The XRD analysis of the three systems see Figure 8.5 shows that the coatings A and B produce very similar patterns to P-phase with slight peak shifts occurring due to the chemistry changes. It can be assumed, therefore, that the diffusion of Pt into Co or Ni based MCrAlYs produces P-phase and the performance, as regards a bondcoat, would be similar.

## **Chapter 9 - Discussion**

### **9.1 - Introduction**

The prime goal of the research programme undertaken was to develop a bondcoat system that offered improved performance over the systems that were available at the outset. In order to achieve this, several areas of interest had to be studied. This chapter aims to review those areas and discuss them with respect to current thinking, as reported in associated literature, and hence determine the effectiveness of the approach taken and hence the contribution this thesis makes to the understanding of the bonding mechanisms in substrate/bondcoat/TBC systems.

### **9.2 - Bondcoat Developments**

This programme of work was carried out as a way of assessing the current state of the art bondcoat systems, whilst at the same time comparing their performance with that achieved by novel bondcoats designed and produced specifically for this study.

State of the art bondcoat systems could be categorised into two main generic types, diffusion and overlay coatings. Both of these types of system were taken from existing environmental coating development, making the assumption that the requirements of a coating that performed well in one role would be applicable to the other. This assumption seemed reasonable considering the requirements placed on each type of coating. Environmental coatings were designed to generate a rapidly forming,

continuous, highly stable and slow growing protective oxide scale, that was, ideally, free from cracks and pores, and was both adherent and coherent. This design brief is equally true for bondcoats, with the added requirement that the oxide scale provided a high level of adhesion to PYSZ.

The temperatures that these coatings would experience in modern aero gas turbines, required the formation of an alumina scale [39]. Alumina offers stability far in excess of the temperature requirements of the metallic coatings. Prior to this study it was generally believed that the failure mechanisms involved in EBPVD TBC loss were directly related to the bondcoat no longer being capable of generating pure alumina [90, 91]. Bondcoat development was, therefore, aimed at extending the time at temperature that a coating was capable of growing alumina. The industry had become divided as to the type of coating most suited to the aero engine environment.

Some manufacturers believing that diffusion coatings offered the ideal solution, being relatively cheap and mechanically robust, whilst others preferred the improved protection offered by overlay coatings, despite their propensity to crack and plastically deform at temperature [92].

The selection of the experimental coatings used for this research was not influenced by any prejudice towards one type or another, as it was presumed that bondcoat development did not necessarily require the same rationale as environmental coating development. The key difference between the two types of coating being that environmental coatings have the luxury of regenerating the protective scale if the

original was lost through spallation. Loss of the oxide scale in TBC systems automatically leads to loss of the TBC, with no way of regenerating the thermal protection. With this approach, it was possible to combine research techniques in an attempt to design better performing systems.

The improvements gained by the combination of Pt with aluminide systems have been well documented. [26, 27, 94, 95], as have the merits of rare earth (RE) additions to MCrAl type coatings [96, 97, 98]. The initial research programme of this study examined the levels of adhesion offered by state of the art systems and compared their performance with that offered by development coatings. The development coatings were attempts at combining the benefits of Pt and RE additions, by producing multi layered coatings, see Chapter 4.1.

In order to be able to rank the performance of the bondcoats, a tool was required that could differentiate the levels of adhesion between various bondcoat and TBC combinations. The modified form of the scratch test allowed these comparisons to be made, see Chapter 4.1.1.

Previous work, [38] has shown that this technique could successfully be used to monitor the residual levels of adhesion, upto the point of spallation, after increasing exposure to time or temperature. Within this study, it was shown that high initial levels of adhesion, in the as-processed condition, did not necessarily mean the bondcoat would perform well after exposure to temperature. In fact the majority of the bondcoats examined demonstrated a similar level of adhesion in this condition; with

over 55% of the systems recording levels of adhesion between 45 and 60N. This was not a surprising result as all the systems examined were designed to generate an alumina scale onto a grit blasted surface during the TBC deposition stage, identical for all systems. The variations seen in the initial levels of adhesion were more likely to be related to the surface condition of the bondcoat prior to TBC deposition, this was not, however, proven.

Supporting evidence for this theory comes from three of the systems which displayed higher than average as processed adhesion, coatings 9, 17 and 18 received a more intense finishing operation prior to TBC deposition and showed initial adhesion levels of 85, 70 and 100N respectively. Standard processing for coating 9 included a cut-wire peen of 10A intensity see Chapter 6.1, whilst the samples prepared for coatings 17 and 18 were surface ground prior to the Pt deposition. Both these techniques introduce a significant degree of work into the surface region of the coating, but exactly how this could effect the bond strength considering subsequent vacuum heat treatments is uncertain. More useful data with regard to bondcoat development was gained from the aged samples, comparing the ways in which different bondcoat systems degraded with temperature. In all but two cases the adhesive strength of the metal/ceramic interface steadily decreased with exposure to increasing temperature. The two exceptions to the above were produced through the EBPVD route. It is possible that the mechanisms discussed in Chapter 4.2.3 could explain the different degradation seen in these two coatings. The fine dispersion of Y within the body of the EBPVD coating would not become significant until thermal exposure occurred. During alumina growth the Y would become incorporated into the scale to a greater degree that it would in non-

optimised LPPS equivalents. The benefits of RE additions are stated in the associated literature, all of which would tend to increase the resistance to crack propagation through the scale. In an attempt to reduce the number of tests required to complete the matrix of test pieces a “gated” process was used. It was already known from previous work that coating 10 could achieve 100 hours at 1100°C when used in conjunction with MarM002 as a substrate material. It was decided, therefore, that coating systems that could not achieve this target could be removed from further testing schedules. Testing showed that only 50% of the systems examined passed this initial gate. None of the aluminide systems retained the ceramic after the first test, it was concluded, therefore, that this generic group of bondcoats were not suitable for further work. Coating 4, the Pt enhanced aluminide diffusion coating, did successfully pass the 100h at 1100°C test, however this was not universally true of the other Pt-Al coatings. Coatings 5 and 6 were attempts at improving on the standard coating, coating 4. It has been shown that the increased levels of Cr in MCrAlY coatings increases the propensity of a coating to grow an alumina scale ie. much lower levels of Al are required to generate alumina. It was supposed that an increased level of Cr in the Pt-Al system would act in the same way, this was not successfully achieved here. This was probably due to an excess of Cr resulting in the worst performance of all.

In theory, a cleaner gas phase aluminide should out perform a pack aluminised equivalent, because of the lower levels of contaminant that would be expected in the coating. In retrospect, a change from an inwardly grown aluminide to a high temperature, low activity outwardly grown Pt-Al should offer greater performance, as the coating is additive to the substrate and, therefore, remote from the detrimental

elements present in the substrate. Although this would not be the ultimate solution, a benefit to performance should result. Considering the relatively poor performance of the Pt-Al systems examined it was decided not to pursue the development of diffusion coatings for use as bondcoats within this study.

In comparison to the diffusion coating results, all the overlay MCrAlY type coatings passed the initial gate, with one exception, coating 8 a high Al content (12 mass%) NiCoCrAlY deposited by LPPS. This result did not seem to follow the general trend of the rest of the group, and in order to clarify this result, coating 8 was included in further testing. It was assumed, at this stage, that poor/non-optimised spraying parameters were responsible for the limited performance of this coating. As discussed in Chapter 6, porous coating structures can lead to internal oxidation and hence cause the rapid degradation of the coating through exaggerated rate of usage of the Al content. This theory was supported by evidence gained during the LPPS optimisation programme, where gun nozzles used to produce coating 8 compositions rapidly burned reducing the efficiency and effectiveness of the gun, coatings produced by this route tended to be more porous than when alternative gun-nozzles were used. The coating most similar in composition and structure within the test matrix was the 8 mass% Al CoNiCrAlY, coating 7. It was supposed that the lower levels of Al in this coating would result in worse performance at higher temperatures, as the rate of oxidation increased. As can be seen, the coating did not pass the 100h exposure at 1150°C, it did, however, successfully pass the 1100°C retaining a measurable degree of adhesion at the interface. This improvement in performance over coating 8 may be explained by coating 7 being more dense as a result of better spraying parameters, the coating suppliers having more

experience with the latter coating were able to produce a better coating. The final LPPS coating examined was the NiCoCrAlYSiHf, coating 9. As with coating 7 there was a considerable degree of adhesion remaining after the 1100°C test, as with the other systems, however, there appeared to be a “cliff” in performance beyond 1100°C, where the adhesion levels dropped off. Spallation of the TBC occurred in all the LPPS systems after 100h at 1150°C. Examination of the microstructures indicated that the TBC loss was not related to the inability of the coating system to grow an alumina scale. This was particularly evident in the case of coating 9 where more than 50% of the thickness of the coating retained the Al rich  $\beta$ -phase, indicating more than a sufficient level of Al still present.

As shown in Chapter 4.2 the effect of Ti diffusing through the coating was probably the cause of the degradation of bonding strength. The movement of Ti along the rapid diffusion paths present in a porous coating could explain the drop-off in performance after exposure to 1150°C. Metallography has shown that at these temperatures the Ti, Ta carbides begin to dissolve in the diffusion zone of the coatings. This process would release Ti to be free to diffuse to the bonding interface. The change in focus of interest from MarM002 to CMSX-4 resulted in this process not being examined further and so was not proven.

The final group of coatings examined were the combined systems, where the benefits seen from environmental testing, in one type of coating were combined with those from the other. ie. the benefits seen in diffusion coatings through the addition of Pt were

combined with the benefits observed in corrosion performance and oxidation through the complex chemistry and the effects of RE additions of overlay type systems.

The combined systems can be sub-divided into three further groupings, examining the effects of combining:

- i) Aluminides with overlays
- ii) Pt-aluminides with overlays
- iii) Pt with overlays

The effect of (i) was seen in the performance of coating 12, where coatings 7 and 2 were combined. The duplex coating demonstrated no improvement in performance over that seen by the outer portion of the coating when used in isolation. The aluminide of coating 2, being predominantly an outwardly grown coating, failed to incorporate any of the MCrAlY chemistry, the overlay effectively acting as an extension to the substrate. Similar performance was observed with the coatings of group (ii), coatings 13 and 14. The adhesion of these coatings in the as processed condition was worse than that seen in any of the constituent coatings. Although this was not clarified, the work completed in Chapter 6.7 on the pre-TBC grit blasting operation suggested that systems are vulnerable to excessive or inadequate surface preparation. It is highly likely that the grit blasting prior to the TBC deposition in the case of coatings 13 and 14 was not adequate. A reduced blasting operation may have been used as an attempt to ensure that the Pt-Al system remained intact. Despite the above, coating 15, out performed either of its component parts, returning a measurable

level of adhesion after 100h at 1150°C. This increase in performance was probably due to a number of factors. Firstly, the MCrAlY received an intense cut-wire peening operation post LPPS, this is known to “seal” the surface of the coating whilst densifying the general structure.

This process would ensure that a significant proportion of the RE additions would remain active during furnace testing and not become combined in internal oxides. It is suggested that the main failure mechanism observed for coating 9 was the formation of brittle glassy Si-rich oxides at the surface. Capping the MCrAlYHfSi with a Pt-Al layer would reduce the tendency for Si to migrate to the interface, as Pt forms relatively stable compounds with Si [99]. This coating system seemed to have successfully achieved the goal of the combined systems of incorporating the RE's and the complex MCrAlY type chemistry with the improvements gained from Pt in the Pt-Al systems.

This coating system could not be pursued, however, because of patent restrictions on the MCrAlY composition but the concept was proven and showed that in theory this type of improved performance could be achieved with available compositions.

The final group of combination systems examined the effect of Pt on MCrAlY compositions. In all three cases Pt was added as an electro-plated layer to coating 7. Three variants of this system were produced, coatings 16, 17 and 18. The production method used in Pt-Al systems was to Pt plate and then aluminise through the Pt layer. This route was represented by coating 16, were approximately 7.5µm (3/10 thou”) of Pt

were electro-plated onto the substrate material, the MCrAlY was then sprayed over the top.

The levels of adhesion in the as-processes and aged conditions were slightly higher than the standard coating 7, but the coating still failed to retain the ceramic after the 1150°C test. In optical metallographic terms, the Pt at the substrate/coating boundary produced a phase similar in appearance to P-Phase. It's positioning in the coating system failed to demonstrate any of the benefits seen in later coatings. The formation of the Pt-rich phase caused Al to be used from the base of the MCrAlY whilst the alumina formation used Al from the outer portion. This two way leaching of the Al did not, however, produce significant problems as borne out by the performance of the system. The coating systems discussed here were all assessed in conjunction with a MarM002 substrate; this material is relatively benign, with regard to TBC adhesion, when compared to CMSX-4. It is possible that the Pt-rich layer at the interface between the substrate and the overlay coating would increase the performance of the system over that of the overlay coating alone.

The Pt layer would combine with the diffusing Ti to form a stable phase, increasing the time taken at a particular temperature to significantly effect TBC bonding. A similar increase in performance was demonstrated by diffusing a thin layer of Pt into the surface of the MCrAlY. This may be considered unusual especially as a slightly thicker layer of Pt produces such a marked effect, with significant levels of adhesion being measured after 100h at 1150°C. Examination of the microstructures reveals the difference between the two systems. The thin Pt layer when diffused into the MCrAlY

does not form a continuous band of P-phase, see Chapter 5, but simply enriches the outer  $\beta/\gamma$  structure with Pt. Later chapters have shown that the formation of continuous P-phase is critical in maintaining the levels of adhesion and the life of the TBC system. The higher temperatures of 1150°C, where the carbides begin to dissolve, highlighted the need for the continuous band of P-phase. The transition elements (in particular Ti) are not arrested purely by the presence of Pt but by the presence of P-phase.

Gaps in the P-phase allow the diffusion of detrimental elements to pass to the oxide interface relatively unchecked, resulting in TBC spallation. In the case of coating 17 no P-phase was formed and so TBC spallation occurred after 100h at 1150°C.

Coating 18, however, retained a considerable degree of TBC adhesion even after the 1150°C furnace soak, and also maintained a continuous band of P-phase.

The effects of elements diffusing through from the substrate material were further highlighted by the use of the single crystal superalloy CMSX-4. CMSX-4 does not have the requirement for grain boundary strengtheners, (there are no grain boundaries) and hence has very low levels of C. The need to retain a high ratio of  $\gamma$  to  $\gamma'$  ensures that relatively high levels of Ti, a strong  $\gamma'$  former, are present in the alloy. The diffusion of Ti from CMSX-4 can occur at much lower temperatures than MarM002 because of the lack of relatively stable Ti containing carbides, and so can affect TBC bonding to a far greater degree.

### 9.3 – The Effects of Substrate Chemistry

Very little mention is made in the literature regarding the effect on TBC bonding of the composition of the substrate material. It has, however, clearly been shown within this study that the substrate chemistry plays a significant role. A considerable portion of the work discussed within this study was aimed at identifying both the critical elements concerned with the disruption of TBC bonding and the mechanisms associated with them. A significant step towards this goal was made in examining the effect of changing from a multigrained substrate MarM002 to a single crystal alloy CMSX-4. The removal of grain boundaries eliminated the requirement for grain boundary strengtheners, commonly transition element carbides. The need to retain alloy strength resulted in relatively high levels of Ti being maintained, Ti being a strong  $\gamma'$  former (see chapter 3.1). The breakdown of  $\gamma'$  during the ageing process of the alloy releases levels of Ti, which then diffused towards the oxygen-rich surface. This process did not occur so readily in MarM002 because of the over abundance of C 'mopping-up' the released Ti to form stable carbide phases. The difficulty observed in attempting to identify the critical elements causing TBC loss was due to the relatively low levels required to disrupt the oxide scale. The argument put forward in Chapter 4 has subsequently been reinforced by work within Rolls Royce, completed on a series of single crystal alloys with varying levels of Ti; which has unfortunately fallen outside the remit of this study. Those alloys with higher levels of Ti have consistently shown poorer performance with regard to TBC bonding.

The mechanisms by which the Ti disrupts the oxide scale bonding are discussed in Chapter 4.3.6, with the strongest argument being put forward by Fox and Tatlock [78]. The suggestion was made that the presence of Ti ions reduces the Al<sub>2</sub>O<sub>3</sub> scale, leading to voids in the oxide; the presence of these voids leads to growth stresses causing buckling of the scale. It has been shown that fast-diffusion paths, such as grain boundaries (see Figure 4.18), cause concentrations of Ti in the scale, in MCrAlY based systems these concentrations occur at sites of Y-based pegs. Stresses induced by the mismatch of coefficients of thermal expansion ( $\Delta\alpha$ ) of the bondcoat, oxide and TBC systems cause the voids (micro cracks) to propagate into larger cracks leading to spallation of the oxide and TBC. The presence of the Pt layer at the outer part of the MCrAlY bondcoat seemed to delay the effect of the Ti by a number of processes.

Firstly, a diffused band of electroplated Pt has a very few grain boundaries within it, hence removing the number of fast diffusion paths for the Ti. This is supported by evidence of detailed examination of the P-phase region by BSE imaging and EDX analysis, summarised in the schematic diagram in Figure 9.1. The evidence of removal of diffusion tracks, although circumstantial, is convincing and is demonstrated by the significantly reduced number of Y pegs seen at the outer surface of the Pt modified bondcoat.

Secondly, the phase formed by the addition of Pt to the MCrAlY, P-phase, has the ability to maintain higher levels of Ti than either the  $\gamma$ -phase immediately beneath the Al<sub>2</sub>O<sub>3</sub> scale or the  $\gamma$ -phase beneath the P-phase. The WDS analysis presented in Chapter

5 showed that the Ti content of P-phase was approaching twice that of the adjacent phases after thermal exposure.

The third process that Pt plays in the Ti process is that of inhibiting the movement of transition elements [20, 26] towards the oxide scale.

The combination of these three points enabled the modified MCrAlY coating to outperform the unmodified equivalent by an approximately 60°C improvement on the ultimate temperature capability, and a fourfold increase in time to spall at a particular temperature.

The attempts to mimic this type of role through other processes proved to have little effect. The attempts to replace the C lost through the modification of the substrate, by the addition of a NiCr/CrC layer in the bondcoat met with mixed success. Although the performance of the MCrAlY bondcoat was not improved, in fact it was worse, the principle of the additional layer was proven. The breakdown of CrC to replaced by (Ta/Ti)C was successful as highlighted in the WDS analysis. The level of Ti at the oxide interface was not, however, reduced and so subsequently no improvement in the performance was achieved. The relative success of this process suggests that this should be revisited at a later date, as an attempt to improve on the ultimate system. A degree of refinement in the composition and selection of the production process should offer improvements.

Of all the bondcoat systems investigated, the Pt modified MCrAlY, coating 18, was the only one which offered substantial improvements in performance.

#### **9.4 – Definition of P-phase**

The MCrAlY+Pt bondcoat offered a similar improvement to the performance seen of standard MCrAlY type bondcoats, as that demonstrated by Pt-Al systems over standard aluminides. Furnace testing of the MCrAlY+Pt bondcoat on CMSX-4 highlighted that the stability of the outer phase of the coating was integral to the improvement in performance. The outer P-phase was still in evidence even after exposure of 25 hours at 1210°C. The stability of P-phase was linked directly to the performance of the coating as a bondcoat; when the bond of P-phase began to break down and become discontinuous, the TBC spalled. WDS analysis of the P-phase indicated that it predominantly consisted of Pt, Al and Ni in the ratio 20:35:25 respectively, in the as-processed condition. After thermal exposure this ratio changed to 10:32:34 as the Pt diffused further into the coating, being replaced by similar amounts of Co. and Ni.

XRD analysis of the P-phase showed it to be a large, approximately cubic phase, similar in size to eight combined  $\gamma$ -phase cells, and despite the initial compositional change, remained very stable to temperatures of the order of 1200°C. The inability to find an exact match from the JCPDS files suggested that the formation of this phase for a specific purpose was novel. As the breakdown of P-phase was linked with the loss of the TBC, it was essential to understand the process of decomposition, as this may have

lead to further improvements to the bondcoat system. The WDS analysis of P-phase showed it to contain Ti at approaching twice the level of the surrounding material. It is probable that on breakdown of P-phase that the store of Ti becomes released and diffuses to the oxide scale causing de-bonding. The process that causes P-phase to break down remains unclear, as no progressive change in the composition was seen. It is most probable, however, that the stability of the phase is linked to the level of Pt and Al. As the Pt continues to diffuse inward, a critical composition of the surrounding Pt- $\gamma$  phase is reached, whereby it becomes more favourable for the Pt to go into solution from the P-phase. The drop in Al level exaggerates this change as it becomes incorporated within the scale and is lost by diffusion to the substrate. The Al cycle is illustrated in Figure 5.4. The rapid degradation of P-phase at temperatures in excess of 1180°C is indicated by the image analysis work presented in Figure 7.5, where the volume of the phase, expressed as % area, reduces rapidly with elevated temperatures.

### **9.5 – Improvements to the MCrAlY System**

Evidence from optical metallography, WDS analysis and SIMS supported the furnace-testing programme and the ranking produced by the modified scratch test, in that bondcoat chemistry was not the only factor altering bondcoat performance. The inherent structure produced during coating deposition played a critical part in the degradation of the system. It was shown that the more open/porous structures, produced by some processes, significantly reduced the life of the system. It was also demonstrated that the porosity was often linked to the surface, allowing penetration of

oxygen into the coating. These oxygen paths resulted in a much larger surface-area-to-volume ratio for oxidation to take place. This internal oxidation, as well as using up the reserve of Al within the coating, also prevented Y from becoming incorporated into the bonding scale by tying it up as internal oxide. The degree to which this was occurring only became apparent after changes were made to the processing route. Some of the changes made to the MCrAlY processing were retrograde, with regard to TBC bonding. Removal of the 10A-scale peening operation and the move to the polished-only standard of coating, were such steps. These changes were, however, required from a component integrity and aerothermal performance standpoint (see Chapter 6).

The removal of the peening operation revealed the degree of internal porosity that had previously been disguised by the closing of the near surface region of the coating. Moves towards polishing the component, to provide a smooth gas-washed surface, left the channels of porosity open for oxidation. It became apparent that in order to make a significant improvement to the MCrAlY, then a radical process change was necessary. The Taguchi optimisation of the spraying parameters offered the potential for this improvement.

The three-phase programme used for the optimisation of the spraying parameters could have been reduced in size, given prior knowledge of the interacting terms that occurred. Without this knowledge, however, the three-phase programme proved to be the ideal route.

The spraying parameters that resulted from the Taguchi programme did not vary by a great deal over the original parameters; the resultant small changes, however, produced significant enhancement to the resulting coatings. The limited changes demonstrated how important the attempts were to make the parameters as robust as possible, through operator interaction and experience.

Not all the variable parameters were changed as a result of the Taguchi optimisation process. Those that were included B, D, H, I and K; powder flow rate, primary gas (Ar) pressure, spray distance, sample preheat temperature and the carrier gas (Ar) pressure. See Chapter 6.2.2.

The most straightforward parameter changes to understand are those that control the introduction of the powder into the plasma plume; namely the powder flow rate and the carrier gas pressure. As was shown in chapter 3.4.2.2, the placement of the powder into the plasma plume is critical to ensure uniform and complete melting of the particles and efficient material usage. It would be expected that B and K would interact because of the dependent nature of one on the other, however, the investigation into the potential interactions in phase 2 proved this not to be the case. The only interaction clearly identified was that of B and C, powder flow rate and gun current; this is the more difficult to understand. It is most likely that the relationship between B and C is not direct, however, it is no less critical. The temperature of the plasma plume is related to the efficiency of the gun current in ionising the gases. Figure 3.9 shows that for Ar and He (the process gases of interest), the gas mixture must be heated to a greater degree than other mixtures. To this end, the gun current was set as high as possible. In order to

transfer this heat into the powder, the flow rate of the powder into the plume was reduced. The downside of this reduction in powder flow rate would appear to be a slightly increased processing time, however, it must be considered that a greater proportion of the powder would be successfully incorporated into the coating.

The reduction in the flow rate of the carrier gas could result in the lowering of the cooling effect on the plasma plume and hence the powder would be heated more efficiently. Surprisingly, the changes to the primary and secondary gas-flow rates did not significantly effect the performance of the resultant coatings; presumably once the arc at the nozzle had sufficient energy to ionise the gases, the flow rates did not significantly alter the efficiency of this process.

None of the latter variables H – J had a significant effect on the process. This is not surprising considering that the heats and velocities of the particles are massively greater than that of the substrate or component. The effects, therefore, become swamped by the changes to the more significant factors.

The other variables, nozzle type and powder fraction (F, G) were selected according to their performance and suitability for the gun type and process.

It may be that the original parameter set was on the knee of a theoretical performance curve, and the new parameters moved the process onto the stable part of the curve. This would indicate that the original parameters would produce a variable product, sometimes good, sometimes bad, and this may be the reason that the porosity was

overlooked for some of the test pieces. Figure 9.2(i) sums up the performance improvement that the new parameters offered. The  $\beta$ -depletion is shown to be comparable to that of the EB-PVD system. It is worth noting that the EB-PVD equivalent had previously been shown to offer up to half the level of  $\beta$ -depletion seen in LPPS coatings. An added benefit, one that was hoped for but not designed in through the Taguchi Method, was seen in the form and distribution of Y content of the MCrAlY. The dark contrast oxide seen in the near surface region of the LPPS coating in Figure 9.2(b) are Y-pegs, indicating the metallic nature of the Y content of the coating. This fine distribution of Y-pegs had not previously been observed. Deep etching in a Br/CH<sub>2</sub>OH etch had revealed oxide pegs (see Figure 9.3), in earlier standards of LPPS coatings; but these were much more coarse in structure and less evenly distributed.

The optimised MCrAlY when combined with the Pt electroplate was examined, using the SIMS technique described in Chapter 5.5, the results of which are summarised in Figure 9.4. The results supported the observation made above, revealing much less oxide within the body of the coating. In this case, however, very few Y-pegs were seen due to the blocking effect of the P-phase (see Chapter 9.3).

Seemingly lesser important improvements to the processing were made; these did not radically change the performance of the finished product but did help generate and maintain a robust manufacturing route. The peening stage, reintroduced after spraying and polishing, ensured a degree of quality assurance into the manufacturing route. The role played by the peening was changed by the modifications to the intensity and timing

within the processing route. By moving the peening operation from before to after the polishing stage of the MCrAlY, there was no longer the danger of folding over the asperities and trapping surface oxide and contamination into the near surface region of the coating. The examination of the effect of the less intense peening operation, as discussed in chapter 6.5, showed that the modified parameters introduced significantly less bulk mechanical deformation. The micro hardness work demonstrated that some work hardening did occur. The dislocations causing this apparent hardening were fully annealed out after the heat treatment cycle representing the Pt diffusion heat treatment. The aim of the low intensity peen was two fold: firstly it acted as a quality assurance check on the integrity of the interfacial diffusion bond; and secondly closed up any micro fissures present at the surface of the coating.

The change from 10A ceramic bead peening to 10N stainless steel shot peening significantly reduced the overall cost of the process, and when coupled with the other processing improvements, did not reduce the performance of the resultant system.

The other minor change of the processing route was that of the grit blasting operation prior to the EB-PVD TBC deposition. Grit blasting is normally considered a non-invasive operation, however, when used on thin coatings it can be destructive. The role of the grit blasting was to clean the component surface of any traces of oxide, grease or debris that may inhibit the formation of a good bond between the metal and the ceramic coating. The pressures typically used for grit blasting are capable of causing significant material loss, given enough time and proximity to the work piece. The relatively soft nature of the Pt layer of interest was particularly susceptible to material loss as a result

of excessive grit blasting. This was a major concern as the deposited Pt layer was only 10µm thick and critical to the performance of the bondcoat. The results of the grit blasting, addressed in Chapter 6.6, showed that the operational pressures and distances could be significantly reduced and yet still result in adequately cleaned and prepared surfaces. The main drawback in trying to achieve this required results using the 'soft' parameters in a production environment comes through the operators. Operators who are more used to the feel of higher pressures find it difficult to appreciate the effectiveness of lesser parameters and a convincing argument must be put forward in order to maintain the correct parameter usage.

#### **9.6 – Variations to the CoNiCrAlY+Pt Bondcoat**

The attempts made to improve the performance of the MCrAlY+Pt metals demonstrated potential. Although no benefits with regard to TBC adhesion were identified, some elements and combinations of elements showed an increase in the phase stability of the resultant coating. The addition of Rh, as an alloying element to Pt, increased the stability of the P-phase from the limiting temperature of 1210°C up to 1230°C (for an exposure of 25 hours). It is likely that given the mechanism of failure of TBC adhesion in the P-phase based bondcoats, and allowing for development, that this observed increase in stability could lead to an extension in ultimate TBC capability.

The addition of Ir to the MCrAlY also produced a stable phase similar to the P-phase. The Ir/Al phase proved to be too stable, not releasing Al to the scale, resulting in

breakaway oxidation of the near surface region. It has been suggested that after long term, low temperature exposures MCrAlY-based coatings fail through loss of Al to the substrate. It may be possible to utilise the stability of the Ir-P-phase by producing a thin diffusion barrier beneath the MCrAlY layer and hence limit Al loss.

Sputtering offers the ability to deposit a wide range of alloy systems that are not available through traditional coating processes. It may be possible to generate a coating of pure P-phase composition without the reliance on the LPPS MCrAlY layer. In doing so, the parasitic weight of the coating system on the component could be reduced, improving the mechanical properties of the coating/component combination. Sputter processing would also allow close control of thickness distributions around the aerofoil sections, helping to maintain critical dimensions and hence aero thermal performance.

The experiments examining the effect of the MCrAlY composition showed that the P-phase is self-regulating. Despite the various base chemistries examined, P-phase was generated after Pt was diffused into the surface, It was demonstrated that Pt, Ni and Co were interchangeable in the P-phase, but the best performance was observed in systems with all three elements present, namely the CoNiCrAlY based bondcoats.

## **Chapter 10 – Conclusions**

### **10.1 – Bondcoat developments**

1. Diffusion aluminides are out performed in terms of ultimate temperature capability with regard to EB-PVD TBC adhesion by diffusion platinum aluminide coatings.
2. MCrAlY based systems generally out perform diffusion based systems in terms of ultimate temperature capability with regard to TBC adhesion.
3. In general the combination of diffusion and overlay compositions offers no improvement to the performance of the outer most component of the coating system.
4. An exception to point 3 is the addition of a layer of Pt to MCrAlY coatings. This type of coating significantly out performed all other types of coating within this study.

### **10.2 – Adhesion Testing**

1. The modified scratch test proved to be a useful tool with regard to ranking the performance of TBC systems.
2. Cyclic furnace testing offers an automatic method of ranking bondcoats, producing a ranking order similar to the modified scratch test.

3. Pt modified MCrAlY coatings can maintain TBC adhesion for up to 25 hours at a maximum temperature of 1210°C on MarM002 and CMSX-4 substrates.

### **10.3 – Sensitivity of TBCs to Substrate Materials**

1. The composition of the substrate significantly affects the performance of bondcoat systems.
2. The presence of free Ti within the substrate is the major cause of degradation of the bond between Al<sub>2</sub>O<sub>3</sub> and bondcoat after exposure to high temperatures.

### **10.4 – Characterisation of the MCrAlY+Pt bondcoat**

1. The MCrAlY+Pt bondcoat system is defined by the formation of the Pt enriched layers at the near surface region of the coating, the predominant phase has been ascribed as P-phase.
2. P-phase is a previously unidentified phase and can be recognised by a distinct XRD pattern, indicating a large distorted cubic structure with unit cell dimensions of:  $a = 3.14\text{Å}$ ,  $b = 3.53\text{Å}$ ,  $c = 2.76\text{Å}$   
 $\alpha = 89.8^\circ$ ,  $\beta = 90.4$ ,  $\gamma = 94.0$
3. The composition of P-phase can vary depending on the composition of the substituent MCrAlY layer.
4. P-phase remains stable for up to 25 hours at 1210°C.

5. P-phase limits the concentration of rare earths and transition elements in the outer portion of the bondcoat and hence enables TBC adhesion to be retained for longer periods at higher temperatures than comparable systems.

### **10.5 – Improvements to MCrAlY+Pt processing**

1. Intense peening operations on as sprayed LPPS MCrAlY coatings results in surface-oxide entrapment, leading to exaggerated Al usage from the coating. Improvements were made to the processing to allow this operation to be removed.
2. The Taguchi Method offered significant processing improvements resulting in a more robust manufacturing route, increasing spraying efficiency and bondcoat performance.
3. In order to generate P-phase and maintain the optimal performance the MCrAlY layer must exceed 50 $\mu$ m in thickness.
4. The Pt diffusion heat treatment should be as high as is practicable in order to produce the best performing system possible. Temperatures were limited to 1190°C within this study.
5. In order to produce clean grit blasted surfaces prior to TBC deposition the parameters can be significantly reduced over those that are generally held to be necessary; namely from 40psi air pressure and 100mm operating distance to 15psi and 175mm.

## **10.6 – Improvements to the MCrAlY+Pt system**

1. Pt appears to be unique in its ability to improve the performance of bondcoat/TBC adhesion.
2. The addition of Rh to the MCrAlY+Pt system increased the ultimate stability of the P-phase. The Pt/Rh phase proved to be stable out to 25 hours at 1230°C; TBC adhesion was not, however, improved.
3. Ir additions to the MCrAlY produced a very stable phase. Initial trials suggested that this Ir/Ni/Al phase inhibits Al diffusion.

## **10.7 – The effects of MCrAlY composition on bonding**

1. In general, the composition of the MCrAlY layer had very little effect on the performance of the MCrAlY+Pt bondcoat. The best performance overall was demonstrated, however, by the CoNiCrAlY based system. (No investigations were carried out using Fe based systems).

## **10.8 – Overall Conclusions**

1. This study successfully developed a novel bondcoat system that out performed the state of the art coatings currently available.

2. The processing route was subsequently developed into a robust, production worthy manufacturing process.
3. The study also helped to identify and understand the degradation modes operating on bondcoat systems for EB-PVD TBCs.

## **Chapter 11 – Future Work**

This study has demonstrated the importance of bondcoat chemistry and that of the substrate in TBC adhesion. The development of a robust production method has led to a bondcoat that is capable of maintaining TBC adhesion for up to 25 hours at 1210°C. This chapter describes some potential improvements which may extend this capability further, and briefly discusses additional testing which is essential to give a fuller simulation prior to use in an aero gas turbine engine.

### **11.1 - Bondcoat Improvements**

Given the degradation modes identified in this study, it is likely that performance improvements could be made to the system by a combination of a number of factors. The Pt level may be increased through a thicker initial deposit. This could increase the time taken for the Pt content of the surface region to drop to the level where P-phase cannot be sustained. It is likely, however, that there is an upper limit beyond which P-phase is not generated after one hour at 1150°C heat treatment.

Increasing the Al content of the MCrAlY in conjunction with the Pt layer should increase the time taken for the level of Al to drop below the critical level. The Al level of MCrAlY may be maintained by the use of a selective Ir-based diffusion layer between the MCrAlY and the substrate. This would inhibit the loss of Al to the substrate.

Further study into the combined role of Pt and Rh may produce a Rh-modified P-phase which as well as remaining stable at higher temperatures may also offer increased levels of TBC adhesion too. The most effective way to improve the bonding between the bondcoat and TBC would be the removal of Ti from the equation, either by the substrate development or through the use of Ti blockers in the MCrAlY layer, i.e. C or Nb.

It is most likely that the combination of the above improvements would produce the ultimate bondcoat given the current understanding. The bondcoat would support TBC adhesion for longer times at more elevated temperatures than any other state-of-the-art system available.

## **11.2 – Hot Corrosion Testing**

Despite the emphasis placed on high temperature oxidation within this study, a considerable proportion of the life of a turbine component is spent at more moderate temperatures. Given the correct conditions of temperature and environment, it is possible that components could experience hot corrosion. It is suggested, therefore, that a programme of type I and type II hot corrosion testing should be undertaken on this type of bondcoat system.

### **11.3 – Component Lifting**

In order to support safe component design, a programme of work should be undertaken to more fully understand the failure mechanisms of bondcoat systems. This work would support modelling activities designed to predict TBC spallation on specific components exposed to a wide range of operational conditions. These lifting activities would enable scheduled engine re-builds to fit into the component rework requirements where appropriate. In order to support the above, studies into the effective reworking of components with regard to TBC and bondcoat should be initiated.

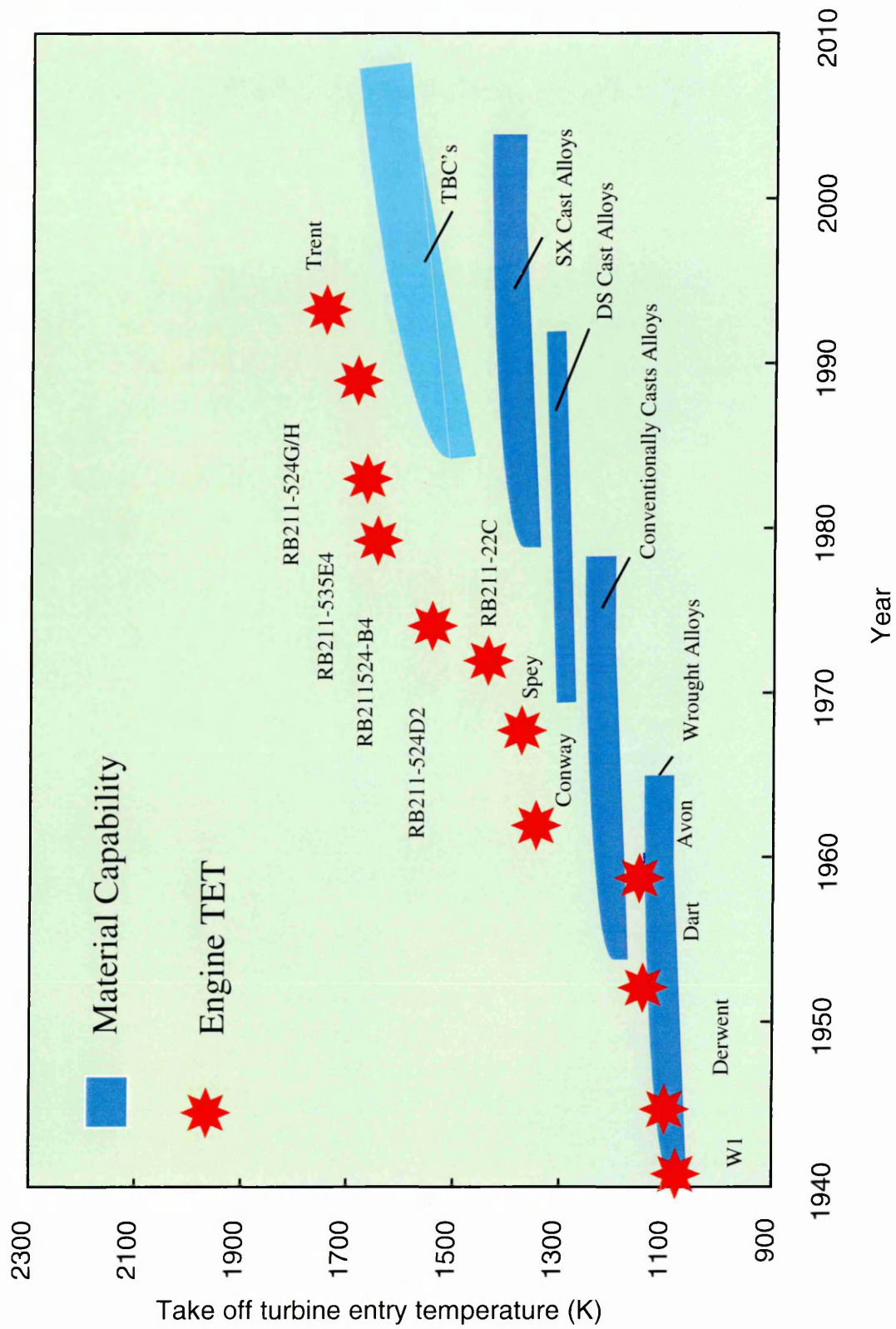


Figure 1.1: Diagram of engine development and associated rise in turbine temperature

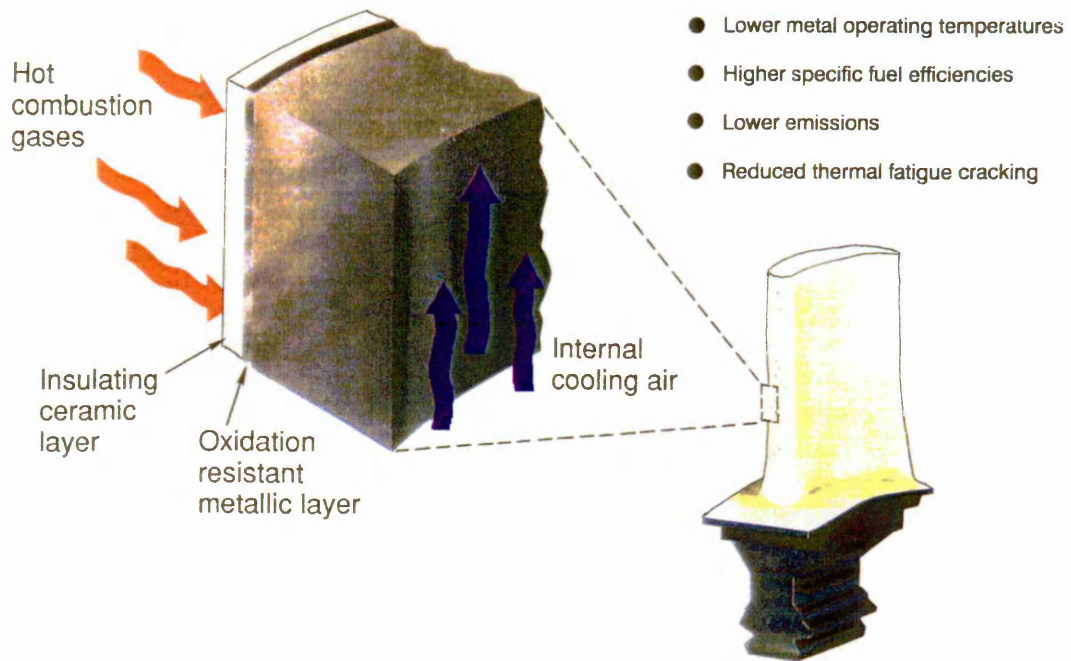


Figure 1.2: A state of the art TBC system

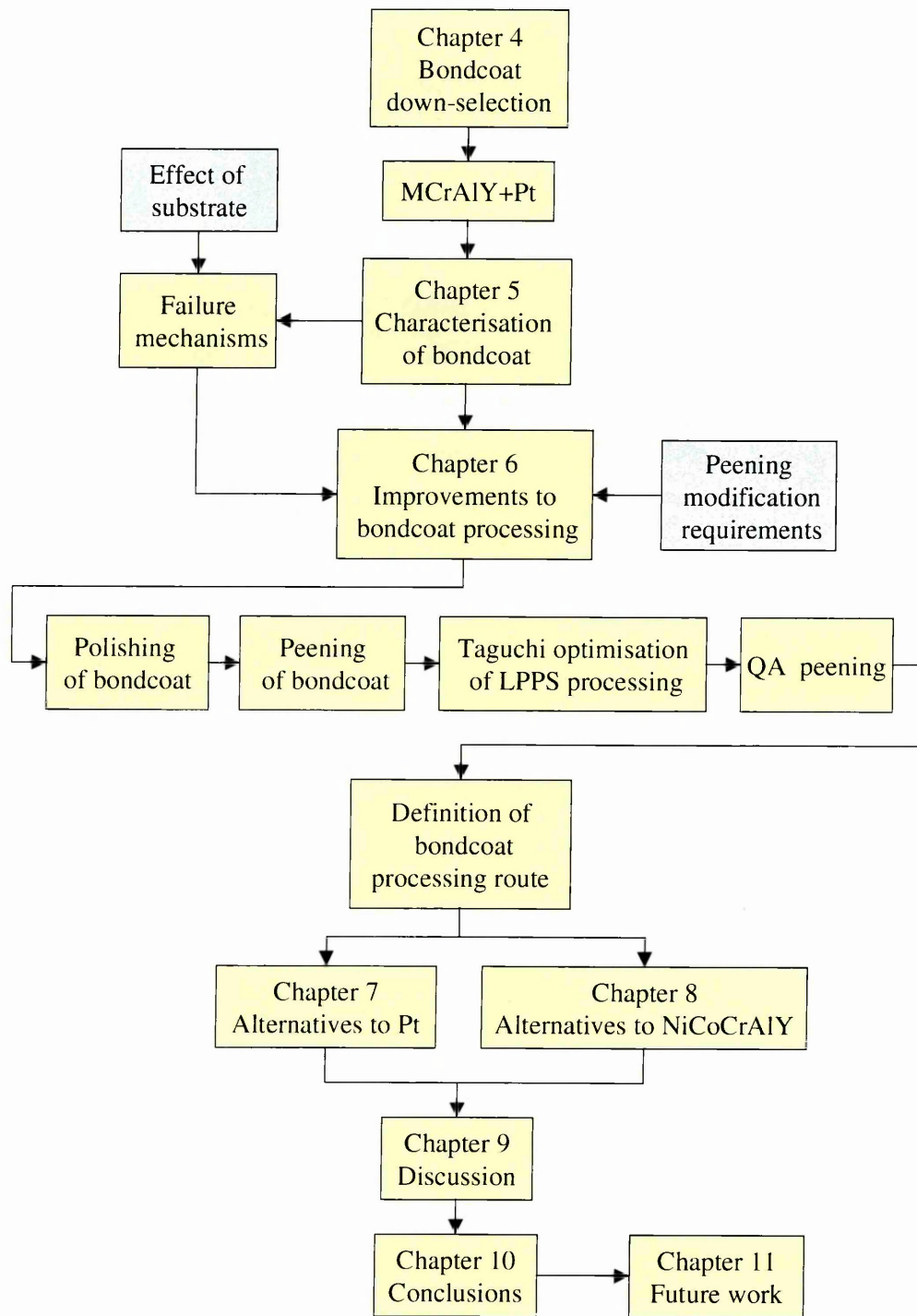


Figure 1.3: Schematic diagram of the research programme undertaken

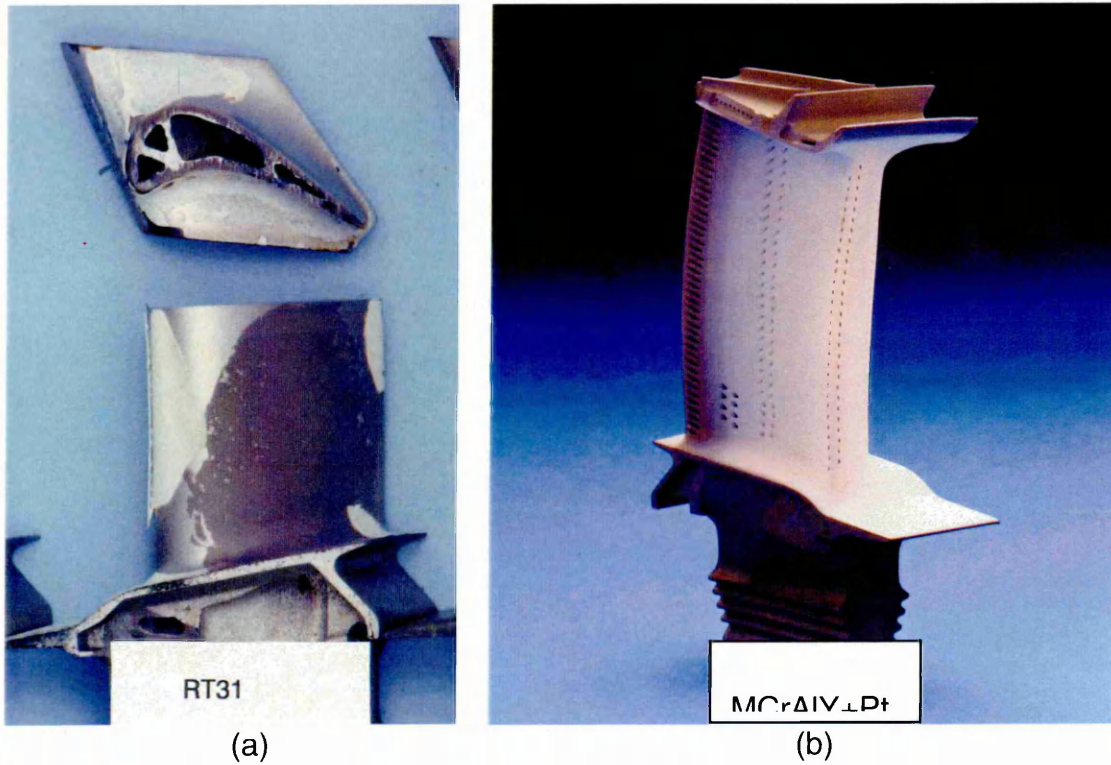


Figure 1.4: Aged components before and after bondcoat development programme

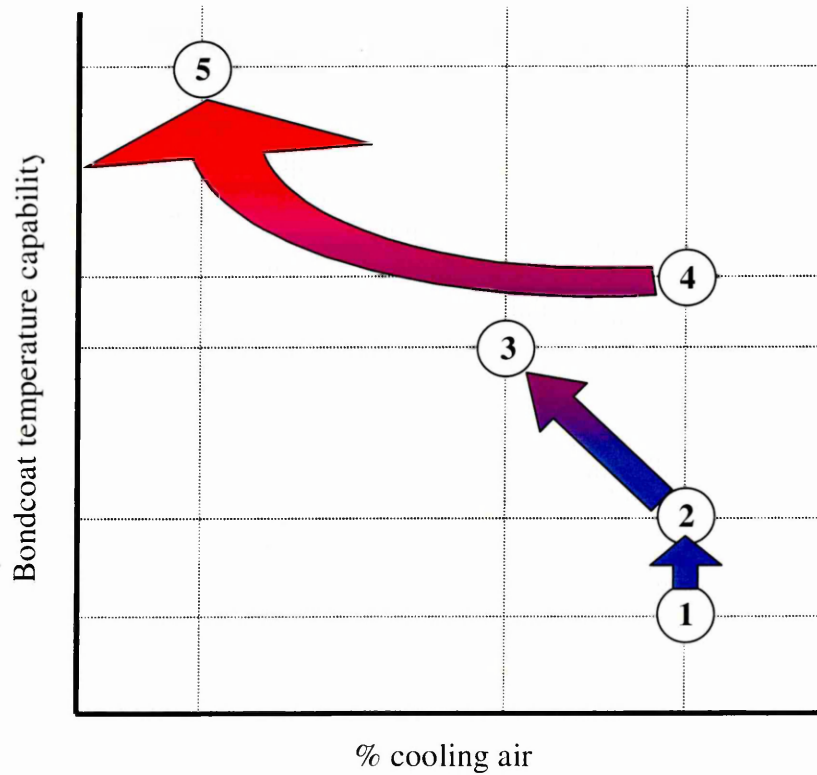


Figure 2.1: Design considerations for a fail-safe component

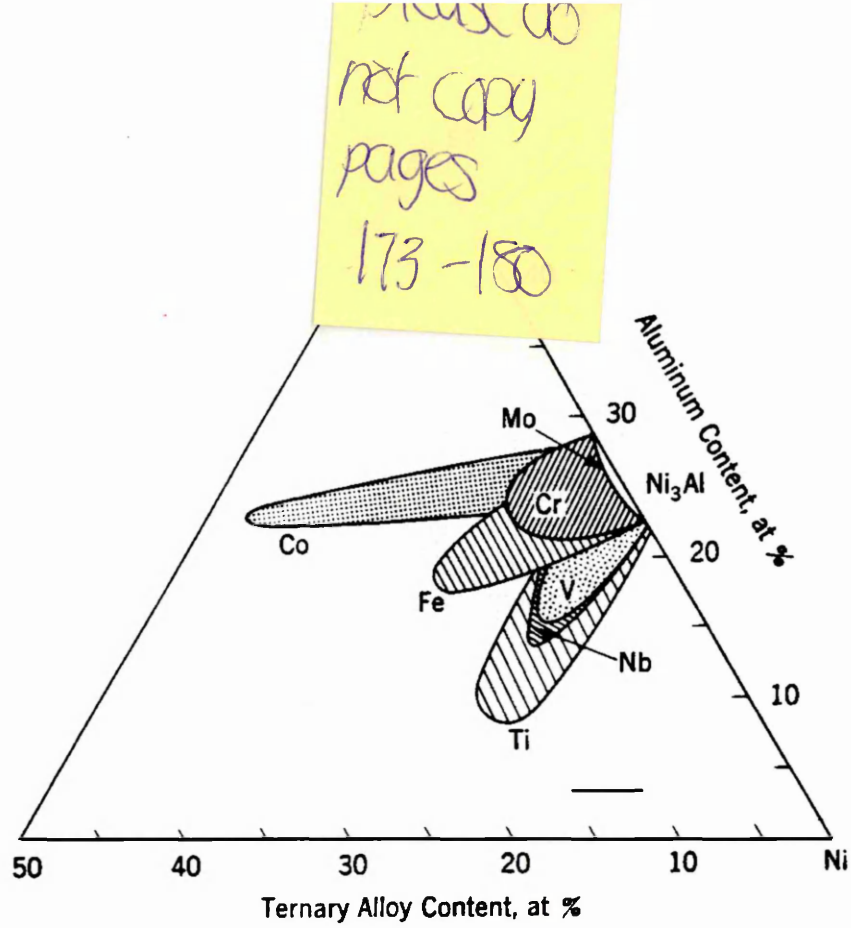


Figure 3.1: Tertiary schematic indicating the relative solubilities of elements in the  $\gamma'$ -phase

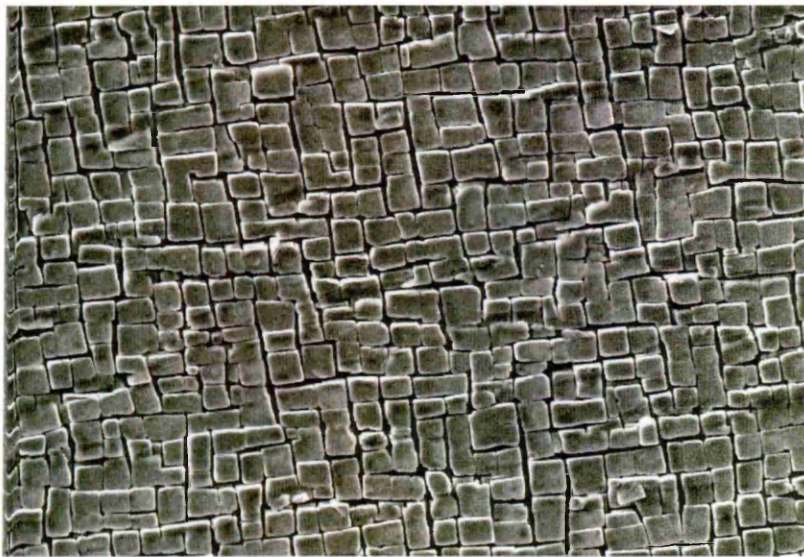


Figure 3.2: Etched micro specimen indicating the cubic  $\gamma/\gamma'$  structure of a Ni-based superalloy

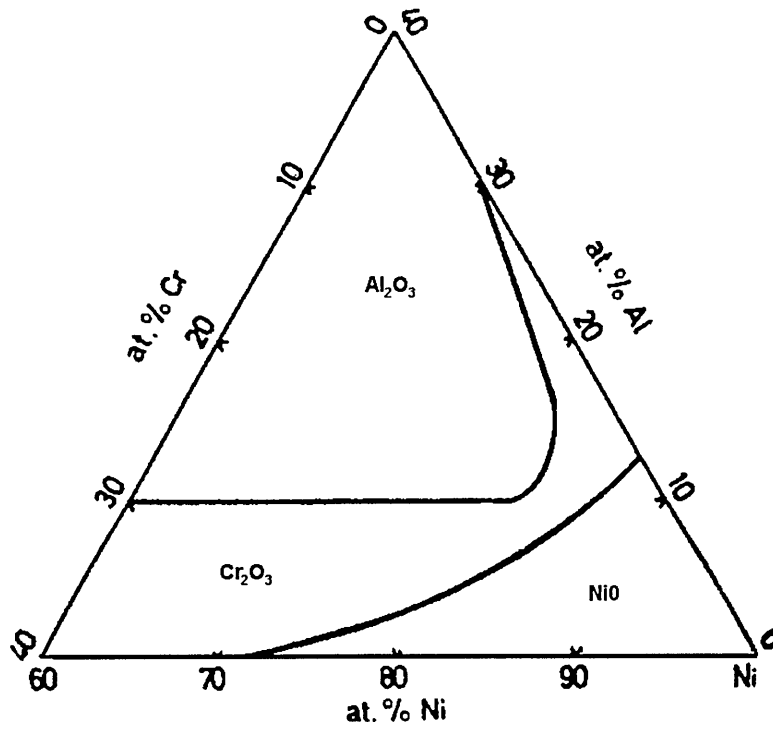


Figure 3.3: Tertiary schematic representing the effect of composition on oxide formation

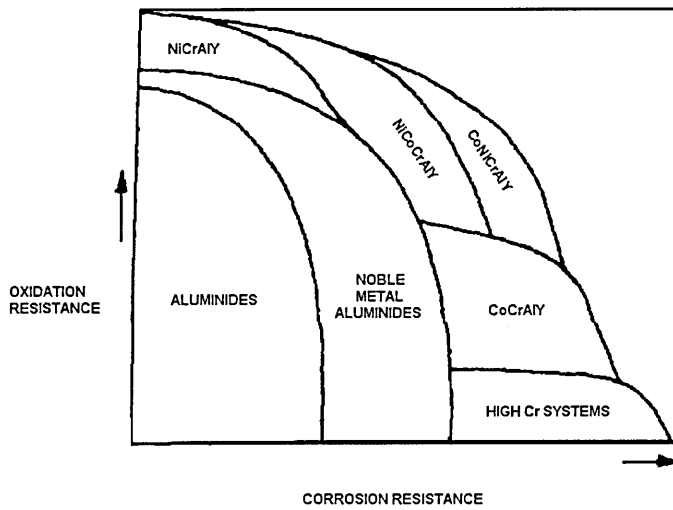


Figure 3.4: Schematic graph comparing the relative performance of coating compositions

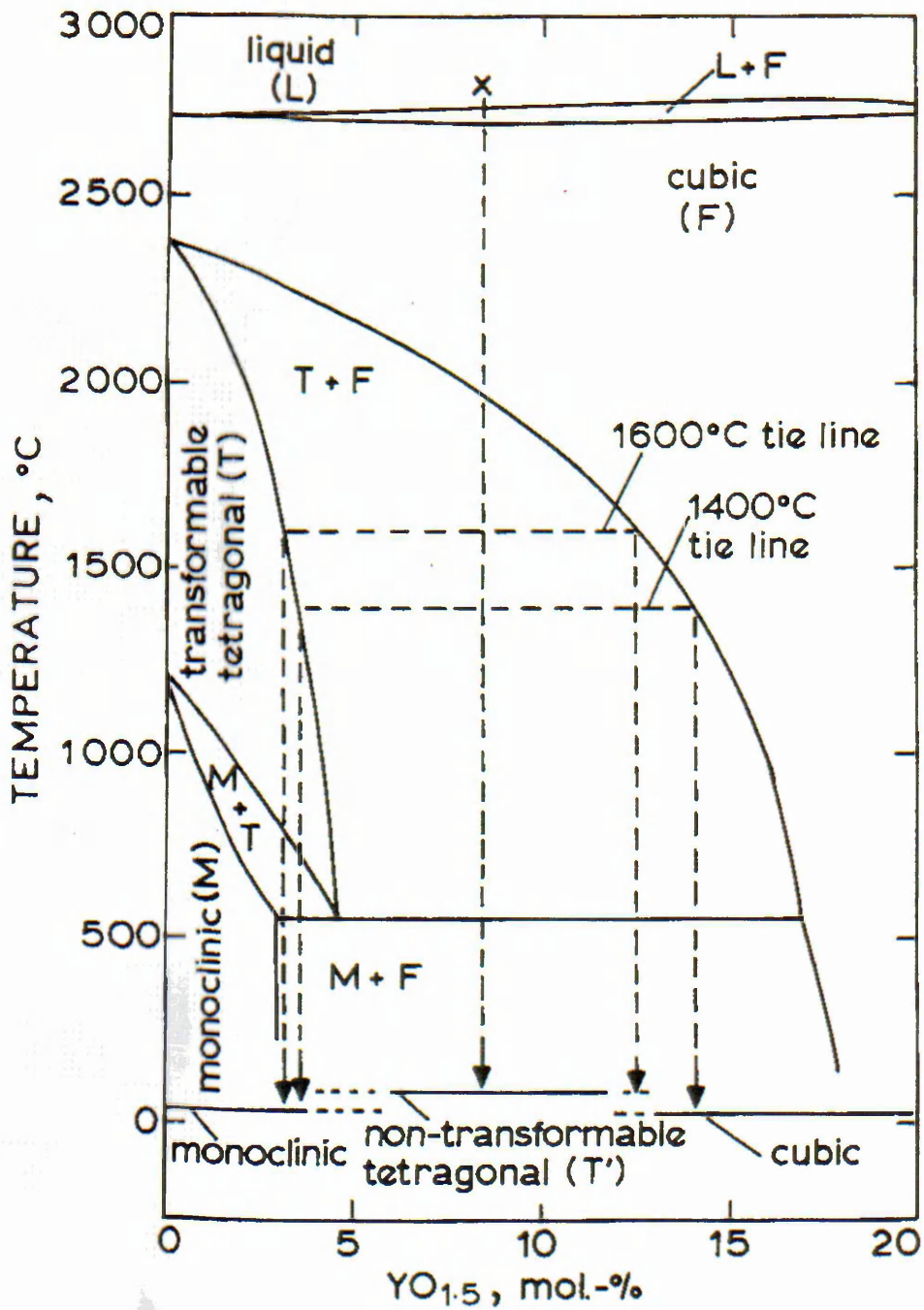


Figure 3.5: Partial phase diagram of the  $ZrO_2$ - $Y_2O_3$  system

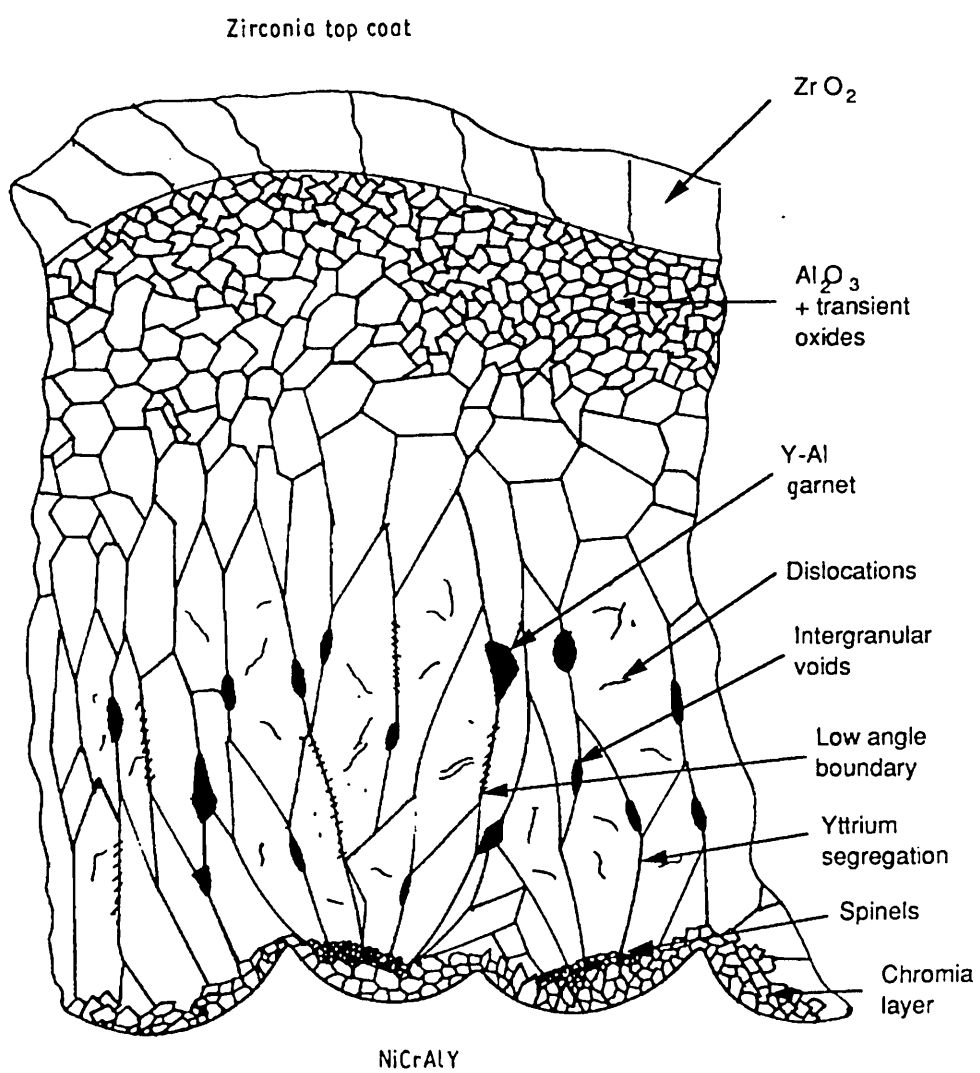


Figure 3.6: Schematic of the cross-sectional structure of the bonding  $\text{Al}_2\text{O}_3$  scale in a typical TBC system

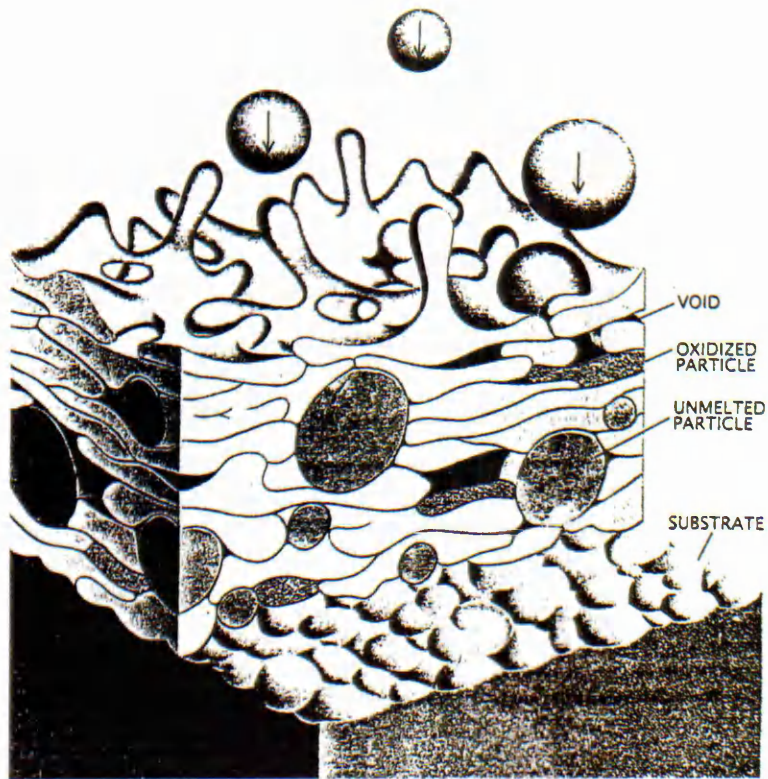


Figure 3.7(a): Diagram of the build up a thermally sprayed deposit



Figure 3.7(b): Micrograph of the structure of a thermally sprayed deposit

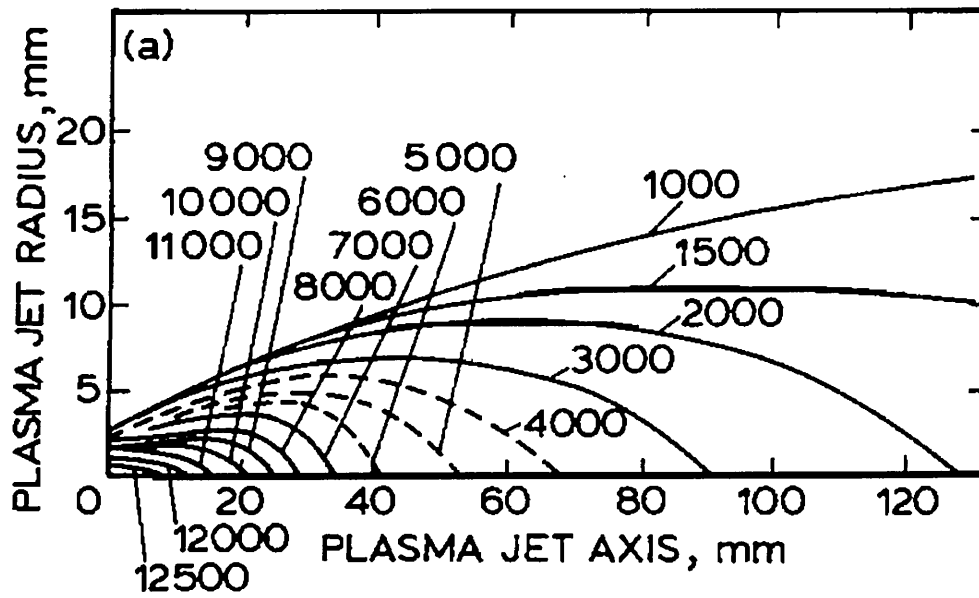


Figure 3.8: Diagram of the temperature profile within a plasma plume

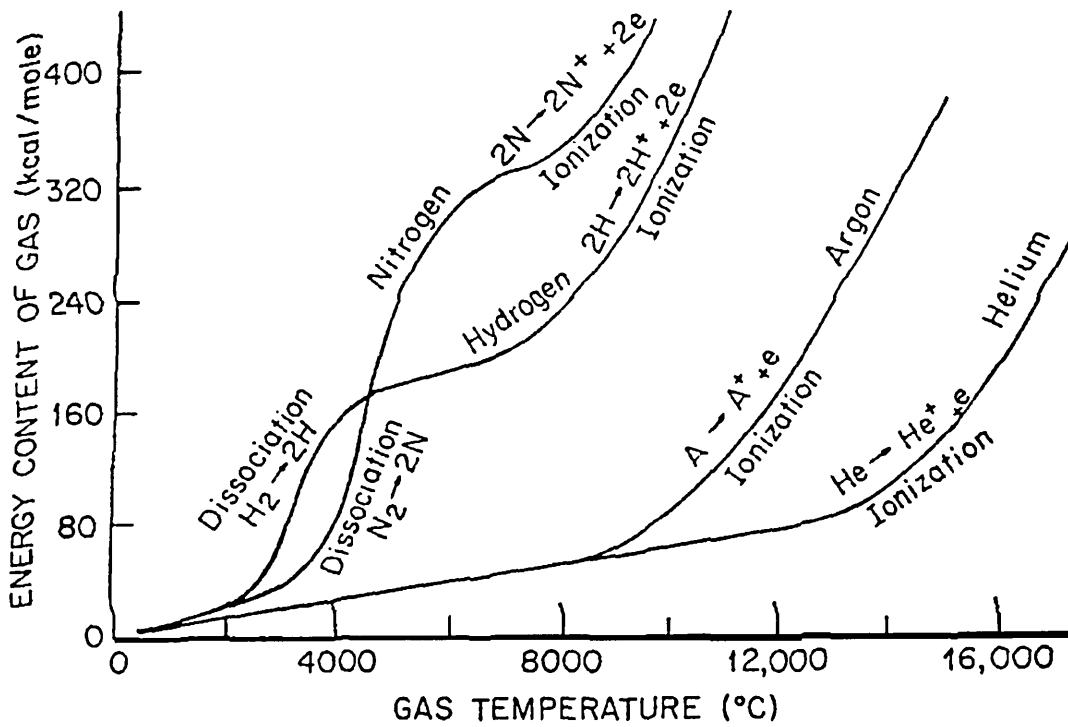


Figure 3.9: Diagram comparing the energy content of a gas to its temperature

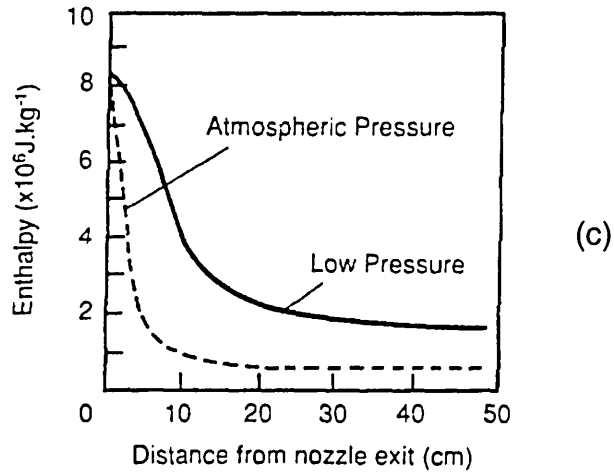
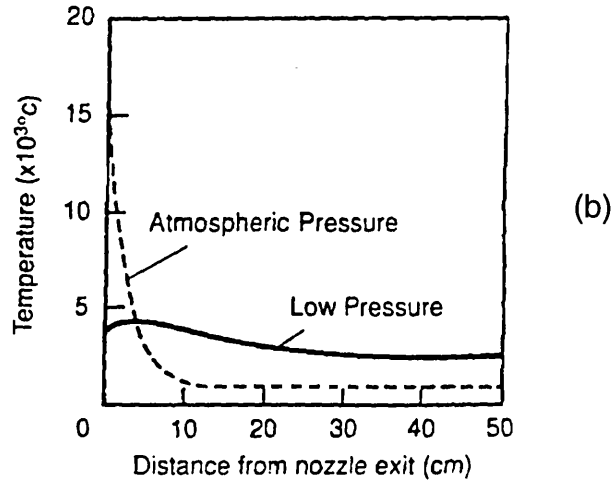
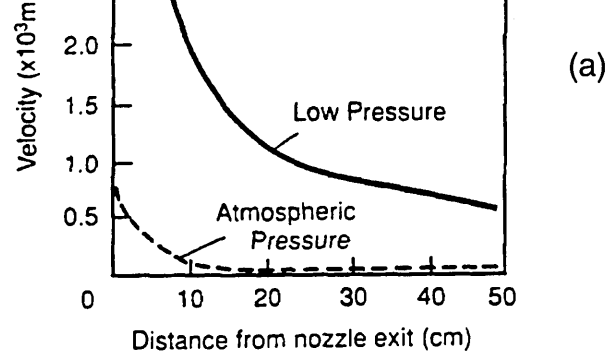


Figure 3.10(a-c): Graph of gas velocity against distance in a plasma plume  
 Graph of gas temperature against distance in a plasma plume  
 Graph of gas enthalpy against distance in a plasma plume

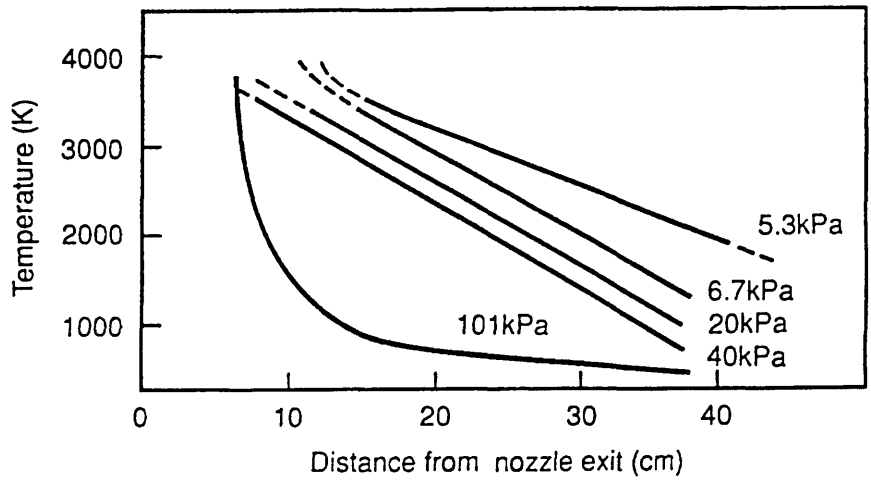


Figure 3.11: Graph of temperature against distance for different operating pressures in a plasma plume

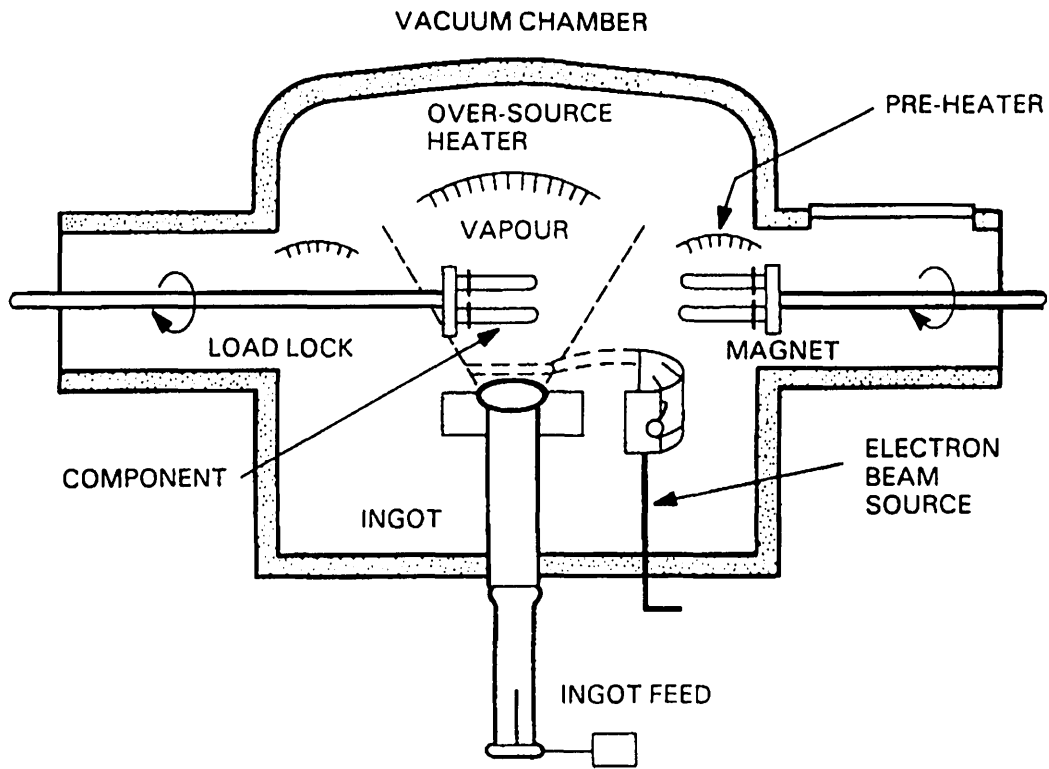


Figure 3.12: Schematic of an EB-PVD coating rig

<b>System Reference Number</b>	<b><u>Diffusion Coatings</u></b>
1	RPS320 – low temperature pack aluminide
2	RT21 – pack aluminide
3	RT69 – out of pack (gas phase) aluminide
	<b><u>Diffusion Coatings Platinum-Aluminides</u></b>
4	RT22LT – low temperature pack Pt-Al
5	RT22(Cr) – Cr modified, low temperature pack Pt-Al
6	**** - out of pack (gas phase) Pt-Al
	<b><u>Overlay Coatings</u></b>
7	RT122 – LPPS CoNiCrAlY
8	PWA276 – LPPS high Al NiCoCrAlY
9	PWA286 – LPPS high Al NiCoCrAlYHfSi
10	RT31 – EB-PVD CoNiCrAlY
11	PWA270 – EB-PVD high Al NiCoCrAlY
	<b><u>Modified Coatings</u></b>
12	RT122+RT21 – CoNiCrAlY + pack aluminide
13	RT122+RT22LT – CoNiCrAlY + pack Pt-Al
14	PWA276+RT22LT – high Al NiCoCrAlY + pack Pt-Al
15	PWA 286+RT22LT – high Al NiCoCrAlYHfSi + pack Pt-Al
16	Pt+RT122 – Pt layer under CoNiCrAlY
17	RT122+Pt(thin) – CoNiCrAlY under thin Pt layer
18	RT122+Pt – CoNiCrAlY under Pt layer

Figure 4.1: Sample identification for phase 1 of the programme

<b>Media</b>	<b>Size</b>	<b>Lubricant</b>	<b>Time</b>
SiC paper	120 grit	water	until planer
SiC paper	220 grit	water	2 mins
SiC paper	320 grit	water	2 mins
SiC paper	500 grit	water	2 mins
SiC paper	1200 grit	water	2 mins
SiC paper	2400 grit	water	2 mins
SiC paper	4000 grit	water	2 mins
⟨ Struers DP nap	1μm diamond	Struers blue	1 min
Struers OP chem	OPS (0.05μm Al <sub>2</sub> O <sub>3</sub> )	none	2 mins

Figure 4.2: The polishing procedure used for examination of metallic bondcoats  
 ⟨ for use with Pt containing bondcoats only

<b>Media</b>	<b>Size</b>	<b>Lubricant</b>	<b>Time</b>
SiC paper	120 grit	water	until planer
SiC paper	220 grit	water	2 mins
SiC paper	320 grit	water	2 mins
SiC paper	500 grit	water	2 mins
SiC paper	1200 grit	water	2 mins
SiC paper	2400 grit	water	2 mins
SiC paper	4000 grit	water	2 mins
Struers pan-W	6μm diamond	Struers blue	6 mins
Struers pan-W	1μm diamond	Struers blue	6 mins
Struers OP chem	OPS (0.05μm Al <sub>2</sub> O <sub>3</sub> )	none	2 mins

Figure 4.3: The polishing procedure used for examination of ceramic top coats

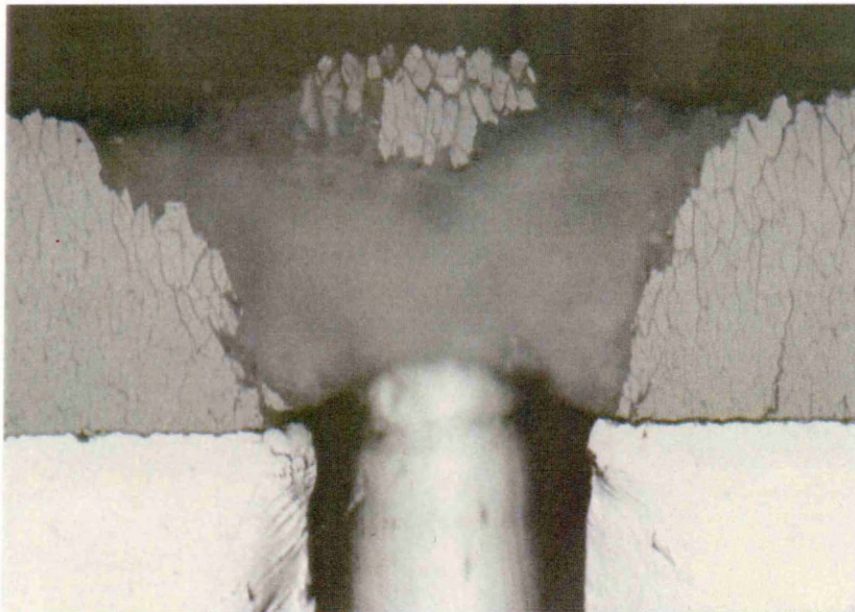


Figure 4.4: Micrograph of scratch track through the bondcoat/TBC interface

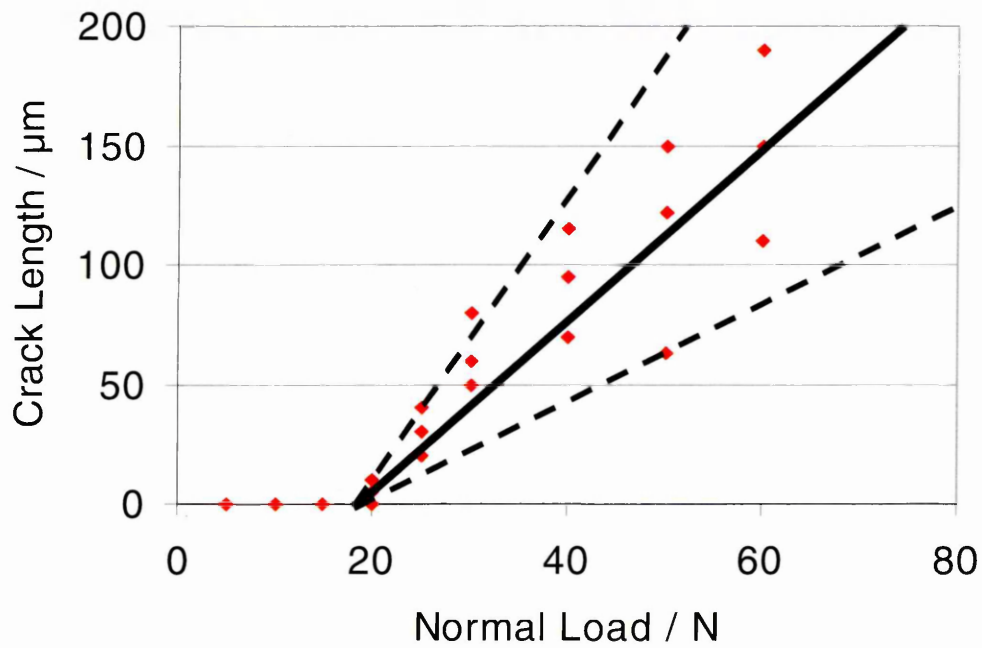


Figure 4.5: Graph of crack extension vs. normal load showing the typical spread of results for one sample. Critical load to cause failure =  $20N \pm 5N$

<b>Bondcoat scoping trials</b>						
			scratch test results for Lc / N			
coating number	commercial code	bondcoat type	as-rec	100h @ 1050°C	100h @ 1100°C	100h @ 1150°C
1	RPS320	diffusion	60	-	0	-
2	RT21	diffusion	55	-	0	-
3	RT69	diffusion	85	-	0	-
4	RT22LT	diffusion	60	30	10	0
5	Cr mod. PtAl	diffusion	30	-	0	-
6	gas phase PtAl	diffusion	45	-	0	-
7	RT122(10A)	overlay	55	45	35	0
8	PWA276	overlay	45	35	0	0
9	PWA286	overlay	85	65	45	0
10	RT31	overlay	55	55	60	35
11	PWA270	overlay	40	70	45	5
12	RT122+RT21	modified overlay	45	-	0	-
13	RT122+RT22	modified overlay	30	-	0	-
14	PWA276+RT22	modified overlay	15	-	0	-
15	PWA286+RT22	modified overlay	55	25	20	10
16	Pt+RT122	modified overlay	85	65	40	0
17	RT122+Pt(thin)	modified overlay	70	65	30	0
18	RT122+Pt	modified overlay	100	65	45	50

Figure 4.6: Results from the initial phase of the bondcoat selection procedure

	Cr	Co	Mo	W	Re	Al	Ti	Ta	Hf	Zr	C
<b>C1023</b>	15.5	9.7	8.3	-	-	4.1	3.6	-	-	-	0.15
<b>MarM002</b>	9	10	-	10	-	5.5	1.5	2.5	1.5	0.06	0.15
<b>CMSX-4</b>	6.5	9.5	0.6	6.4	3	5.6	1	6.5	0.1	-	-

Figure 4.7: Compositions of superalloys

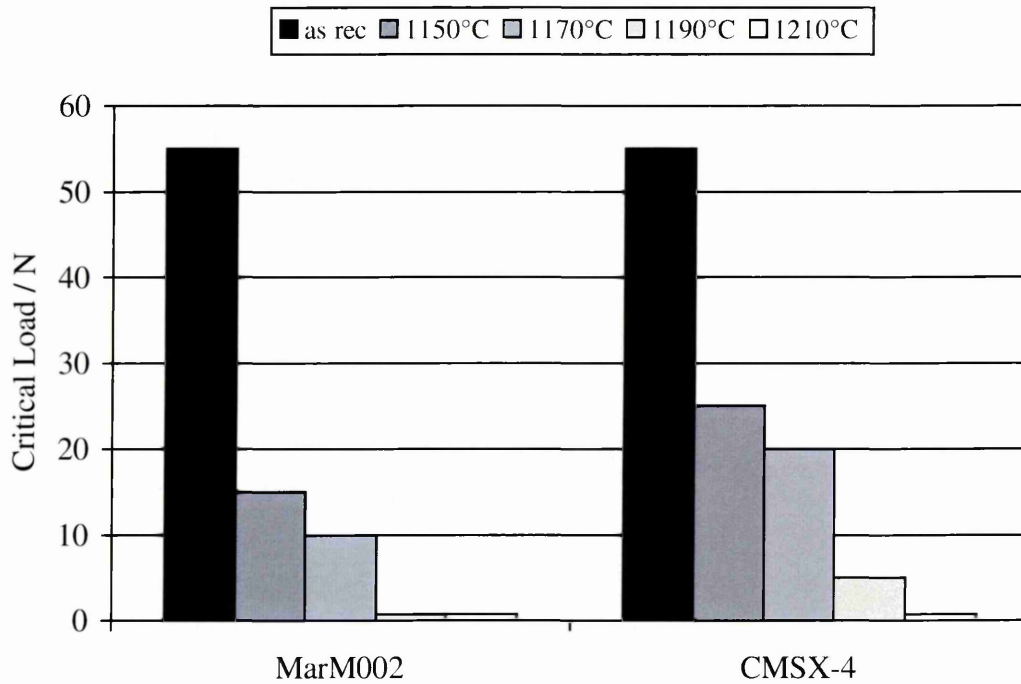


Figure 4.8: Scratch test results for an MCrAlY bondcoat (RT122) on two different substrates after exposure for 25 hours

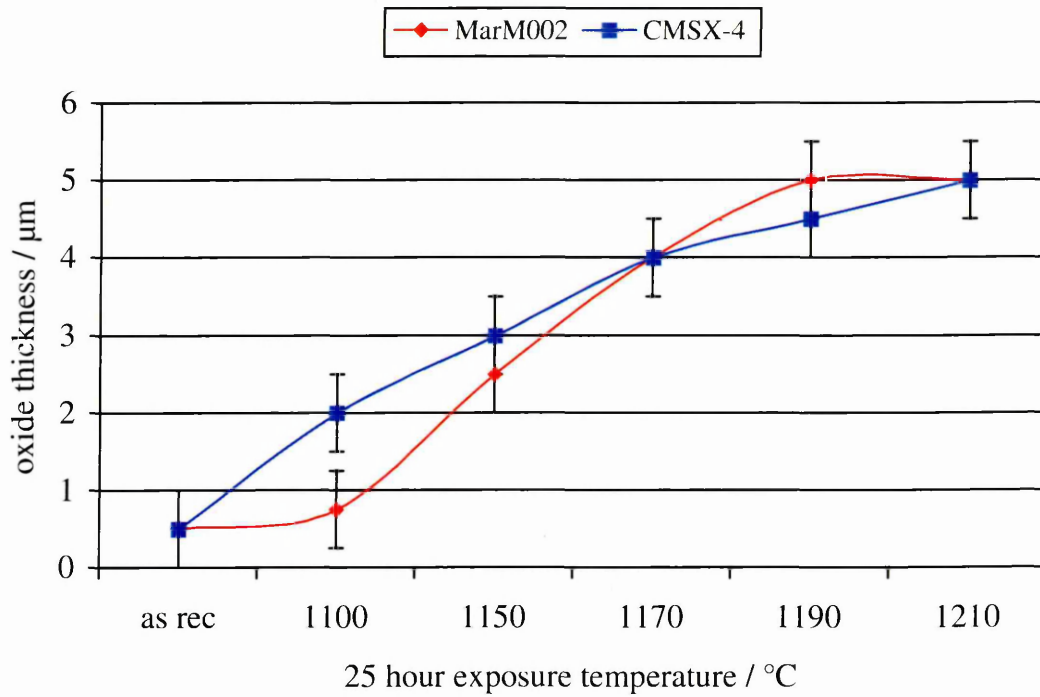


Figure 4.9: Oxide thickening rates for the same bondcoat (RT122+Pt) on two different substrates

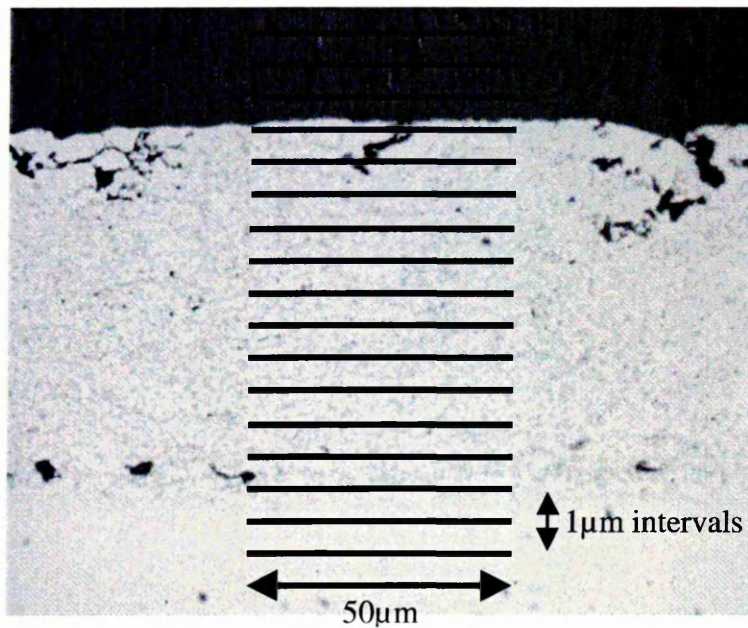


Figure 4.10: Schematic of the WDS ladder scan process showing the path of the rastered beam on a 10A peened MCrAlY bondcoat system

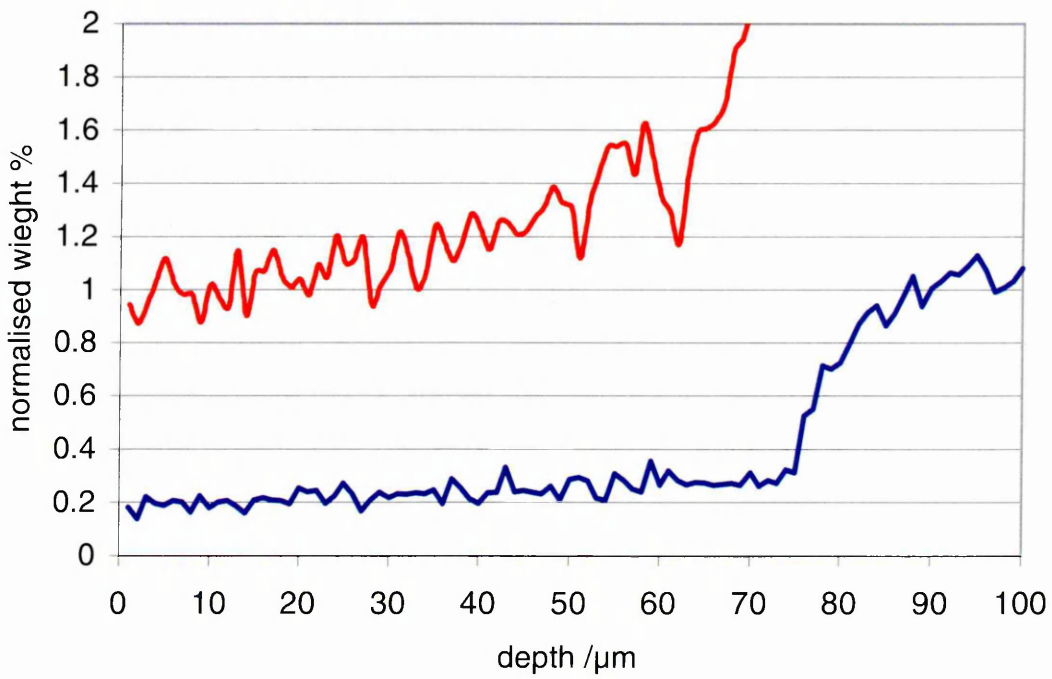
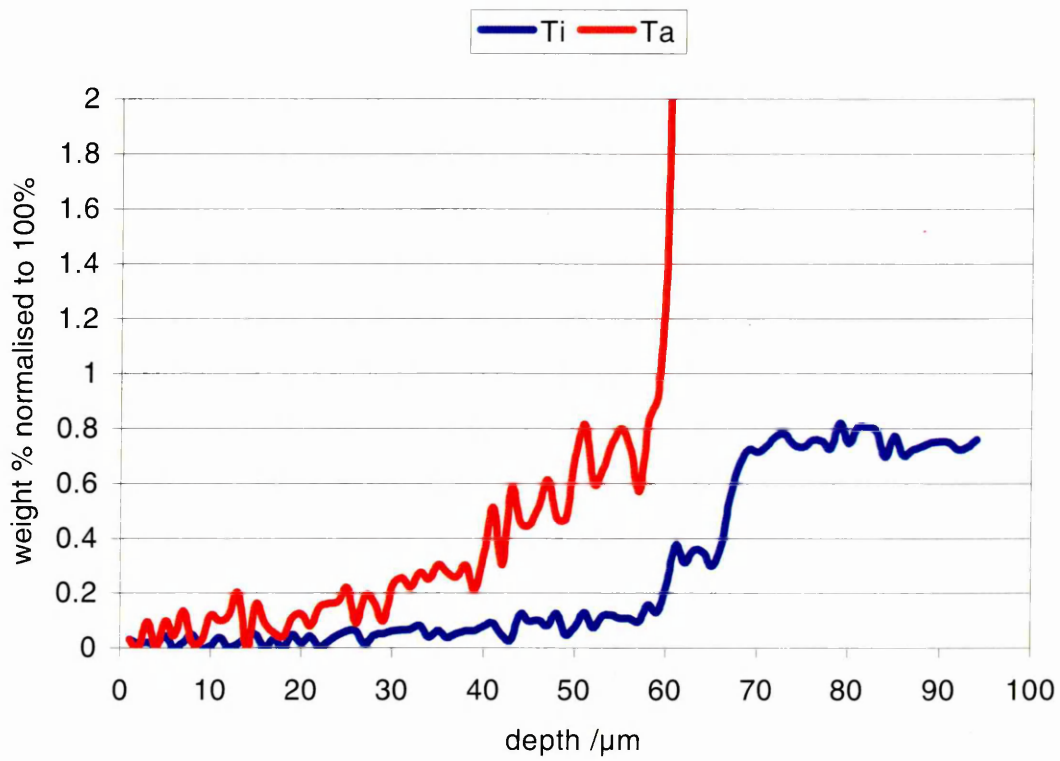


Figure 4.11: WDS traces for Ti and Ta from the (RT122) MCrAlY/CMSX-4 system in the as processed and aged states

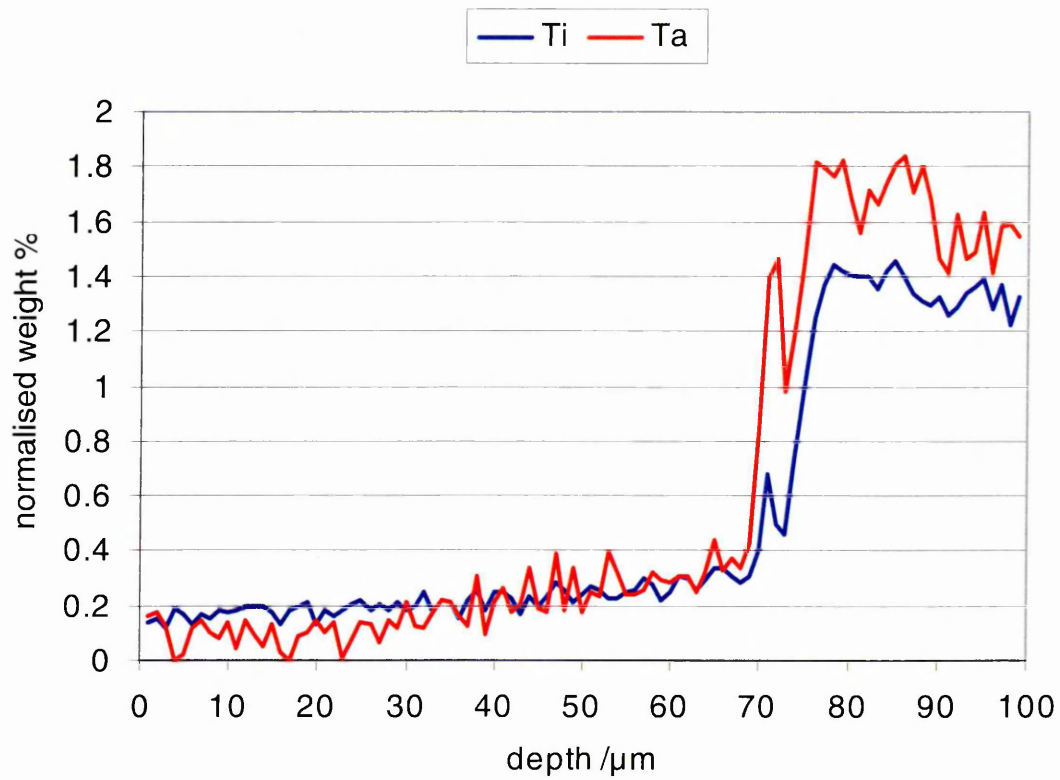


Figure 4.12: WDS traces for Ti and Ta from the aged MCrAlY/MarM002 system

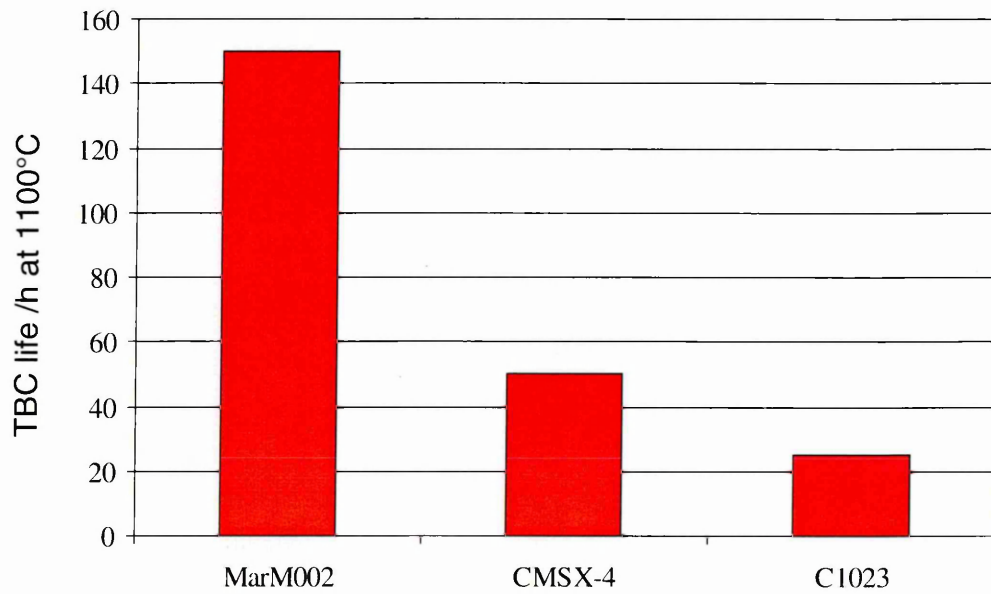


Figure 4.13: Schematic representation of the relative time to spall for an MCrAlY bondcoat on different substrate materials

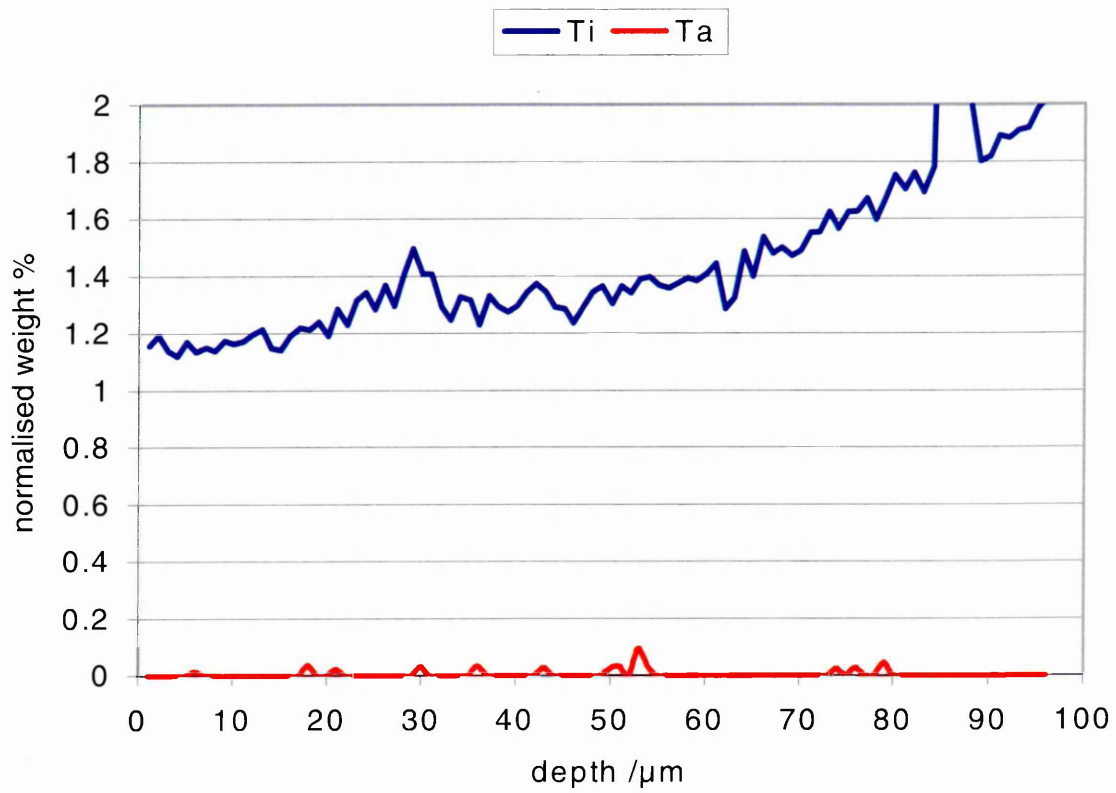


Figure 4.14: WDS traces for Ti and Ta for the aged MCrAlY/C1023 system

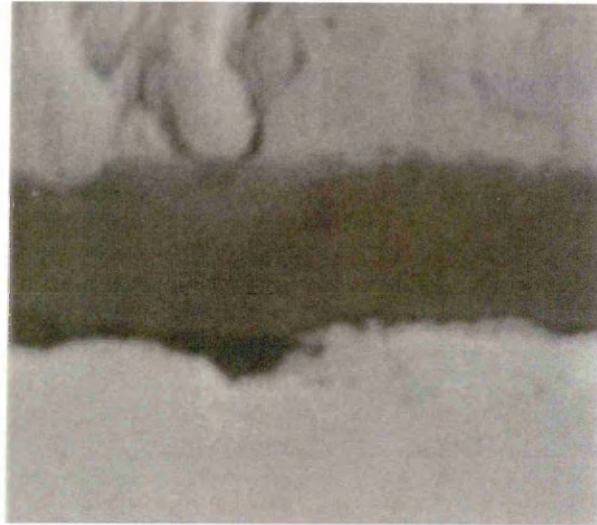


Figure 4.15: Detail of the TGO in a TBC system showing evidence of debonding

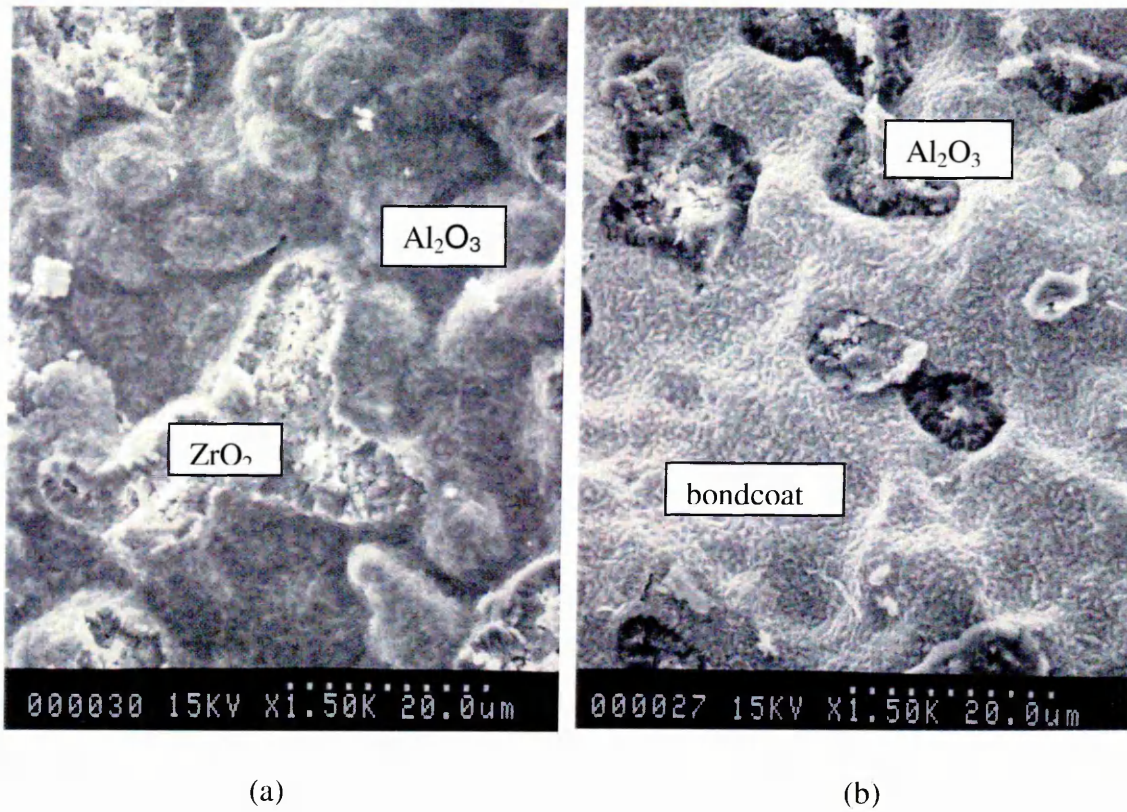
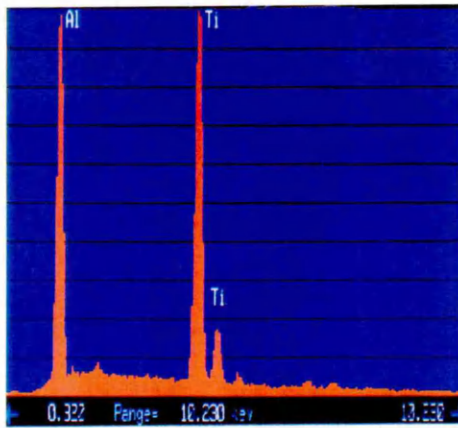
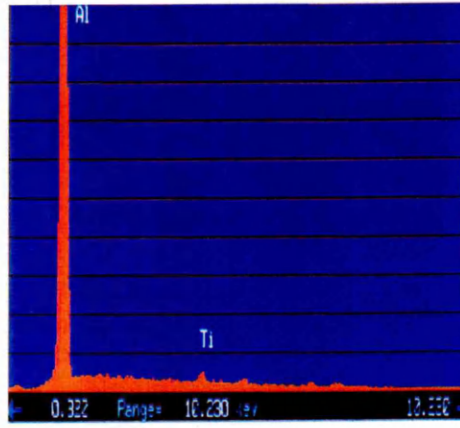


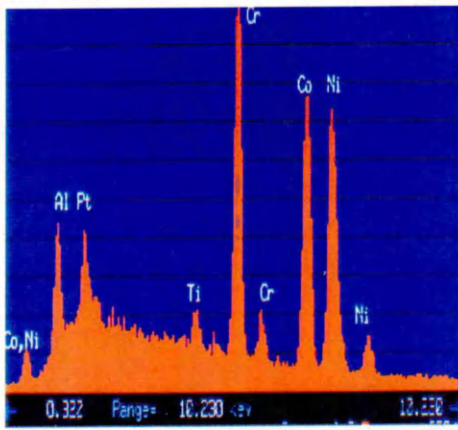
Figure 4.16: SEM micrographs showing detail from  
(a) the underside of the spalled ZrO<sub>2</sub> (TGO still adherent)  
(b) the surface of the bondcoat after TBC loss



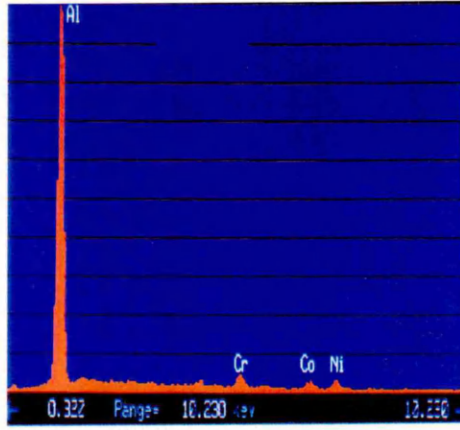
analysis area A



analysis area



analysis area



analysis area D

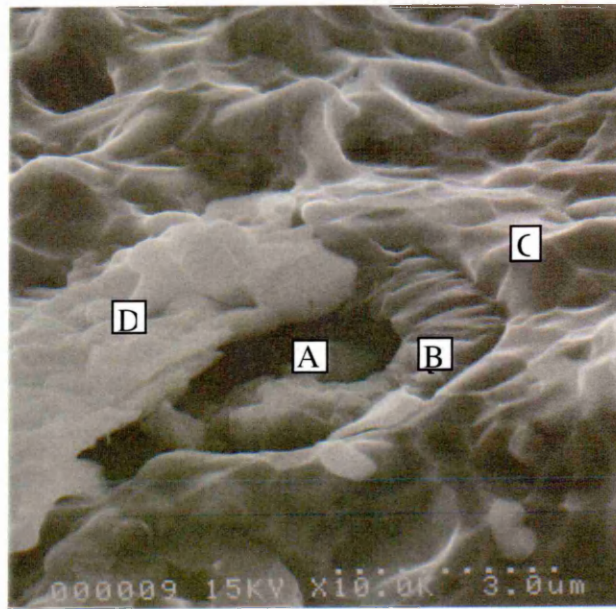


Figure 4.17: EDX analysis of a sheared off oxide peg

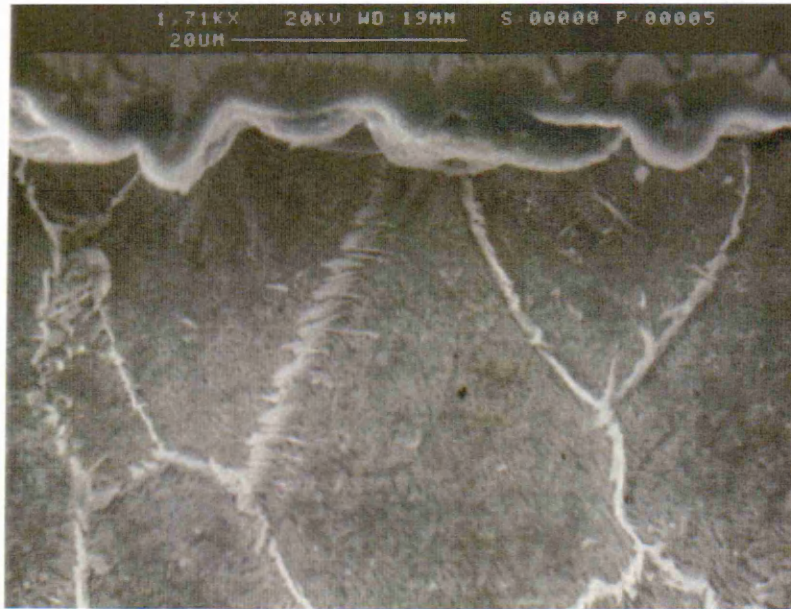


Figure 4.18: SEM image of an etched bondcoat showing grain boundary transport of substrate elements

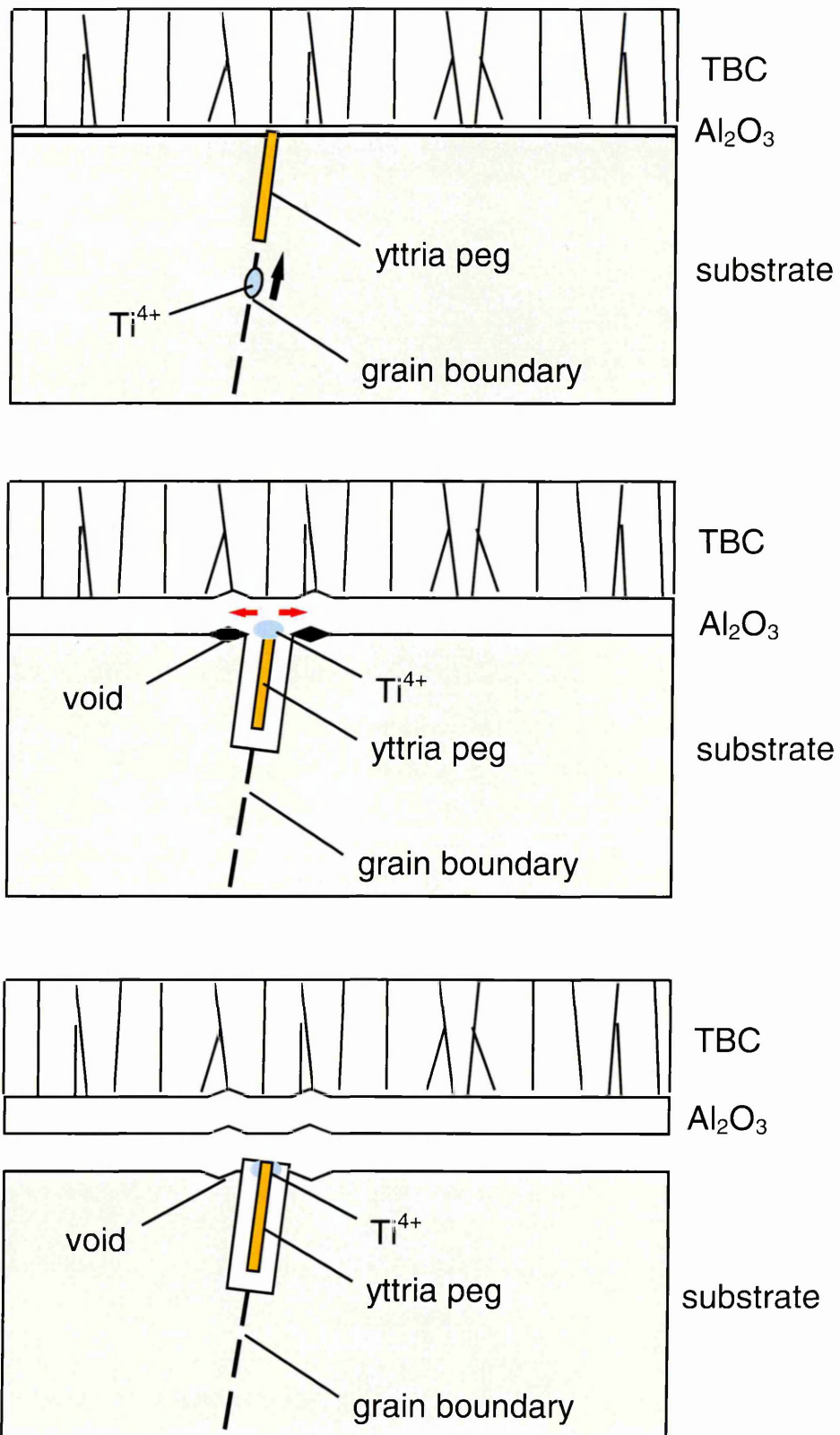


Figure 4.19: Schematic of oxide-peg and void growth

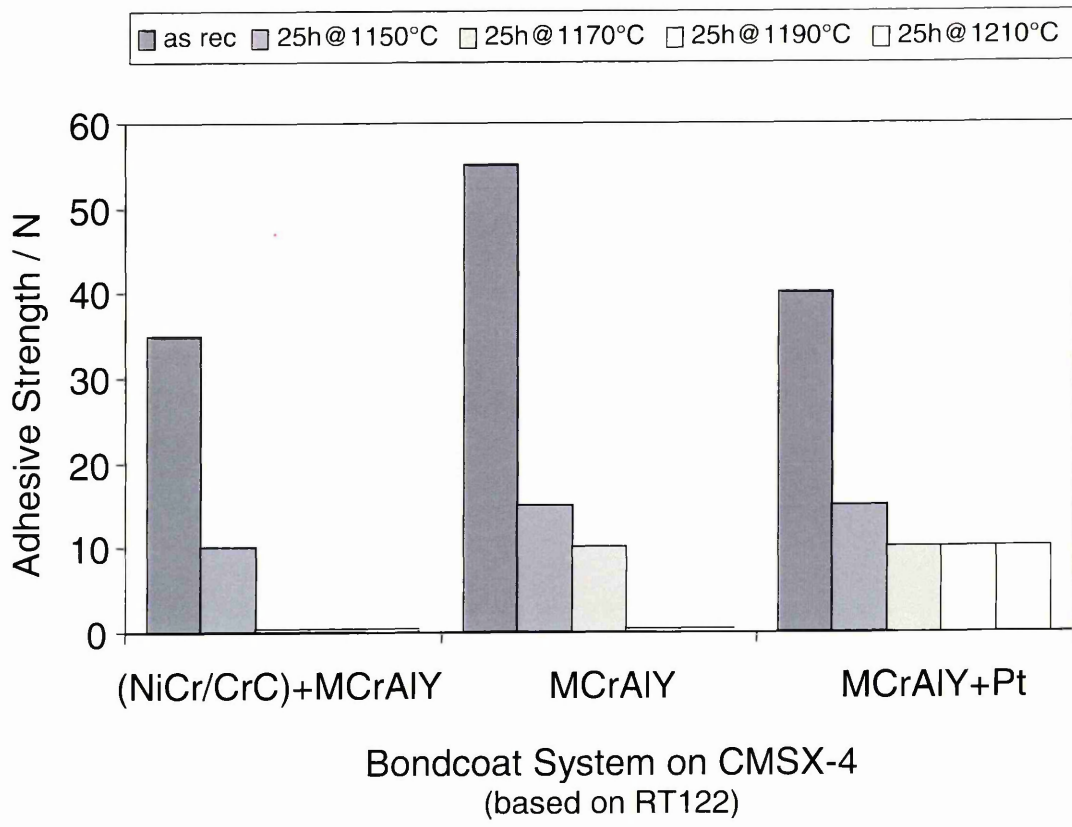


Figure 4.20: Comparison of the relative adhesion levels of MCrAlY based bondcoat systems

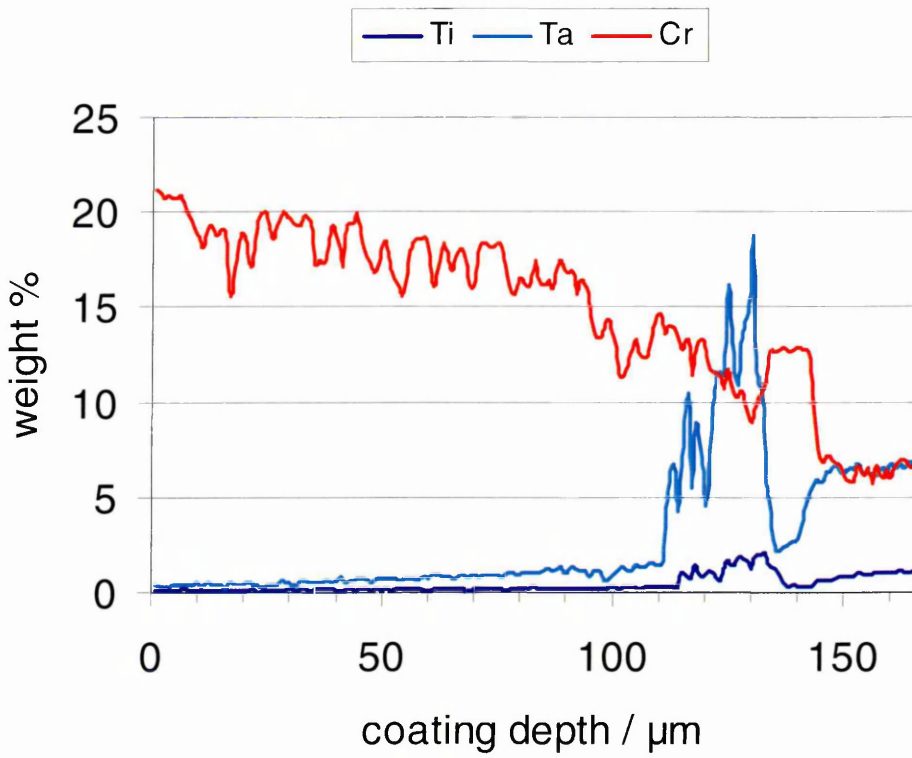
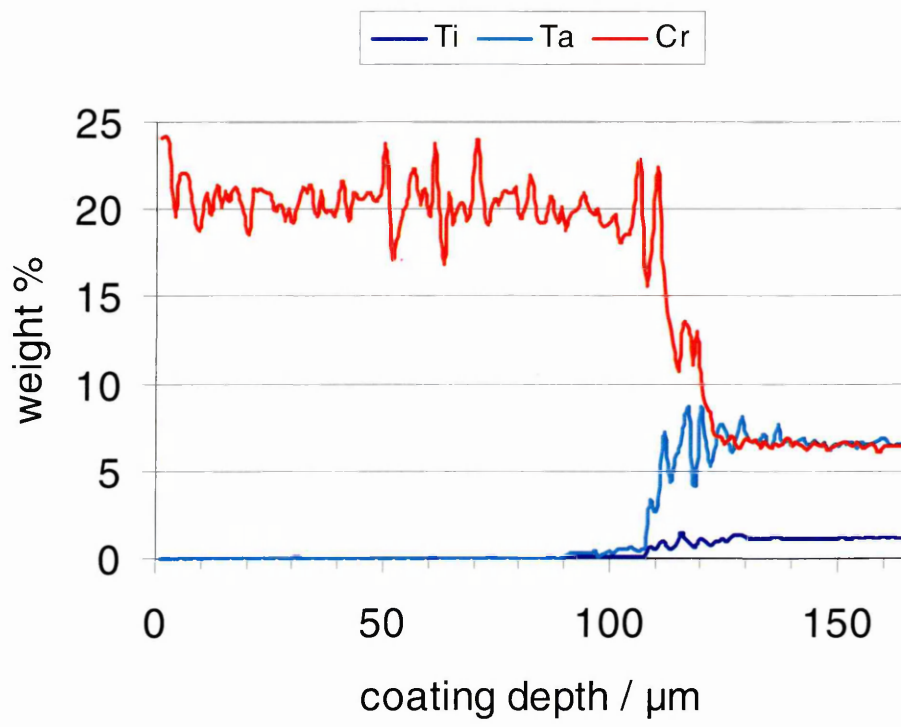


Figure 4.21: WDS ladder scan traces of the NiCr/CrC + MCrAlY system as processed and after 25 hours at 1150°C

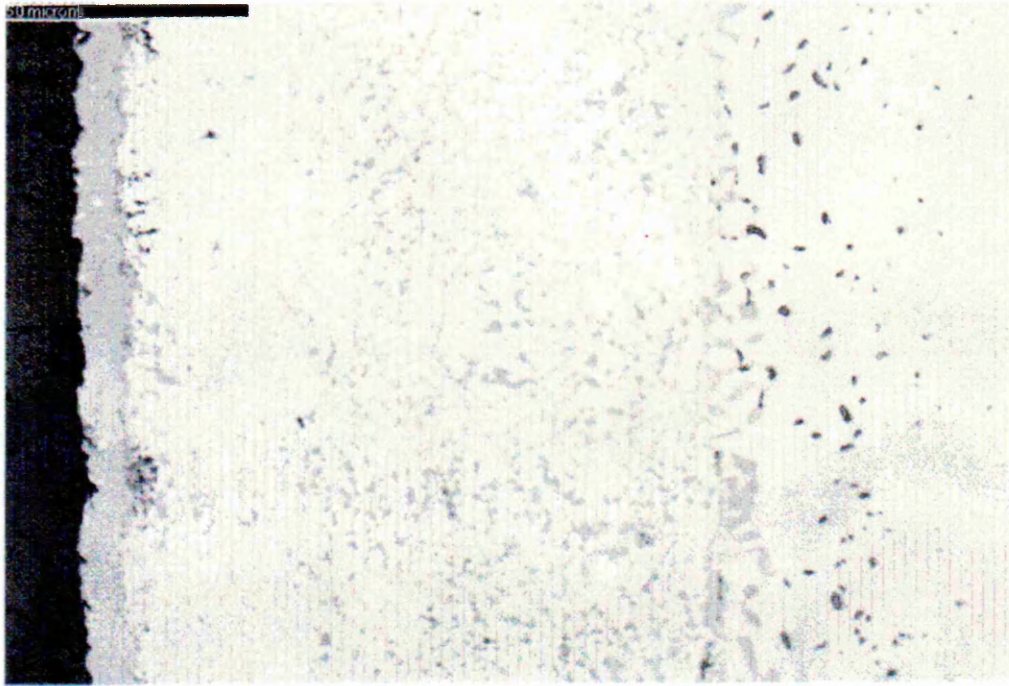


Figure 5.1: MCrAlY+Pt as processed



Figure 5.2: MCrAlY+Pt as processed (etched)

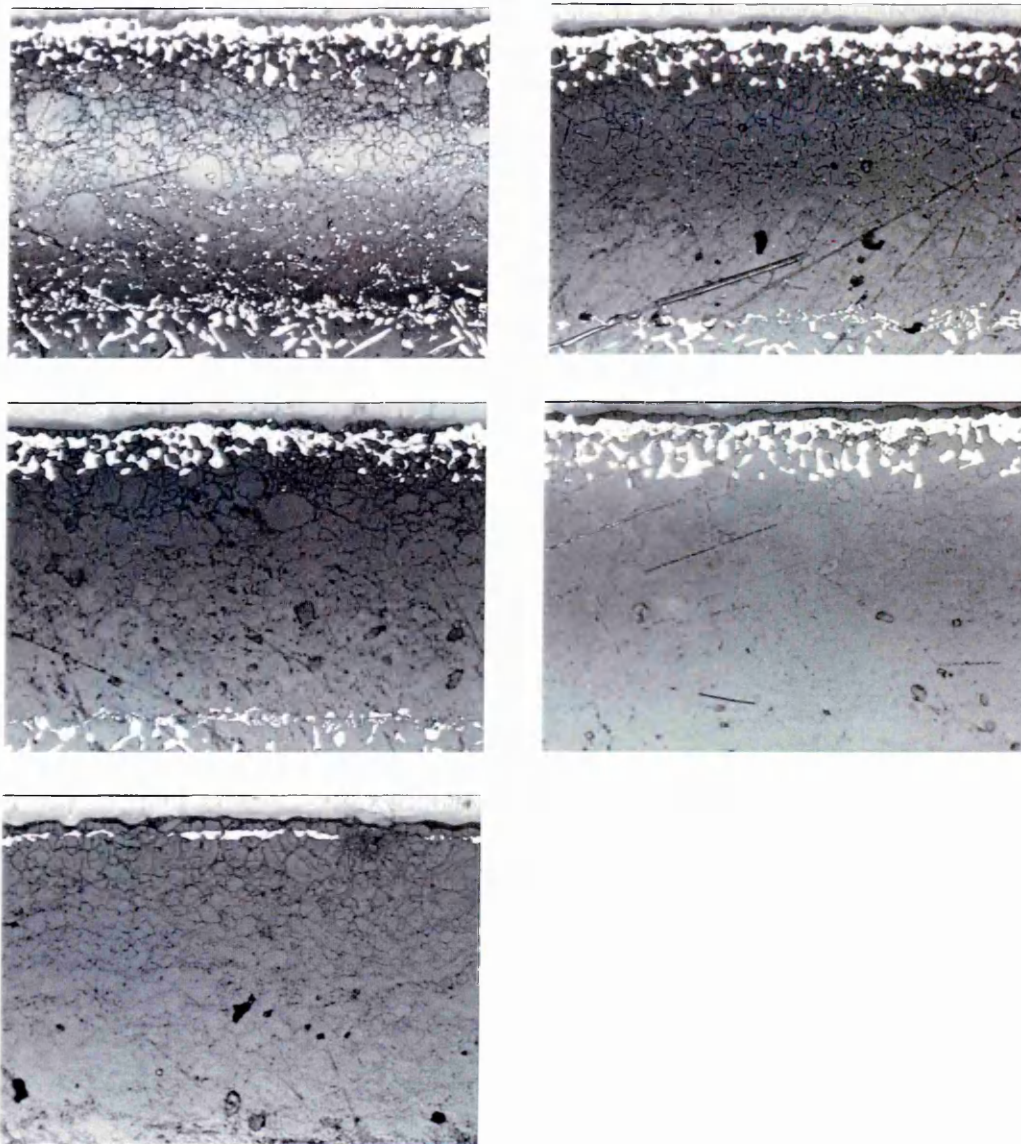


Figure 5.3(a-e): MCrAlY+Pt after 25hour isothermal soaks at 1100, 1150, 1170, 1190 and 1210°C respectively

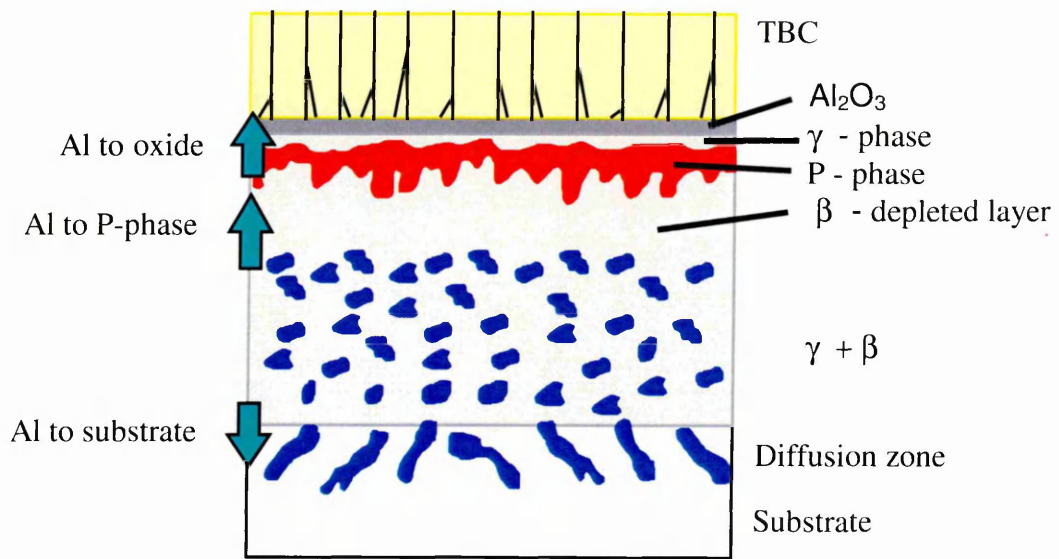


Figure 5.4: Schematic of the Al exchange during the ageing of the MCrAlY+Pt system

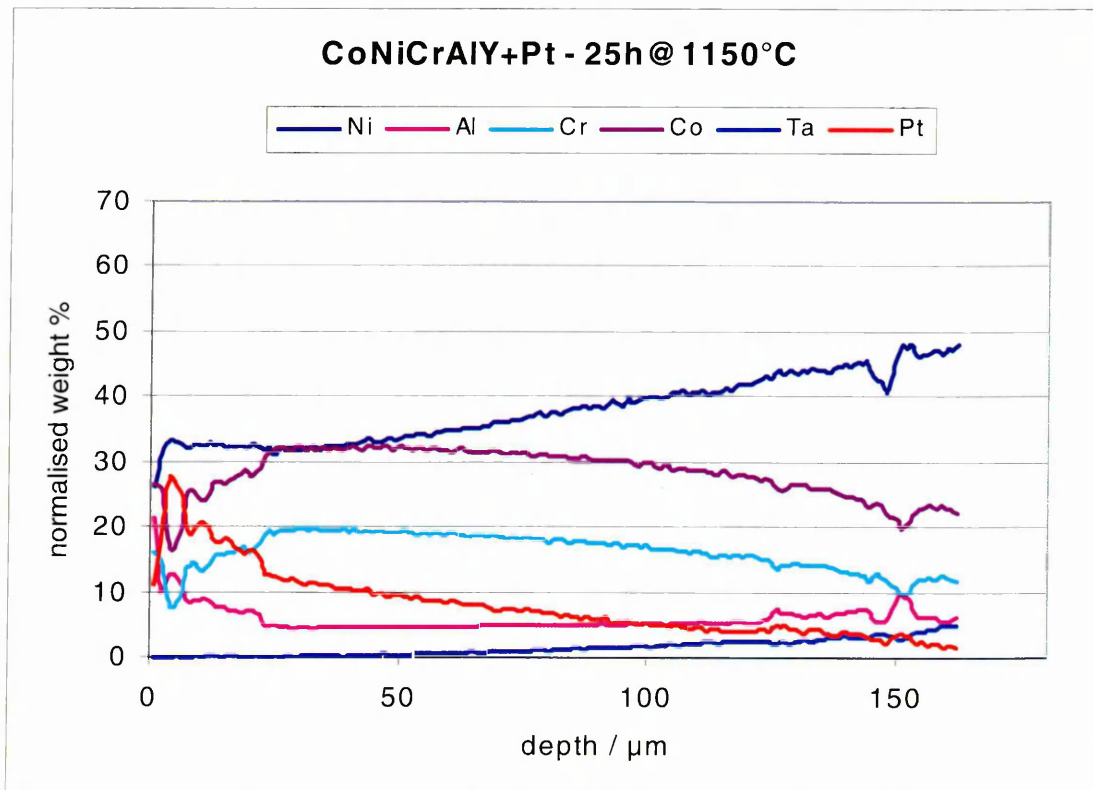
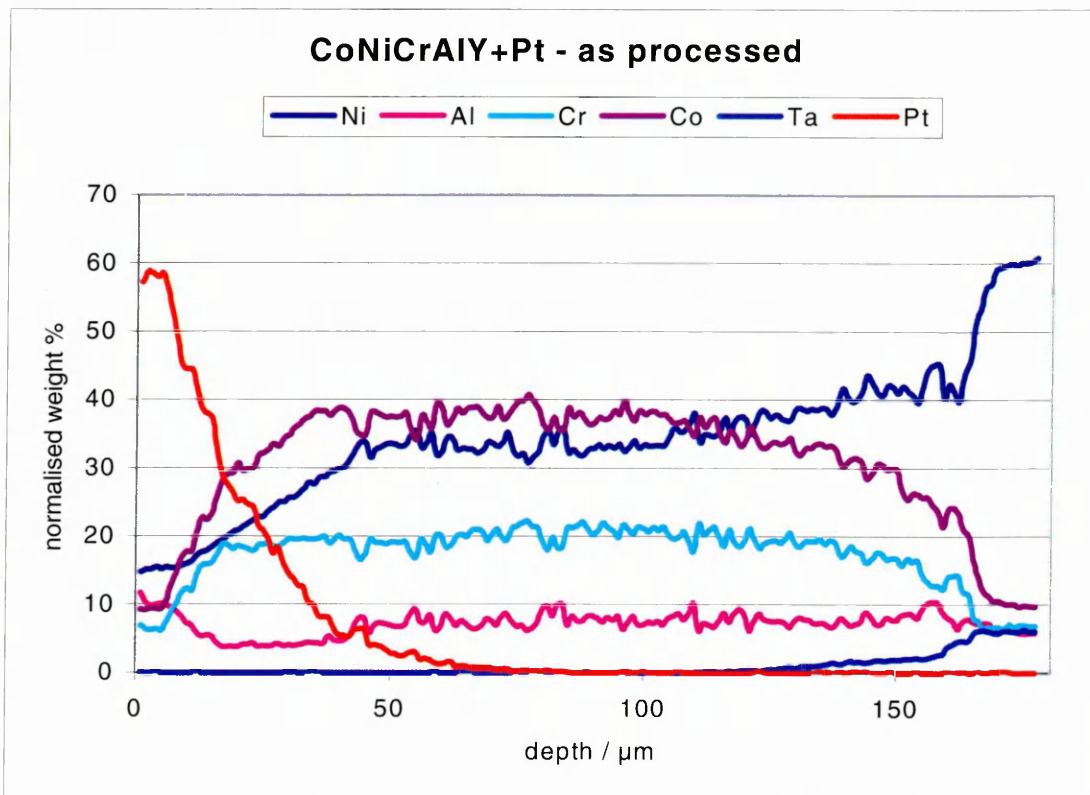


Figure 5.5: WDS ladder scans of the MCrAlY+Pt system

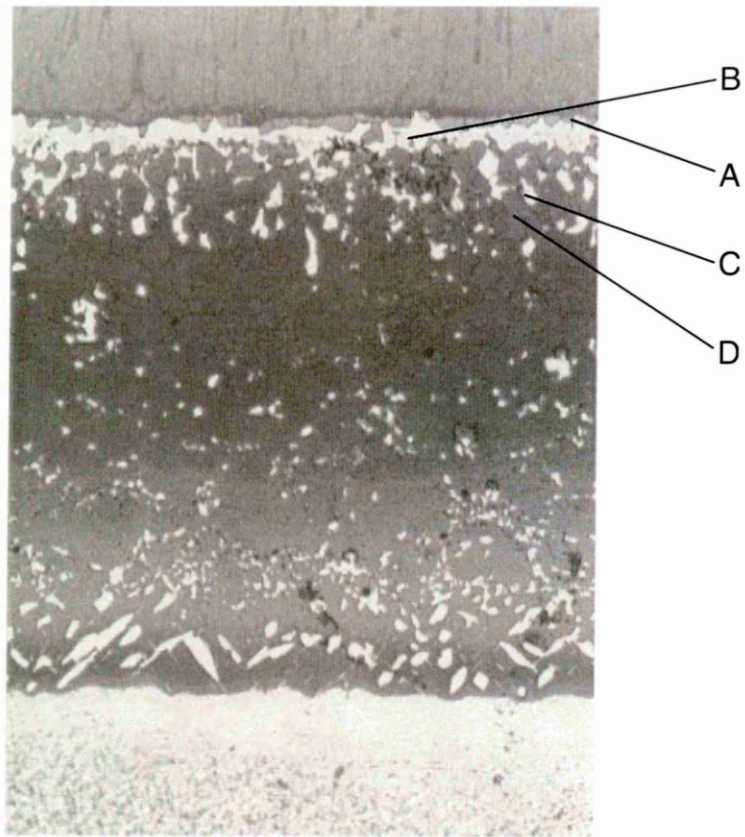


Figure 5.6: BSE image of the MCrAlY+Pt system

<b>Element</b>	<b>atom %</b>	<b>norm wt %</b>
Pt	21	53
Al	34	12
Ni	26	20
Co	11	9
Cr	7	5
Ta	0.25	0.6
Ti	0	0
W	0	0
Re	0	0
Y	0	0

Figure 5.7: Composition of P-phase by WDS analysis

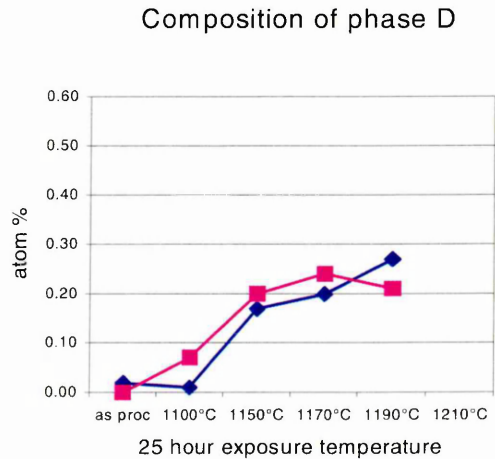
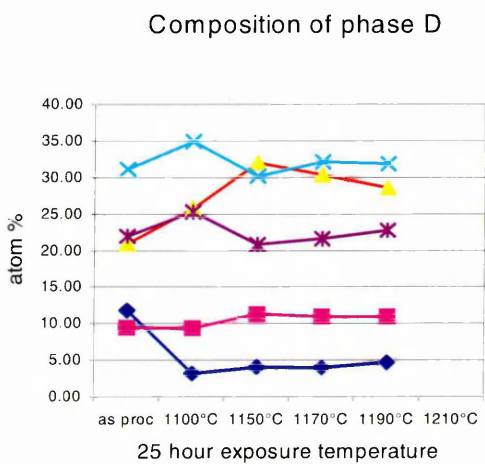
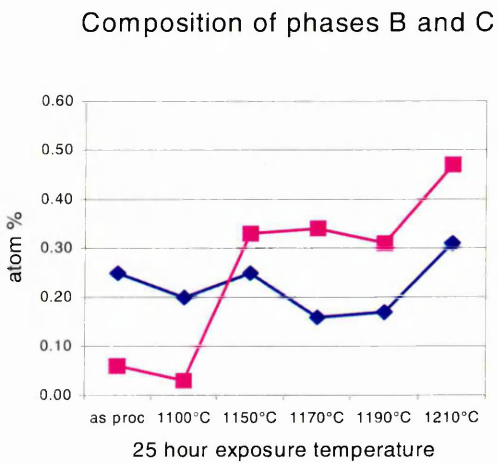
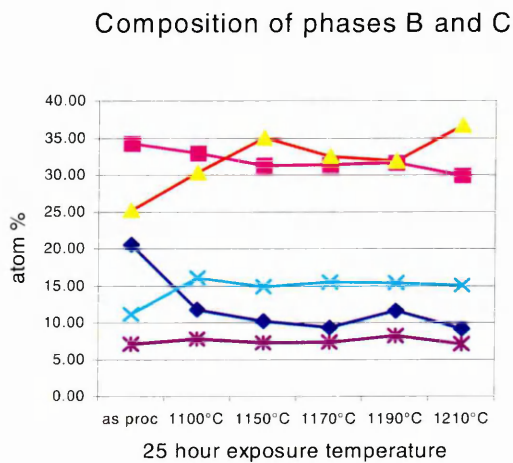
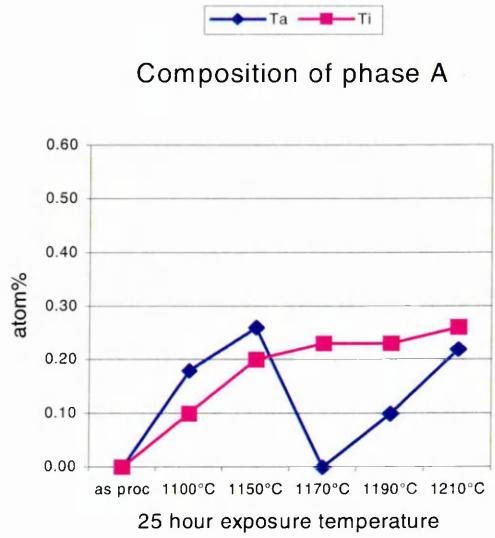
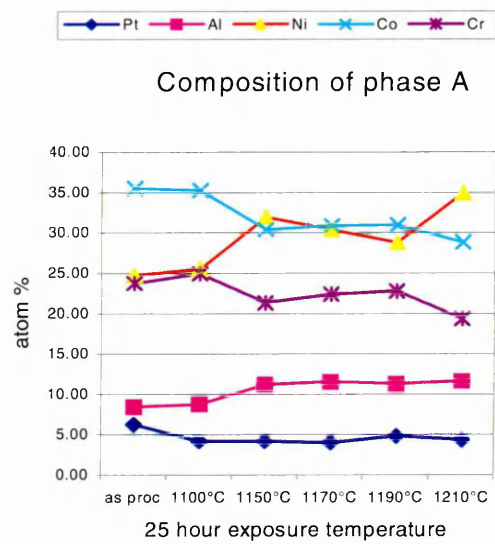


Figure 5.8: WDS analysis showing how the compositions of the phases identified in Figure 5.7 vary on exposure to temperature

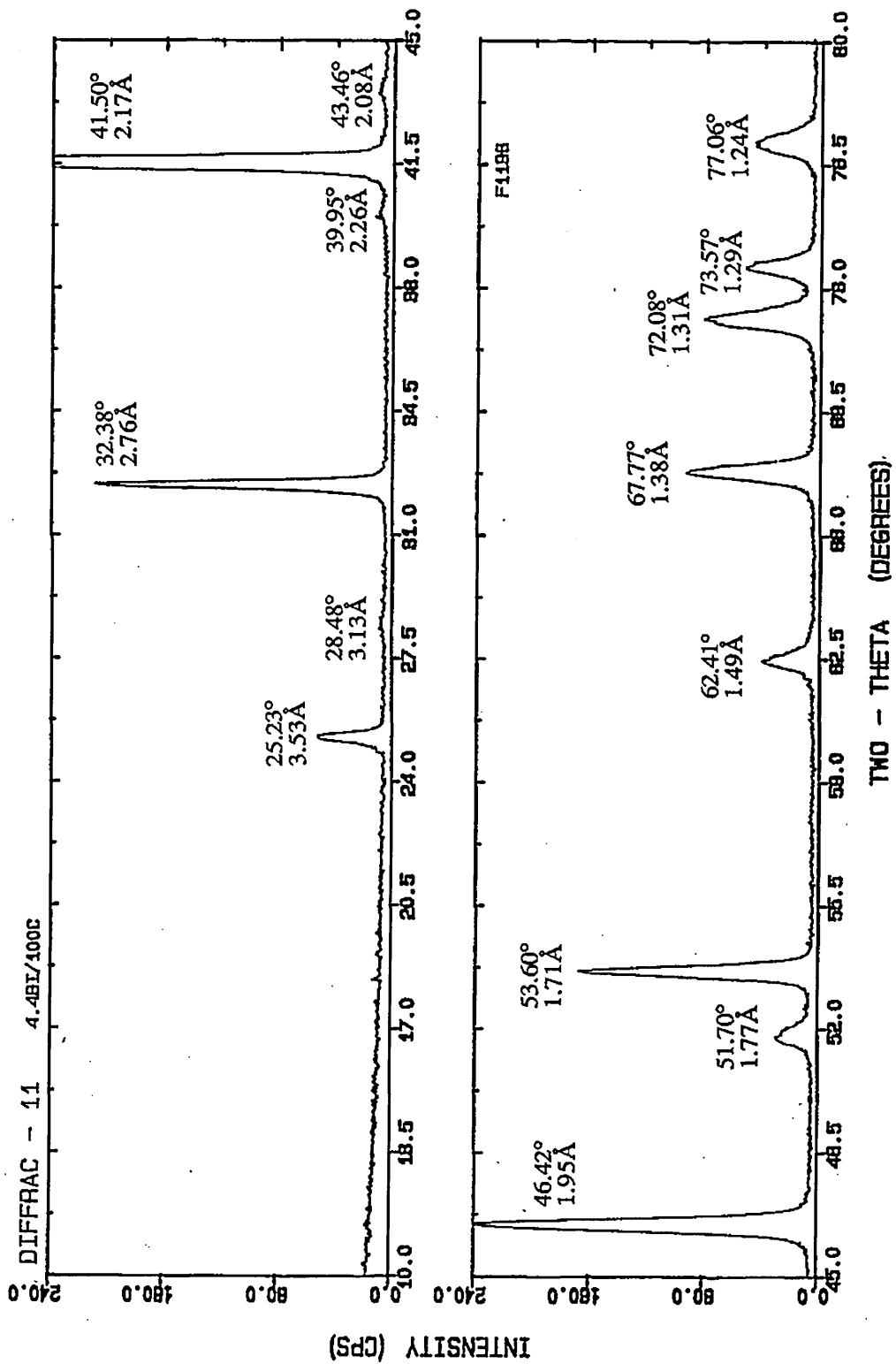


Figure 5.9: XRD analysis of MCrAlY+Pt in the as processed condition

<b>Bragg Angle (<math>^{\circ}2\theta</math>)</b>	<b>Interplanar spacing d (<math>\text{\AA}</math>)</b>	<b>Relative Intensity</b>
25.23	3.53	8
28.48	3.13	2
32.38	2.76	34
39.95	2.26	2
41.50	2.17	100
43.46	2.08	2
46.42	1.95	40
51.70	1.77	4
53.60	1.71	27
62.41	1.49	6
67.77	1.38	15
72.08	1.31	13
73.57	1.29	8
77.06	1.24	7
82.68	1.17	19

Figure 5.10: Table of  $2\theta$ ,  $\text{\AA}$ , intensity from XRD data for P-phase

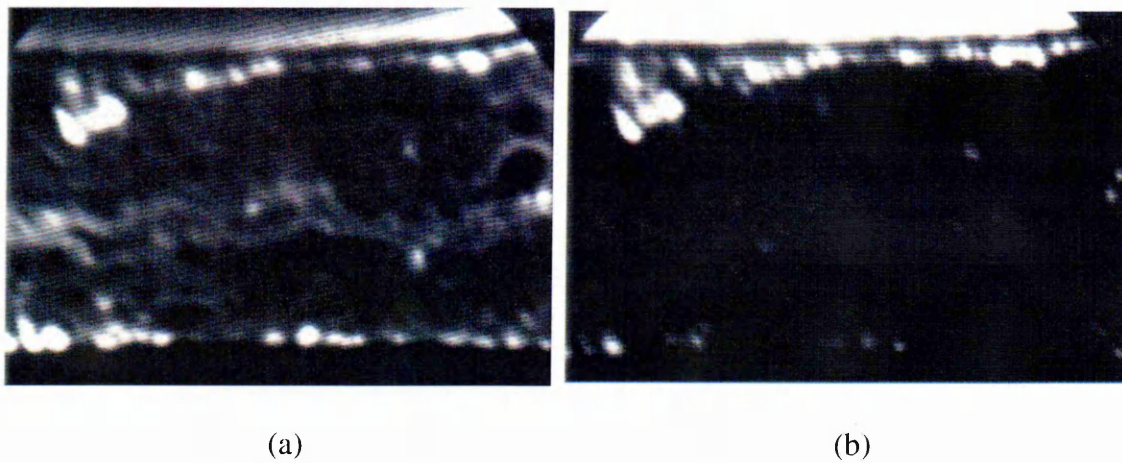
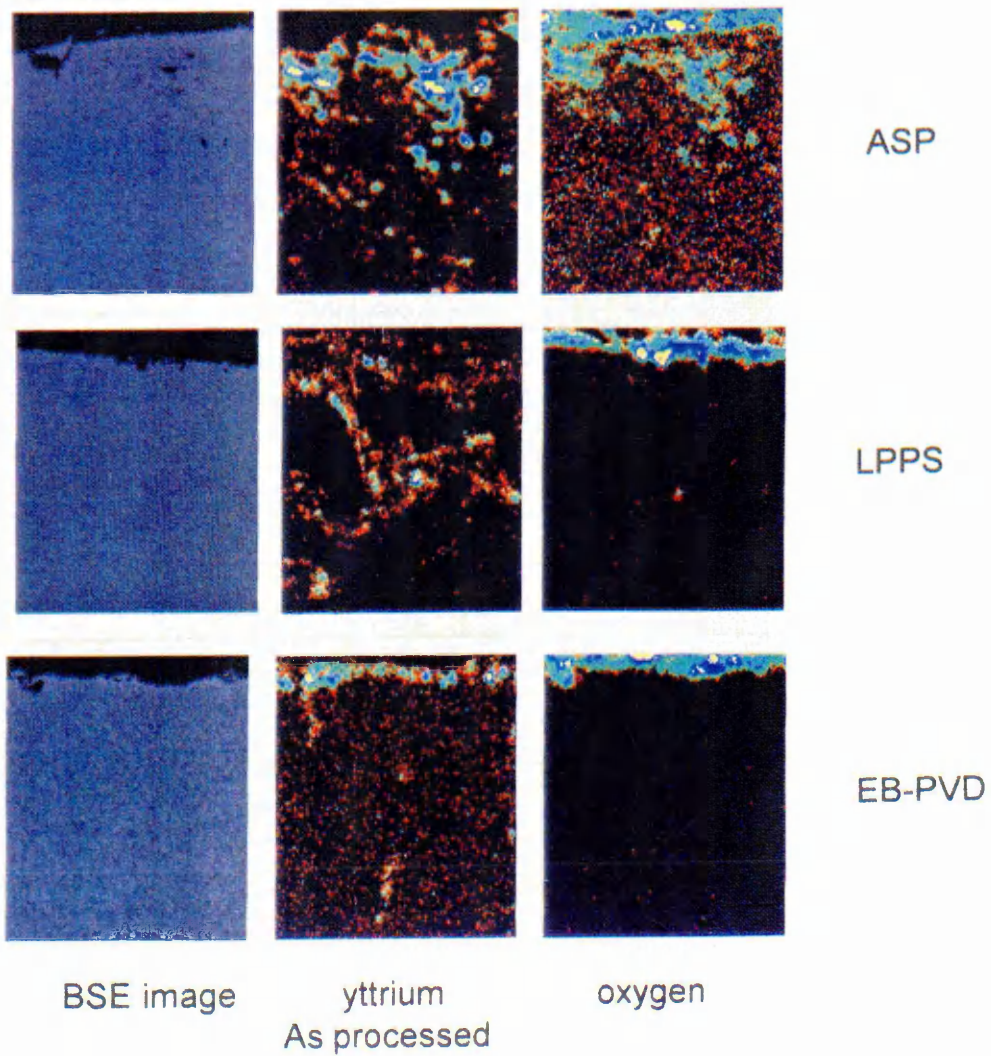


Figure 5.11: SIMS images of the CoNiCrAlY+Pt coating system

- (a)  $Y_{(\text{metal})}$  distribution –  $O^+$  primary beam
- (b)  $Y_2O_3$  distribution –  $Ar^+$  primary beam



yttrium maps after 100h @ 1100°C

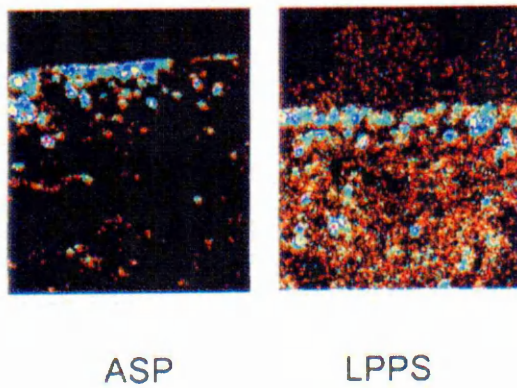


Figure 5.12: Colour enhanced WDS maps of yttrium and oxygen in three standards of MCrAlY

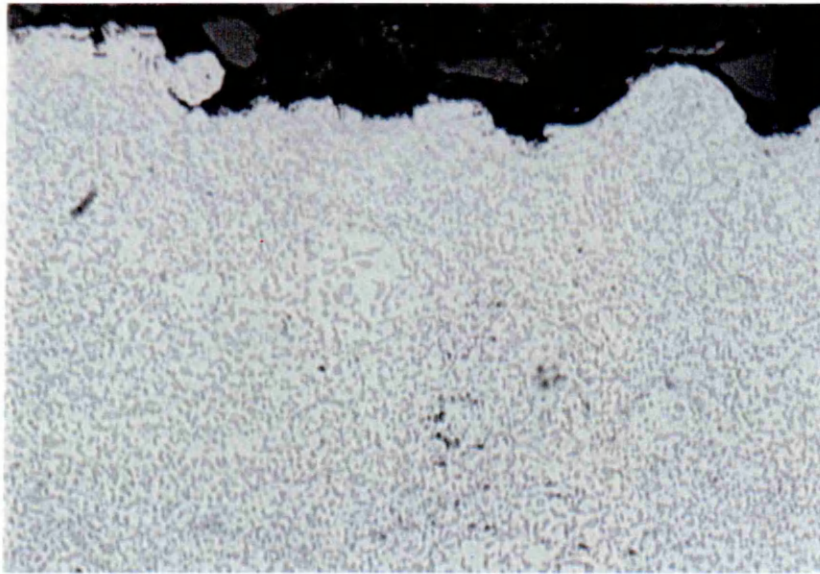


Figure 6.1: Typical as-sprayed MCrAlY surface finish

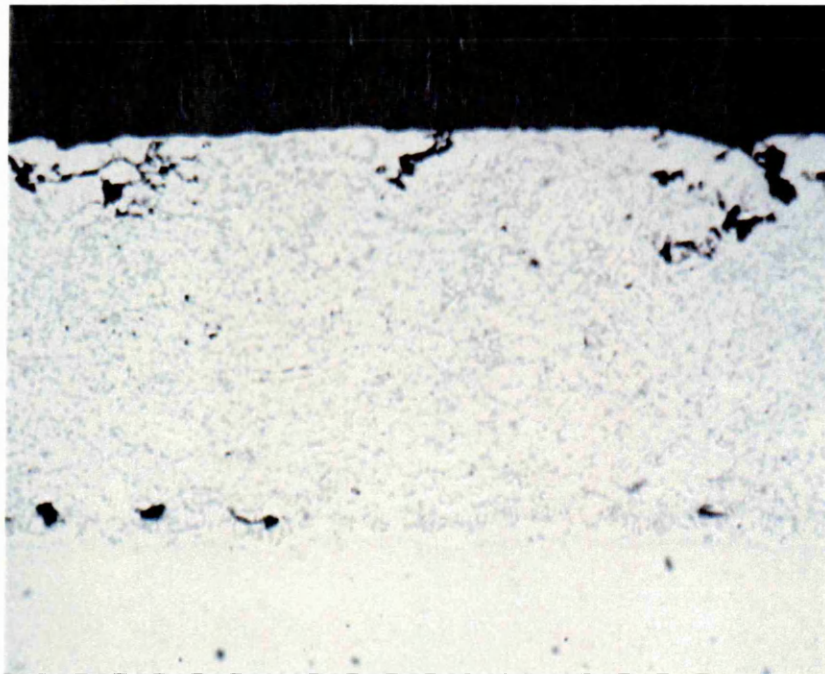


Figure 6.2: Fully processed MCrAlY(RT122) showing detail of surface "rag" entrapped due to peening

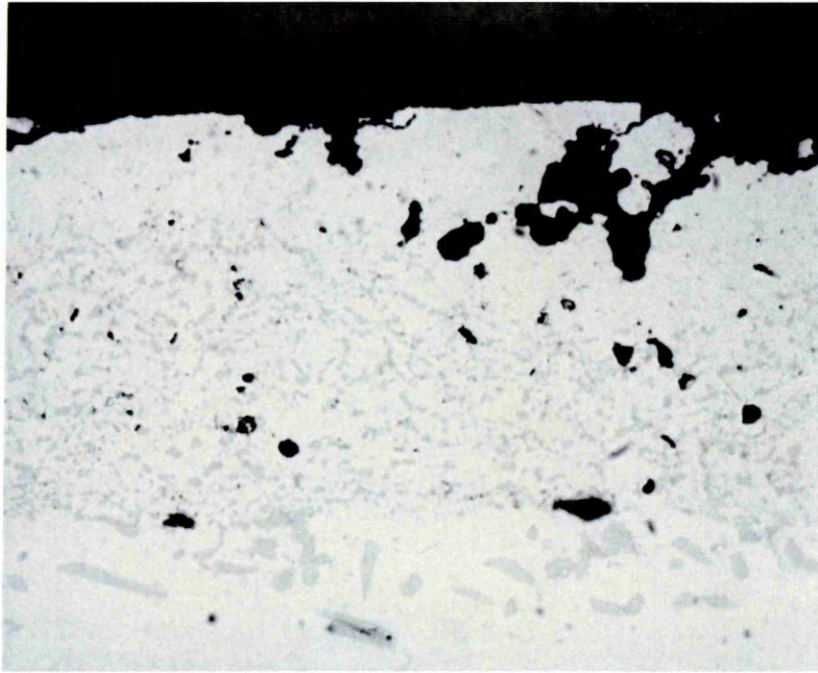
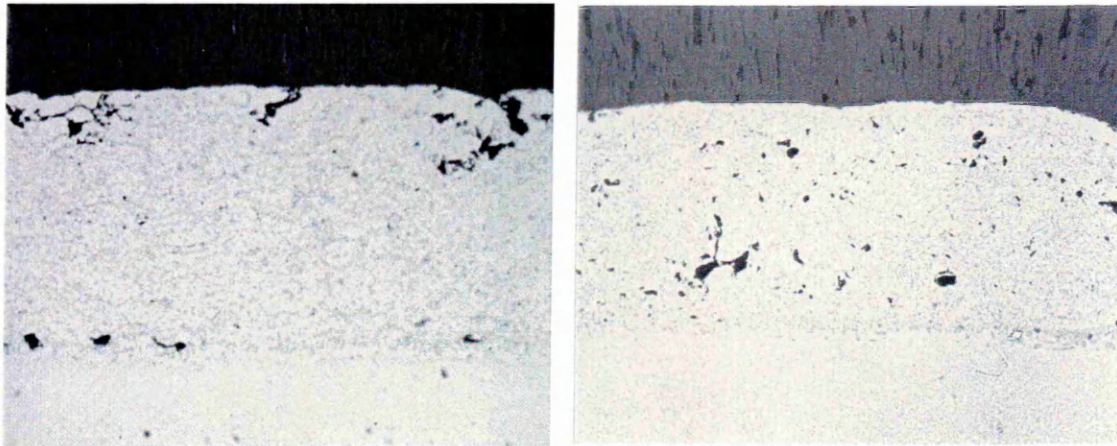


Figure 6.3: Indication of the effect of oxidation around surface rag on the remnant aluminium content of the coating



(a)

(b)

Figure 6.4: Comparison of 10A peened (a) and polished (b) MCrAlY (RT122) microstructures

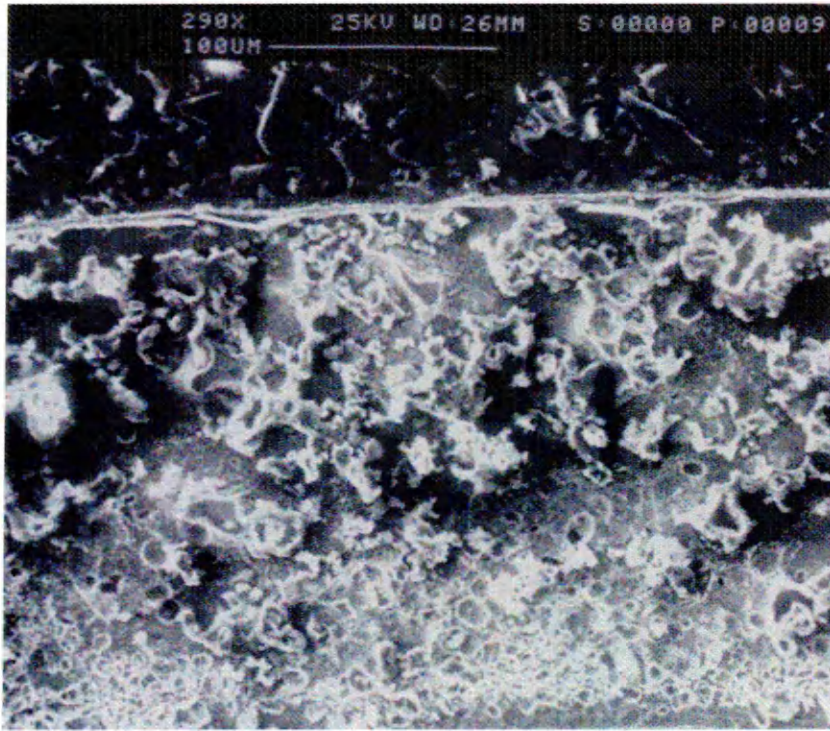


Figure 6.5: SEM image of a sample deeply etched in Br/CH<sub>2</sub>OH showing surface connected oxide (high relief)

<b>Peening Media</b>	<b>Intensity</b>	<b>Coverage</b>
ceramic bead	14 – 18A	400%
ceramic bead	10 – 12A	400%
ceramic bead	4 – 6A	400%
stainless steel cut wire	10 – 12A	400%
stainless steel shot	6 – 8A	100%
wet glass bead	8 – 12N	200%
wet glass bead	6 – 8A	200%

Figure 6.6: Peening media, intensities and coverage used during the initial peening trials

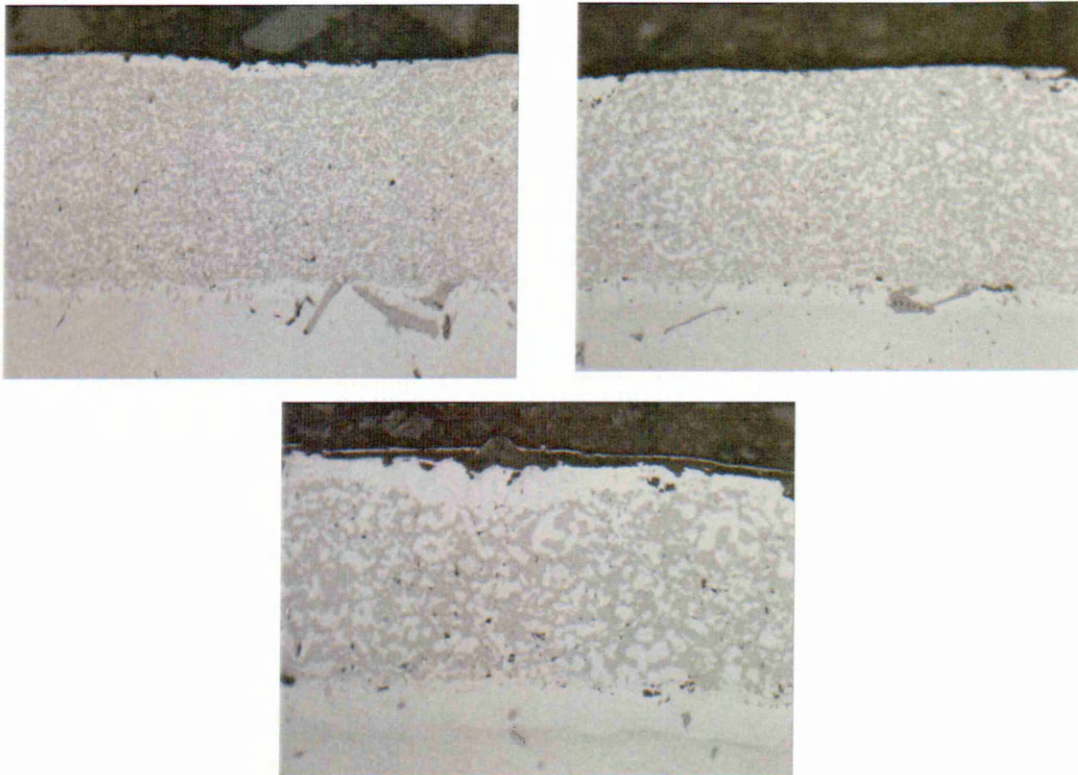


Figure 6.7: Comparison of the microstructures of the MCrAlY used for the peening trials

- (a) As processed and 15A peened
- (b) As processed , 15A peened and heat treated
- (c) 15A peened, heat treated and aged

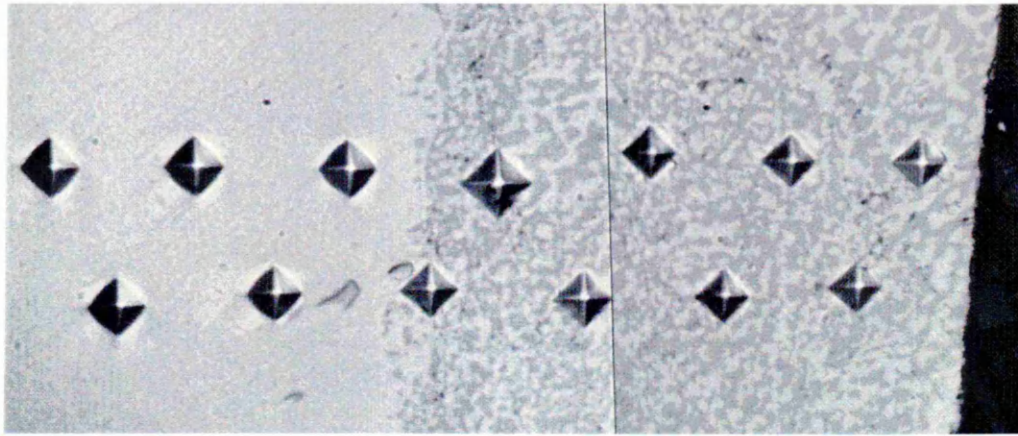


Figure 6.8: Idealised micro-hardness analysis through the thickness of the MCrAlY (PWA 286) coating

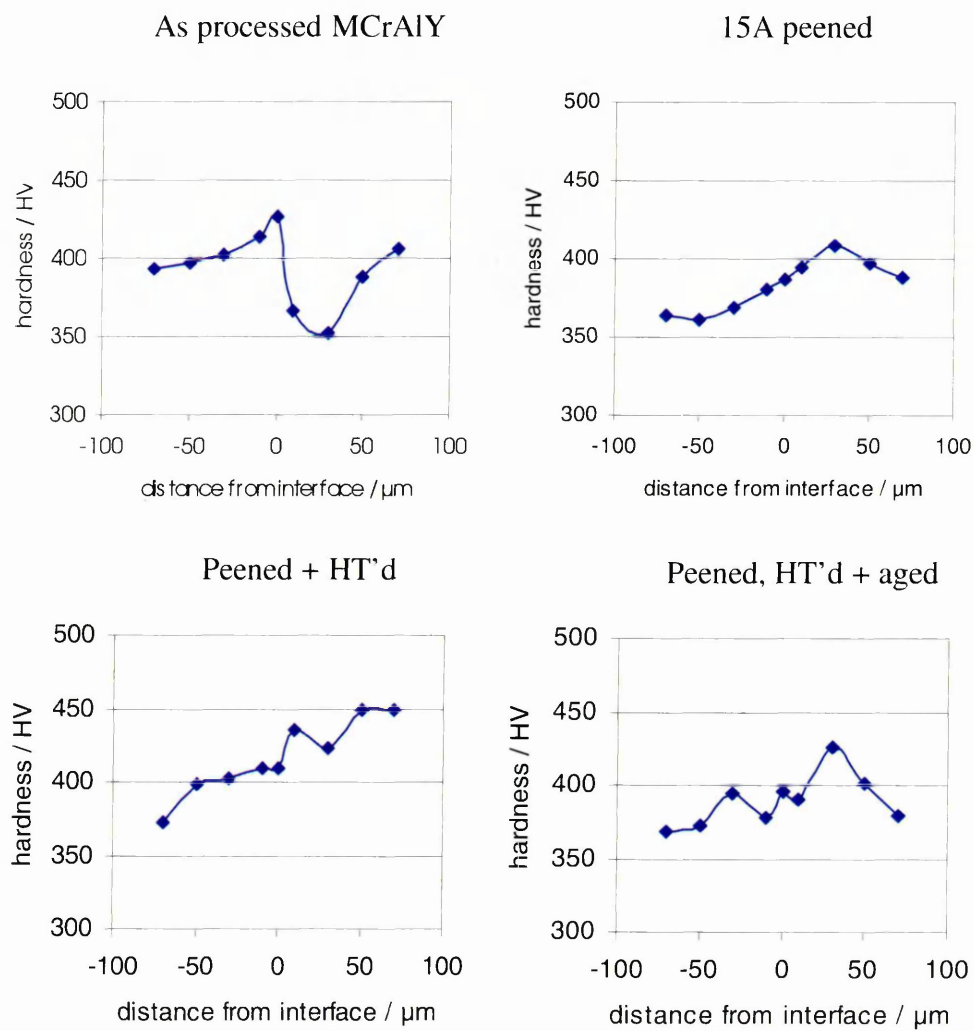


Figure 6.9: Micro hardness profiles demonstrating the effect of processing on an MCrAlY coating

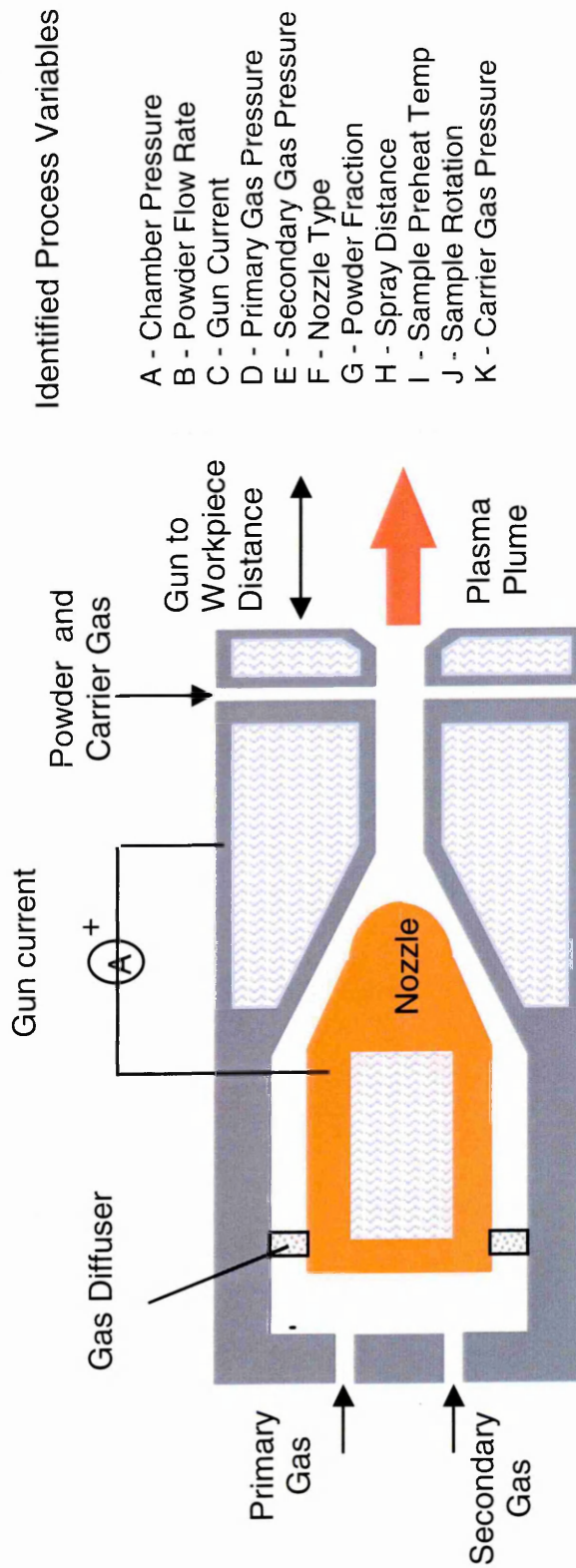


Figure 6.10: Schematic of an LPPS system and associated variable parameters

$L_{12}$	A	B	C	D	E	F	G	H	I	J	K
1	1	1	1	1	1	2	1	1	1	1	1
2	1	1	1	1	1	1	2	2	2	2	2
3	1	1	2	2	2	2	1	1	2	2	2
4	1	2	1	2	2	2	2	2	1	1	2
5	1	2	2	1	2	1	1	2	1	2	1
6	1	2	2	2	1	1	2	1	2	1	1
7	2	1	2	2	1	2	2	2	1	2	1
8	2	1	2	1	2	1	2	1	1	1	2
9	2	1	1	2	2	1	1	2	2	1	1
10	2	2	2	2	1	2	1	2	2	1	2
11	2	2	1	1	1	1	1	1	1	2	2
12	2	2	1	1	2	2	2	1	2	2	1

Figure 6.11:  $L_{12}(2^{11})$  orthogonal array (1 = low setting, 2 = high setting)

$L_8$	A	B	C (AxB)	D	E (AxD)	F (AxD) (BxD)	G
1	1	1	1	1	1	1	1
2	1	1	1	2	2	2	2
3	1	2	2	1	1	2	2
4	1	2	2	2	2	1	1
5	2	1	2	1	2	1	2
6	2	1	2	2	1	2	1
7	2	2	1	1	2	2	1
8	2	2	1	2	1	1	2

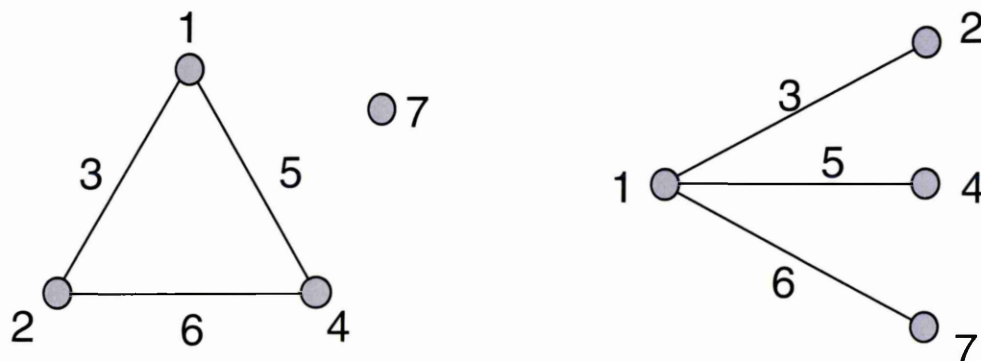


Figure 6.12:  $L_8(2^7)$  orthogonal array and linear graphs

<b>L<sub>8</sub></b>	<b>B</b> powder feed	<b>K</b> carrier gas pressure	<b>BK</b>	<b>C</b> gun current	<b>BC</b>	<b>BI</b> or <b>KC</b>	<b>I</b> sample pre-heat
<b>1</b>	10	100		1100			low
<b>2</b>	10	100		1500			high
<b>3</b>	10	140		1100			high
<b>4</b>	10	140		1500			low
<b>5</b>	30	100		1100			high
<b>6</b>	30	100		1500			low
<b>7</b>	30	140		1100			low
<b>8</b>	30	140		1500			high

Figure 6.13: L<sub>8</sub> (2<sup>7</sup>) orthogonal array showing factor levels and location of interacting factors

	<b>B</b>	<b>C</b>	<b>W</b>	<b>X</b>	<b>Y</b>	<b>Z</b>	<b>A</b>	<b>D</b>	<b>E</b>	<b>I</b>	<b>K</b>	<b>P</b>	<b>Q</b>
<b>1</b>	1	1	1	1	1	1	1	1	1	1	1	1	1
<b>2</b>	1	1	1	1	1	2	2	2	2	2	2	2	2
<b>3</b>	1	2	2	2	2	1	1	1	1	2	2	2	2
<b>4</b>	1	2	2	2	2	2	2	2	2	1	1	1	1
<b>5</b>	2	1	1	2	2	1	1	2	2	1	1	2	2
<b>6</b>	2	1	1	2	2	2	2	1	1	2	2	1	1
<b>7</b>	2	2	2	1	1	1	1	2	2	2	2	1	1
<b>8</b>	2	2	2	1	1	2	2	1	1	1	1	2	2
<b>9</b>	3	1	2	1	2	1	2	1	2	1	2	1	2
<b>10</b>	3	1	2	1	2	2	1	2	1	2	1	2	1
<b>11</b>	3	2	1	2	1	1	2	1	2	2	1	2	1
<b>12</b>	3	2	1	2	1	2	1	2	1	1	2	1	2
<b>13</b>	4	1	2	2	1	1	2	2	1	1	2	2	1
<b>14</b>	4	1	2	2	1	2	1	1	2	2	1	1	2
<b>15</b>	4	2	1	1	2	1	2	2	1	2	1	1	2
<b>16</b>	4	2	1	1	2	2	1	1	2	1	2	2	1

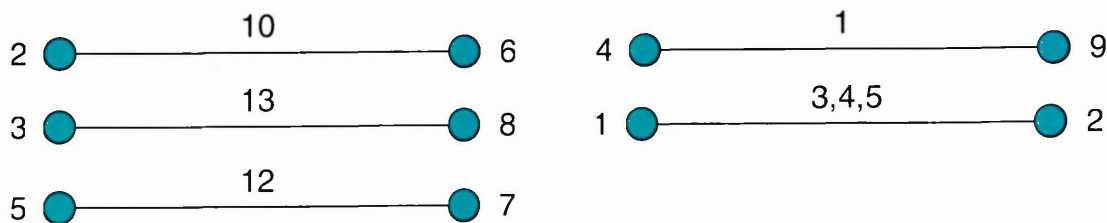
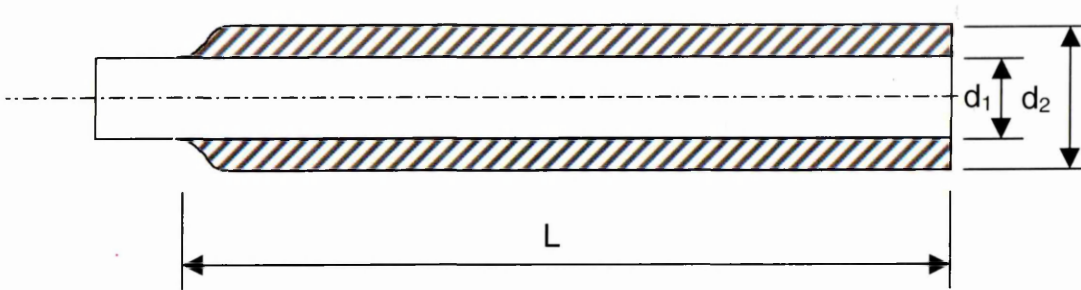


Figure 6.14:  $L_{16}$  (b)  $4/2$  mixed level array and linear graphs



$$\rho_{\text{coating}} = [L\pi/4(d_2^2 - d_1^2)]^{-1} \cdot mg$$

Figure 6.15: Schematic of coated testpiece and coating density calculation

Factor	chamber pressure mmHg A	powder flow rate g/min B	gun current A C	argon flow rate scfh D	helium flow rate scfh E	nozzle type F	powder fraction (size) G	spray distance inches H	preheat temp. I	sample rotation rpm J	carrier gas pressure psi K
9	50	10	1250	300	196	93	1	14	high	25	100
11	50	30	1250	300	132	93	1	10	low	50	130
5	20	30	1500	145	196	93	1	14	low	50	100
2	20	10	1250	145	132	93	1A	14	high	50	130
8	50	10	1500	145	196	93	1A	10	low	25	130
6	20	30	1500	300	132	93	1A	10	high	25	100
4	20	30	1250	300	196	141	1A	14	low	25	130
7	50	10	1500	300	132	141	1A	14	low	50	100
12	50	30	1250	145	196	141	1A	10	high	50	100
3	20	10	1500	300	196	141	1	10	high	50	130
1	20	10	1250	145	132	141	1	10	low	25	100
10	50	30	1500	145	132	141	1	14	high	25	130

Figure 6.16:  $L_{12}$  array showing the order of experiments and factor levels

<b>Trial number</b>	<b>A</b>	<b>B</b>	<b>C</b>
<b>1</b>	1	1	1
<b>2</b>	1	2	2
<b>3</b>	2	1	2
<b>4</b>	2	2	1

Figure 6.17:  $L_4(2^3)$  array

Trial Number	AVERAGE RESPONSES		
	surface finish / Ra	density / kgm <sup>-3</sup>	β-depletion / μm
1/13	34.5	6.654	63.125
2/14	32.0	6.989	50.625
3/15	39.0	6.510	23.750
4/16	37.0	6.643	208.750
5/17	54.5	6.904	20.000
6/18	47.5	7.362	15.000
7/19	36.5	6.482	36.250
8/20	34.5	6.954	21.875
9/21	41.5	6.661	33.125
10/22	52.5	6.956	39.375
11/23	68.0	6.799	100.000
12/24	52.5	6.965	69.375

Factor		AVERAGE EFFECTS		
		surface finish / Ra	density / kgm <sup>-3</sup>	β-depletion / μm
A	1	40.8	6.844	65.2
	2	47.6	6.803	50.0
B	1	36.3	6.708	38.1
	2	52.0	6.938	75.4
C	1	44.2	6.785	87.5
	2	44.1	6.861	30.5
D	1	43.4	6.904	44.1
	2	44.9	6.743	69.5
E	1	45.2	6.874	50.7
	2	43.2	6.773	62.8
F	1	46.3	6.945	40.1
	2	42.0	6.702	73.4
G	1	48.3	6.747	46.6
	2	40.0	6.899	67.0
H	1	46.0	6.874	48.9
	2	42.3	6.772	64.7
I	1	44.2	6.739	75.0
	2	44.2	6.907	38.5
J	1	41.2	6.872	63.5
	2	47.1	6.775	50.0
K	1	44.5	6.838	39.5
	2	41.2	6.808	74.1

Figure 6.18: Measured responses and calculated average effects for the L<sub>12</sub> array

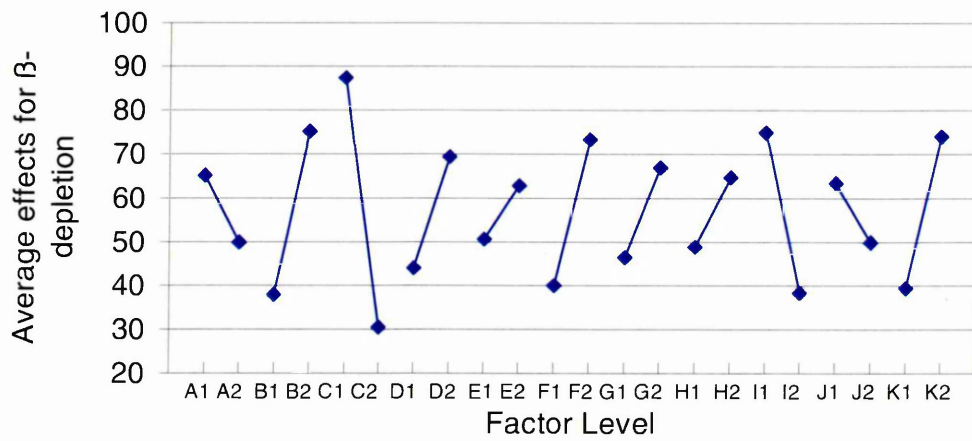
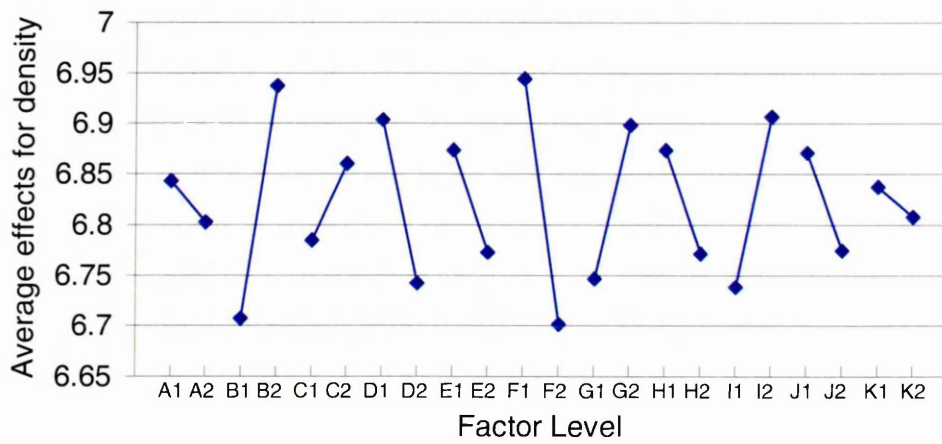
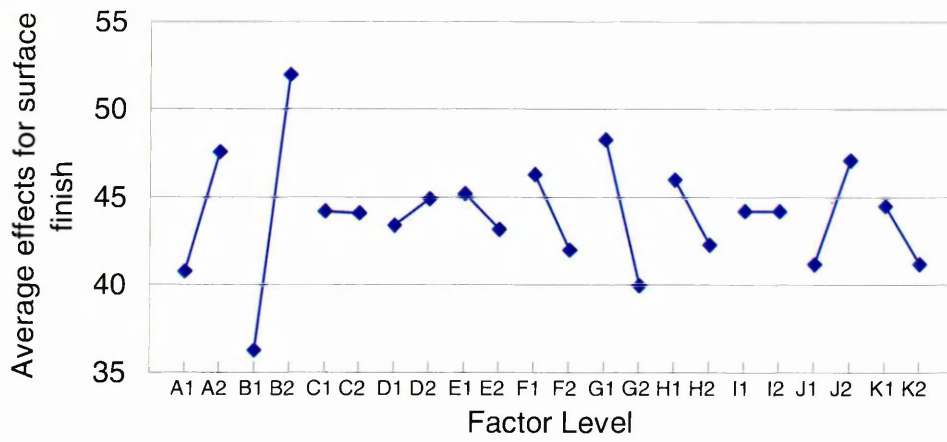


Figure 6.19(a),(b),(c): Average response graphs for phase 1 of the Taguchi design for density, surface roughness and  $\beta$ -depletion

	A	B	C	D	E	F	G	H	I	J	K
surface finish	1	1	2	1	2	2	2	2	1/2	1	2
density	1	2	2	1	1	1	2	1	2	1	1
$\beta$ -depletion	2	1	2	1	1	1	1	1	2	2	1

Figure 6.20: Table showing the optimal parameters for each response according to the results from phase 1

Trial Number	AVERAGE RESPONSE	
	$\beta$ -depletion / $\mu\text{m}$	sprayability
1/9	55.0	6.5
2/10	32.0	7.5
3/11	48.8	7.0
4/12	23.1	7.5
5/13	415.1	4.8
6/14	19.4	6.5
7/15	608.8	7.5
8/16	20.5	5.2

Factor		AVERAGE EFFECTS	
		$\beta$ -depletion / $\mu\text{m}$	sprayability
A	1	34.7	7.1
	2	266.0	6.0
B	1	128.0	6.3
	2	175.3	6.8
C	1	176.8	6.7
	2	126.6	6.4
D	1	281.9	6.4
	2	24.4	6.7
E	1	35.9	6.3
	2	267.4	6.9
F	1	128.4	6.0
	2	174.9	7.1
G	1	176.6	7.0
	2	126.8	6.1

Figure 6.21: Measured responses and calculated average effects for the  $L_8$  array

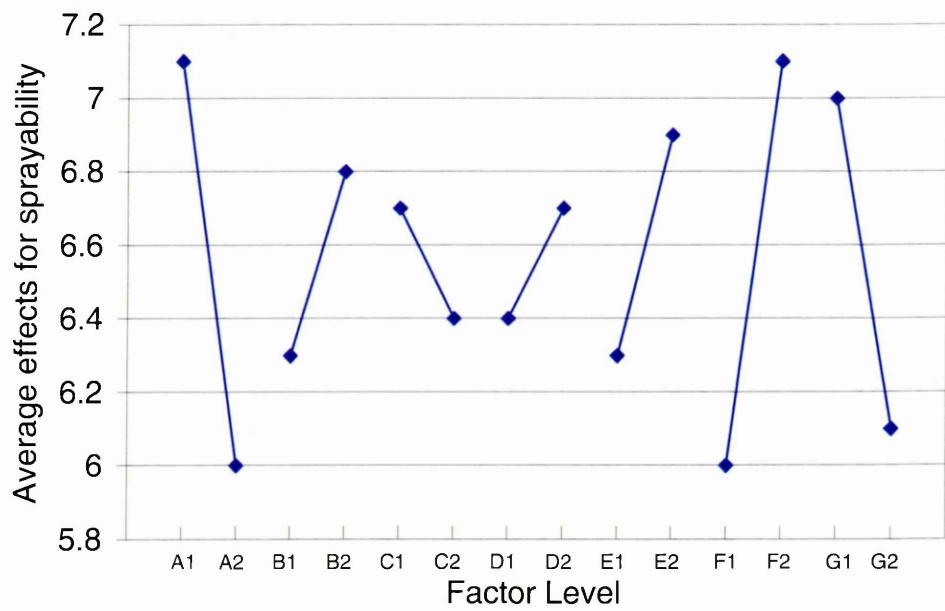
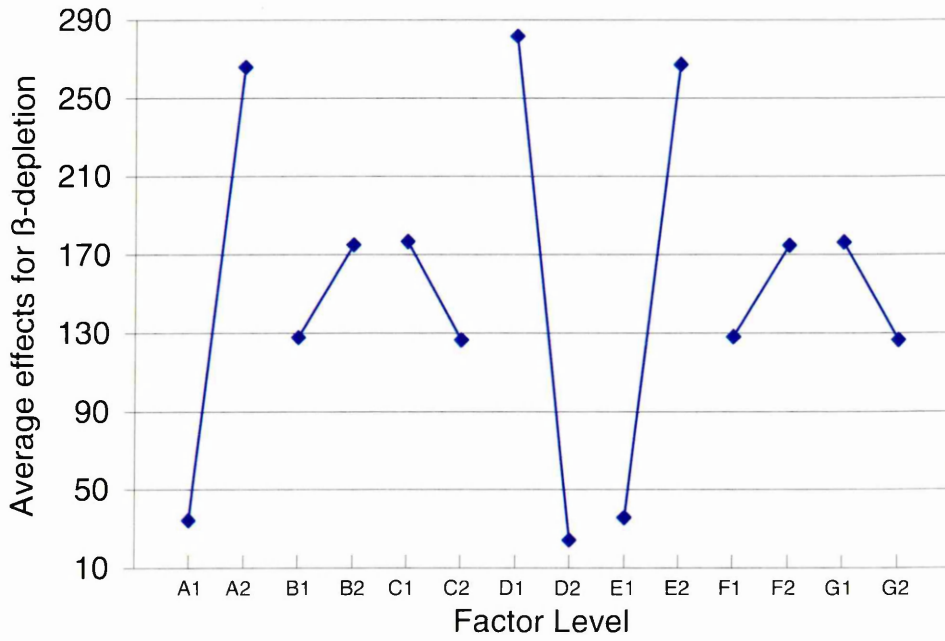


Figure 6.22(a),(b): Average response graphs for  $\beta$ -depletion and sprayability for phase 2 of the Taguchi design

Trial Number	AVERAGE RESPONSE	
	$\beta$ -depletion / $\mu\text{m}$	sprayability
1/17	19.9	9
2/18	17.6	6
3/19	13.0	9
4/20	14.4	7
5/21	13.8	8
6/22	17.7	5
7/23	12.8	10
8/24	13.4	2
9/25	16.9	6
10/26	17.4	8
11/27	12.6	1
12/28	14.4	7
13/29	20.2	3
14/30	14.9	7
15/31	13.6	4
16/32	13.6	8

Factor	AVERAGE EFFECTS		
	$\beta$ -depletion / $\mu\text{m}$	sprayability	
A	1	16.2	7.75
	2	14.4	6.25
	3	15.3	5.50
	4	15.6	5.50
B	1	17.3	6.50
	2	13.5	6.00
C	1	15.4	6.00
	2	15.4	6.50
D	1	15.6	6.62
	2	15.1	5.88
E	1	15.7	5.62
	2	15.0	6.88
F	1	15.4	6.25
	2	15.4	6.25
G	1	15.0	8.25
	2	15.8	4.25
H	1	15.2	5.88
	2	15.5	6.62
I	1	16.2	5.88
	2	14.6	6.62
J	1	15.8	6.25
	2	15.0	6.25
K	1	15.0	5.75
	2	15.8	6.75
L	1	15.6	5.88
	2	15.2	6.62
M	1	16.0	6.38
	2	14.7	6.12

Figure 6.23: Measured responses and calculated average effects for the L<sub>16</sub> array

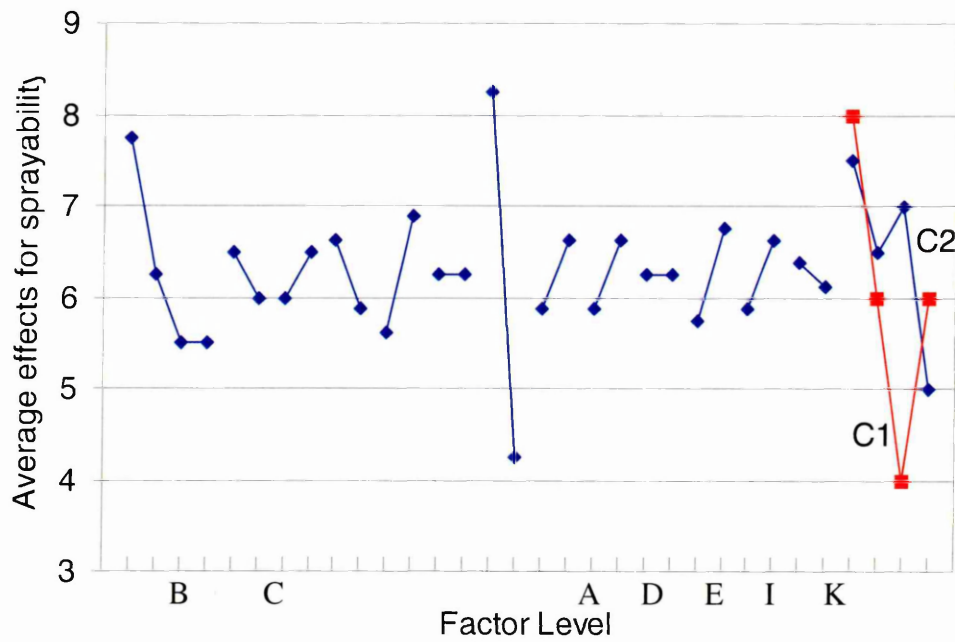
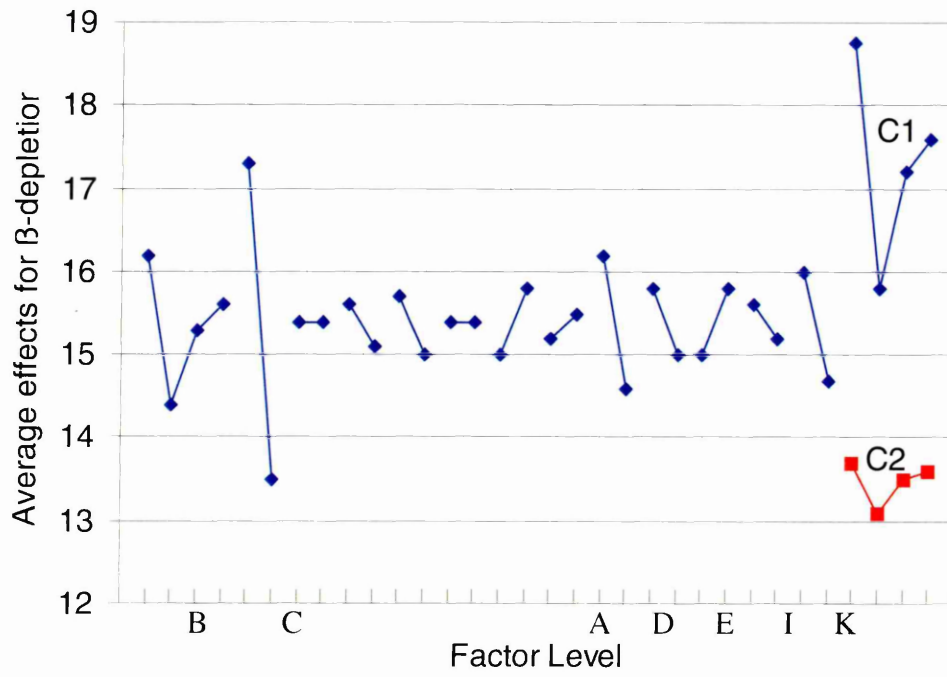


Figure 6.24(a),(b): Average response graphs for the  $L_{16}$  array for  $\beta$ -depletion and sprayability

variable factor	original parameters	optimised for $\beta$ -depletion	optimised for sprayability	compromise parameters
A – chamber pressure mm/Hg	35	35	35	35
B – powder flow rate g/min	20	17	10	17
C – gun current amps	1500	1500	1250	1500
D – primary gas flow rate (Ar) scfh	100	60	80	80
E – secondary gas flow rate (He) scfh	225	225	225	225
F - nozzle type	93	93	93	93
G – powder fraction	1A	1A	1A	1A
H – spray distance inches	13	10	10	10
I – sample preheat	medium	high	high	high
J – sample rotation rpm	25	25	25	25
K – carrier gas pressure (Ar) psi	130	80	100	80

Figure 6.25: Comparison of the optimised and the original LPPS parameters

optimised spraying parameters	A1	B2	C2	D2	E2	F2	G2	H1	I2	J1	K2

Figure 6.26: The optimised parameters taken from the appropriate orthogonal array

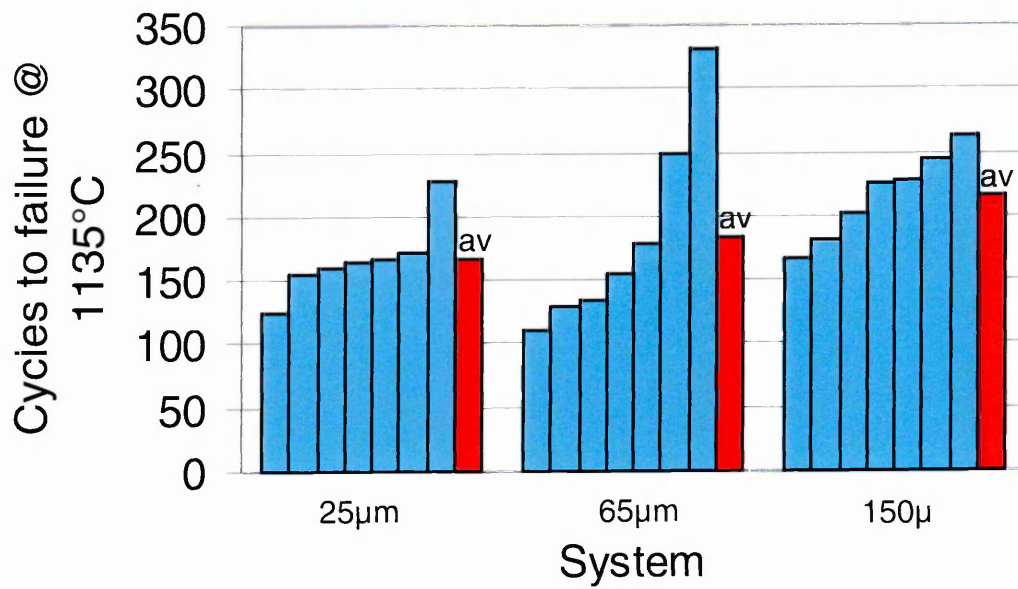


Figure 6.27: Number of cycles to cause spallation of the TBC from different thicknesses of MCrAlY – average result on right

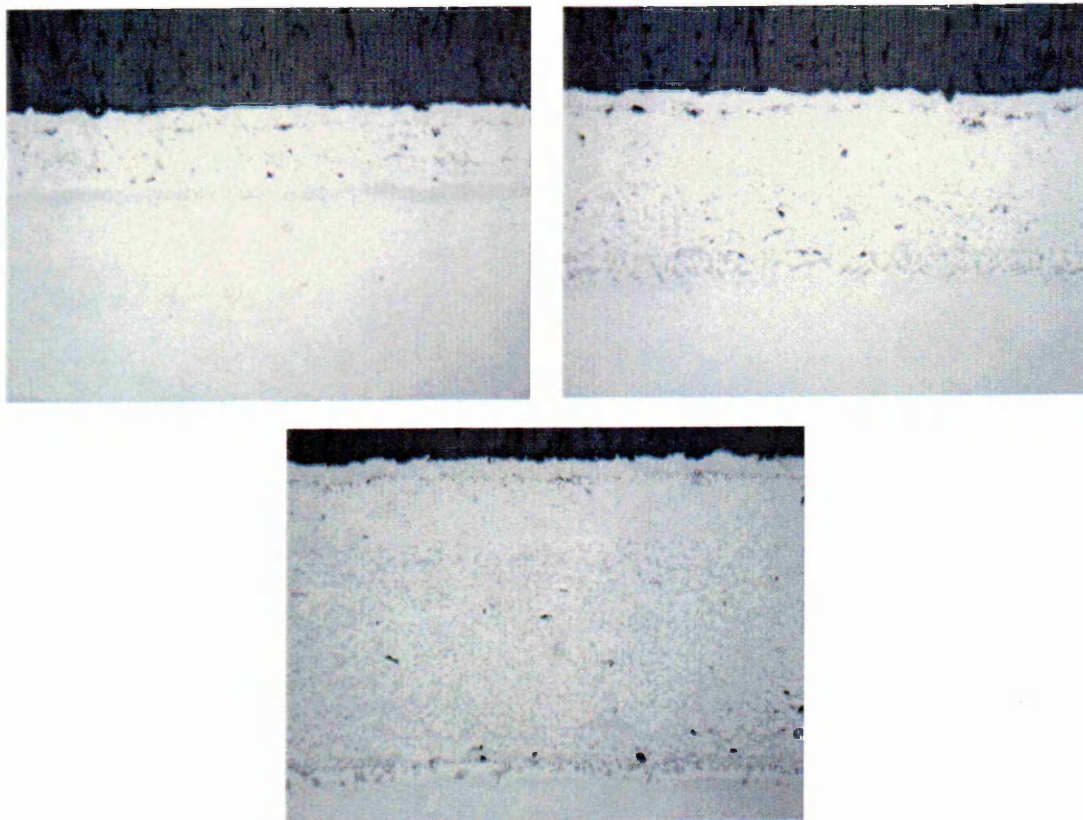


Figure 6.28(a-c): Micrographs of the MCrAlY thickness optimisation trials

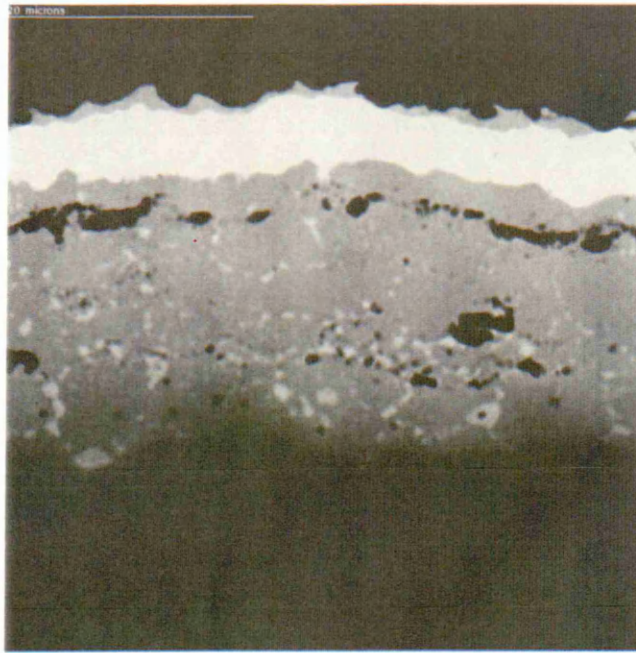


Figure 6.29: Thin MCrAlY +Pt

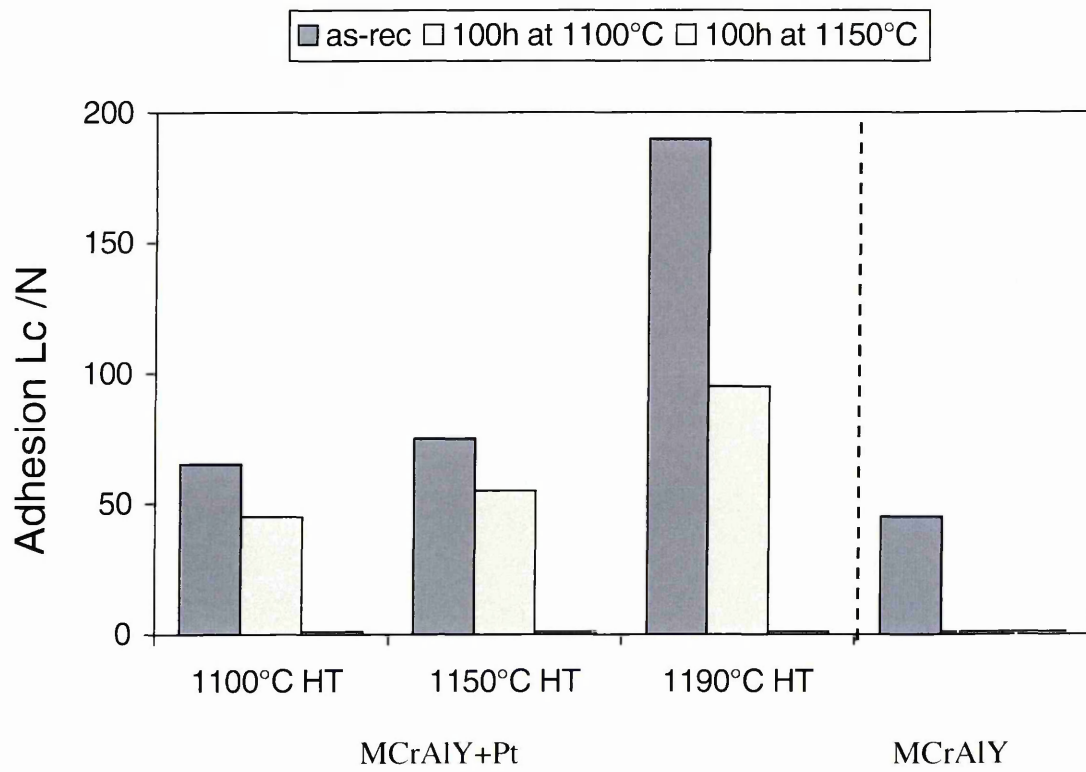


Figure 6.30: Scratch testing results from MCrAlY heat treatment trials

Peening Media	Intensity	Coverage
MI1 10H stainless steel shot	8 - 12N	200%
MI1 10H stainless steel shot	8 - 12N	400%
wet AF glass bead	8 - 12N	200%
wet AF glass bead	8 - 12N	400%

Figure 6.31: Matrix of the peening media, intensities and coverage used in phase 2 of the peening optimisation

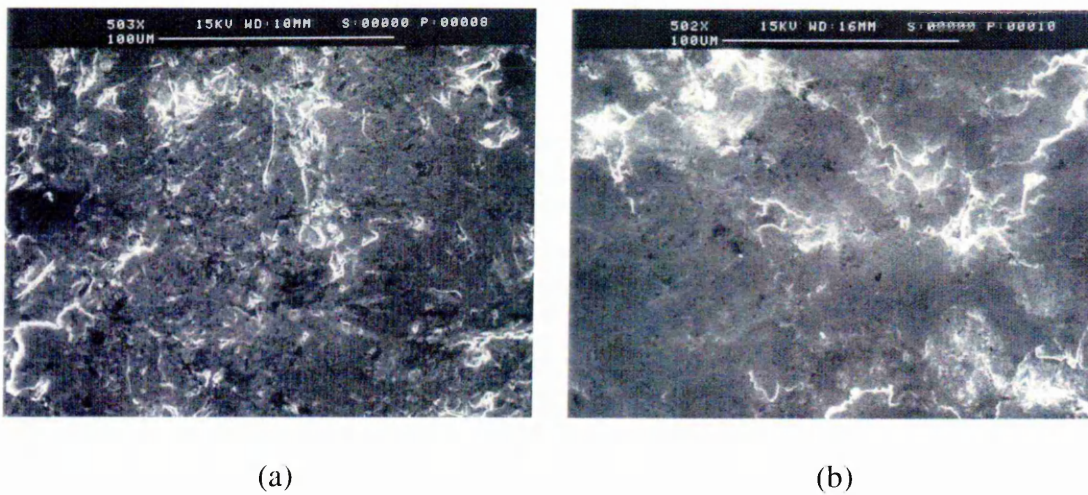


Figure 6.32(a) (b): Comparison of the surface finishes produced by peening with ceramic bead and steel shot respectively

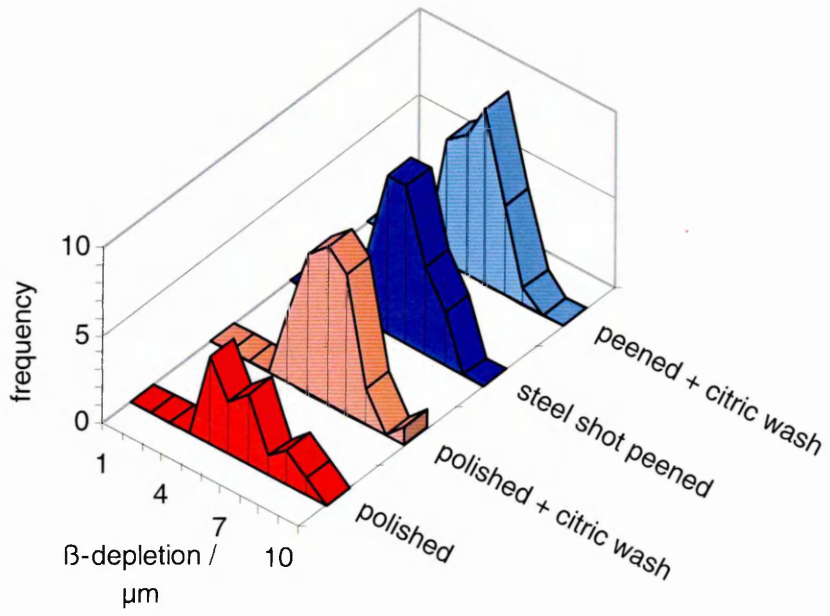


Figure 6.33:  $\beta$ -depletion distribution chart for phase 2 peening trials

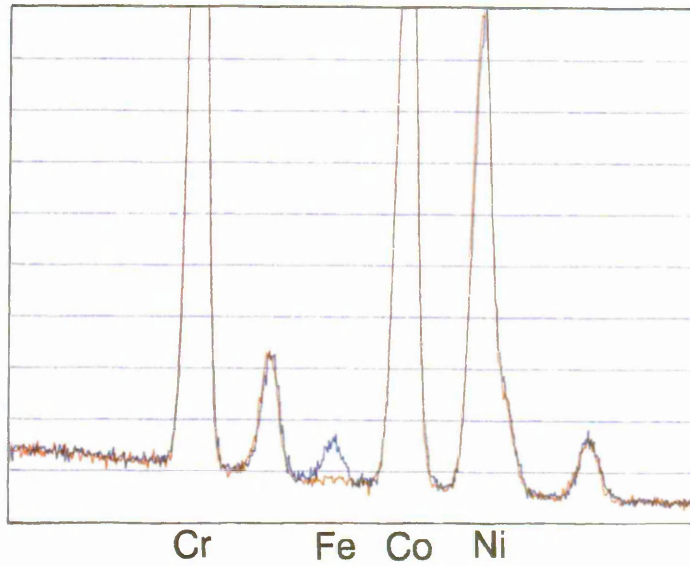


Figure 6.34: Surface EDX analysis showing detail before (blue) and after (red) citric acid washing

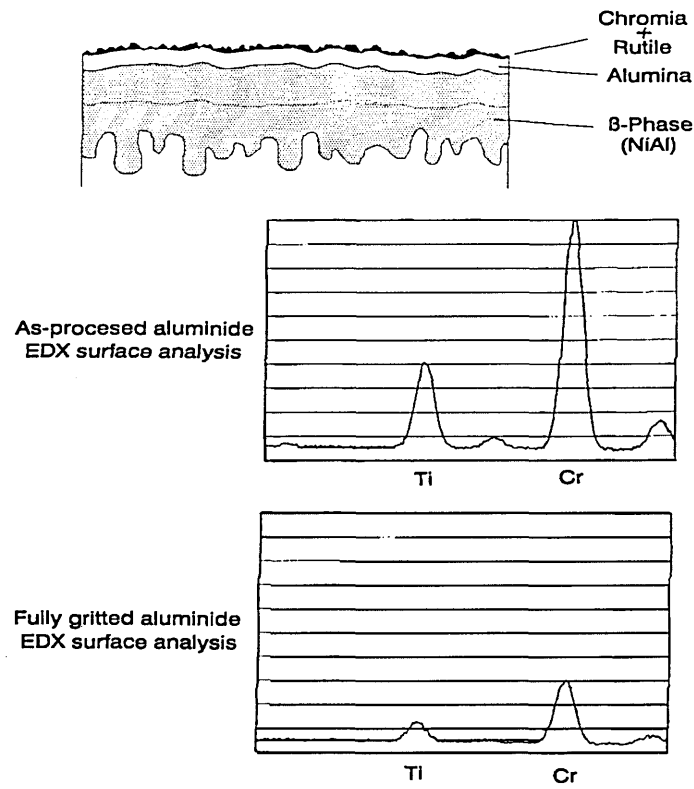
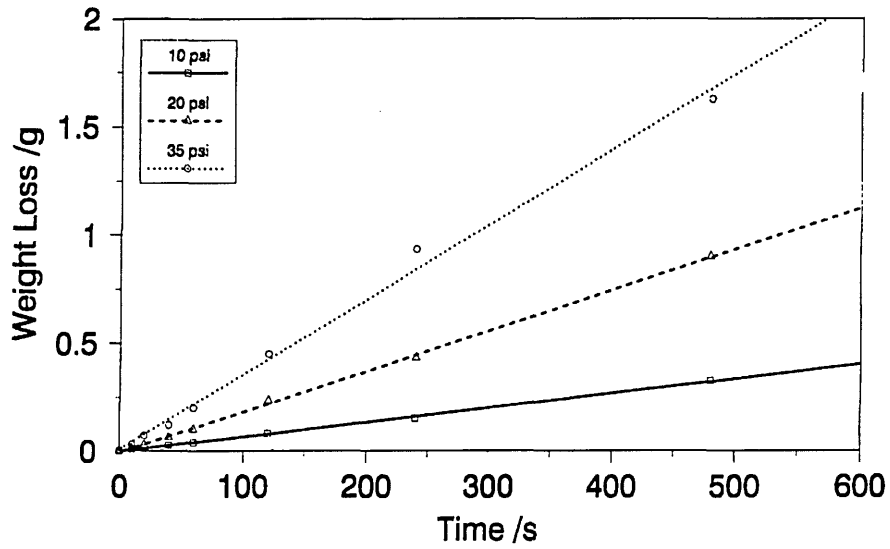


Figure 6.35: EDX analysis before and after grit blasting demonstrating the removal of surface contamination

Pressure / psi	Time / s	Nozzle – workpiece distance / cm
10	10, 20, 40, 60, 120, 240, 480	10, 15, 22.5
20	10, 20, 40, 60, 120, 240, 480	10, 15, 22.5
30	10, 20, 40, 60, 120, 240, 480	10, 15, 22.5

Figure 6.36: Table of parameters used during grit blasting optimisation trials

Gritting Trials - Effect of Pressure  
4", 220 grit



Gritting Trials - Effect of Distance  
20 psi, 220 grit

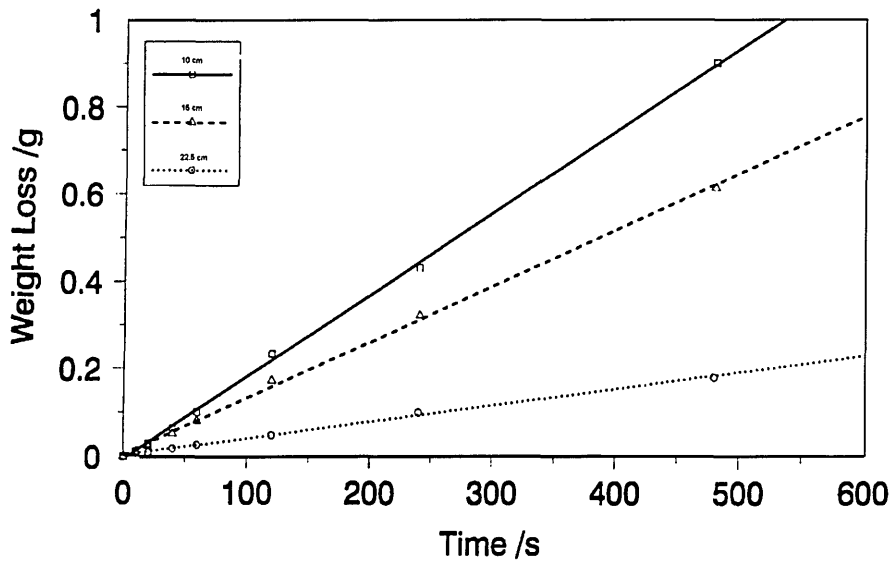


Figure 6.37: Graphs of weight loss against time showing the effects of pressure and distance respectively

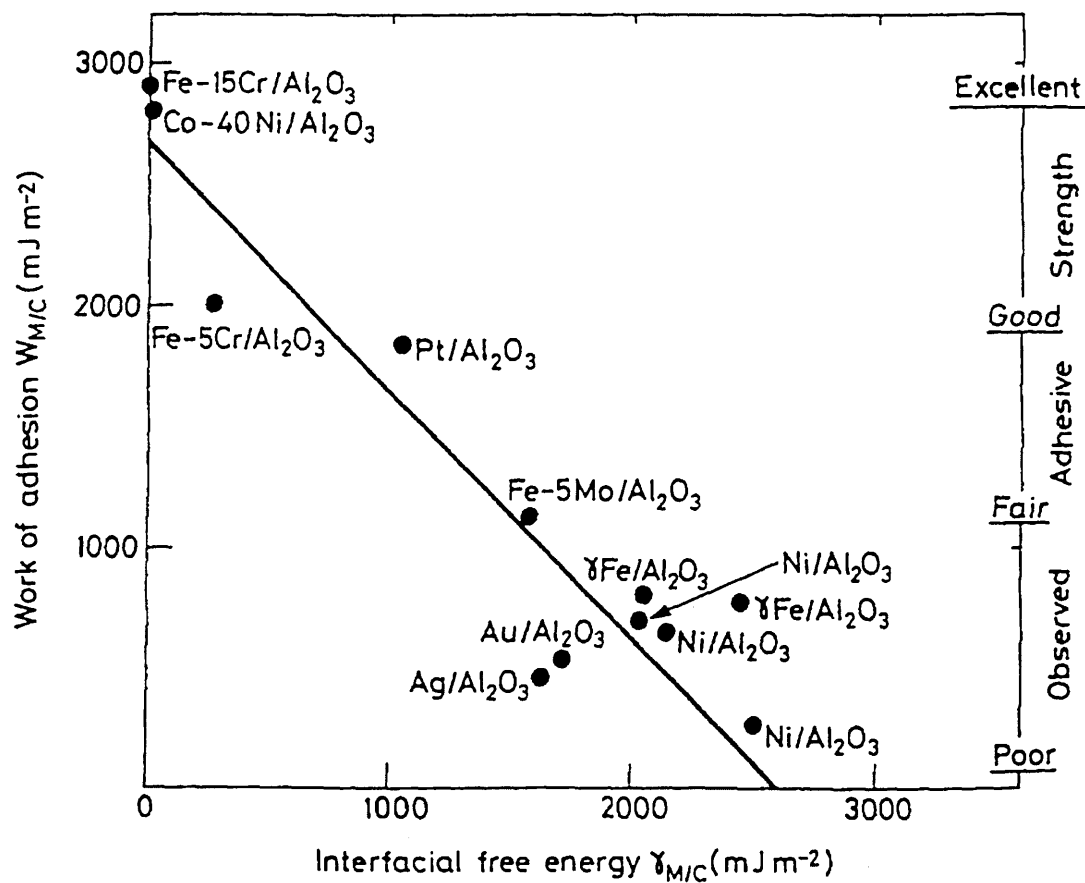


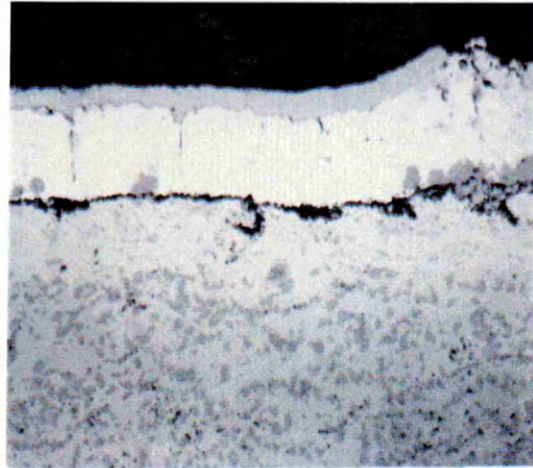
Figure 7.1: Graph of the empirical relationship between a number of metal/ceramic diffusion bonds

Precious metal addition	Plating process	Thickness / $\mu\text{m}$
Pd	electroplate	7.5
Ir	sputter	8.0
Ru	sputter	6.0
Rh/Pt	two-stage electroplate	2.5/5.0

Figure 7.2: Table of precious metal coating systems assessed



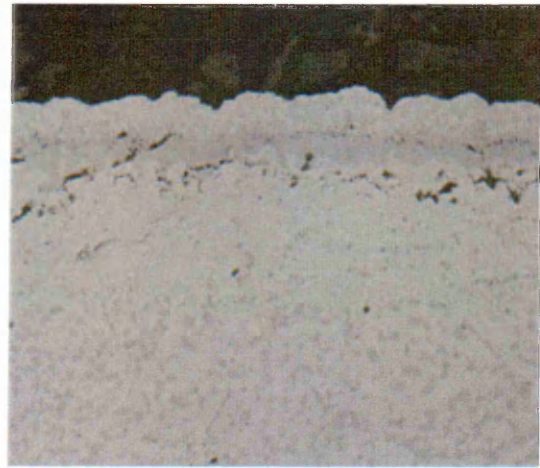
(a)



(b)



(c)



(d)

Figure 7.3(a-d): Micrographs of the systems based on alternatives to Pt, (Pd, Ru, Ir, Pt/Rh)

<b>Compositions of Pd modified MCrAlY</b>					
	<b>mass %</b>				
	<b>Ni</b>	<b>Co</b>	<b>Cr</b>	<b>Al</b>	<b>Pd</b>
<b>darker phase</b>	30	11.5	3	18	37
<b>lighter phase</b>	30	43	21	3.5	2

<b>Compositions of Ru modified MCrAlY</b>					
	<b>mass %</b>				
	<b>Ni</b>	<b>Co</b>	<b>Cr</b>	<b>Al</b>	<b>Ru</b>
<b>darker phase</b>	30	11.5	3	18	37
<b>lighter phase</b>	30	43	21	3.5	2

<b>Compositions of Ir modified MCrAlY</b>					
	<b>mass %</b>				
	<b>Ni</b>	<b>Co</b>	<b>Cr</b>	<b>Al</b>	<b>Ir</b>
<b>darker phase</b>	7	5	3.5	13	72
<b>lighter phase</b>	14	23	21	2	40

<b>Compositions of Pt/Rh modified MCrAlY</b>						
	<b>mass %</b>					
	<b>Ni</b>	<b>Co</b>	<b>Cr</b>	<b>Al</b>	<b>Pt</b>	<b>Rh</b>
<b>darker phase</b>	10	5	3	15	37	29
<b>lighter phase</b>	15	25	21	2	35	1.5

Figure 7.4: Comparison of the compositions of the P-type phases shown in Figure 7.3



Figure 7.5: Detail of the oxide formed on the MCrAlY+Ir system after 25 hours at 1100°C

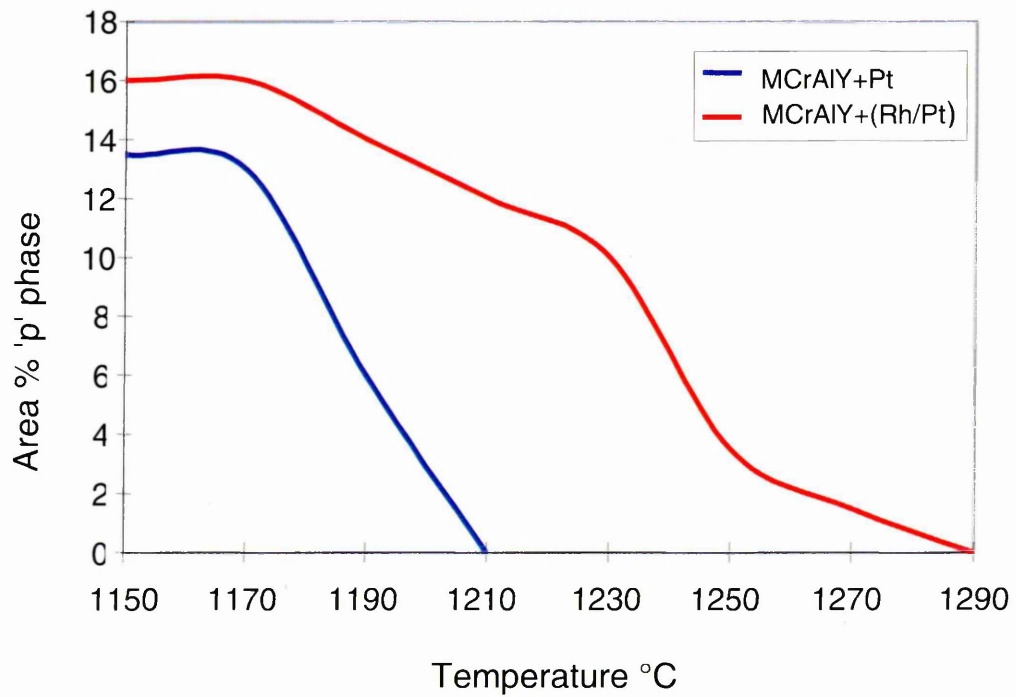


Figure 7.6: Phase stability of P-phase showing the effect of the addition of Rh

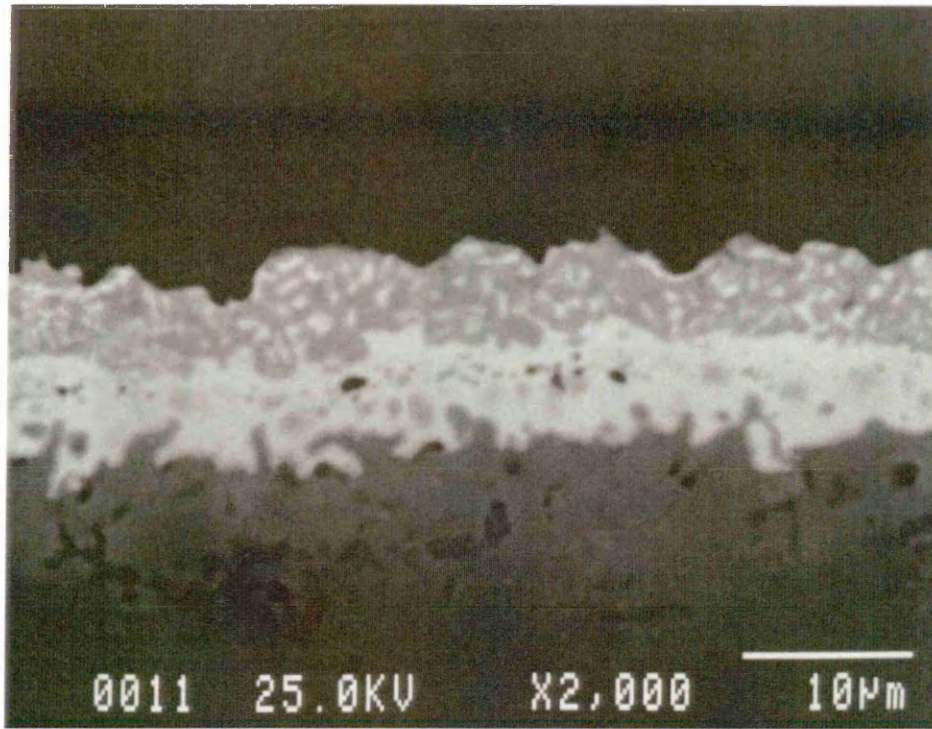


Figure 7.7: BSE micrograph of the Rh enhanced P-phase

<b>Composition of “base-coating”</b>					
	<b>weight %</b>				
	<b>Co</b>	<b>Ni</b>	<b>Cr</b>	<b>Al</b>	<b>Y</b>
<b>Coating A</b>	75	-	15.5	9	0.5
<b>Coating B</b>	65	-	25.5	9	0.5
<b>Std.</b>	36	34	21.5	8	0.5

Figure 8.1: Compositions of the MCrAlY type coatings examined

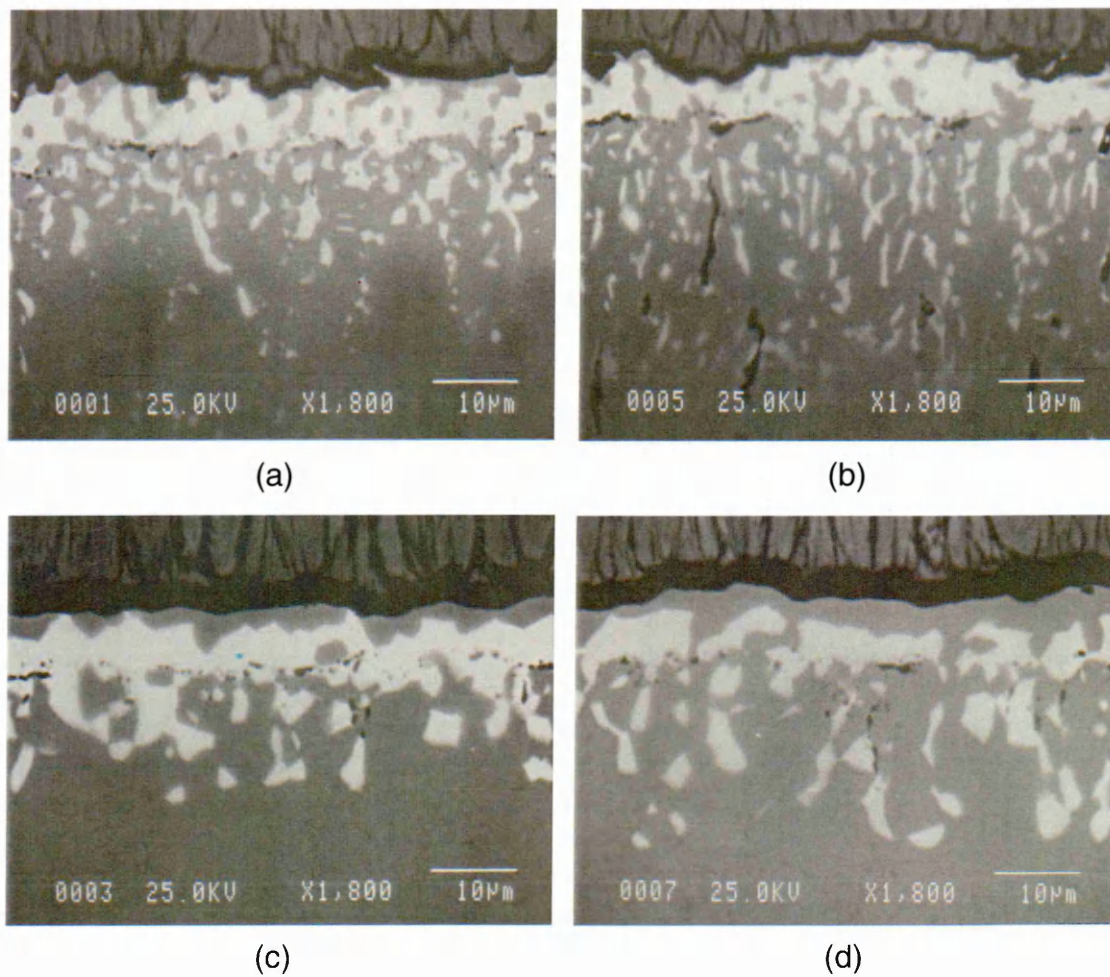


Figure 8.2(a-d): (a) Coating A as processed  
 (b) Coating B as processed  
 (c) Coating A after 25h @ 1150°C  
 (d) Coating B after 25h @ 1150°C

<b>Scratch Test Results / N</b>						
	<b>25 hour isothermal soaks</b>					
	<b>As proc.</b>	<b>1100°C</b>	<b>1150°C</b>	<b>1170°C</b>	<b>1190°C</b>	<b>1210°C</b>
<b>Coating A</b>	110	60	40	10	10	5
<b>Coating B</b>	80	35	20	20	10	0
<b>Std.</b>	100	50	45	20	15	10

Figure 8.3: Scratch test results for coatings A and B

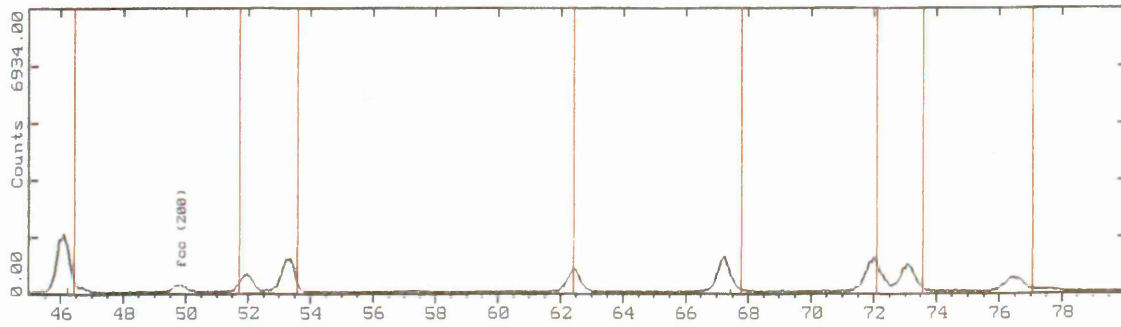
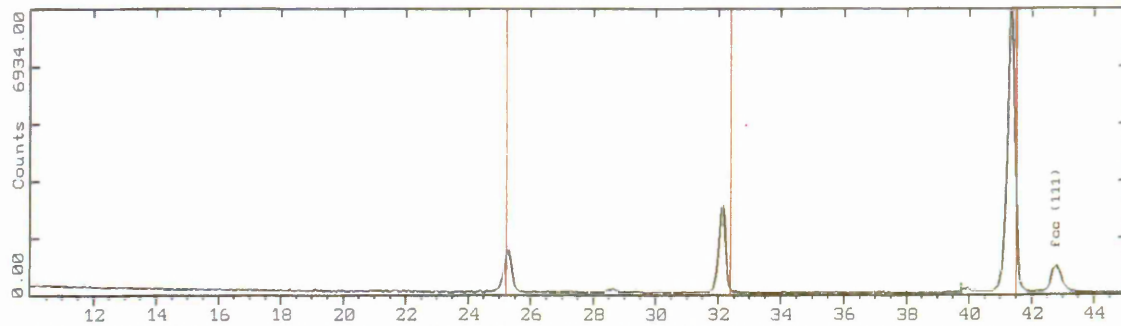
<b>P-phase Equivalent (as processed)</b>					
	<b>atomic %</b>				
	<b>Pt</b>	<b>Al</b>	<b>Co</b>	<b>Cr</b>	<b>Ni</b>
<b>Coating A</b>	34	37	22	7	0.3
<b>Coating B</b>	31	37	21	11	0.5
<b>Std.</b>	21	34	11	7	25

<b>Pt-enriched bonding <math>\gamma</math>-phase (as processed)</b>					
	<b>atomic %</b>				
	<b>Pt</b>	<b>Al</b>	<b>Co</b>	<b>Cr</b>	<b>Ni</b>
<b>Coating A</b>	10	7	62	21	0.3
<b>Coating B</b>	9	7.5	52	31	0.5
<b>Std.</b>	6	8.5	36	24	25

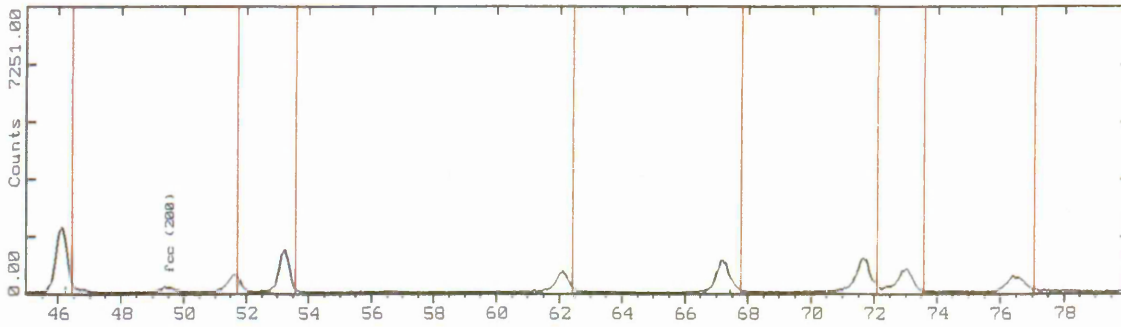
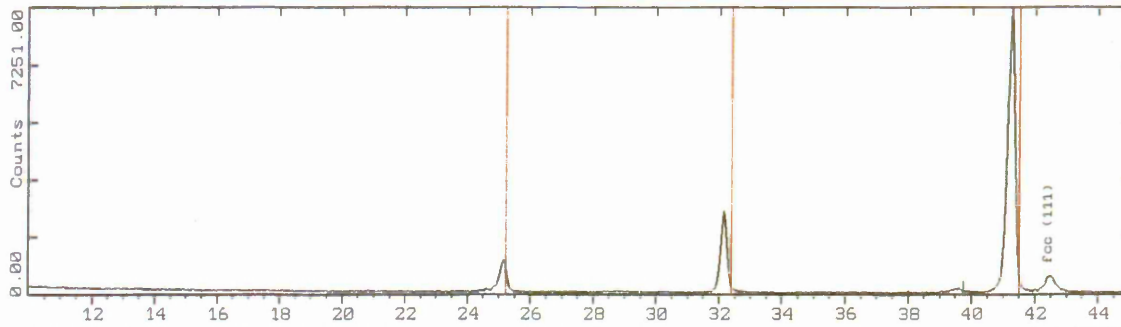
<b>P-phase Equivalent (25h at 1150°C)</b>					
	<b>atomic %</b>				
	<b>Pt</b>	<b>Al</b>	<b>Co</b>	<b>Cr</b>	<b>Ni</b>
<b>Coating A</b>	18.5	34	28	6	12
<b>Coating B</b>	18.5	35	25	9	12
<b>Std.</b>	10	31	15	7	35

<b>Pt-enriched bonding <math>\gamma</math>-phase (25h at 1150°C)</b>					
	<b>atomic %</b>				
	<b>Pt</b>	<b>Al</b>	<b>Co</b>	<b>Cr</b>	<b>Ni</b>
<b>Coating A</b>	5	9	57	19	9
<b>Coating B</b>	5	8	51	27	8
<b>Std.</b>	4	11	30	22	32

Figure 8.4: Compositions of phases in coatings A and B as processed and aged



Coating A



Coating B

Figure 8.5: XRD traces of coating A and B in the as processed condition

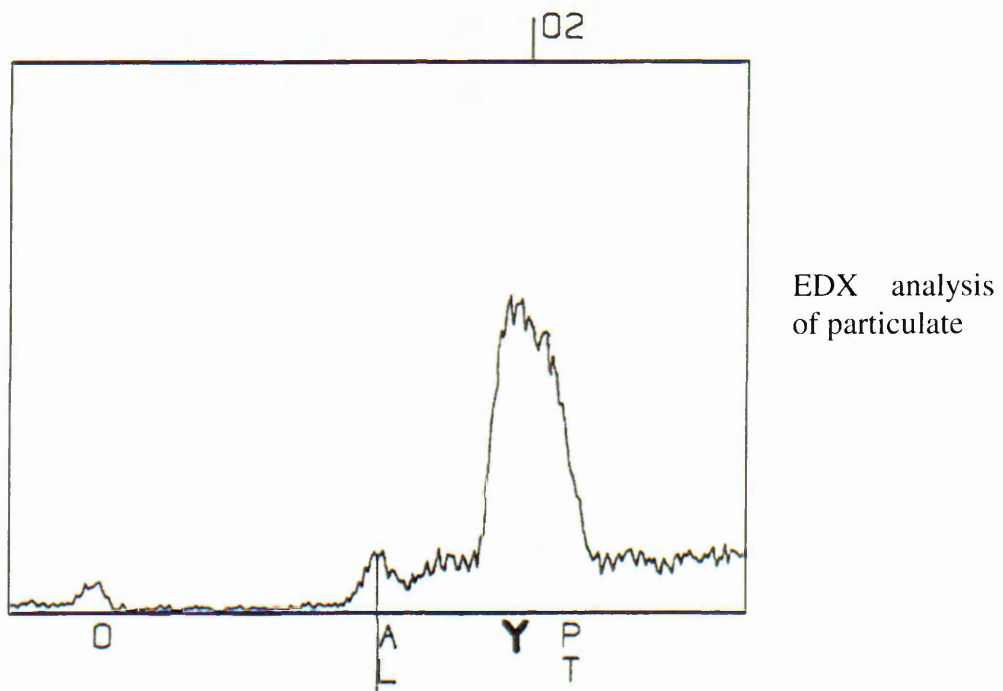
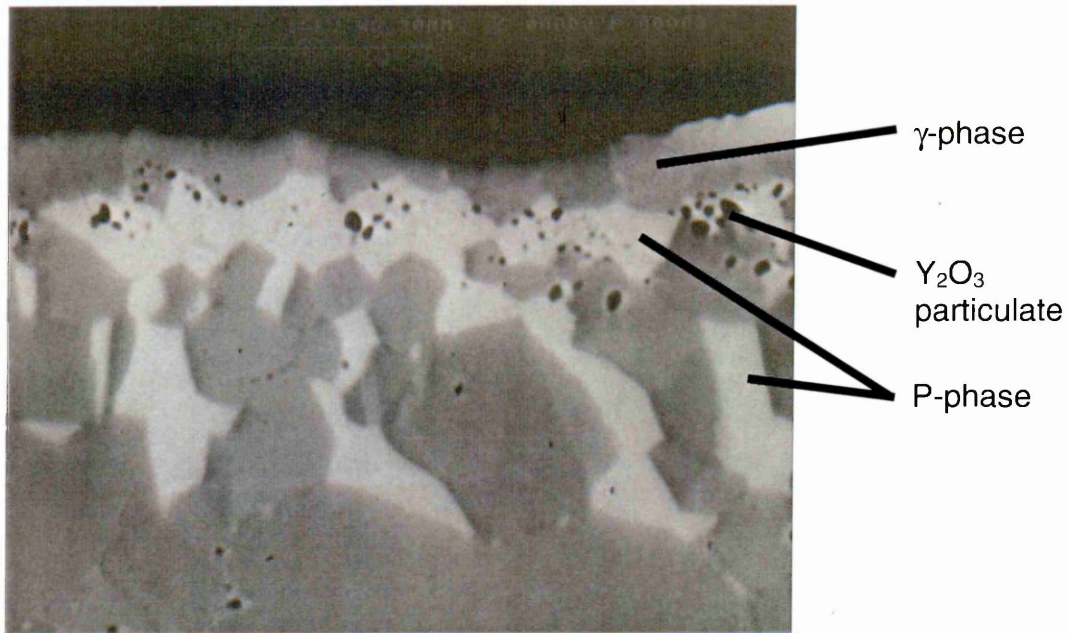
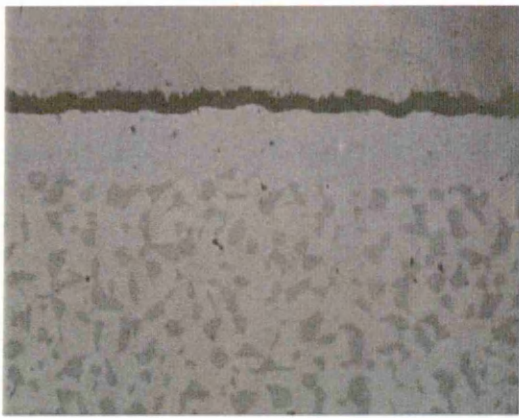
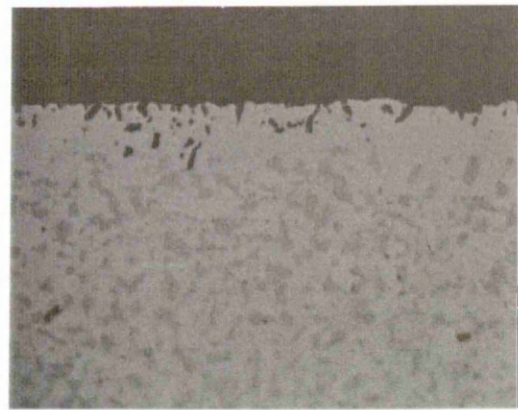


Figure 9.1: BSE image of Optimised MCrAlY+Pt and EDX analysis of the dark-contrast yttrium rich particulate



(a)



(b)

Figure 9.2: Comparison of the  $\beta$ -depletion zones of (a) EB-PVD and (b) Taguchi optimised LPPS MCrAlYs after 25 hours at 1100°C in air

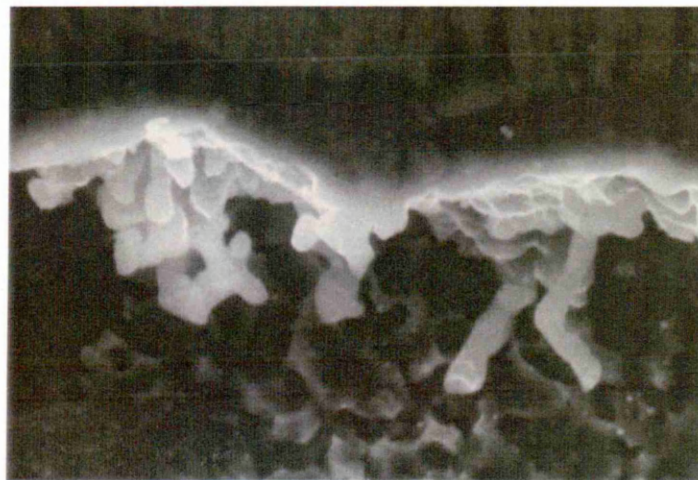
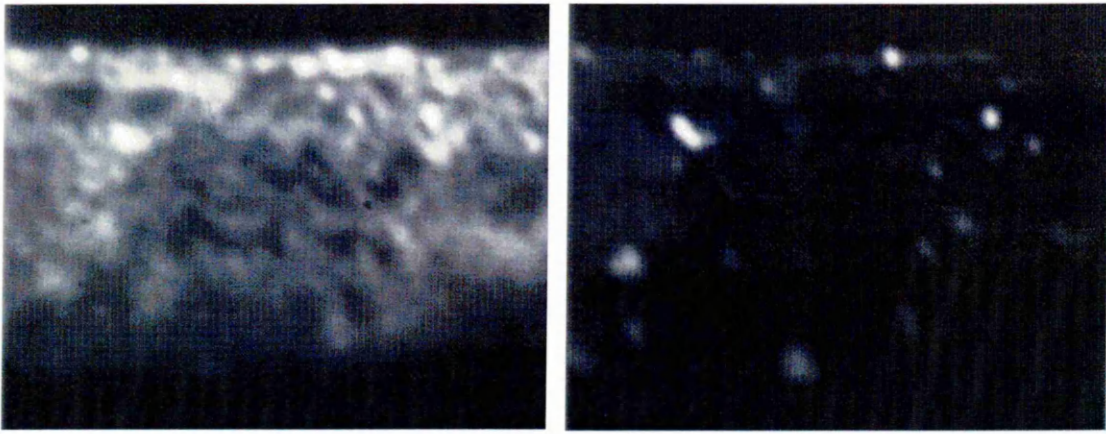


Figure 9.3: Detail of a deep etched MCrAlY showing  $Y_2O_3$  pegs



(a)

(b)

Figure 9.4: SIMS images of (a) Y and (b) Y<sub>2</sub>O<sub>3</sub> in the Taguchi optimised MCrAlY+Pt system

## References

1. A. Bennett, F. C. Toriz, A. B. Thakker, Surface & Coatings Technology, **32** 1987, p359
2. F. S. Pettit, G. W. Goward, Coatings for High Temperature Applications, Applied Science Pub., 1983, p341
3. S. M. Meier, D. K. Gupta, K. D. Sheffler, JoM, March, 1991, p50
4. J. R. Nicholls, D. J. Stephenson, Metals and Materials, March, 1991, p156
5. J. K. Tien, S. Purushothaman, Properties of High Temperature Alloys Ed. Z. A. Foroulis, F. S. Pettit, 1976, p3
6. D. L. Anton, Intermetallic Compounds v2, Ed. J. H. Westbrook, R. L. Fleischer, John Wiley & Son Ltd, 1994, p3
7. G. W. Meetham, Metals Technology, **11**, 1984, p414
8. C. T. Sims, A history of superalloy metallurgy for superalloy metallurgists, Proc. Int Symp. Superalloys, AIME, 1984, Ed M. Gell, p399
9. H. T. Michels, W. Z. Friend, Corrosion of Nickel & Nickel-based Alloys Ed. W. Z. Friend, Electrochemical Soc. Inc, 1980, p43
10. A. K. Jena, M. C. Chaturvedi, J of Materials Science **19**, 1984, p3121
11. G. P. Sabol, R. Stickler, Phys. Stat. Sol. **35**, 11, 1969, p11
12. E. W. Ross, C. T. Sims, Superalloys II, Ed. C.T. Sims, N. S. Stoloff, W.C. Hagel John Wiley & Son Ltd, 1987, p97
13. G. W. Meetham, Materials & Design, **10**, 2, 1989, p77
14. C. T. Sims, A history of superalloy metallurgy for superalloy metallurgists, Proc. Int Symp. Superalloys, AIME, 1984, Ed M. Gell, p399
15. R. F. Decker, Strengthening mechanisms in Ni-based superalloys, Strengthening Steels
16. R. J. E. Glenny, J. E. Northwood, A. Burwood-Smith, International Metal Review **20**, 1975, pl
17. G. W. Meetham, Materials & Design, **9**, 4, 1988, p213

18. B. M. Warnes, D. C. Punola, Power Generation Technology. Int. Review of Primary Power Production, Ed. R. Knox, Sterling, 1995
19. P. Strieff, Jn de Physique IV. Colloque C9. supplement au Jn de Phvsique 111 3, 1993, p17
20. J. Schaffer, G. M. Kim, G. H. Meier & F. S. Pettit: The role of active elements in the oxidation behaviour of high temperature metals and alloys, Ed. E. Lang, Elsevier Applied Science, 1991, p231
21. G. W. Goward & L. W. Cannon: Transactions of ASME, 110, 1988, p 150
22. G. W. Goward & D. H. Boone: Oxidation of Metals, 3, 5, 1971 p475
23. C. Duret & R. Pichoir: Coatings for High Temperature Applications Ed. E. Lang, Applied Science Publishers, 1984, p33
24. J. R. Nicholls, D. J. Stephenson: Metals and Materials, March, 1991, p156
25. D. F. Bettridge & R. G. Wing: ASME International Gas Turbine Conference, Dusseldorf June 1986
26. H. M. Tawancy, N. M. Abbas & T. N. Rhys-Jones: Surface & Coatings Technology, 49, 1991, p 1
27. M. S. Farrel, D. H. Boone & R. Streiff: Surface and Coatings Technology, 32, 1987, p69
28. P. C. Patnaik: Surface Modifications Technologies II, Ed. T. S. Sudarshan & D. G. Bhat, The Minerals, Metals & Materials Soc. 1989
29. M. M. Morra, R. D. Sisson Jr. & R. R. Biederman: A microstructural study of MCrAlY coatings
30. J. Stringer: Surface Engineering, Ed. R. Kossowsky & S. C. Singhal, NATO ASI series E: Applied Science, 85, 1984
31. L. Peichl & D. F. Bettridge: Materials for Advanced Power Engineering, part I, p717, 1994
32. N. Czech, V. Kolarik, W. J. Quadackers & W. Stamm: Surface Engineering, 13, 5, 1997, p384
33. D. K. Gupta et al. U. S. Patent 4,419,416, Dec. 1983
34. A. Bennett, Materials Science & Technology, 12, 1986, p257

35. T. N. Rhys-Jones, Corrosion Science, **29**, 6, 1989, p623
36. S. M. Meier, D. K. Gupta & K. D. Sheffler: Ceramic thermal barrier coatings for commercial gas turbine engines, J. O. M. March, 1991
37. H. E. Evans: Materials Science and Engineering, **A120**, 1989, p139
38. R. E. Jones: Interface Studies on EB-PVD Ceramics, MSc Sheffield Hallam University / University of Hull, September 1993
39. R. Prescott, M. J. Graham, Oxidation of Metals, **38**, 3/4, 1992, p233
40. H. Hindman, D. P. Whittle, Oxidation of Metals, **18**, 5/6, 1982, p245
41. J. G. Li, In American Ceramic Society, **75**, 11, p3118
42. J. Doychak, J.L. Smialek & C. A. Barrett, Oxidation of High Temperature Intermetallics. Ed. T. Grobsten & J. Doychak, Minerals, Metals & Materials Soc, 1989, p41
43. H. M. Tawancy: Journal of Materials Science, **28**, 1993, p561
44. J. L. Smialek, G. H. Meier, Superalloys II, Ed. C. T. Sims, N. S. Stoloff, W.C. Hagel, John Wiley & Son, 1987, p293
45. J Jedlinski, S. Mrowec, Materials Science & Engineering, **87**, 1987, p281
46. L. Lelait, S. Alperine, & R. Mevrel: Journal of Material Science, **27**, 1992, p5
47. M. Schutze: Materials Science and Technology, May 1988, **4**, p407
48. F. H. Stott & G. C. Wood, Materials Science & Engineering, **87**, 1987, p267
49. B. C. Wu, E. Chang, C. H. Chou & M. L. Tsai: Journal of Materials Science, **25**, 1990, p1112
50. L. B. Pfeil, U.K. patent 459848, 1937
51. H. M. Tawancy, N. M. Abbas & A. Bennett: Surface and Coatings Technology, **68/69**, 1994, p10
52. A. M. Huntz: The Role of Active Elements in the Oxidation Behaviour of High Temperature Metals and Alloys, Ed. E. Lang Elsevier Applied Science
53. B. A. Pint Oxidation of Metals, **45**, 1/2, 1996, p1

54. Y. Ikeda, K. Nii, & K. Yoshihara: Transcript of Japanese Institute of Metals Supplement, 1982, p207
55. P. Y. Hou & J. Stringer: Oxidation of Metals, **38**, 5/6, 1992, p323
56. C. Forest & J. H. Davidson: Oxidation of Metals, **43**, 5/6, 1995, p479
57. J. L. Smialek: Effect of Sulphur Removal on Alumina Scale Adhesion, manuscript submitted Nov. 1989
58. A. W. Funkenbusch, J. G. Smeggil & N. S. Bornstein: Metallurgical Transactions A, **16A**, 1985, p1164
59. H. J. Grabke, G. Kurbatov, H. J. Schmutzler, Oxidation of Metals, **43**, 1/2, 1995, p97
60. K. L. Luthra, C. L. Briant, Oxidation of Metals, **26**, 5/6, 1986 p397
61. F. H. Stott, The Role of Active Elements in the Oxidation Behaviour of High Temperature Metals and Alloys, Ed. E. Lang, Elsevier Applied Science, 1991, p3
62. J. L. Smialek: Microscopy of Oxidation Proceedings, Ed. M. J. Bennett & G. W. Lorimer, March 1990
63. R. Kingswell: PhD Thesis – Properties of Vacuum Plasma Sprayed Alumina and Tungsten Coatings, Brunel University, 1991
64. H. Herman: Scientific American, September 1988, p78
65. A. Vardelle, J. M. Baronnet, M. Vardelle & P. Fauchais: I.E.E.E Transcripts, Plasma Science, **8**, 1980, p417
66. G. R. Jordon & L. A. King: British Journal of Applied Physics, **16**, 1965, p431
67. K. J. Takeda: Japanese Metallurgical Society, **10**, 1985, p822
68. K. Takeda, K. Hayashi & T. Ohasi: 7<sup>th</sup> Int Symposium on Plasma Chemistry, **B61**, 1985
69. P. C. Wolf & F. N. Longo: Proc. 9<sup>th</sup> Int. Thermal Spray Conference, 1980, p187
70. H. Herman: M.R.S. Bulletin, December 1988, p60

71. A. R. Nicholl, H. Gruner, R. Prince & G. Wuest: Surface Engineering, 1985, **1**, No. 1, p59
72. R. K. Roy, A Primer on the Taguchi Method, Van Nostrand Reinhold, 1990
73. Y. Wu & W. H. Moore: Quality Engineering – Product and Process Optimisation, Dearborn, American Supplier Institute
74. P. M. Burgman: Manufacturing Engineering, May 1985, p44
75. Y. Wu: Orthogonal Arrays and Linear Graphs, Dearborn, American Supplier Institute
76. D. S. Rickerby: Internal Memorandum, Rolls-Royce plc, June 1995
77. A. Atkinson: Materials Science and Technology, December 1988, **4**, p1046
78. P. Fox & G. J. Tatlock: Materials Science & Technology, **5**, 1989, p816
79. E. Lopez, F. Beltzung & G. Zambelli: Journal of Materials Science Letters, **8**, 1998
80. G. M. Hamilton & L. E. Goodman: Journal of Applied Mechanics, **33**, 1966, p371
81. P. J. Burnnett & D. S. Rickerby: Thin Solid Films, **154**, 1987, p403
82. S. J. Bull, D. S. Rickerby, A. Matthews, A. Leyland, A. R. Pace & J. Valli: Surface Coatings Technology, **36**, 1988, p503
83. AEA Technology, Harwell: ENCO Club Report AERE-G5445
84. W. Y. Chan, P. K. Datta, G. Fisher & J. S. Burnell-Grey: Interim Progress Report for 1997, EPSRC Contract Number GR/K02367
85. E. D. Hondros: Science of Hard Materials, 1986, p121
86. International Nickel Ltd: Rhodium, 1965
87. International Nickel Ltd: Iridium, 1965
88. U.S. Patent Specification Number 1259157
89. U.S. Patent Specification Number 3754903
90. U.S. Patent Specification Number 3676085

91. M. Gobel, A. Rahme, M. Schutze, M. Schorr & W. T. Wu: Materials at High Temperature, **00**, 0, 1993, p1
92. H. M. Tawancy, N. M. Abbas & T. N. Rhys-Jones: Surface & Coatings Technology **54/55**, 1992, p1
93. P. Morrell: Rolls-Royce plc report DNS34325
94. J. A. Gobel, R. H. Barkalow & F. S. Pettit: Proc. Tri Service Conf on Corrosion, Ed. M Levy & J. Brown, Metals and Ceramics, 1978, p165
95. H. M. Tawancy, N. Sridhar, B. S. Tawabini, N. M. Abbas & T. N. Rhys-Jones: Journal of Materials Science, **27**, 1992, p6463
96. C. Forest, J. H. Davidson, Oxidation of Metals, **43**, 5/6, 1995, p479
97. K. N. Strafford: High Temperature Technology, **1**, 6, November 1983, p307
98. C. J. Spengler, S. Y. Lee & S. T. Scheirer: Hot Corrosion Evaluation of High Temperature Metal Protective Coatings for Combustion Turbines, pre-print for Thin Solid Films, 1979
99. R. Wehrmann: High Temperature Materials Technology, Ed. I. E. Campbell, E. M. Sherwood, John Wiley & Sons Inc. London, 1967